

UNIVERSITÀ DELLA CALABRIA



UNIVERSITÀ DELLA CALABRIA

Dipartimento di Fisica

Dottorato di Ricerca in

Scienze e Tecnologie Fisiche, Chimiche e dei Materiali (STFCM)

XXX CICLO

**SELF-ASSEMBLED MONOLAYERS OF ORGANIC MOLECULES
ON NOBLE METALS AND TWO-DIMENSIONAL MATERIALS**

Settore Scientifico Disciplinare: FIS/01

Coordinatore: Ch.mo Prof. Vincenzo Carbone

Vincenzo Carbone

Supervisore/Tutor: Dott. Tommaso Caruso

Tommaso Caruso

Dottorando: Dott. Oreste De Luca

Oreste De Luca

*Dedicated to the people
who fill my life everyday*

Abstract

This thesis reports a study of several two-dimensional supramolecular networks deposited on gold surface and two-dimensional materials. The work aims to evidence the formation of the molecular assemblies and their related interaction with the underlying substrates.

First, the metal-organic interface between Zn(II) tetraphenyl porphyrin (ZnTPP) and Au(111) is systematically characterized as a function of the molecular coverage. We found that the interaction between the gold surface and the molecular monolayer is considerable, unlike one might expect from this particular system. Moreover, the molecular diffusion process is also evidenced.

Afterwards, the self-assembly of the Nile red molecules on Au(111) substrate, from sub- to mono- layer coverages, is reported for the first time. The dependence of molecular packing from the thermal treatments of the samples is evidenced, while further information are also gained on the intermolecular interaction and on molecular mobility.

Later, supramolecular assembly of two carboxylic acids, i.e. benzene-1,4-dicarboxylic acid (terephthalic acid, TPA) and benzene-1,3,5-tricarboxylic acid (trimesic acid, TMA) deposited on graphene substrate were investigated. After determining the monolayer packing, the structural transition that occurs as molecular deposition proceeds over the monolayer coverage is determined. We evidence that, despite the chemical similarity between the two molecules, their monolayer-to-thin-film transitions are dramatically different.

Finally, the effect of the deposition of the electron acceptor 7,7,8,8-tetracyanoquinodimethane (TCNQ) molecules on the surface of a prototypical topological insulator, i.e. bismuth selenide (Bi₂Se₃), is reported. The molecular assembly was determined, while a negligible charge transfer between the molecular layer and the substrate are also found.

In addition to the main topic of the work, the thesis also reports other research activities connected to the two-dimensional systems. In particular, the growth and characterization of graphene films on copper foil, by means of Chemical Vapor Deposition (CVD) are performed. The different coupling of graphene layer on the Cu foil and the possibility to induce a variation of the graphene coupling with respect to the Cu substrate by visible-light irradiation above a proper power threshold are evidenced. Finally, the nucleation and growth of iron cluster on MgO/Ag(100) surface is considered. Relevant information are obtained on the cluster size dependence from deposition temperature of the substrate and from the nominal coverage.

Keywords: Scanning tunneling microscopy (STM), X-ray photoelectron spectroscopy (XPS), self-assembly, supramolecular architectures, graphene, topological insulator, chemical vapor deposition, Raman spectroscopy, metal clusters.

Astratto

Questo lavoro di tesi riporta uno studio di diversi assemblati molecolari bidimensionali depositati su superfici di oro e su materiali bidimensionali. Il lavoro si propone in particolare di evidenziare sia la formazione degli assemblati molecolari che la loro interazione con i substrati sottostanti.

Per prima cosa, l'interfaccia metallorganica tra la Zinco-Tetrafenilporfirina (ZnTPP) e la superficie cristallina di Au(111) è stata sistematicamente caratterizzata in funzione del ricoprimento molecolare. L'interazione stimata tra la superficie dell'oro e il monostrato molecolare è considerevole, più di quanto ci si potesse aspettare da questo particolare sistema.

In seguito, viene riportato, per la prima volta, l'auto-assemblaggio delle molecole di Rosso Nilo sulla superficie di oro, al variare del ricoprimento molecolare, ovvero dal ricoprimento parziale della superficie fino al monostrato molecolare. In particolare, è stata evidenziata la dipendenza dell'impacchettamento molecolare dai trattamenti termici dei campioni, mentre ulteriori informazioni sono state ottenute sulle interazioni intermolecolari e sulla mobilità molecolare.

A seguire, gli auto-assemblati molecolari di due acidi carbossilici, ovvero l'acido tereftalico (TPA) e l'acido trimesico (TMA) sono stati studiati sulla superficie di grafene. Dopo aver determinato l'impacchettamento molecolare del monostrato, è stata evidenziata inoltre la differente transizione strutturale che si verifica quando la deposizione delle molecole procede oltre la copertura del monostrato.

Infine, viene riportato l'effetto della deposizione di molecole accettori di elettroni, ovvero il TCNQ, su un isolante topologico, ovvero il bismuto selenio (Bi_2Se_3). L'analisi effettuata ha consentito di determinare l'impacchettamento molecolare, ed ha ulteriormente messo in evidenza un trasferimento di carica trascurabile tra lo strato molecolare e il substrato.

Oltre al tema principale del lavoro, la tesi riporta anche altre attività di ricerca connesse ai sistemi bidimensionali. In particolare, sono state eseguite la crescita e la caratterizzazione di film di grafene su fogli di rame (Cu), mediante Deposizione Chimica da Vapori (CVD). Il differente accoppiamento dello strato di grafene sul foglio di Cu e la possibilità di indurre una variazione dell'accoppiamento di grafene rispetto al substrato stesso mediante irradiazione di luce visibile, al di sopra di una ben determinata soglia di potenza, sono stati evidenziati in seguito all'analisi effettuata. Infine, viene considerata la nucleazione e la crescita di cluster di ferro sulla superficie di ossido di magnesio (MgO) cresciuto su Ag (100). Informazioni rilevanti sono ottenute sulla dipendenza dalle dimensioni del cluster dalla temperatura di deposizione del substrato e dalla copertura nominale.

Parole chiave: Microscopia a Scansione Tunnel (STM), spettroscopia fotoelettronica a raggi (XPS), auto-assemblaggio, architetture molecolari, grafene, isolante topologico, deposizione chimica da vapore, spettroscopia Raman, cluster metallici.

Contents

Abstract (English/Italian)	i
Contribution	vii
Introduction	1
References	4
1. Methods	7
1.1 Scanning Tunneling Microscopy	8
1.1.1 Quantum Tunneling	9
1.1.2 Bardeen approximation	11
1.1.3 STM imaging	14
1.2 Scanning Tunneling Spectroscopy (STS)	15
References	17
Part I: Molecular Self-Assembly	18
2. STM and XPS investigation of ZnTPP adsorption on Au(111) surface: from monolayer to multilayer transition	19
2.1 Introduction	20
2.2 Experimental section	22
2.3 Results and discussion	23
2.3.1 STM investigation of ZnTPP self-assembly on Au(111) at Room Temperature	23
2.3.2 XPS investigation of ZnTPP coverage dependence on Au(111)	29
2.4 Surface diffusion of the ZnTPP 2 nd layer	34
2.5 Conclusions	36
References	37
2.6 Appendix section	41

3. Investigation of Nile Red self-assembled monolayer on Au(111)	43
3.1 Introduction	44
3.2 Experimental section	44
3.3 Results and discussion	47
3.3.1 Nile Red assembly at submonolayer coverage	47
3.3.2 Monolayer Regime of Nile Red on Au(111)	50
3.3.3 Nile Red mobility	58
3.4 Conclusions	59
References	61
4. TMA and TPA self-assemblies on graphene	63
4.1 Introduction	64
4.2 Experimental section	66
4.3 Results and discussion	68
4.3.1 Monolayer structure of TMA and TPA on HOPG and graphene	68
4.3.2 Resolving the structure of TMA thin-films	72
4.3.3 Structural transition in TPA thin-films	78
4.4 Conclusions	81
References	82
4.5 Appendix section	85
5. TCNQ physisorption on the Bi₂Se₃ Topological Insulator	99
5.1 Introduction	100
5.2 Experimental section	101
5.3 Results and discussion	102
5.4 Conclusions	106
References	107
5.5 Appendix section	111

Part II: CVD graphene on Cu foil	114
6. Coupled and freestanding behaviour of monolayer graphene deposited by low pressure CVD (LP-CVD) on Cu foil	115
6.1 Introduction	116
6.2 Experimental section	117
6.3 Results and discussion	118
6.3.1 Monolayer graphene coupling on Cu foil	118
6.3.2 Laser-induced transition from coupled- to freestanding- graphene	128
6.4 Conclusions	132
References	133
7. Characterization of graphene grown on copper foil by Chemical Vapor Deposition (CVD) at ambient pressure conditions	137
7.1 Introduction	138
7.2 Experimental section	139
7.3 Results and discussion	141
7.4 Conclusions	148
References	150
7.5 Appendix section	153
Part III: Metal clusters on metallic surface	155
8. Nucleation and growth of iron clusters on MgO/Ag(100)	156
8.1 Introduction	157
8.2 Nucleation and growth	157
8.2.1 Clusters irreversible growth	159
8.2.2 Ostwald and Smoluchowski Ripening	161
8.3 Nucleation and growth of Fe clusters on MgO/Ag(100)	164
8.3.1 Experimental setup	164
8.3.2 Results and discussion	165

8.3.3 Conclusions and outlooks	171
References	172
9. Conclusions and outlooks	174
References	175
Acknowledgements	178
Curriculum Vitae	179

Contribution

I. Co-Authorship Declaration

This thesis incorporates material that is result of joint research, as follows:

Chapter 2: The XPS measurements were acquired at Elettra Synchrotron (APE beamline) and analysed by Dr. Marco Papagno, Dr. Daniela Pacilé (Department of Physics – Università della Calabria, Italy) as well as her PhD student Ilenia Grimaldi.

Chapter 4: The AFM, TEM results, as well as the graphene grown on the copper foil and successive transfer on the TEM grid, were gained by Dr A. J. Marsden, Z. P. L. Laker under the supervision of the Prof. N. R. Wilson at the Department of Chemistry – University of Warwick (UK)

Chapter 5: The Bi_2Se_3 samples were synthesized under the supervision of Dr. E.V. Chulkov at the Saint Petersburg State University. STM data were acquired and analysed by Dr. Ada Della Pia at the Giovanni Costantini laboratory – Department of Chemistry – University of Warwick (UK), while the DFT calculation was performed by Dr. A. Arnau (Donostia International Physics Center (DIPC), Donostia-San Sebastian, Spain)

Chapter 6 - 7: The Raman acquisitions and analysis was performed in collaboration with the Raman spectroscopy group (Prof. Enzo Cazzanelli, Dr. Marco Castriota) – Department of Physics – Università della Calabria (Italy) and with the Prof. G. Mariotto – Department of Computer Science – Università di Verona (Italy).

Chapter 8 reports the experimental results collected during my PhD stage at the École Polytechnique Fédérale de Lausanne (EPFL) – Prof. Harald Brune research group.

I have obtained the permission from each of the co-author(s) to include the above material(s) in my thesis. I certify that, with the above qualification, the thesis, and the research to which it refers, is the product of my own work.

II. Declaration of Previous/Current Publication

The work of this thesis is based on the following publications (published, submitted or in preparation) reported below.

Thesis chapter	Publication title/ Full citation	Publication status
Chapter 2	<i>“STM and XPS investigation of Zinc(II) tetraphenylporphyrin (ZnTPP) adsorption on Au(111) surface”</i> . <u>O. De Luca</u> , T. Caruso, I. Grimaldi, D. Pacilé, A. Policicchio, V. Formoso, M. Papagno and R.G. Agostino.	In preparation
Chapter 3	<i>“Investigation of Nile Red self-assembled monolayer on Au(111)”</i> . T. Caruso, <u>O. De Luca</u> , M. Turano, A. Ionescu, N., Godbert, A. Policicchio and R.G. Agostino.	In preparation
Chapter 4	<i>“Monolayer-to-thin-film transition in supramolecular assemblies: the role of topological protection”</i> . A. J. Marsden, Z. P. L. Laker, <u>O. De Luca</u> , A. Della Pia, L. M. A. Perdigao, G. Costantini, N. R. Wilson. <i>Nanoscale</i> , 2017, 9, 11959–11968	Published*
Chapter 5	<i>“TCNQ physisorption on the Bi₂Se₃ topological insulator”</i> . A. Della Pia, S. Lisi, <u>O. De Luca</u> , D. Warr, M. M. Otrokov, Z. S. Aliev, E. V. Chulkov, R. G. Agostino, A. Arnau, M. Papagno and G. Costantini.	Submitted
Chapter 6	<i>“Different spectroscopic behavior of coupled and freestanding graphene monolayer deposited by CVD on Cu foil”</i> . E. Cazzanelli, M. Castriota, A. Fasanella, R. Grillo, <u>O. De Luca</u> , A. Policicchio, G. Desiderio, R.G. Agostino, M. Giarola, and G. Mariotto.	In preparation*
Chapter 7	<i>“Characterization of graphene grown on copper foil by Chemical Vapor Deposition (CVD) at ambient pressure conditions”</i> . E. Cazzanelli, <u>O. De Luca</u> , D. Vuono, A. Policicchio, M. Castriota, G. Desiderio, M. P. De Santo, A. Aloise, A. Fasanella, T. Rugiero, R. G. Agostino.	Accepted

*The publication (published or in preparation) is included inside the chapter. However, some sections of the same chapter are not comprised in the publication.

Other related publications that this thesis is not directly based on but where I have contributed as an author are listed below:

1. *“FePc Adsorption on the Moiré Superstructure of Graphene Intercalated With a Co Layer”*. G. Avvisati, S. Lisi, P. Gargiani, A. Della Pia, O. De Luca, D. Pacilé, C. Cardoso, D. Varsano, D. Prezzi, A. Ferretti, and M. G. Betti. *J. Phys. Chem. C*, 2017, 121 (3), pp 1639–1647.
2. *“Chemical bond and charge transfer dynamics of a dye-hierarchical TiO₂ hybrid interface”*. C. Castellarin-Cudia, T. Caruso, E. Maccallini, A. Li Bassi, P. Carrozzo, O. De Luca, A. Goldoni, V. Lyamayev, K. C. Prince, F. Bondino, E. Magnano, R. G. Agostino, C. S. Casari. *J. Phys. Chem. C*, 2015, 119 (16), pp 8671–8680

III. Scientific collaborations with national and foreign research groups

Dr. Marco Papagno, Dr. Daniela Pacilé – Department of Physics – Università della Calabria, Italy

Prof. Giovanni Costantini – Department of Chemistry – University of Warwick, UK

Prof. Enzo Cazzanelli, Dr. Marco Castriota – Department of Physics – Università della Calabria, Italy

Dr. Nicolas Godbert, Dr. Andreea Ionescu – Department of Chemistry – Università della Calabria, Italy

Dr. Maria Penelope De Santo – Department of Physics – Università della Calabria, Italy

Dr. Danilo Vuono – Department of Chemical and Environmental Engineering – Università della Calabria, Italy

Introduction

Synthesizing and controlling advanced functional nanostructured materials and devices is one of the most important scientific challenges to be faced in the next years. The development of these next-generation devices promise to revolutionize several fields in which they will find application, including electronics, physics, chemistry, biology and medicine.

In order to realize these functional materials, the nanofabrication methods are divided into two major categories, i.e. the “top–down” and the “bottom–up” approaches. While the top-down method allows creating nano-functional devices with the desired shapes and characteristics starting from larger dimensions of the components and reducing them to the required values, by using several lithography methods^[1-3], the “bottom-up” fabrication aims to create multifunctional nanostructured materials and devices by the self-assembly of atoms or molecules.

The most obvious advantage of the last methodology concerns the possibility to directly control the atomic or molecular assemblies. Some of the most prominent bottom–up nanofabrication methods include atomic layer deposition,^[4] sol–gel nanofabrication,^[5] vapor phase deposition of nanomaterials^[6] and molecular self-assembly.^[7] Among the last techniques, self-assembly of molecular compounds was well-acknowledged as one of the efficient bottom-up approaches to synthesize various materials with controllable architectures and novel properties.^[8-11]

Molecular self-assembly (MSA) is the process by which molecules assemble themselves without the presence of outside interactions.^[12,13] Relevant examples of self-assembly structures are present in nature, including the formation of the lipid bilayer of the membranes of cells, the cellular membranes and the folding and aggregation of peptides and proteins. In order to create new types of supramolecular networks, the most versatile and prominent MSA strategy is based on the Self Assembled Monolayers (SAMs) approach. As a matter of facts, SAMs represent one of the most effective strategy for surface functionalization. As a result, in these last years, a huge amounts of organic molecules were deposited on the semi-conductors, noble metal surfaces and two dimensional materials in order to achieve this goal.

The synthesis and growth of such two-dimensional architectures is driven by the interplay of intricate intermolecular and molecule-substrate interactions. If on one hand the stability and the order of the molecular networks arise from the ensemble of multiple intermolecular non-covalent interactions such as hydrogen bonding,^[14,15] van der Waals forces,^[16] hydrophobic and electrostatic interactions,^[17-19] dipole–dipole interactions^[20-22] and coordination

interactions,^[23,24] on the other hand the covalent or non-covalent interaction with the underlying substrate influence the final assembly^[25] and consequently the resulting surface functionalization.

Indeed, molecular self-assemblies strongly bonded to the surface, i.e. through chemical bonding, allows to strictly modify its properties. For instance, a much studied system is the case of thiol networks on metal surfaces,^[26-28] where molecules are bonded to the solid substrate by a reactive head that provides a strong molecule–substrate bond. Conversely, the non-covalent self-assemblies show a weak interaction with the surface (including hydrogen bonds and van der Waals interaction), i.e. in this particular case, molecules are physisorbed on the underlying substrate. The surface functionalization by means of weak interacting molecular assemblies shows obvious advantages with respect to the covalent one. Firstly, the surface properties can be functionalized by the self-assembly deposition without “chemically” modify the substrate, that is, in other words, the pristine surface is preserved. Furthermore, the lacking of anchored groups allows to investigate the molecular cores, which express a precise functionality because directly interacting with the surfaces. In addition, the surface can also be employed as an “inert” template in order to study the molecular self-assembly and the mechanisms underlying its formation.

In that background, the main purpose of this thesis is to investigate non-covalent self-assemblies of organic molecules on noble metals and two-dimensional materials, as reported in the **Part I** of this work. In particular, Scanning Tunneling Microscopy (STM) technique allows us to determine the molecular organization of self-assembled networks with an atomic resolution. Moreover, the electronic properties of molecular networks can also be obtained by using X-ray Photoemission Spectroscopy (XPS). Combined analysis of STM imaging and XPS measurements permit to obtain deep information regarding the molecular packing structure, from submonolayer to few- layers coverage, and the interaction between the supramolecular network and the substrate. In particular, **Chapter 2** reports the investigation performed on the zinc-tetraphenylporphyrin (ZnTPP) molecular network on the Au(111) surface. Relevant information about the molecular packing and the molecules-substrate interaction were gained by using a combined STM and XPS analysis. Furthermore, the formation of the molecular second layer, in terms of growth and molecular mobility, was also investigated. In **Chapter 3** the self-assembly of the Nile red molecules on the Au(111) substrate, from sub- to mono- layer coverages, was reported for the first time. STM imaging and semi-empirical calculations performed on this system allow to gain

essential information about the molecular packing, substrate-molecules interaction as well as intermolecular bonding. In **Chapter 4** the supramolecular assembly of benzene-1,4-dicarboxylic acid (terephthalic acid, TPA) and benzene-1,3,5-tricarboxylic acid (trimesic acid, TMA) deposited on graphene were investigated. Combining STM, electron diffraction and acTEM imaging, the structural transition that occurs as molecular deposition proceeds was evidenced, and the critical thickness beyond which the film structure is no longer defined by the molecular 2D crystal at the substrate surface is determined. Despite the chemical similarity between the two molecules, their monolayer-to-thin-film transitions are dramatically different. **Chapter 5** reports the effect of the deposition of the electron acceptor 7,7,8,8-tetracyanoquinodimethane (TCNQ) molecules on the surface of a prototypical topological insulator, bismuth selenide (Bi_2Se_3). STM investigation allows to determine the molecular packing, while the photoemission spectroscopy measurements demonstrates a negligible charge transfer between the molecular layer and the substrate.

All the investigated cases represent model systems that allow us to study both the molecular assemblies of the molecules, as a function of the particular compound and substrate, and the interaction with the surface. Furthermore, in some cases the evolution of the molecular film beyond the monolayer case is also presented.

In addition to the main topic of the work, the thesis also reports other research activities performed during the PhD course, still related to the two-dimensional systems. In particular, **Part II** describes the growth and characterization of graphene films on copper foil, by means of Chemical Vapor Deposition (CVD). **Chapter 6** reports the possibility to induce the a variation of the graphene coupling with respect to the Cu substrate by visible-light irradiation above a proper power threshold, while **Chapter 7** both evidences the dependence of the graphene film quality by varying the exposure time to the carbon flux and two distinct graphene films, at the same time, on the copper substrate.

Finally, **Part III**, which contains only the **Chapter 8**, reports the nucleation and growth of iron clusters on MgO/Ag(100) surface. Here, relevant information were obtained on the cluster size dependence from deposition temperature of the substrate and from the nominal coverage.

References

- [1] B. D. Gates, Q. Xu, M. Stewart, D. Ryan, C. G. Willson and G. M. Whitesides, *Chemical Reviews* 105 (4) (2005): 1171-1196
- [2] S. P. Li, D. Peyrade, M. Natali, A. Lebib, Y. Chen, U. Ebels, L. D. Buda, and K. Ounadjela, *Physical Review Letters* 86(6) (2001): 1102.
- [3] D.S. Ginger, H. Zhang and C. A. Mirkin, *Angewandte Chemie International Edition* 43(1) (2004): 30-45.
- [4] H. Kim and W.J. Maeng, *Thin Solid Films* 517(8) (2009): 2563-2580.
- [5] M. R. Weatherspoon, Y. Cai, M. Crne, M. Srinivasarao and K. H. Sandhage, *Angewandte Chemie International Edition* 47(41) (2008): 7921-7923.
- [6] A. Reina, X. Jia, J. Ho, D. Nezich, H. Son, V. Bulovic, M.S. Dresselhaus and J. Kong, *Nano Letters* 9(1) (2008): 30-35.
- [7] L. C. Palmer and S. I. Stupp, *Accounts of Chemical Research* 41(12) (2008): 1674-1684.
- [8] G.M. Whitesides and M. Boncheva, *Proceedings of the National Academy of Sciences* 99(8) (2002): 4769-4774.
- [9] J. Zhang, Y. Li, X. Zhang and B. Yang, *Advanced Materials* 22(38) (2010): 4249-4269.
- [10] Y. Li, L. Liu, R. Subramani, Y. Pan, B. Liu, Y. Yang, C. Wang, W. Mamdouh, F. Besenbacher and M. Dong, *Chemical Communications* 47(32) (2011): 9155-9157.
- [11] L. Piot, D. Bonifazi and P. Samorì, *Advanced Functional Materials* 17(18) (2007): 3689-3693.
- [12] S. Zhang, *Nature Biotechnology* 21 (10) (2003): 1171-1178.
- [13] S.A. DiBenedetto, A. Facchetti, M. A. Ratner and T. J. Marks. *Advanced Materials* 21(14-15) (2009): 1407-1433.
- [14] S. Clair, S. Pons, A. P. Seitsonen, H. Brune, K. Kern and J. V. Barth, *The Journal of Physical Chemistry B* 108, no. 38 (2004): 14585-14590.
- [15] W. Xu, M. D. Dong, H. Gersen, E. Rauls, S. Vázquez-Campos, M. Crego-Calama, D. N. Reinhoudt, I. Stensgaard, T. R. Linderoth and F. Besenbacher, *Small*, 2008, 4(10),1620–1623.
- [16] H. Ascolani, M. W. van der Meijden, L. J. Cristina, J. E. Gayone, R. M. Kellogg, J. D. Fuhr and M. Lingenfelder, *Chemical Communications* 50(90) (2014): 13907-13909.
- [17] G. Tomba, M. Stengel, W. D. Schneider, A. Baldereschi and A. de Vita, *ACS Nano*, 2010, 4, 7545–7551.
- [18] N. Abdurakhmanova, A. Floris, T. C. Tseng, A. Comisso, S. Stepanow, A. de Vita and K. Kern, *Nature Communication* , 2012, 3, 940.
- [19] S. Stepanow, R. Ohmann, F. Leroy, N. Lin, T. Strunskus, C. Woll and K. Kern, *ACS Nano*, 2010, 4, 1813–1820.
- [20] L. Cui, X. Miao, L. Xu, Y. Hu and W. Deng, *Physical Chemistry Chemical Physics* 17(5) (2015): 3627-3636.
- [21] A. E. Baber, S. C. Jensen and E. C. H. Sykes, *Journal of the American Chemical Society* 129(20) (2007): 6368-6369.
- [22] A. C. Papageorgiou, A. Alavi and R. M. Lambert, *Chemical Communication*, 2012, 48, 3394–3396.

- [23] Z. Shi, J. Liu, T. Lin, F. Xia, P. N. Liu and N. Lin, *Journal of the American Chemical Society* 133(16) (2011): 6150-6153.
- [24] Z. Shi, T. Lin, J. Liu, P. N. Liu and N. Lin, *CrystEngComm* 13, no. 18 (2011): 5532-5534.
- [25] A. Kumar, K. Banerjee and P. Liljeroth, *Nanotechnology* 28(8) (2017): 082001.
- [26] D.I. Rozkiewicz, B.J. Ravoo and D.N. Reinhoudt, *Langmuir* 21(14) (2005): 6337-6343.
- [27] M. Lessel, O. Bäumchen, M. Klos, H. Hähl, R. Fetzer, M. Paulus, R. Seemann and K. Jacobs, *Surface and Interface Analysis* 47(5) (2015): 557-564.
- [28] V. Y. Kutsenko, Y. Y. Lopatina, L. Bossard-Giannesini, O. A. Marchenko, O. Pluchery and S. V. Snegir, *Nanotechnology* 28(23) (2017): 235603.

Chapter 1

Methods

This chapter describes the main experimental technique used in this thesis, scanning tunneling microscopy (STM). The working principle, the theory of quantum tunnelling and the STM spectroscopic mode will be discussed in detail.

1.1 Scanning Tunneling Microscopy

The invention of the scanning tunneling microscope (STM) has revolutionized the field of microscopy, providing for the first time resolution down to the atomic scale. It was developed in 1981 by Binnig and Rohrer, awarded five years later by the Nobel Prize, at the IBM labs in Zurich.

The ability to resolve the surface at atomic level, related to its local electronic properties, and the opportunity to obtain further information on the local density of states (LDOS) by the spectroscopic mode (STS – Scanning Tunneling Spectroscopy), make the STM a fundamental investigative technique in the nanotechnology field.

The working principle of the STM is relatively straightforward. It uses a sharp metal tip to probe the sample and to image its surface. By applying an appropriate voltage between the metallic tip and the (conductive) sample, a current flows from the tip to the sample (or vice versa), when their distance is in the order of 0.5-1nm. This quantum tunneling current, classically forbidden, allow gaining fundamental information about the electronic properties of the surface.

The STM tip fine movements towards the surface and in the lateral direction can be controlled with high precision by a piezoelectric scanner tube with electrodes, which can contract or extend under the action of an applied voltage. A schematic view of an STM is shown in Fig. 1.

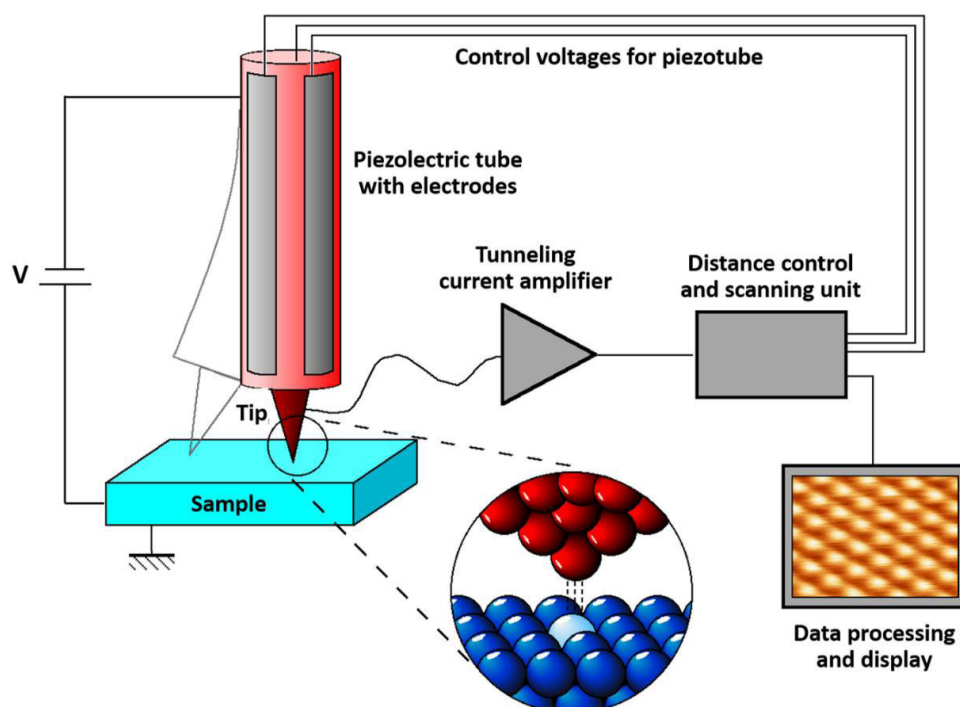


Figure 1. Schematic setup of an STM. Figure adapted from [1].

1.1.1 Quantum Tunneling

The basic phenomenon of the STM is the quantum tunneling of electrons between two electrodes separated by a thin potential barrier. The simplest case of tunneling through a potential barrier occurs for a particle in one dimension (1D), as shown in Fig. 2.

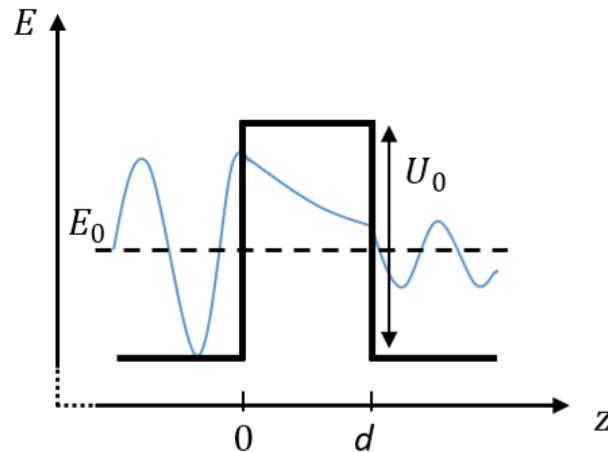


Figure 2. Schematic representation of the electron tunneling through a potential barrier (1D-case).

Consider an electron with energy E that is incident on a potential barrier U such that

$$U(z) = \begin{cases} U_0 & , \quad 0 < z < d \\ 0 & , \quad \text{else} \end{cases} \quad (1.1)$$

In the 1-dimensional case, the Schrödinger wave equation is given by

$$-\frac{\hbar^2}{2m} \frac{d^2\psi}{dx^2} + U(z)\psi = \varepsilon\psi \quad (1.2)$$

where ψ is the wave function, \hbar the reduced Planck constant, m the mass of the electron, U the time-independent potential and ε the energy of the particle.

The solutions to the Schrödinger equation for the wavefunction in the barrier region, in the case $E_0 < U_0$, are given by

$$\psi(z) = \alpha e^{-kz}, \quad k = \sqrt{2m(U_0 - E_0)/\hbar} \quad (1.3)$$

where $1/k$ is the lengthscale of the potential barrier at which tunneling can occur. The vacuum potential barrier represents the energy needed to remove an electron from the

material, i.e. the work function. In the STM case, its typical value ranging from 3 to 5 eV. As a consequence, the typical tunneling lengthscale is $k^{-1} \sim \text{\AA}$.

The probability that an electron passes through the potential barrier, having height U_0 and thickness d , is given by

$$|\psi(z = d)|^2 \propto e^{-2kd} \quad (1.4)$$

As a result, the width of the potential barrier must be approximately $d \sim k^{-1}$ for electrons to tunnel across the barrier. For this reason, the STM tip must be near to the surface in order to measure a tunneling current. Moreover, the exponential dependence of (1.4) means that if $k^{-1} \sim 1 \text{\AA}$, for 1 \AA change in vertical direction the tunneling probability increases by an order of magnitude.

The tunneling probability in (1.4) is directly related to the tunneling current. As a consequence, as a first approximation, the tunneling current scales exponentially with the barrier width d .

In the particular case of STM, the potential barrier lies between the tip and sample, which are located to a distance d . A schematic representation of the energetic landscape of an electron that moves along a metallic-substrate/insulator/metallic-tip tunneling junction is shown in Fig. 3.^[2]

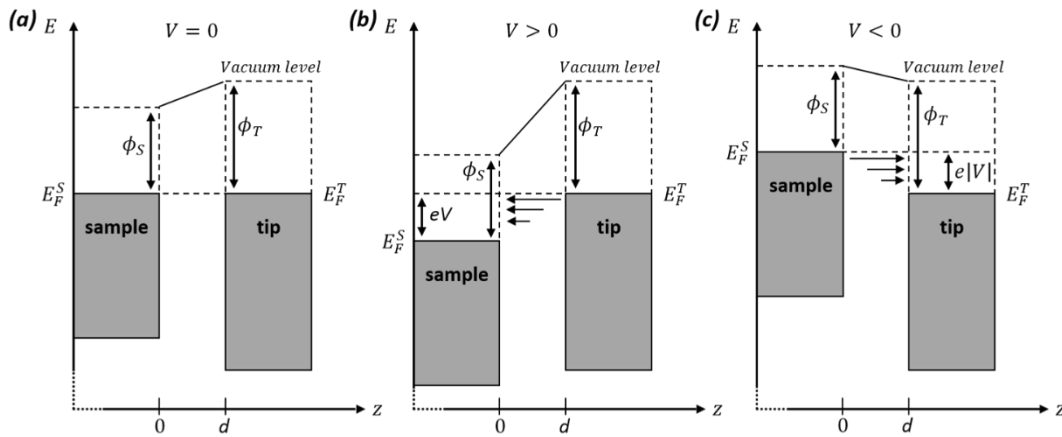


Figure 3. Energy profile the electrons moving along a tip-vacuum-sample junction. z is the surface normal direction while s is the tip-sample distance. $\phi_{T,S}$ and $E_F^{T,S}$ are the work functions and the Fermi levels of tip and sample, respectively. The gray boxes represent the Fermi-Dirac distribution at 0 K. (a) At equilibrium, a trapezoidal potential barrier is created between the two electrodes. (b) At positive and (c) negative sample bias, the electrons tunnel between the junction from the tip to the sample and vice versa, respectively. Figure adapted from [2].

At equilibrium, the tip and sample have the same Fermi level while their work functions, ϕ_T and ϕ_S respectively, are generally different (i.e. different materials). As a result, a trapezoidal potential barrier between the two electrodes is created, which is higher than the typical thermal energy (KT) of the electrons. Although particles can pass through the tip-sample barrier for the quantum tunneling effect, in the absence of a voltage applied between the two electrodes there is no net charge flow, i.e. tunneling current, in a particular direction. Conversely, by applying a polarized (or bias) voltage between the tip and sample, and adopting the convention for which the voltage is applied to the sample while the tip is grounded, the Fermi level of the sample is shifted by $-eV$ and a net tunneling current occurs, whose direction depends on the sign of V (see Figure 3(b) and (c)). In the case $V > 0$, the electrons tunnel from occupied states of the tip into unoccupied states of the sample. As a consequence, imaging at positive bias allow investigating the conduction band, or the analogous Lowest Unoccupied Molecular Orbitals (LUMOs) in organic chemistry, of the sample. On the contrary, the valence band or the Highest Occupied Molecular Orbitals (HOMOs) of the sample can be investigated at negative bias, when the tunnelling current flows from the occupied states of the sample towards the empty ones of the tip. Clearly, electrons near the Fermi level have a higher probability to pass through the potential barrier.

1.1.2 Bardeen approximation

Bardeen's model for tunneling in metal-insulator-metal junctions^[3,4] can be transferred to the STM case to gain the expression of the tunneling current I_t . The basic idea is to consider the electronic structure of the tip and sample separately, as an unperturbed system described by two stationary one-particle Schrödinger equations:

$$(T + U_S)\psi_\alpha = E_\alpha\psi_\alpha \quad (1.5a)$$

$$(T + U_T)\chi_\beta = E_\beta\chi_\beta \quad (1.5b)$$

where T is the electron kinetic energy, ψ_α and χ_β the unperturbed wave functions, U_S and U_T the electron potentials and E_α and E_β the energy of the particles.

The Fermi golden rule gives the transition probability per unit time $\omega_{\alpha\beta}$ of an electron that passing from the sample state ψ_α to the tip state χ_β

$$\omega_{\alpha\beta} = \frac{2\pi}{\hbar} |M_{\alpha\beta}|^2 \delta(E_\alpha - E_\beta) \quad (1.6)$$

where $M_{\alpha\beta}$ is the matrix element

$$M_{\alpha\beta} = \int \chi_\beta^*(\mathbf{x}) U_T(\mathbf{x}) \psi_\alpha(\mathbf{x}) d^3\mathbf{x} \quad (1.7)$$

The total current will be given by the sum of $\omega_{\alpha\beta}$ over all the possible tip and sample states, multiplied for the electron charge e

$$I_t = e \cdot \sum_{\alpha,\beta} \omega_{\alpha\beta} \quad (1.8)$$

After introducing the density of states $\rho(\varepsilon)$, the summation in (1.8) can be replaced by an energy integral

$$\sum_{\alpha,\beta} \omega_{\alpha\beta} \rightarrow 2 \int f(\varepsilon) \rho(\varepsilon) d\varepsilon \quad (1.9)$$

where the factor 2 accounts for the spin degeneracy, while f is the Fermi-Dirac distribution function,

$$f(E) = \frac{1}{e^{(E-E_F)/k_B T} + 1} \quad (1.10)$$

in which E_F is the Fermi energy, k_B the Boltzmann constant and T the temperature. (1.10) takes into account Pauli's exclusion principle and the electronic state population at finite temperatures.

Assuming that the matrix element does not depend strongly on two particular states ($M_{\alpha\beta} \rightarrow M$), the total current can be written as

$$I_t = \frac{4\pi e}{\hbar} \int_{-\infty}^{+\infty} [f_T(E_F^T - eV + \varepsilon) - f_S(E_F^S + \varepsilon)] \rho_T(E_F^T - eV + \varepsilon) \rho_S(E_F^S + \varepsilon) |M|^2 d\varepsilon \quad (1.11)$$

where E_F is the Fermi energy and the indexes T and S refer to the tip and the sample, respectively.

A more manageable expression of the tunneling current can be obtained in the low temperature limit ($kT \ll eV$), where the Fermi-Dirac distributions can be approximated by step functions. The resulting current became

$$I_t = \frac{4\pi e}{\hbar} \int_0^{eV} \rho_T(E_F^T - eV + \varepsilon) \rho_S(E_F^S + \varepsilon) |M|^2 d\varepsilon, \quad \text{if } V > 0 \quad (1.12a)$$

$$I_t = \frac{4\pi e}{\hbar} \int_{-e|V|}^0 \rho_T(E_F^T - eV + \varepsilon) \rho_S(E_F^S + \varepsilon) |M|^2 d\varepsilon, \quad \text{if } V < 0 \quad (1.12b)$$

Despite this last consideration, the tunneling current expression is still not easy to solve because the calculation of the matrix elements is too complicated. However, a satisfactory approximation can be obtained by considering that the tunneling current flows only between the last atom of a perfectly sharp tip and the surface atom directly underneath, in the small bias voltage range ($\pm 2V$).^[5] In this case, $|M|^2$ can be expressed by a simple one-dimensional WKB tunneling probability, while the probability $D(\varepsilon)$ that an electron with energy ε tunnels through a potential barrier $U(z)$ of arbitrary shape, in WKB approximation^[6] is given by:

$$D(\varepsilon) = \exp \left\{ -\frac{2}{\hbar} \int_0^d \sqrt{2m(U(z) - \varepsilon)} dz \right\} \quad (1.13)$$

Considering a squared barrier of average height rather than a trapezoidal one, as shown in Fig. 3,

$$\phi_{eff}(V) = (\phi_T + \phi_S + eV)/2 \quad (1.14)$$

the (1.13) equation became

$$D(\varepsilon) = \exp \left\{ -2 \sqrt{\frac{2m}{\hbar^2}} (\phi_{eff} - \varepsilon) d \right\} = \exp^{-2kd} \quad (1.15)$$

The (1.15) relation shows as the actual probability that an electron pass through a potential barrier depends strongly on the distance between the tip and the sample. Due to this exponential dependence, small variations of distance d (~ 0.1 nm) lead to large changes in the tunneling current (around one order of magnitude). This behavior evidences the high vertical resolution of STM.

The substitution of the tunneling probability for the squared matrix element in the total current expression ($V > 0$) leads to the relation

$$I_t = \frac{4\pi e}{\hbar} \int_0^{eV} \rho_T(E_F^T - eV + \varepsilon) \rho_S(E_F^S + \varepsilon) e^{-2kd} d\varepsilon \quad (1.16)$$

As shown in equation (1.16), the tunneling current strictly depends on the sample-tip distance (d), applied bias (V) and the tip and sample density of states (ρ_T and ρ_S respectively). In particular, the density of states refer to the last atom of the tip and to the corresponding atom of the surface, in the Lang approximation.^[5] As a consequence, ρ_S can be referred to the local density of states (LDOS).

1.1.3 STM imaging

STM allows imaging at constant current and constant height modes. In the first case, the voltage applied on the z piezo-element is continuously adjusted through a feedback circuit, so that the tunneling current is set to the same value. During the scanning of the surface the tip-sample distance changes in order to maintain a constant current value. This mode is the most frequently used. On the contrary, in the constant height mode the bias applied on the piezo along the z direction is kept constant, while the tunneling current variations are monitored. In this case, the tip-sample distance is kept constant while the current changes result from variations of the tip-sample distance. This imaging mode can be used only in very small areas and for flat samples, in order to avoid the tip crash on the sample.

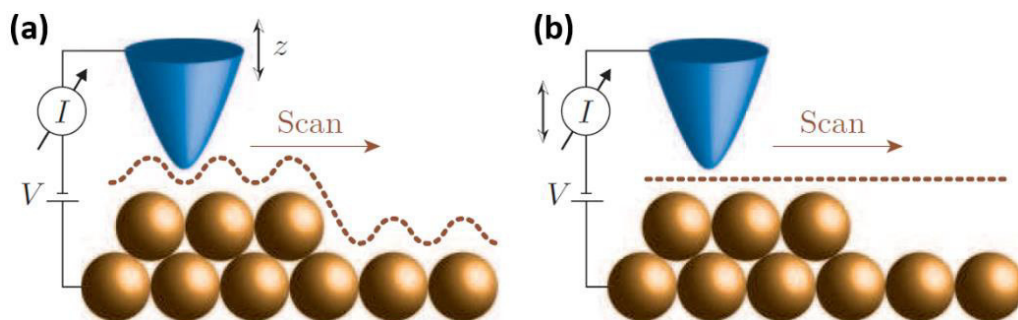


Figure 4. (a) Constant-current and (b) constant-height STM operating modes. Figure adapted from [7].

1.2 Scanning Tunneling Spectroscopy (STS)

Beyond imaging, STM allow gaining spectroscopic information on the local electronic properties of surfaces with high spatial resolution. The STM spectroscopic mode (STS) give access to both the occupied and non-occupied states of the sample by changing the polarity of the bias voltage. As a result, STS can be considered in this sense a complementary technique respect to the *Ultraviolet Photoemission Spectroscopy* (UPS), with the additional advantage to investigate the electronic properties of the surface at small scale. As shown in equation (1.16), the tunneling current only depends on the bias voltage V and on the tip-sample distance d . This dependence can be used in a STS experiment, where the relation between two of these three parameters is measured while the remaining one is kept constant. As a result, three spectroscopic modes can be employed in an STS experiment: the $I_t(V)$, $I_t(s)$ and $s(V)$ spectroscopies. Among them, $I_t(V)$ spectroscopy is the most widely used spectroscopic mode because it provides information about the local density of states (DOS) of the sample. In this case, the tip-sample distance is kept constant (i.e. the feedback control is disabled) while the tunneling current is measured as a function of the bias voltage. The differential conductance for a positive sample bias is obtained by differentiating the total current I_t (equation 1.16) at a constant tip-sample separation, as shown by (1.17)

$$\begin{aligned} \frac{dI_t(V)}{dV} \propto & \rho_T(E_F^T) \rho_S(E_F^S + \varepsilon) D(eV, V, d) + \int_0^{eV} \rho_T(E_F^T - eV + \varepsilon) \rho_S(E_F^S + \varepsilon) \frac{\partial D(\varepsilon, V, d)}{\partial V} d\varepsilon \\ & + \int_0^{eV} \frac{d\rho_T(E_F^T - eV + \varepsilon)}{dV} \rho_S(E_F^S + \varepsilon) D(\varepsilon, V, d) d\varepsilon \end{aligned}$$

The dI/dV dependence on the sample local density of states (LDOS) is contained in the first term, while the other two terms show the voltage dependence of the transmission coefficient D and the tip DOS ρ_T , respectively. However, the equation (1.17) can be simplified by assuming small bias voltages and constant ρ_T . In this case, the second term can be neglected while the third one vanishes, respectively. The resulting relation is given by

$$\frac{dI_t(V)}{dV} \propto \rho_S(E_F^S + \varepsilon) D(eV, V, d) \quad (1.18)$$

As a consequence, the differential conductance can be considered a good representation of the sample density of states (LDOS) under the assumption of small voltages and constant ρ_T , because the monotonous dependence of D on V ensures that any possible structure in dI/dV

is only due to the voltage dependence of ρ_S . In the case of higher biases, the voltage dependence of D cannot be neglected. In this case, the normalized differential conductivity, i.e. $(dI/dV)/(I/V)$, is a better representation of ρ_S ,^[8] as both the numerator and denominator depend on the tunneling probability D . Although this procedure lacks a robust mathematic base, a good experimental agreement is found between the sample LDOS and the normalized differential conductivity especially in the case of semiconductors.^[9]

References

[1] <http://www.iap.tuwien.ac.at>

[2] A. Della Pia and G. Costantini. "Scanning tunneling microscopy." *Surface Science Techniques*. Springer Berlin Heidelberg, 2013. 565-597.

[3] J. Bardeen, *Physical Review Letters* 6(2) (1961): 57.

[4] A.D. Gottlieb, L. Wesoloski, *Nanotechnology* 17(8), R57 (2006).

[5] N.D. Lang, *Physical Review B* 34(8) (1986): 5947.

[6] L.D. Landau, E.M. Lifshitz, *Quantum Mechanics. Non-relativistic Theory* (Pergamon Press, Oxford, 1977).

[7] Ø. Fischer, M. Kugler, I. Maggio-Aprile, C. Berthod and C. Renner, *Reviews of Modern Physics* 79(1) (2007): 353.

[8] J.A. Stroscio, R.M. Feenstra, A.P. Fein, *Physical Review Letters* 57(20) (1986): 2579.

[9] M. Passoni, F. Donati, A.L. Bassi, C.S. Casari, C.E. Bottani, *Physical Review B* 79(4) (2009): 045404.

Part I: Molecular Self-Assembly

Chapter 2

STM and XPS investigation of ZnTPP adsorption on Au(111) surface: from monolayer to multilayer transition

Bottom-up self-assemblies of organic molecules offer the most realistic solution toward the fabrication of next-generation functional materials and devices. In this chapter we present a focused investigation on the monolayer assemblies of a particular porphyrin, i.e. the zinc-tetraphenylporphyrin (ZnTPP), on the Au(111) surface. A combined analysis of STM imaging and XPS measurements allows to gain fundamental information about the molecular packing, the molecules-substrate interaction as well as the intramolecular interaction. Furthermore, essential information are also gained by the formation of the molecular second layer, in terms of growth and molecular mobility of the second ZnTPP layer.

2.1 Introduction

Assemblies of molecular architectures on metal surfaces are appealing systems due to the possibility of synthesizing advanced functional nanostructured materials and devices through molecular manipulation. The structure and stability of the well-ordered and two-dimensional molecular crystal grown is determined by the molecule-molecule and molecule-surface interactions. The resulting features of these materials significantly depend on the properties of the molecules-metal interface, which in turn are tightly connected to the interaction between the particular organic/inorganic components used. Molecules-surface interactions can in fact affect the shape of the adsorbed molecules^[1] and their electronic structure^[2-4] as well as their magnetic properties.^[5,6] In particular, the deposition of electron donor or acceptor molecules allow to create interfaces with well-defined electronic properties, which can be employed in several fields.

Among all organic compounds, porphyrins are a well-known and versatile popular class of molecules, which has attracted over the years the attention for their significant electronic, optical and biological properties exploitable in a wide range of emerging technologies including field-effect transistors,^[7-10] dye-sensitized solar cells,^[11-14] sensors,^[15,16] organic light emitting diode^[17-20] and synthetic bio-mimetic devices.^[21,22] A noteworthy porphyrin derivative is tetraphenylporphyrin (TPP), which consists of a porphyrin macrocycle with four phenyl groups bound to the pyrrole subunits by a carbon bridge. TPP molecules, with or without the metal transition atom (Ni, Co, Fe, Zn, Cu) base at the center, exhibit a prominent self-assembling behavior on noble metal surfaces such as Au(111),^[23-28] Ag(111),^[29-34] and Cu(111)^[35-37] as well as on TiO₂^[38] even at room temperature.

As a result of the adsorption, these molecules typically form a stable molecular packing driven by the interaction on the plane between the phenyl groups, and the resulting unit cell is typically nearly square, where the porphyrin macrocycle stays either flat and parallel or distorted on the metal surface.^[35,39-44] The molecular arrangement and the adsorption geometry of these systems have been extensively studied in the last years by using Scanning Tunnelling Microscope (STM) and Near Edge X-Ray Absorption Fine Structure (NEXAFS) techniques.

Bearing all this in mind, in this chapter, we investigate the adsorption of the Zinc(II) tetraphenylporphyrin (ZnTPP) (see molecular structure in Fig. 1) on the Au(111) substrate by using scanning tunneling microscopy (STM) and X-ray photoemission spectroscopy (XPS).

Although this system was already studied by means of STM,^[23,24,26] a combined analysis of microscopic and electronic investigations is still lacking. STM and XPS measurements allow to gain essential information about the interaction between the ZnTPP molecules and Au(111) surface. In particular, STM imaging shows that the typical herringbone (HB) reconstruction of the Au(111) disappears when the molecular overlayer is present on the surface. This electronic rearrangement of the gold substrate, which can be seen in terms of anisotropic surface stress,^[45] is in fact an obvious signal of the significant interaction between the molecules and substrate. XPS core level and valence band measurements also confirm this finding. The chemical shifts of the N1s and Zn3d core levels clearly indicate a considerable interaction of ZnTPP molecules on Au(111) in the few-layers regime, supporting as well the charge dishomogeneity revealed by the STM imaging, which also does not exclude an asymmetrical shape of the ZnTPP molecules on the gold substrate. In addition, the mono- to bi-layer transition is examined, which shows that the second layer was epitaxially formed on the ZnTPP monolayer. Furthermore, the molecular diffusion involving a partial coverage of second layer molecules was also investigated by STM at room temperature. To the best of our knowledge, these surface diffusion effects were never reported for this specific system.

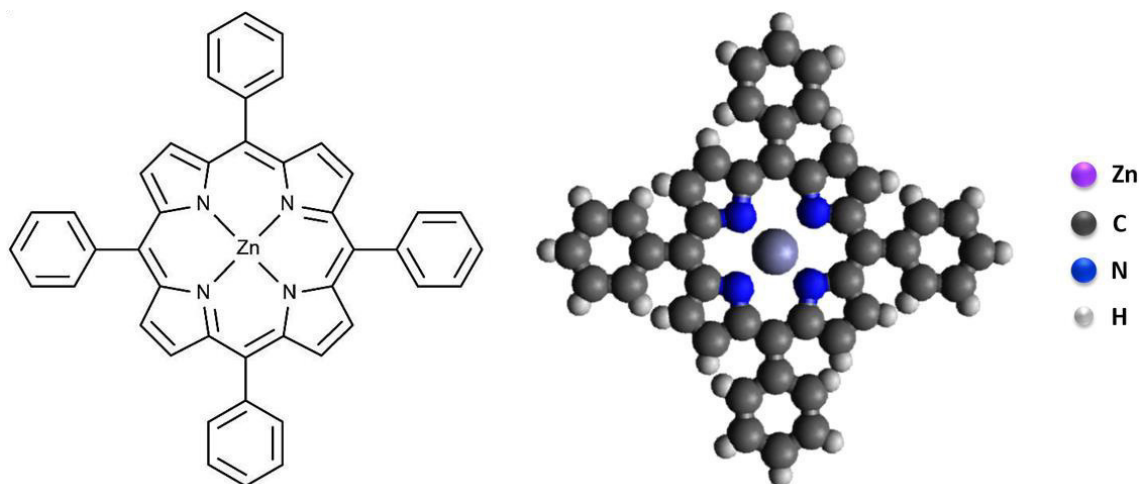


Figure 1. Molecular structure of the ZnTPP molecule, which exhibits the zinc at the center of the macrocycle and the four phenyl groups.

2.2 Experimental section

All STM measurements were performed at “*Laboratorio Idruri Metallici*” (SPES Group, Department of Physics, Università della Calabria, Italy) at room temperature and in UHV conditions (base pressure of 5×10^{-10} mbar) with an Aarhus SPM 150 equipped with KolibriSensor™ from SPECS^[46] and with a Nanonis Control system. The sharp STM W-tip was cleaned in situ via Ar⁺-sputtering. In the STM images shown, the tunneling bias voltage (U_t) is referred to the sample and the tunneling current (I_t) is that collected by the tip. Photoemission measures were carried out at APE beamline of the Elettra synchrotron light source (Basovizza (TS), Italy). All XPS and valence band spectra were recorded at room temperature and in a normal emission geometry. A Shirley background was subtracted from all XPS spectra and the data were normalized to the photon flux. In addition, some STM measurements were also acquired at APE beamline, at room temperature and in UHV condition (base pressure of 1×10^{-10} mbar), with a home-built STM. These measures were employed to confirm the molecular coverage related to the XPS core level measures. The Au(111) surface [*Phasis, Au(111) on mica with 200 nm of thick gold layer, 99.99% purity*], was cleaned by performing several cycles of argon ion sputtering ($I_s=6 \mu\text{A}$ for 20 min) and annealing procedures ($T_{\text{ann}}=450^\circ\text{C}$ for 20 min). After the cleanliness procedure, STM and XPS were used to confirm the quality of the pristine Au surface. ZnTPP molecules [*Porphyrin Systems, Zn(II) meso-tetraphenylporphine >98% purity*] were deposited at room temperature on Au(111) by organic molecular beam deposition (OMBD) in a high vacuum environment (base pressure of 3×10^{-8} mbar) using a home-built evaporator. The evaporation temperature ranging from 280°C to 300°C . Although a ZnTPP monolayer sublimated in UHV can also be prepared by a molecular multilayer deposition followed by a thermal annealing to desorb the thick molecular deposition and leave only the monolayer on the surface,^[24] in this study a proper ZnTPP dose was deposited on the cleaned Au(111)/mica crystalline surfaces to have a molecular monolayer regime. Starting from the submonolayer regime, the ZnTPP coverage was estimated by measuring the intensity ratio of N 1s e Au 4f photoemission lines, through comparison with STM results at the monolayer regime. All STM images were processed using the WSxM software (8.3 version).^[47]

2.3 Results and discussion

2.3.1 STM investigation of ZnTPP self-assembly on Au(111) at Room Temperature

Before deposition of ZnTPP molecules on Au(111), the pristine surface was extensively characterized by STM. Large and small scale STM images of the bare substrate were acquired (for further information see Appendix section, Fig. A1), which exhibit large terraces up to 200 nm separated by monoatomic steps and the typical herringbone (HB) reconstruction with atomic resolution superimposed to it.

In the monolayer regime, ZnTPP molecules form well-ordered and large domains on the Au(111) surface. In particular, three molecular rotational domains were found on the gold surface and each domain, which has the same molecular packing respect to the other two, is rotated of about $30^\circ \pm 2^\circ$ relative to one another, as shown in Fig. 2(a). The rotation angle between the domains clearly suggests that these different orientations are due to the 6-fold symmetry of the Au(111) surface.^[48]

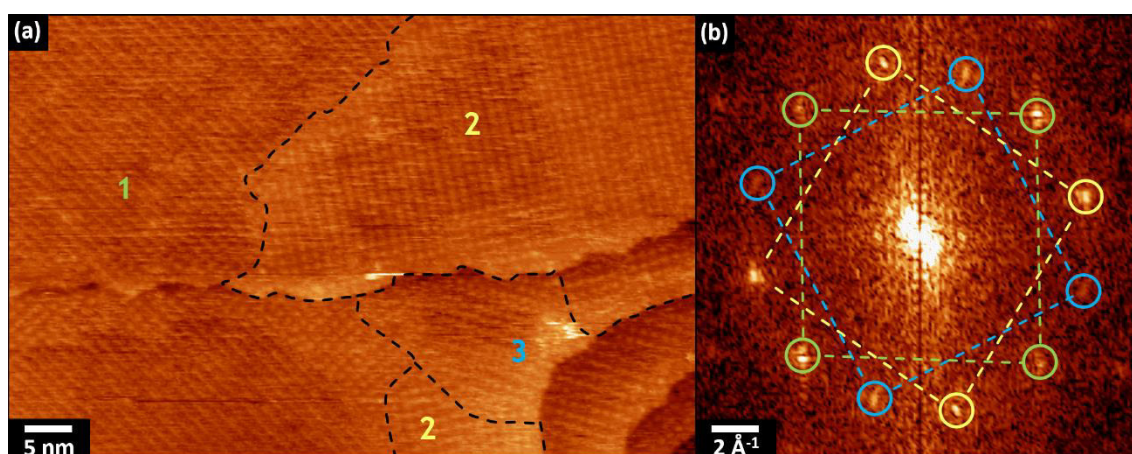


Figure 2. (a) $85 \times 58 \text{ nm}^2$ room temperature STM image depicting three rotational domains of ZnTPP molecules on Au(111). Tunneling parameters: $U_t=1.2 \text{ V}$, $I_t=0.1 \text{ nA}$. (b) Fourier analysis of the image in (a) that clearly show the presence of the rotational islands.

A representative high-resolution STM image of the ZnTPP molecular packing on Au(111) is shown in Fig. 3. Here the two evident brighter structures, circled by black dashed line, indicate molecules of the second layer, while the other molecules are representative of the first layer.

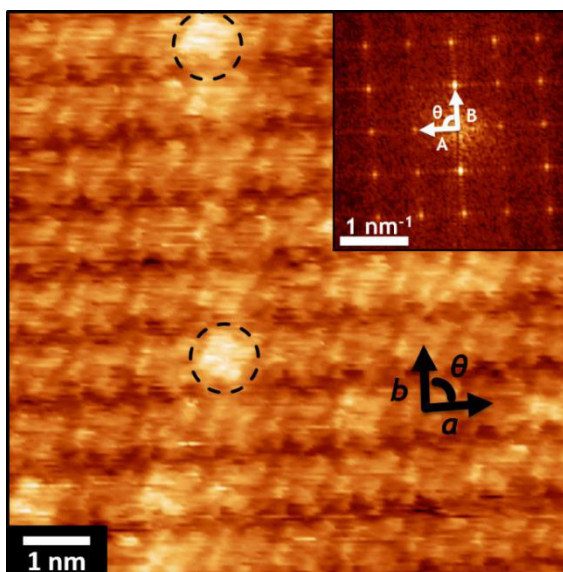


Figure 3. $12 \times 12 \text{ nm}^2$ room temperature STM image of ZnTPP on Au(111). Tunneling parameters: $U_t = 0.9 \text{ V}$, $I_t = 0.1 \text{ nA}$. a , b and θ are the unit cell parameters. Inset: FFT analysis of the STM acquisition; A , B and θ are the lattice parameters in the reciprocal space. The relation between the parameters in the real and reciprocal space is given by $A = 1/(a \cdot \sin \theta)$, $B = 1/(b \cdot \sin \theta)$.

Firstly, the ZnTPP arrangement within the molecular array is discussed. ZnTPP molecules self-assemble in a stable molecular pattern and the measured nearly square unit cell, with lattice parameters $a = 14.0 \text{ \AA} \pm 0.1 \text{ \AA}$, $b = 13.6 \text{ \AA} \pm 0.1 \text{ \AA}$ and $\theta = 89.0^\circ \pm 0.8^\circ$, is comparable with the related literature data.^[23,24,26] The resulting molecular density is $0.53 \text{ molecules/nm}^2$. These values are the results of a wide statistical analysis performed on several filtered images, the so-called “self-correlated” pictures, as shown in Fig. 4.

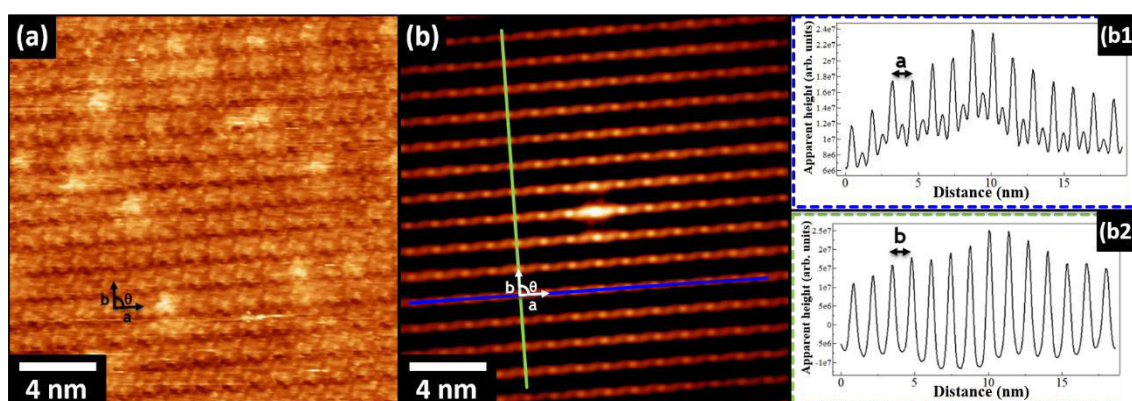


Figure 4. (a) $20 \times 20 \text{ nm}^2$ room temperature STM image of ZnTPP on Au(111). Tunneling parameters: $U_t = 0.9 \text{ V}$, $I_t = 0.1 \text{ nA}$. (b) Filtered (i.e. self-correlated) image of the previous STM picture. The blue and green lines identify the directions of the unit cell parameters a and b , while the corresponding line profiles are represented in (b1) and (b2), respectively (see the dashed blue and green lines).

STM image in Fig. 3 shows ZnTPP molecules slightly darker at the center and with small protrusions at the corners. The faint darker spots, close to the center of the molecules, are related to the position of the Zinc atoms and can be explained, as already reported in literature,^[24,26] by considering the electronic configuration of the Zinc ion and the relationship between its electronic configuration and the tunneling parameters used to acquire the images. In this case, the dark spot at the center of the macrocycle is due to the small contribution to the tunneling current of the Zn atom, which has a filled $3d^{10}$ orbital, for a +0.9V applied bias. The lower tunnel probability of the filled d orbital produces the same effect in other molecular self-assemblies, as NiTPP^[25] and metal phthalocyanines.^[49,50]

Fig. 3 also exhibits that the internal structure of the porphyrin ring, i.e. the Zn porphyrin macrocycle, is well-defined, while the four meso-phenyl groups can be associated to the protrusions below the ZnTPP core. However, the position of the ZnTPP phenyl groups is not well-defined as in previous literature data.^[23,24] Furthermore, the molecules seem to have lost their typical four-fold structure, i.e. the D_{4h} symmetry (see Fig. 1), after deposition on the Au(111) surface, which cannot exclude that the molecules could be distorted on the gold surface.

In order to clarify these aspects concerning the molecular packing, a filtered STM image of the ZnTPP molecule is calculated, as shown in Fig. 5 (b). This last picture consists of identical porphyrin molecules, which were obtained by summing several ZnTPP one above the other starting from an acquired image. As a consequence, the noise reduction due to the summing procedure lead to a more clear shape of the “averaged” molecule. This particular procedure, though unconventional in the STM analysis, is a useful tool in order to explain the molecular packing. Each pyrrolic group can be easily identified on the surface (see the superimposed molecular macrocycles in Fig. 5(b)) and these moieties could be not equivalent on the Au(111) surface. On the contrary, the phenyl groups do not appear so evident and not correspond to the typical position reported in literature^[24] (see the red circles in Fig. 5(c)).

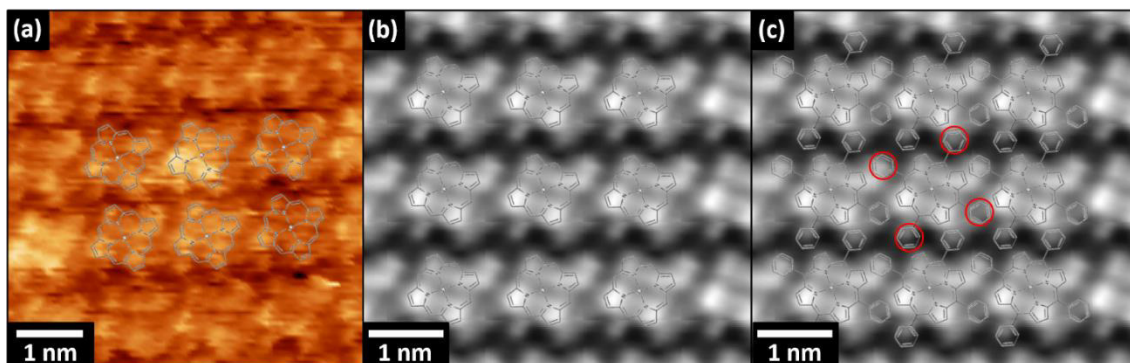


Figure 5. (a) $6 \times 6 \text{ nm}^2$ room temperature STM image of ZnTPP on Au(111). Tunneling parameters: $U_t = 0.9 \text{ V}$, $I_t = 0.1 \text{ nA}$. The ZnTPP macrocycle structure is superimposed on the image. (b)-(c) Filtered molecular image on which only the ZnTPP macrocycle and the ZnTPP molecular model are superimposed, respectively. The red circles in (c) point out the impossibility to the phenyl groups to be located in the position indicated by the molecular model superimposed on the acquired picture.

By considering the previous STM studies carried out on the ZnTPP deposition on the Au(111) surface,^[23,24,26] they suggest that ZnTPP molecules lie flat on the gold substrate, with the porphyrin macrocycle parallel to the surface. The phenyl groups are instead rotated upon adsorption, which gives rise to the so-called T-shaped stacking, which is the most energetically favorable geometry involving the phenyl groups.^[51] NEXAFS studies performed on similar systems, confirm the rotation of the phenyl groups of TPP molecules adsorbed on metallic surfaces.^[30,41,43,52] However, low temperature STM (LT-STM) and NEXAFS studies performed on other TPP molecules deposited on Au(111) exhibit usually the reduced C_{2v} symmetry, compared to the four-fold structure (i.e. D_{4h} symmetry) of the free molecule.^[35,39,40,41,44] This reduced symmetry of the porphyrin macrocycle arises from the molecules-surface bending and leads to the so-called “saddle” geometry, which is then induced by the adsorption. In this molecular conformation, the porphyrin ring is not flat but alternately pyrrolic units are bent upward and downward relative to the surface. Therefore, the interaction between the core and the metallic surface leads to the deformation of the porphyrin core. Moreover, although not experimentally measured, it can be assumed that the Zn^{2+} large ion can cause an inherent stress on the porphyrin core, which might lead to a modified adsorption of the TPP molecule on the surface.^[53]

The structural complexity of the ZnTPP molecule, in terms of rotational degrees of freedom of the phenyl-groups and flexibility of the porphyrin macrocycle, can complicate the interpretation about the conformational adaptation of the molecule after the adsorption on the gold surface, by using only the STM investigation. In our study, if on one hand the STM

experimental results shows a unit cell comparable with the literature data, on the other side the loss of the four-fold symmetry, the unusual position of the phenyl groups as well as the assumed non-equivalence of the pyrrolic moieties not exclude a charge dishomogeneity present at surface, perhaps connected to a distorted ZnTPP molecules on the Au(111) surface. As a consequence, the T-stacking adsorption could not be confirmed in our case. Other information both regarding the adsorption sites of the molecules and the molecular orientation with respect to the high symmetry directions of the Au(111) surface cannot be gained.

However, it is worth noting that the fundamental result of our STM investigation is that the gold herringbone (HB) reconstruction is no longer detected after the ZnTPP deposition (see Fig. 3 in the chapter and also Fig. S2 in the Appendix section). This behavior is not usual considering both the previous works of ZnTPP on Au(111)^[23,24,26] rather than other organic self-assembled monolayer adsorbed on Au(111),^[44,54,55] even those in which the molecules show the saddle geometry.^[35] The HB reconstruction is in fact usually observed beneath the adlayer, when the interaction between the molecules and surface is not strong enough to destroy or lift the electronic properties of the Au(111) surface. Here, as a result, the complete absence of gold HB reconstruction suggests that the interaction between the molecules and surface is not as weak as one could expect from this particular system.

In another study of ZnTPP deposited on Au (111),^[24] a relaxing effect of the herringbone was observed, but the gold superstructure is still revealed. That work reports that the Au(111) surface stress anisotropy between the $[\bar{1}\bar{1}2]$ and $[1\bar{1}0]$ directions is reduced by the ZnTPP molecular adsorbates. In their model, Ruggieri et al.^[24] suppose that the anisotropic surface stress is most likely linked to the inequivalent pyrrole orientation with the result that the pyrrole groups closer to the surface Au atoms exert a force on these atoms, altering the pristine surface energetics. In our work, the total absence of HB reconstruction is instead ascribed to a considerable interaction between the porphyrin core and the gold surface. In other words, after the molecular deposition, a gold surface reorganization occurs. Charge transfer or charge redistribution between the adsorbate and substrate^[45] and mechanical stress applied by the ZnTPP molecules on the Au substrate^[56] are the main effects that can produce the surface reorganization, although they usually are not completely distinguished from each other. As a result, STM investigation shows a ZnTPP molecule considerably interacting with the Au(111) substrate on the Au(111).

In addition, STM investigation allows to gain essential information regarding the partial second layer array of ZnTPP molecules. The STM image and the corresponding FFT analysis, shown respectively in Fig. 6(a)-(b), confirm that the molecular lattice of the incomplete second layer, i.e. the brighter features in the image below, is the same of the first one (i.e. the dark pattern). In particular, the well-defined spots of the Fourier analysis (see Fig. 6(b)) ensure that only one periodicity is present on the surface. In other words, the second layer is organized as the first one. Literature data also suggest that molecules can be absorbed on the Au(111) substrate in a layer-by-layer configuration, at least until the third layer.^[23] This last phenomenon that leads to the formation of stacking layers of ZnTPP is considered a peculiar property of this molecule, in which a particular attractive intermolecular interaction between the stacked molecular plane can be supposed.^[26] Furthermore, regarding the reciprocal position between the first and second layer molecules, STM measures show that the second layer was epitaxially formed on the first ZnTPP monolayer (see Fig. 6(c)). This results is also consistent with the literature data.^[26]

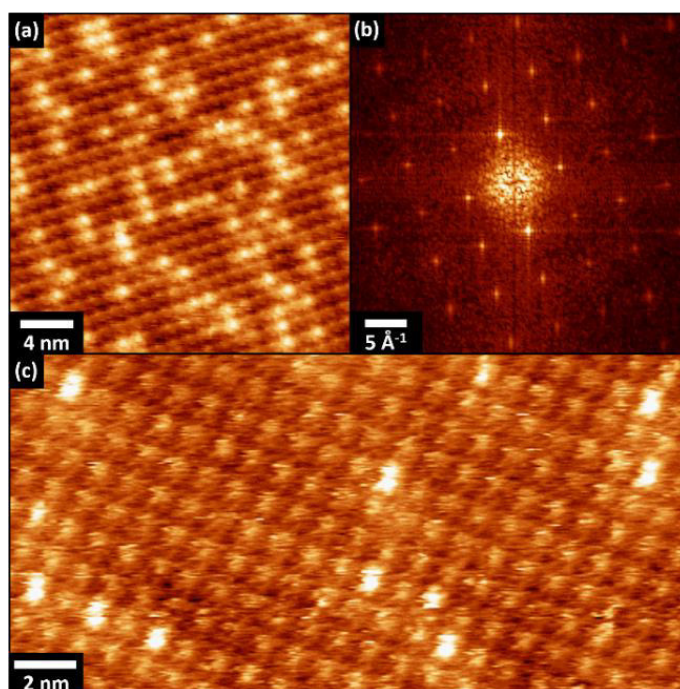


Figure 6. (a) $30 \times 30 \text{ nm}^2$ and (c) $30 \times 15 \text{ nm}^2$ room temperature STM images of ZnTPP molecules on gold surface. The second layer molecules are clearly evidenced by the brighter features. (b) FFT analysis of the previous STM picture. Tunneling parameters: (a) $U_t = 1.1 \text{ V}$, $I_t = 0.1 \text{ nA}$; (c) $U_t = 1 \text{ V}$, $I_t = 0.1 \text{ nA}$.

2.3.2 XPS investigation of ZnTPP coverage dependence on Au(111)

To shed light on the bonding between ZnTPP and Au(111), photoemission experiments on both core-levels and valence band as a function of molecular coverage were performed. In order to understand the adsorption mechanism in the few layers regime, photoemission measurements from sub-monolayer up to about 3 ML thickness are shown, monitoring binding energy shifts and line shape evolution of selected photoemission peaks.

The N1s photoemission peak is very sensitive to the ZnTPP adsorption configuration, as four N atoms are bound both to the central metal atom and the carbon ring skeleton (see Fig. 1), thus revealing any asymmetry in the chemical bond due to the substrate. On the other hand, the “thick” molecular film, where van der Waals forces acting between molecules are prevalent with respect to the substrate influence, can be assumed as reference of the ZnTPP gas-phase molecules.

According to the literature, the gas-phase spectrum shows a single symmetric component of the N 1s photoemission peak, centered at about 398.5 eV of binding energy (B.E).^[41] Deviations from the N 1s line shape of the gas-phase molecules can be inferred to chemical interaction and/or structural mismatch with the substrate.^[35,41] In particular, the adsorption of 1ML ZnTPP molecules on the weakly interacting Ag(110) substrate gives a broad N 1s peak with high binding energy tail,^[41] which has been fitted with two distinct components separated by only 0.37 eV. The double component has been ascribed either to a saddle-distortion of the macrocycle or to a breaking of the D_{4h} symmetry of the ZnTPP molecule, causing different adsorption sites for N atoms on the rectangular substrate. Further, it is worth noting that in metal free porphyrins two well resolved components of equal intensity separated by about 2 eV appear in the N 1s peak. The double-peak structure clearly indicates two types of nitrogen atoms equally distributed, namely aminic (-NH-) and iminic ones (=N-). This interpretation is in line with other photoemission experiments reporting a mixture of metal and metal-free TPP on different substrates, showing the convolution between corresponding components according to the degree of metalation.^[57-60]

Fig. 7(a) shows the N 1s photoemission peak as a function of the ZnTPP coverage on Au(111). Starting from the sub-monolayer regime (0.3 ML), the N 1s peak exhibits at least two main components with different intensity ratio. The separation between the two main components is within 2 eV, which is in between the cases above discussed.

The main component (see the blue filled in Fig. 7(a)), at lower binding energy, exhibits a forward shift by about 0.5 eV going to lower coverage, reaching 397.8 eV of B.E. at 0.3 ML. According to the literature, the shift of monolayer spectra has been assigned to a final state effect, specifically to an improved polarization screening of the core-hole driven by the substrate. The same shift was here observed for C 1s spectra (see Fig. A3 in Appendix section). By comparing the binding energy related to the gas-phase of ZnTPP molecules, centered at about 398.5 eV,^[41] shown by the arrow in Fig.7(a), with that measured at 3.2 ML (i.e. the blue filled in Fig. 7(a)), we estimate in our system a few-layer regime rather than a multi-layer one. The broader minor component (see the red filled in Fig. 7(a)) at higher B.E. is centered at 399.70 eV \pm 0.20 eV regardless of the coverage. Unlike the low binding energy component, which increase with the coverage increasing, this last feature reaches a saturation intensity above 1 ML coverage, as shown in Fig. 7(b). The accuracy of the N 1s intensities analysis is confirmed by the fact that the N1s total intensity is linear with the molecular coverage (see Fig. 7(b)).

The chemical shift of the N 1s peak here reported and its evolution with the coverage suggests the coexistence of several different chemical environments of nitrogen atoms within the molecule. We deduce that the minor component is representative of the monolayer (ML) regime and it refers to an inhomogeneous charge distribution, which can be connected to the STM measurements. We point out that compared to Ag(110),^[41] the N 1s peak on Au(111) here reported exhibits a high binding energy component further separated from the main peak, likely indicating either a stronger molecular distortion or a greater charge inhomogeneity. Moreover, the lack of a continuous shift together with a saturated intensity above 1ML suggests that this component is almost restricted to the sub- and monolayer regime.

On the other hand, the main component here detected is likely due to nitrogen atoms in a chemical environment of flat (i.e. free) molecules. Indeed, the configuration of ZnTPP non interacting with the Au(111) substrate is prevalent above 1 ML, where the thick layer film approaches the gas-phase.

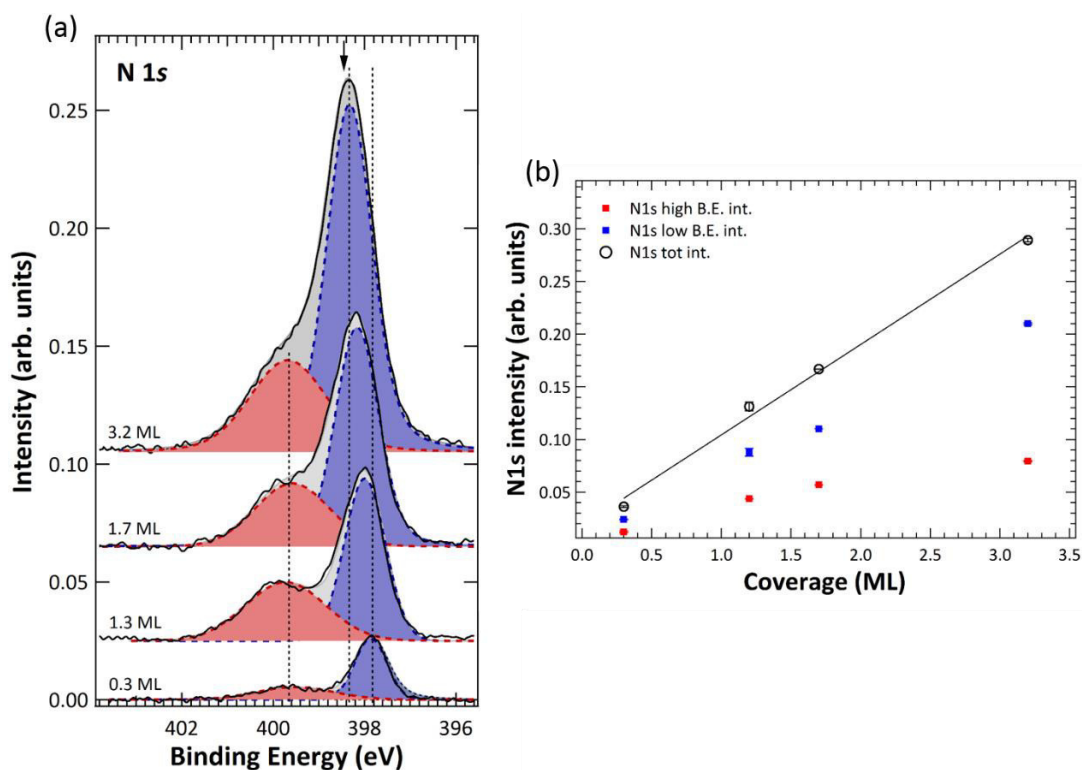


Figure 7. (a) *N 1s* photoemission peak as a function of the ZnTPP coverage on Au(111). Two distinct components are clearly evidenced. All XPS spectra were fitted by using Voigt profile shapes, after Shirley background subtraction. (b) Quantitative *N1s* intensities of the two component as a function of the molecular coverage.

Additional information can also be obtained by the analysis of the Zn 3*d* photoemission peak as a function of the ZnTPP coverage on Au(111), as reported in Fig. 8. It is worth noting that, at odd with several studies where a single Zn 3*d* component has been reported,^[61] here the Zn 3*d* peak can be fitted by two gaussian components, separated by about 0.9 eV. The chemical shift of Zn 3*d* here observed can be caused in principle by initial state effects, which are further influenced by relaxation shifts in a lower energy scale (within 0.5 eV).

In the sub-monolayer regime just the low binding energy component, i.e. the red filled in Fig. 8, is observed. This suggests that the low energy feature is essentially due to Zn atoms affected by the Au(111) substrate. As a consequence, in the sub- and monolayer regime Zn atoms have a single environment, due to the concurrent coordination of N atoms and to the interaction with the substrate. This hypothesis is further confirmed by the fact that the intensity of this feature increases more slowly compared to the other component, as coverage increases. Indeed, the second feature at higher B.E., i.e. the blue filled in Fig. 8, appears only above 1ML and keeps on increasing with the second and third layer population, in line with the results above discussed for the *N 1s* peak. We point out that while the Zn 3*d* peak exhibits a single

component in the sub- and monolayer regime, the N 1s one is instead chemically shifted from the first deposition. This difference most likely indicates that, starting from the submonolayer regime, the four N atoms within the molecule are unequally bound to the substrate.

In summary, the chemical shift of both N 1s and Zn 3d peaks indicates a considerable interaction of ZnTTP molecules on Au(111) in the few-layers regime, supporting as well the charge dishomogeneity revealed by our STM findings.

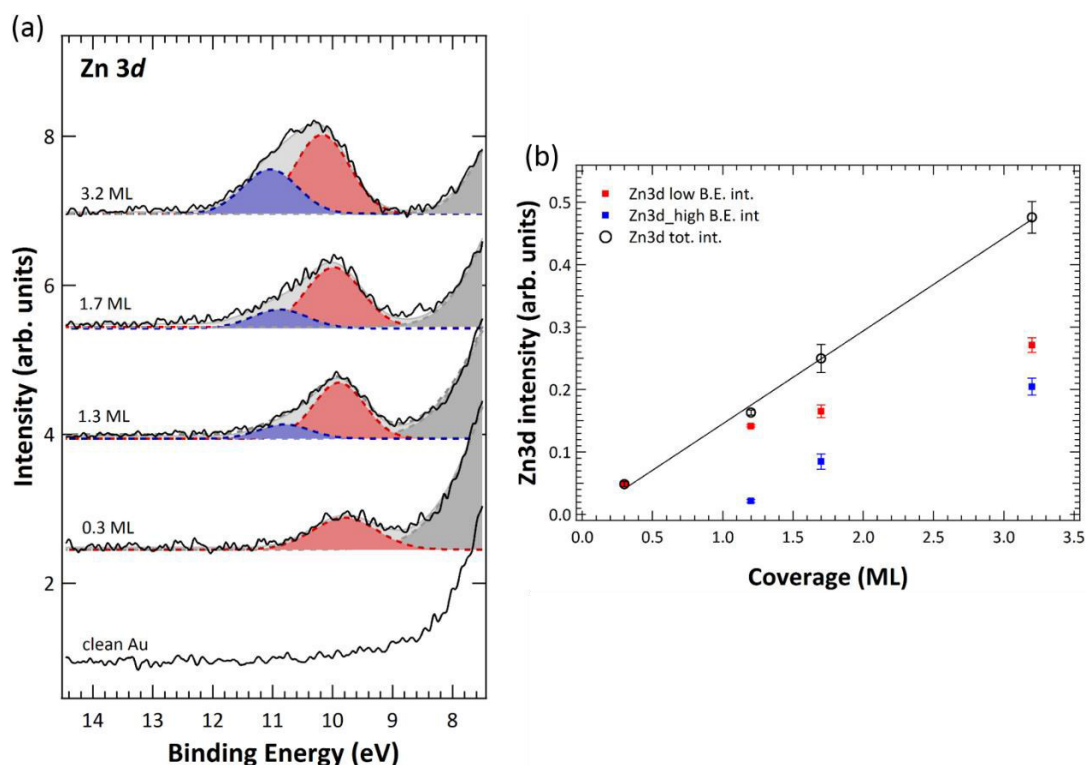


Figure 8. (a) Zn 3d photoemission peak as a function of the ZnTTP coverage on Au(111). Two distinct components are clearly evidenced over the ML coverage. All XPS spectra were fitted by using Voigt profile shapes, after Shirley background subtraction. (b) Quantitative Zn 3d intensities of the two component as a function of the molecular coverage. Once again, the accuracy of the Zn 3d intensities analysis is confirmed by the fact that the total intensity of Zn 3d is linear with the molecular coverage (see Fig. 7(b)).

In addition, the valence band spectra of clean and ZnTTP-covered Au(111) is reported in Fig. 9(a). Here the coexistence of substrate-related features and molecular overlayer ones can be observed. The clean Au(111) spectrum (see the bottom curve of Fig. 9(a)) exhibits 5d related features in the region between 7 eV to 2 eV, while the Fermi level is mainly due to 6s related states. From an initial analysis of the valence band, it worth noting that the ZnTTP components are not well resolved due to their overlapping with gold ones. In fact, the only component which is strictly discernible is the Zn 3d photoemission peak, ranging from 10 eV to 11 eV.

Modification of the substrate-related features as a function of ZnTPP coverage are evident. In particular, the sharp Au feature centered at 2.7 eV, as well as the band centered at 6 eV, show reduced intensities at increasing coverage, i.e. the gold 5d features are attenuated by the molecular overlayer, while the molecular components due to C and N states (*s*, *p* and *sp* hybridized states) fill this valence region.^[61]

However, further information can be obtained by subtracting the clean Au(111) spectrum to the ZnTPP/Au(111) ones at various coverages. This procedure allows to evidence the molecular states in the valence band, as shown in Fig. 9(b). Although the resulting spectra are quite noisy, the evidenced molecular features are compared to the ZnTPP states from literature.^[29] The first two HOMO states near the Fermi level, i.e. at binding energy of about 2.3 eV and 4.0 eV, correspond to the values reported in literature (see the bottom black curve in Fig. 9(b)), while the farthest structures are not matching. Moreover, the Zn 3d peak is splitted at coverages above 1 ML and is found at lower binding energy compared to the calculated ZnTPP states.

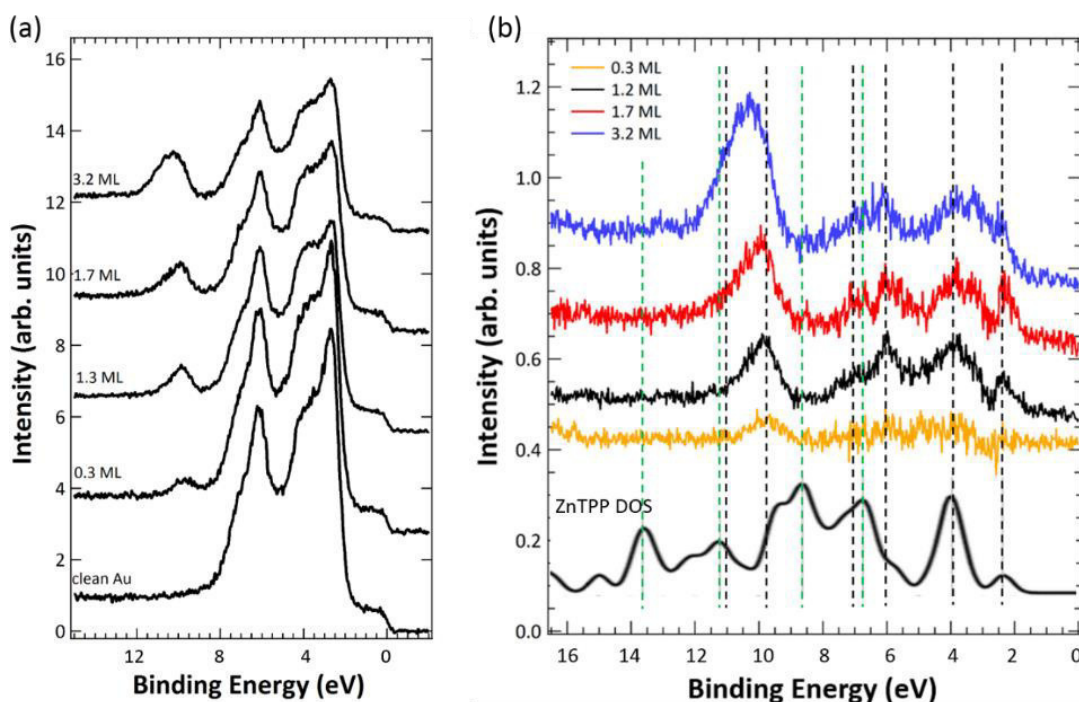


Figure 9. (a) Valence band spectra of clean and ZnTPP-covered Au(111) taken at 450 eV of photon energy. (b) Resulting XPS spectra subtracted the clean Au(111) spectrum at various coverages compared to ZnTPP DOS from literature.^[29] The green dashed lines identify the molecular states from literature, while the black lines evidence the experimental electronic states obtained from experimental data.

In addition, the influence of the molecular deposition of ZnTPP on the Fermi level of Au(111) can also be evidenced. Fig. 10 shows the ratio between the Fermi level and the Au 5d states as a function of the ZnTPP coverage.

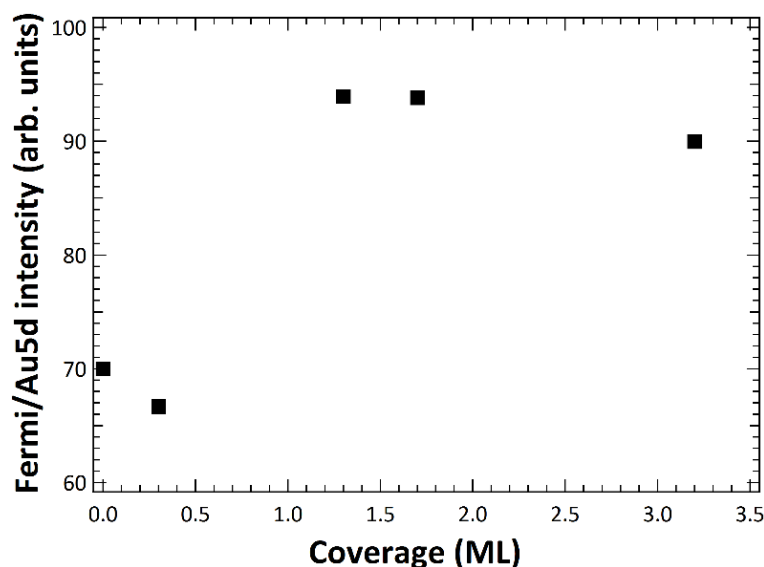


Figure 10. Intensity ratio between the Fermi level and Au 5d states as a function of the ZnTPP coverage. The increase of the ratio over the ML coverage confirms the noticeable interaction between the molecular monolayer and the Au(111) surface.

The Fermi edge/Au 5d peaks intensity ratio is roughly constant by comparing the case of pristine gold surface and submonolayer coverage, while it is drastically increasing by more than 25% over the ML coverage, and then remaining almost constant. This behavior still evidence the worthy interaction of the monolayer coverage on the gold surface.

2.4 Surface diffusion of the ZnTPP 2nd layer

Fig. 11 shows two consecutive STM images acquired on the same sample area. The ZnTPP coverage on the Au(111) is 1.3 ML. As mentioned before, brighter areas in each picture represent second layer molecules, while darker regions are first layer ones. Looking at these two pictures, it is worth noting that most of the second layer molecules remain in the same place in both scans, while some of them no longer occupy their initial position. In particular, molecules circled in blue solid line in Fig. 11(a) no longer occupy the same site in the successive image (see blue dashed line in Figure 11(b)), while molecules circled in black solid line in Fig. 11(b) now occupy positions that were previously free (see black dashed line in Fig. 11(a)).

STM allows to directly measure the ZnTPP molecular diffusion of the second layer molecules, at room temperature. Although the diffusion phenomenon was and it is still today widely studied for organic molecules at metal surfaces,^[62-64] to the best of our knowledge, it is the first time that the surface diffusion is directly observed for this particular system.

In order to study the mobility of ZnTPP molecules, it is worth remembering that STM itself interacts with surface by means of a tunneling current, and this interaction could affect the recorded molecular mobility, especially at room temperature. In other words, STM tip should sweep away some molecules from their adsorbing sites. Tip-surface interactions can have in principle a key role in the diffusion phenomenon. Both theoretical and experimental works proved the influence of the tip-surface interaction on molecular diffusion.^[65-71]

However, this last consideration is fairly unlikely in our particular case. In fact, the tunneling parameters used during the STM acquisitions, i.e. $U_t = 1.1\text{V}$ and $I_t = 0.1\text{nA}$, are such that they do not destabilize the molecular overlayer, because the interaction between the tip and surface is quite weak. In other words, the distance between the probe and the surface is quite large. This ensures that such effects may be considered negligible.^[72] Moreover, the percentage of the second layer mobile molecules is fairly low (< 5%). This other aspect suggests that the molecular diffusion is almost related exclusively to the molecular mobility at room temperature. In fact, the interaction between the first and the second layer of ZnTPP molecules is a weak van der Waals bonding, and at room temperature the thermal energy contribution becomes important to lead to surface diffusion of the second layer molecules. When thermal energies are larger than the minimum energy difference between adjacent sites (i.e. migration energy barrier), the adsorbed molecules are not confined to specific sites but a continuous surface migration occurs, due to the continuous energy exchange between the adsorbate and substrate.

Another important things to keep in mind is that while the first layer of molecules is complete and stable, as the intermolecular bonds on the plane are so stronger to ensure molecular stability, the second layer is incomplete. In fact only the 30% of the second layer surface is covered. The lacking of a complete second layer coverage facilitate the molecular diffusion, because some of these molecules are isolated, or at most they interacted with one or few other. For these molecules it is therefore easier to spread on the surface.

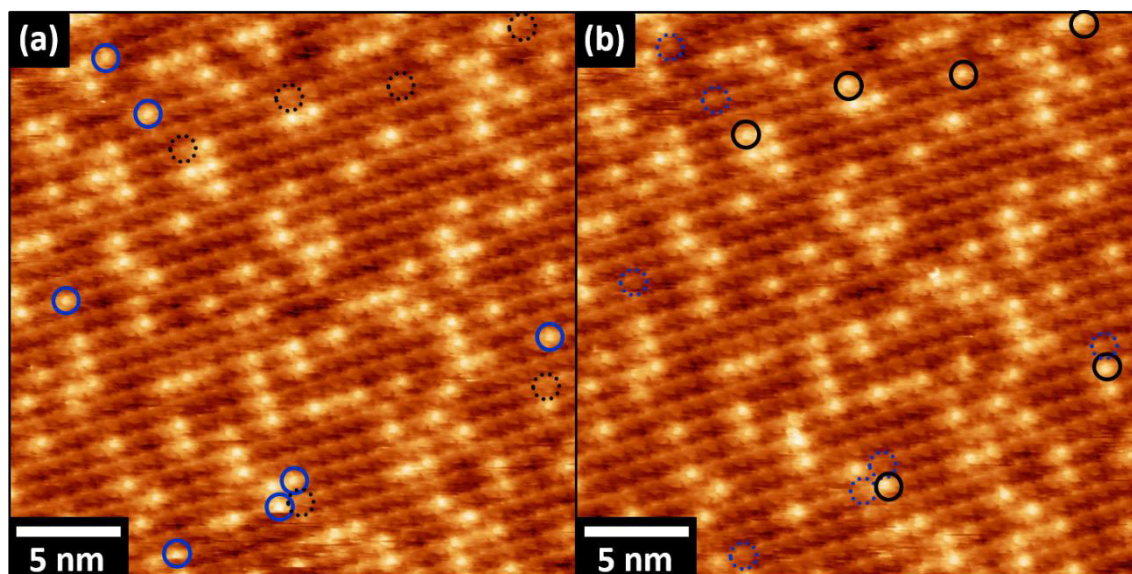


Figure 11. (a) and (b) $30 \times 30 \text{ nm}^2$ and consecutive room temperature STM images of ZnTPP on Au(111). Tunneling parameters: $U_t = 1.1 \text{ V}$; $I_t = 0.1 \text{ nA}$.

2.5 Conclusions

In this chapter the adsorption of ZnTPP molecules on the Au(111) substrate was investigated by using a combination of STM imaging and XPS analysis. The considerable interaction between the ZnTPP molecules in the monolayer regime and Au(111) surface was evidenced by both techniques. In fact, the disappearance of the gold herringbone reconstruction after the molecular adsorption shown by STM imaging, combined with the chemical shifts of the N1s and Zn3d core levels as well as the valence band modification reported by XPS measurements, clearly indicates a considerable interaction, i.e. through chemical bonds, in the monolayer regime.

In addition, the transition between the mono- and bi- layer coverage examined by STM shows that the second layer was epitaxially formed on the ZnTPP monolayer. Furthermore, the molecular diffusion was investigated by STM at room temperature. As a result, molecular mobility involving a partial coverage of second layer molecules is evidenced. To the best of our knowledge, these surface diffusion effects were never reported for this specific system.

References

- [1] T.A. Jung, R.R. Schlittler and J.K. Gimzewski, *Nature* 386(6626) (1997): 696-698.
- [2] A. Ruocco, F. Evangelista, R. Gotter, A. Attili and G. Stefani, *The Journal of Physical Chemistry C* 112(6) (2008): 2016-2025.
- [3] A. Hauschild, K. Karki, B.C.C. Cowie, M. Rohlfing, F.S. Tautz and M. Sokolowski, *Physical Review Letters* 94(3) (2005): 036106.
- [4] L. Romaner, G. Heimel, J.L. Brédas, A. Gerlach, F. Schreiber, R. L. Johnson, J. Zegenhagen, S. Duhm, N. Koch and E. Zojer, *Physical Review Letters* 99(25) (2007): 256801.
- [5] H. Wende, M. Bernien, J. Luo, C. Sorg, N. Ponpandian, J. Kurde, J. Miguel, M. Piantek, X. Xu, P. Eckhold and W. Kuch, *Nature Materials* 6(7) (2007): 516-520.
- [6] P. Gambardella, S. Stepanow, A. Dmitriev, J. Honolka, F.M. De Groot, M. Lingenfelder, S.S. Gupta, D.D. Sarma, P. Bencok, S. Stanescu and S. Clair, *Nature Materials* 8(3) (2009): 189-193.
- [7] C.M. Che, H.F. Xiang, S.S.Y. Chui, Z.X. Xu, V.E.E. Roy, J.J. Yan, W.F. Fu, P.E. Lai and I.D. Williams, *Chemistry—An Asian Journal* 3(7) (2008): 1092-1103.
- [8] M.L. Seol, S.J. Choi, C.H. Kim, D.I. Moon and Y.K. Choi, *Acs Nano* 6(1) (2011): 183-189.
- [9] M.L. Seol, S.J. Choi, J.M. Choi, J.H. Ahn and Y.K. Choi, *ACS Nano* 6.9 (2012): 7885-7892.
- [10] Y.Y. Noh, J.J. Kim, Y. Yoshida and K. Yase, *Advanced Materials* 15.9 (2003): 699-702.
- [11] T. Higashino and H. Imahori, *Dalton Transactions* 44(2) (2015): 448-463.
- [12] S. Mathew, A. Yella, P. Gao, R. Humphry-Baker, B.F. Curchod, N. Ashari-Astani, I. Tavernelli, U. Rothlisberger, M.K. Nazeeruddin, and M. Grätzel, *Nature Chemistry* 6(3) (2014): 242-247.
- [13] M. Urbani, M. Grätzel, M. K. Nazeeruddin and T. Torres, *Chemical Reviews* 114(24) (2014): 12330-12396.
- [14] S. Karthikeyan and J.Y. Lee, *The Journal of Physical Chemistry A* 117(42) (2013): 10973-10979.
- [15] S. Ishihara, J. Labuta, W. Van Rossom, D. Ishikawa, K. Minami, J.P. Hill and K. Ariga, *Physical Chemistry Chemical Physics* 16(21) (2014): 9713-9746.
- [16] L. Lvova, C. Di Natale, R. Paolesse, *Sensors and Actuators B: Chemical* 179 (2013): 21-31.
- [17] R.H. Friend, R.W. Gymer, A.B. Holmes, J.H. Burroughes, R.N. Marks, C.D.D.C. Taliani, D.D.C. Bradley, D.A. Dos Santos, J.L. Bredas, M. Lögdlund and W.R. Salaneck, *Nature* 397(6715) (1999): 121-128.
- [18] O. Fenwick, J.K. Sprafke, J. Binas, D.V. Kondratuk, F. Di Stasio, H.L. Anderson and F. Cacialli, *Nano Letters* 11(6) (2011): 2451-2456.
- [19] K.R. Graham, Y. Yang, J.R. Sommer, A.H. Shelton, K.S. Schanze, J. Xue, and J.R. Reynolds, *Chemistry of Materials* 23(24) (2011): 5305-5312.
- [20] J. R. Sommer, R. T. Farley, K. R. Graham, Y. Yang, J. R. Reynolds, J. Xue and K. S. Schanze, *ACS Applied Materials & Interfaces* 1(2) (2009): 274-278.
- [21] T.S. Balaban, *Accounts of Chemical Research* 38(8) (2005): 612-623.

- [22] S. Cosnier, C. Gondran, R. Wessel, F.P. Montforts, and M. Wedel, *Journal of Electroanalytical Chemistry* 488(2) (2000): 83-91.
- [23] X.L. Zhang, J.W. Jiang, Y.T. Liu, S.T. Lou, C.L. Gao and Q.Y. Jin, *Scientific Reports* 6 (2016): 22756.
- [24] C. Ruggieri, S. Rangan, R.A. Bartynski, and E. Galoppini, *The Journal of Physical Chemistry C* 119(11) (2015): 6101-6110.
- [25] L.G. Teugels, L.G. Avila-Bront, and S.J. Sibener, *The Journal of Physical Chemistry C* 115(6) (2011): 2826-2834.
- [26] S. Yoshimoto, E. Tsutsumi, K. Suto, Y. Honda and K. Itaya, *Chemical Physics* 319(1) (2005): 147-158.
- [27] D.E. Barlow, L. Scudiero and K.W. Hipps, *Langmuir* 20(11) (2004): 4413-4421.
- [28] W. Deng and K.W. Hipps, *The Journal of Physical Chemistry B* 107(39) (2003): 10736-10740.
- [29] C. Ruggieri, S. Rangan, R.A. Bartynski and E. Galoppini, *The Journal of Physical Chemistry C* 120(14) (2016): 7575-7585.
- [30] G. Di Santo, S. Blankenburg, C. Castellarin-Cudia, M. Fanetti, P. Borghetti, L. Sangaletti, L. Floreano, A. Verdini, E. Magnano, F. Bondino, and C.A. Pignedoli, *Chemistry-A European Journal* 17(51) (2011): 14354-14359.
- [31] W. Auwärter, K. Seufert, F. Klappenberger, J. Reichert, A. Weber-Bargioni, A. Verdini, D. Cvetko, M. Dell'Angela, L. Floreano, A. Cossaro and G. Bavdek, *Physical Review B* 81(24) (2010): 245403.
- [32] F. Buchner, I. Kellner, W. Hieringer, A. Görling, H.P. Steinrück and H. Marbach, *Physical Chemistry Chemical Physics* 12(40) (2010): 13082-13090.
- [33] F. Buchner, K.G. Warnick, T. Wölfle, A. Görling, H.P. Steinrück, W. Hieringer and H. Marbach, *The Journal of Physical Chemistry C* 113(37) (2009): 16450-16457.
- [34] A. Weber-Bargioni, J. Reichert, A.P. Seitsonen, W. Auwärter, A. Schiffrin and J.V. Barth, *The Journal of Physical Chemistry C* 112(10) (2008): 3453-3455.
- [35] J. Brede, M. Linares, S. Kuck, J. Schwoebel, A. Scarfato, S.H. Chang, G. Hoffmann, R. Wiesendanger, R. Lensen, P.H. Kouwer and J. Hoogboom, *Nanotechnology* 20(27) (2009): 275602.
- [36] G. Rojas, X. Chen, C. Bravo, J.H. Kim, J.S. Kim, J. Xiao, P.A. Dowben, Y. Gao, X.C. Zeng, W. Choe and A. Enders, *The Journal of Physical Chemistry C* 114(20) (2010): 9408-9415.
- [37] M. Stark, S. Ditze, M. Drost, F. Buchner, H.P. Steinrück and H. Marbach, *Langmuir* 29(12) (2013): 4104-4110.
- [38] S. Rangan, C. Ruggieri, R. Bartynski, J.I. Martínez, F. Flores and J. Ortega, *The Journal of Physical Chemistry C* 120(8) (2016): 4430-4437.
- [39] J. Mielke, F. Hanke, M. V. Peters, S. Hecht, M. Persson and L. Grill, *Journal of the American Chemical Society* 137(5) (2015): 1844-1849.
- [40] S. Müllegger, M. Rashidi, T. Lengauer, E. Rauls, W.G. Schmidt, G. Knör, W. Schöfberger and R. Koch, *Physical Review B* 83(16) (2011): 165416.

- [41] C. Castellarin-Cudia, P. Borghetti, G. Di Santo, M. Fanetti, R. Larciprete, C. Cepek, P. Vilmercati, L. Sangaletti, A. Verdini, A. Cossaro and L. Floreano, *ChemPhysChem*, 11(10), 2248-2255 (2010).
- [42] J. Brede, M. Linares, R. Lensen, A.E. Rowan, M. Funk, M. Bröring, G. Hoffmann and R. Wiesendanger, *Journal of Vacuum Science & Technology B: Microelectronics and Nanometer Structures Processing, Measurement, and Phenomena*, 27(2), 799-804.
- [43] A. Weber-Bargioni, W. Auwärter, F. Klappenberger, J. Reichert, S. Lefrancois, T. Strunskus, C. Wöll, A. Schiffrin, Y. Pennec and J.V. Barth, *ChemPhysChem* 9(1) (2008): 89-94.
- [44] T. Yokoyama, S. Yokoyama, T. Kamikado and S. Mashiko, *The Journal of Chemical Physics* 115(8) (2001): 3814-3818.
- [45] J.T. Sun, L. Gao, X.B. He, Z.H. Cheng, Z.T. Deng, X. Lin, H. Hu, S.X. Du, F. Liu and H.J. Gao, *Physical Review B* 83(11) (2011): 115419.
- [46] S. Torbrügge, O. Schaff and J. Rychen, *Journal of Vacuum Science & Technology B*, 28 (2010).
- [47] I. Horcas, R. Fernández, J. M. Gómez-Rodríguez, J. Colchero, J. Gómez-Herrero and A. M. Baro, *Review of Scientific Instruments* 78(1) (2007): 013705.
- [48] B. Hulsken, R. Van Hameren, P. Thordarson, J.W. Gerritsen, R.J. Nolte, A.E. Rowan, M.J. Crossley, J.A. Elemans and S. Speller, *Japanese Journal of Applied Physics* 45(3S) (2006): 1953.
- [49] X. Lu and K.W. Hipps, *The Journal of Physical Chemistry B* 101 (27) (1997): 5391-5396.
- [50] X. Lu, K. Hipps, X. Wang and U.J. Mazur, *Journal of the American Chemical Society* 118(30) (1996): 7197-7202.
- [51] F. Buchner. *STM Investigation of Molecular Architectures of Porphyrinoids on a Ag (111) Surface: Supramolecular Ordering, Electronic Properties and Reactivity*. Springer Science & Business Media (2010).
- [52] K. Diller, F. Klappenberger, M. Marschall, K. Hermann, A. Nefedov, C. Wöll and J.V. Barth, *The Journal of Chemical Physics*, 136(1), 014705 (2012).
- [53] M.S. Liao and S. Scheiner, *Journal of Chemical Physics* 117(1) (2002): 205-219.
- [54] Z.H. Cheng, L. Gao, Z.T. Deng, Q. Liu, N. Jiang, X. Lin, X.B. He, S.X. Du and H.J. Gao, *The Journal of Physical Chemistry C*, 111(6), 2656-2660 2007.
- [55] L. Scudiero, K. W. Hipps and D.E. Barlow, *The Journal of Physical Chemistry B*, 107(13), 2903-2909 2003.
- [56] O. Schaff, A.K. Schmid, N.C. Bartelt, J. de la Figuera and R.Q. Hwang, *Materials Science and Engineering: A* 319 (2001): 914-918.
- [57] Y. Bai, M. Sekita, M. Schmid, T. Bischof, H.P. Steinrück and J.M. Gottfried, *Physical Chemistry Chemical Physics* 12(17) (2010): 4336-4344.
- [58] M. Chen, X. Feng, L. Zhang, H. Ju, Q. Xu, J. Zhu, J. M. Gottfried, K. Ibrahim, H. Qian and J. Wang, *The Journal of Physical Chemistry C* 114(21) (2010): 9908-9916.
- [59] F. Buchner, K. Flechtner, Y. Bai, E. Zillner, I. Kellner, H.P. Steinrück, H. Marbach and J.M. Gottfried, *The Journal of Physical Chemistry C* 112(39) (2008): 15458-15465.

- [60] C. Bürker, A. Franco-Cañellas, K. Broch, T.L. Lee, A. Gerlach and F. Schreiber, *The Journal of Physical Chemistry C* 118(25) (2014): 13659-13666.
- [61] C. Castellarin-Cudia, T. Caruso, E. Maccallini, A. Li Bassi, P. Carrozzo, O. De Luca, A. Goldoni, V. Lyamayev, K. C. Prince, F. Bondino, E. Magnano, R. G. Agostino and C. S. Casari, *The Journal of Physical Chemistry C*, 119(16), 8671-8680.
- [62] G. Antczak, W. Kamiński, A. Sabik, C. Zaum and K. Morgenstern, *Journal of the American Chemical Society* 137(47), 14920-14929 (2015).
- [63] J.V. Barth, J. Weckesser, G. Trimarchi, M. Vladimirova, A. De Vita, A., C. Cai, H. Brune, P. Günter and K. Kern, *Journal of the American Chemical Society* 124(27), 7991-8000 (2002).
- [64] J. Weckesser, J.V. Barth and K. Kern, *The Journal of Chemical Physics* 110(11), 5351-5354 (1999).
- [65] I. Brihuega, O. Custance and J.M. Gómez-Rodríguez, *Physical Review B* 70(16) (2004): 165410.
- [66] J.M. Carpinelli and B.S. Swartzentruber, *Physical Review B* 58(20), R13423 (1998).
- [67] J. Li, R. Berndt, W.D. Schneider, *Physical Review Letters* 76(11), 1888 (1996).
- [68] M.R. Sørensen, K.W. Jacobsen and H. Jónsson, *Physical Review Letters* 77(25) (1996): 5067.
- [69] M. Bott, M. Hohage, M. Morgenstern, T. Michely and G. Comsa, *Physical Review Letters* 76(8) (1996): 1304.
- [70] Y. W. Mo, *Physical Review Letters* 71(18) (1993): 2923.
- [71] P. Ebert, M.G. Lagally and K. Urban, *Physical Review Letters* 70(10) (1993): 1437.
- [72] P. Grütter, W. Hofer and F. Rosei, eds., 2006. *Properties of single organic molecules on crystal surfaces*. World Scientific.

2.6 Appendix Section

A1. Pristine Au(111) surface

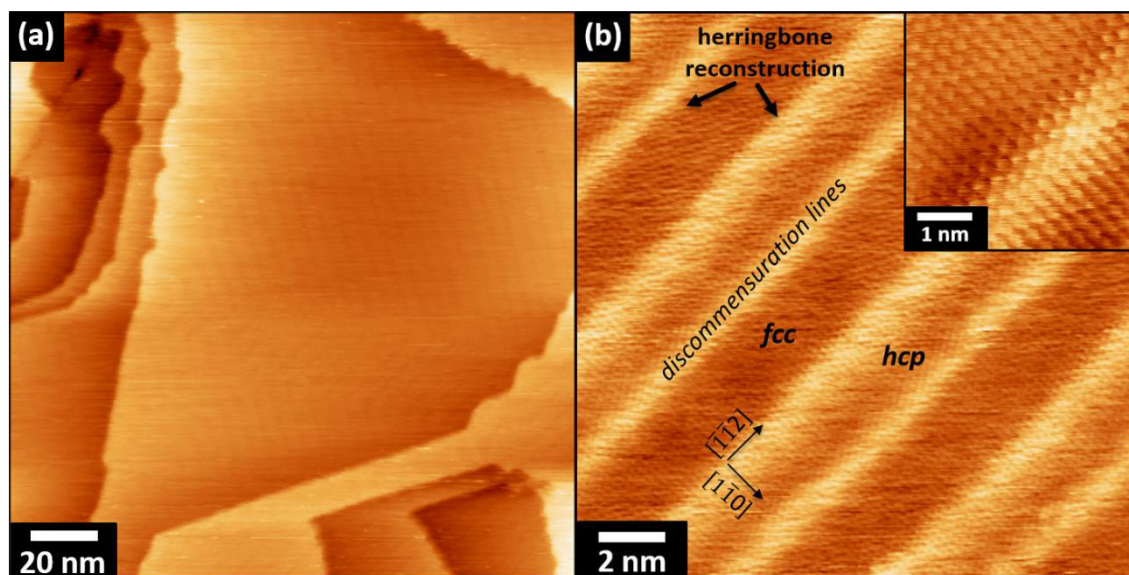


Figure A1. (a) $200 \times 200 \text{ nm}^2$ and (b) $18 \times 18 \text{ nm}^2$ room temperature STM images of Au(111) surface. Tunneling parameters: (a)-(b) $U_t = 0.25 \text{ V}$, $I_t = 0.32 \text{ nA}$.

Large and small scale STM images of the bare substrate are shown in Fig. A1. Au(111) surface exhibits large terraces up to 200 nm wide separated by monoatomic steps (Fig. A1(a)). The apparent height of the Au steps is about 2.3 \AA , consistent with previous literature values for the corresponding steps on Au(111) single-crystal (i.e. 2.4 \AA).^[A1] Fig. A1(b) shows the typical herringbone (HB) reconstruction of a clean Au(111) surface, with atomic resolution superimposed on it. The face-centered cubic (*fcc*) and hexagonal close-packed (*hcp*) atomic sites are separated by bright areas oriented in the $[\bar{1}\bar{1}2]$ directions, the so-called soliton walls or discommensuration lines. The lattice periodicity of the gold unit cell, $2.90 \text{ \AA} \pm 0.05 \text{ \AA}$, and the typical periodicity of the HB reconstruction measured in the Au $[1\bar{1}0]$ direction, i.e. $65 \pm 4 \text{ \AA}$, are consistent with their respective literature values.^[A1,A3]

A2. ZnTPP monolayer on Au(111)

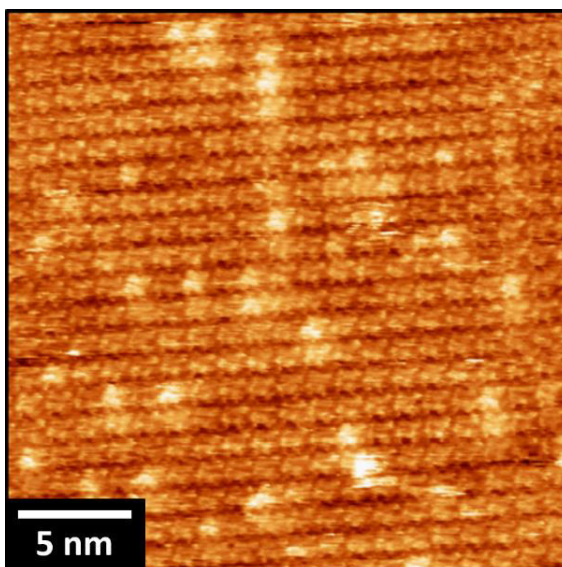


Figure A2. $27 \times 27 \text{ nm}^2$ STM image. Tunneling parameters: (a) $U=0.9 \text{ V}$, $I=0.3 \text{ nA}$.

A3. XPS C1s spectra

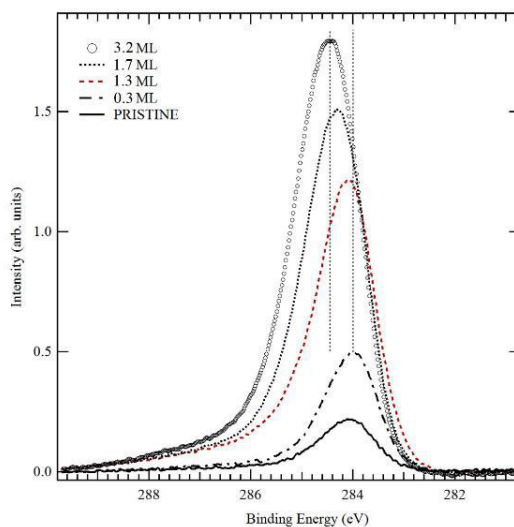


Figure A3. C 1s photoemission spectra at various coverages.

References

- [A1] J.V. Barth, H. Brune, G. Ertl, R.J. Behm, *Physical Review B* 42(15) (1990): 9307.
- [A2] S. Nie, N.C. Bartelt, J.M. Wofford, O.D. Dubon, K.F. McCarty and K. Thürmer, *Physical Review B* 85(20) (2012): 205406.
- [A3] M. Corso, L. Fernández, F. Schiller, J.E. Ortega, *ACS Nano* 4(3) (2010): 1603-1611.

Chapter 3

Investigation of Nile Red self-assembled monolayer on

Au(111)

Self-assembled monolayers (SAMs) on metal surfaces provide the possibility to control the functionality of the substrates. In this chapter, Nile red molecules were deposited on Au(111) substrate, from sub- to mono- layer coverages. STM imaging and semi-empirical calculations performed on this system allow to gain fundamental information about the molecular packing, substrate-molecules interaction as well as intermolecular bonding.

3.1 Introduction

As reported in Chapter 2, self-assembled monolayer (SAMs) of organic molecules provide a convenient and simple method to tailor interfacial properties of metal surfaces. In this chapter, self-assembly of a polar molecule, i.e. the Nile Red, were investigated on the Au(111) surface (for further information about the molecule see the Experimental section below). Literature data report a huge amounts of studies of molecular networks of polar molecules self-assembled on metal surfaces.^[1- 3] However, these works exclusively regards thiols molecules adsorbed on noble metal surfaces forming a covalent bond with the substrate.^[4] Conversely, Nile red molecule is a polar compound without anchoring groups to the surface. To the best of our knowledge, it is the first time that Nile Red self-assembled monolayer were experimentally observed on Au(111) surface. STM investigation combined with semi-empirical calculations allow to gain fundamental information on the molecular packing formed by molecules on the gold surface. Furthermore, the resulting interaction between the molecular assembly and the gold substrate is relatively weak as confirmed by STM analysis, while the intermolecular bond is characterized by the formation of hydrogen bonds. This study represents a preliminary analysis that pave the way to investigation of further polar compounds on metal surfaces that are weakly interacting with the substrate.

3.2 Experimental section

All STM measurements were performed at “*Laboratorio Idruri Metallici*” (SPES Group, Department of Physics, Università della Calabria, Italy) at room temperature and in UHV conditions (base pressure of 5×10^{-10} mbar) with an Aarhus SPM 150 equipped with KolibriSensor™ from SPECS^[5] and with a Nanonis Control system. The sharp STM W-tip was cleaned in situ via Ar⁺-sputtering. In the STM images shown, the tunneling bias voltage (U_t) is referred to the sample while the tunneling current (I_t) is that collected by the tip. The Au(111) surface [Phasis, Au(111) on mica with 200 nm of thick gold layer, 99.99% purity], was cleaned by sputtering ($I_{sp}=6 \mu\text{A}$ for 20 min) and annealing ($T_{ann}=450^\circ\text{C}$ for 20 min) cycles. After the cleaning procedure, STM was used to confirm the quality of the pristine Au surface. Nile red molecules [from Sigma Aldrich] were deposited at room temperature on Au(111) by organic molecular beam deposition (OMBD) in a high vacuum environment (base pressure of 2×10^{-8} mbar) using a home-built evaporator, at a temperature $T=160^\circ\text{C} \pm 5^\circ\text{C}$.

After a proper calibration of the evaporator, the submonolayer coverages, i.e. $\sim 0.1\text{ML}$ and $\sim 0.5\text{ML}$ of molecules, were obtained by way of brief and distinct molecular doses deposited at a fixed temperature (i.e. same deposition rate) on the Au(111) surface. The molecular monolayer regime was also obtained directly depositing a single dose of Nile red molecules on the clean gold substrate. STM measurements were taken after each dosage to determine the molecular coverage and to study the self-assembly behaviour of Nile Red molecules on “as deposited” samples. An alternate method for sub- and mono- layer preparation used in this study starts by depositing the same molecular doses followed by mild annealing procedures of the samples at a temperature below the sublimation one ($T_{\text{ann}}=120^\circ\text{C}$). At annealing temperature over 170°C Nile red molecules desorb from the substrate. The thermal treatments of the samples performed at $T_{\text{ann}}=120^\circ\text{C}$ influence the Nile red molecular assembly. All STM images were processed using the WSxM software.^[6]

Nile red molecule

Nile red (9-diethylamino-5H-benzo[α]phenoxazine-5-one) is a benzophenoxazine dye intensely fluorescent in all organic solvents and hydrophobic lipids.^[7,8] It consists of a flat aromatic core connected to $\text{CH}_3\text{-CH}_2$ terminal groups, as shown in Fig. 1(a). A distinctive feature of the molecule is its strong dipole moment, which is a consequence of a large charge transfer between the donor (diethyl amino) and acceptor (carbonyl oxygen) moieties of Nile Red (see Fig. 1(b)).

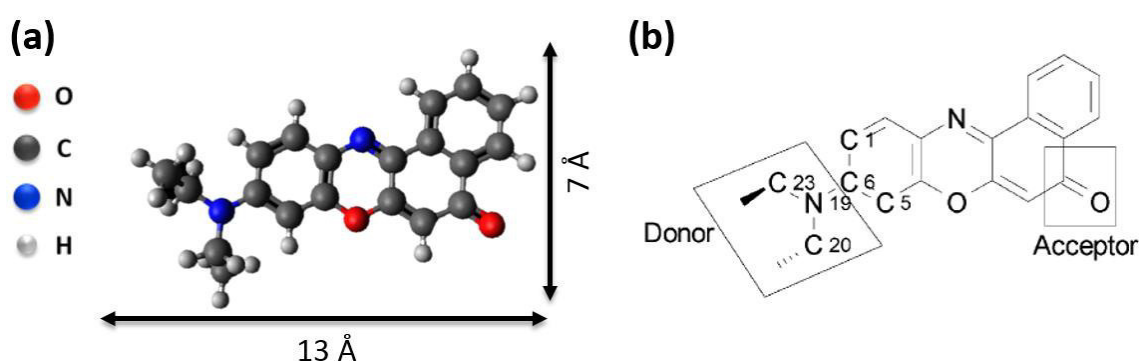


Figure 1. (a) Molecular structure of the Nile Red molecule, which exhibits the flat aromatic core connected to the $\text{CH}_3\text{-CH}_2$ groups. (b) Donor and acceptor moieties of Nile Red molecule. Figure adapted from [9].

By depending upon the relative hydrophobicity of the solvent, Nile Red fluorescence can vary over a range of 60nm, i.e. its color is ranging from golden yellow to deep red.^[8] Moreover, Nile

Chapter 3. Investigation of Nile Red self-assembled monolayer on Au(111)

red exhibits a large red shift in both its absorption and emission spectra as solvent polarity is increased.^[9] This solvent effect is known as solvatochromism and it is connected with high dipole moment μ_g of the molecule in the ground state.^[10]

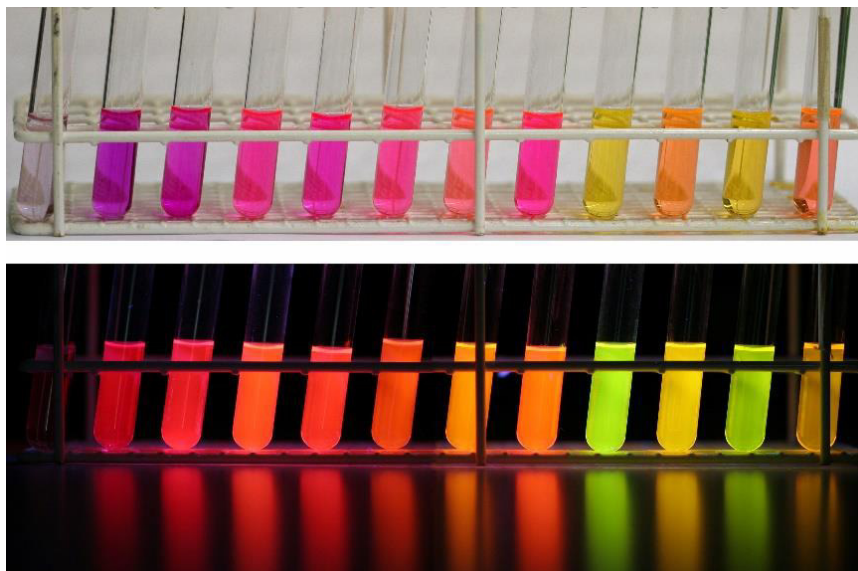


Figure 2. Nile red at daylight (top row) and UV-light (366nm, second row) in different solvents. From left to right: water, methanol, ethanol, acetonitrile, dimethylformamide, acetone, ethyl acetate, dichloromethane, n-hexane, methyl-tert-butylether, cyclohexane, toluene. Figure adapted from [11].

The solvent sensitivity of Nile Red is due to a significant increase in dipole moment from the ground to the excited state, which is a consequence of a large charge transfer between the donor (diethyl amino) and acceptor (carbonyl oxygen) moieties of Nile Red (see Fig. 1(b)).^[9] The effect of solvent polarity on the electronic transitions of Nile Red molecules were recently calculated by Tuck et al.^[9] The Nile Red ability to change the colour it fluoresces, depending upon the nature of its environment, makes this compound so useful in biological studies in order to detect and quantify lipids in various biological systems.^[12, 13]

Moreover, in recent years, Nile Red dye was also used as cyclometalated ligand for the preparation of Pd(II) and Pt(II) metallomesogens.^[14] Discotic mesophases were observed for these organometallic complexes, which were attributed to the assembly through π - π columnar stacking of disk shape dimers of the compounds. The hydrogen bond network was hypothesized between two adjacent Nile Red fragments and further confirmed by theoretical calculations performed on a semi-empirical calculation.^[15] In addition, X-ray crystal structure performed on a single crystal of Nile Red has also been resolved and confirmed in the solid state such dimeric conformation.^[16] (see Fig. 3) The dimeric form of Nile red seems to be the

most stable assembly between the molecules. This result can also be corroborated by the fact that all the hydrogen bond distances, in the X-ray crystal structure, ranging between 2.33-2.35 Å (see Fig. 3(b)), thus showing according to Jeffrey classification of H bonds^[17] a strong and mostly covalent character that in turn renders such dimer highly stable.

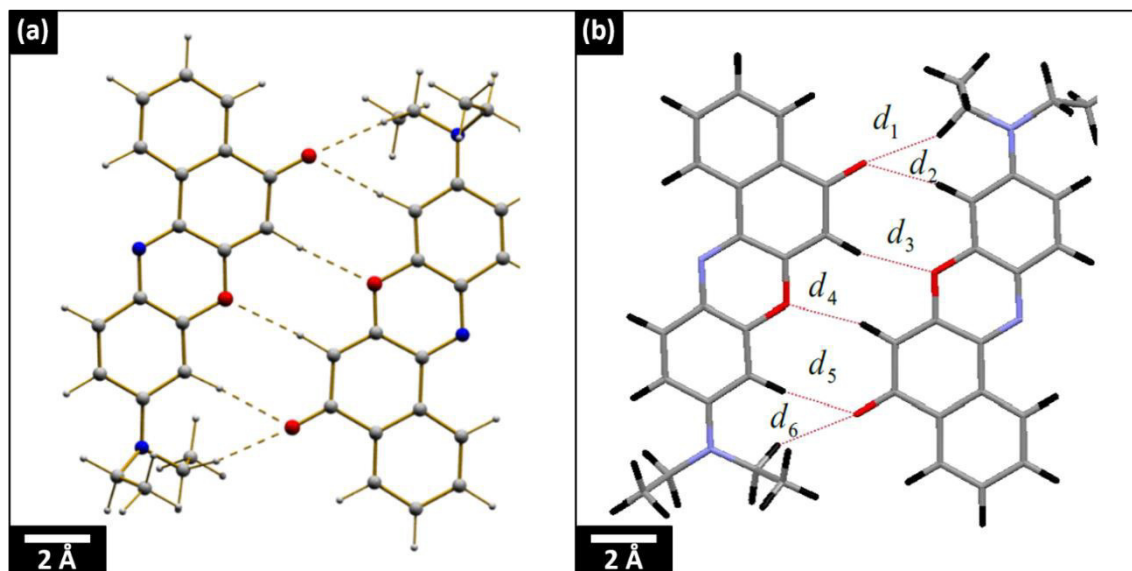


Figure 3. (a) Theoretical and (b) X-ray crystal structure of the Nile Red molecule. Hydrogen bonds distances: d_1 : 2.347 Å, d_2 : 2.337 Å, d_3 : 2.363 Å, d_4 : 2.364 Å, d_5 : 2.342 Å, d_6 : 2.349 Å.

Taking into accounts all these considerations, the present investigation represent an ideal study to shed light on the stable dimeric form of Nile red molecular packing. Moreover, the solvatochromic properties of the dye, which can be explained essentially by the feature of the monomer species, can also be questioned.

3.3 Results and discussion

3.3.1 Nile Red assembly at submonolayer coverage

An STM image of the Au(111) surface after a low-dose (~0.1 ML coverage) exposure to Nile red molecules is shown in Fig. 4. The image exhibits four small terraces separated by three monoatomic steps. The gold HB reconstruction is barely detected, while the small structures evidenced close to the steps are the Nile red molecules, which are bound to the step edges. Moreover, some molecules are also bound between them, always close to the monoatomic steps. As a result, at low coverages, Nile red molecules assembles at the preferential adsorption site of the step edges. Furthermore, the observation of attenuated and rather

“noisy” HB reconstruction on the gold terraces suggests that the molecules are highly mobile (i.e. they are not imaged by STM) and in any case weakly interacting with the Au(111) surface.

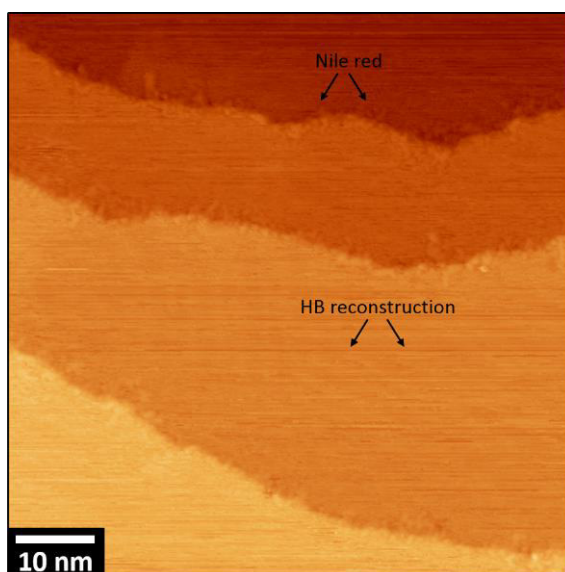


Figure 4. $80 \times 80 \text{ nm}^2$ room temperature STM image of Nile red on Au(111) at low coverage ($\sim 0.1 \text{ ML}$). Tunneling parameters: $U_t = 0.3 \text{ V}$, $I_t = 0.1 \text{ nA}$.

After the low coverage case, the Au(111) surface was exposed to a total coverage of $\sim 0.5 \text{ ML}$. As mentioned in the experimental part, two set of samples were prepared. The first one was mild annealed ($T_{\text{ann}} = 120^\circ \text{C}$) before the STM investigation, while the second one was measured without thermal treatments. The features of these two set of samples were evidenced in Fig. 5, where two representative STM images are shown. The sample measured “as deposited” (see Fig. 5(a)), i.e. without mild annealing after deposition, consists of well-defined regions containing highly ordered array of small features, i.e. the Nile red molecules. In particular, two distinct molecular packings were identified: the labeled “A” islands consist of a more dense molecular assembly, i.e. the “dense chains” structure, while “B” domains show a different molecular packing, less dense than the previous one, called “four-leaf clover” structure. Clearly, the remaining regions are not covered by molecules. Further information on these two molecular networks will be gained below, in the monolayer case. On the contrary, the sample mild annealed after deposition show only the “A” molecular domain and never show the “B” islands (see Fig. 5(b)), i.e. only the “dense chains” network. The thermal treatment would seem to reorganize the molecular packing towards the more densely molecular packing, i.e. the “A” structure. As mentioned before, this behavior is well-explained below, in the monolayer case. In the sub-monolayer regime, it is worth noting that, as coverage

increases, the formation of molecular islands is observed. Moreover, the Au surface continues to show the typical HB reconstruction, both on the bare Au surface and on the covered regions. This suggests that the molecules-substrate interaction is not strong enough to lift the HB reconstruction.

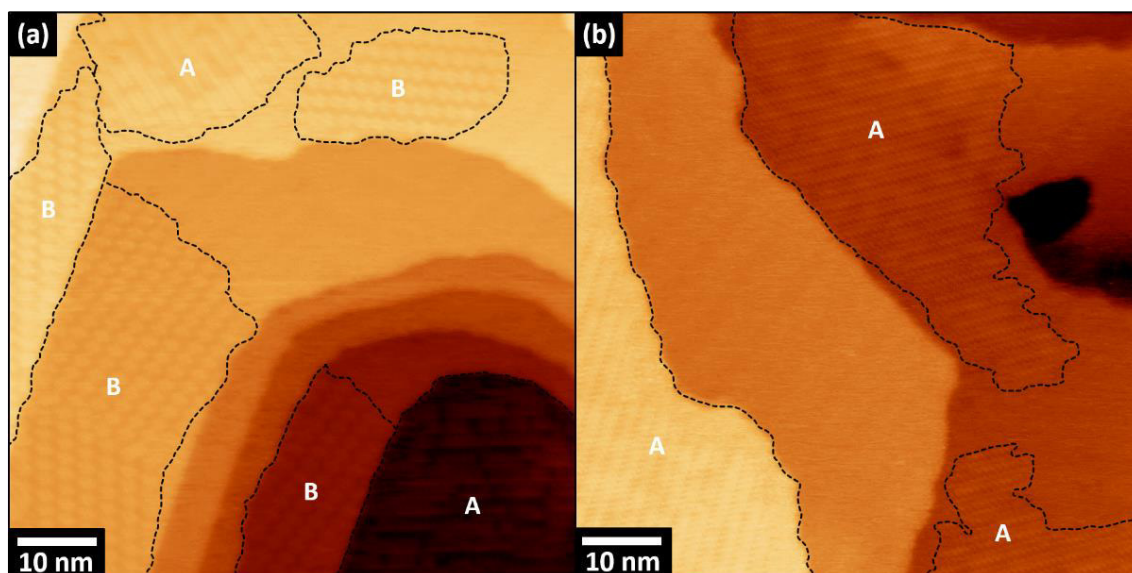


Figure 5. (a) “As deposited” and (b) “mild annealed” 80x80nm² room temperature STM images of Nile red on Au(111) at intermediate sub-monolayer coverage (~0.5 ML). Tunneling parameters: (a) $U_t=0.7V$, $I_t=0.1 nA$; (b) $U_t=0.4V$, $I_t=0.15nA$.

Although previous studies performed with low-temperature STM (LT-STM) on organic self-assembly on Au(111) surface evidenced the elbow sites as preferential nucleation sites,^[18-21] in this study no preferential sites of Nile red molecules were found at sub-monolayer coverages above 0.1 ML. Moreover, as shown in more details below in the monolayer case, molecular packings are oriented randomly with respect to the Au(111) surface. These results confirm again the weak bonding between the molecules and the gold substrate. Briefly summarizing, at low coverages Nile red molecules decorate the high coordination step edge sites. By increasing the coverage, islands of ordered molecules are formed on the gold substrate, but not in preferential sites of the Au(111) surface. Moreover, the presence of mobile molecules during the scanning procedure at room temperature is evidenced by the fact that the Au(111) surface appears a little bit “dirty” in presence of molecular islands. The HB reconstruction is still visible indicating that the molecule–substrate interaction is not strong enough to destroy the electronic properties of the substrate. Furthermore, Nile red are always observed in molecular islands composed by “dense chains” or “four-leaf clover”

structures on gold terraces, and never as isolated molecules, implying that the molecule–molecule stabilization is stronger than the diffusion barrier at the surface. In addition, the Nile red self-assembly have no preferential directions on the Au(111) surface. This clearly point out that the interaction between the molecular-array and the substrate do not play an important role in establishing the equilibrium surface morphology.

3.3.2 Monolayer Regime of Nile Red on Au(111)

Nile Red self-assembly after the thermal treatment

In the monolayer regime, Nile red molecules self-assemble on the Au(111) surface by forming molecular islands that have the same molecular packing, but several rotational domains, as shown in Fig. 6. As mentioned for the sub-monolayer case, the Nile red self-assembly after the mild annealing of the samples is only the more dense molecular packing, the so-called “dense chains” structure. The rotational domains do not follow the 6-fold symmetry of the gold surface. As also shown in the sub-monolayer coverages, the gold herringbone (HB) reconstruction is still observed beneath the monolayer molecular adlayer (see Fig. 6(a)-(b)). As reported in literature for several metal/organic interfaces,^[22-24] this behaviour suggests that the interaction between molecules and Au(111) is weak enough to not change significantly the electronic properties of the substrate. As a consequence, the Nile red islands, which have lateral dimension of tens of nm, are randomly oriented both to each other (see Figs. 6(a1)-(a3)) and respect to the underneath Au(111) herringbone reconstruction (see Fig. 6(b)). In addition, the regions between the molecular islands are characterized by the presence of isolated (i.e. free) molecules, which sometimes are clearly observed.

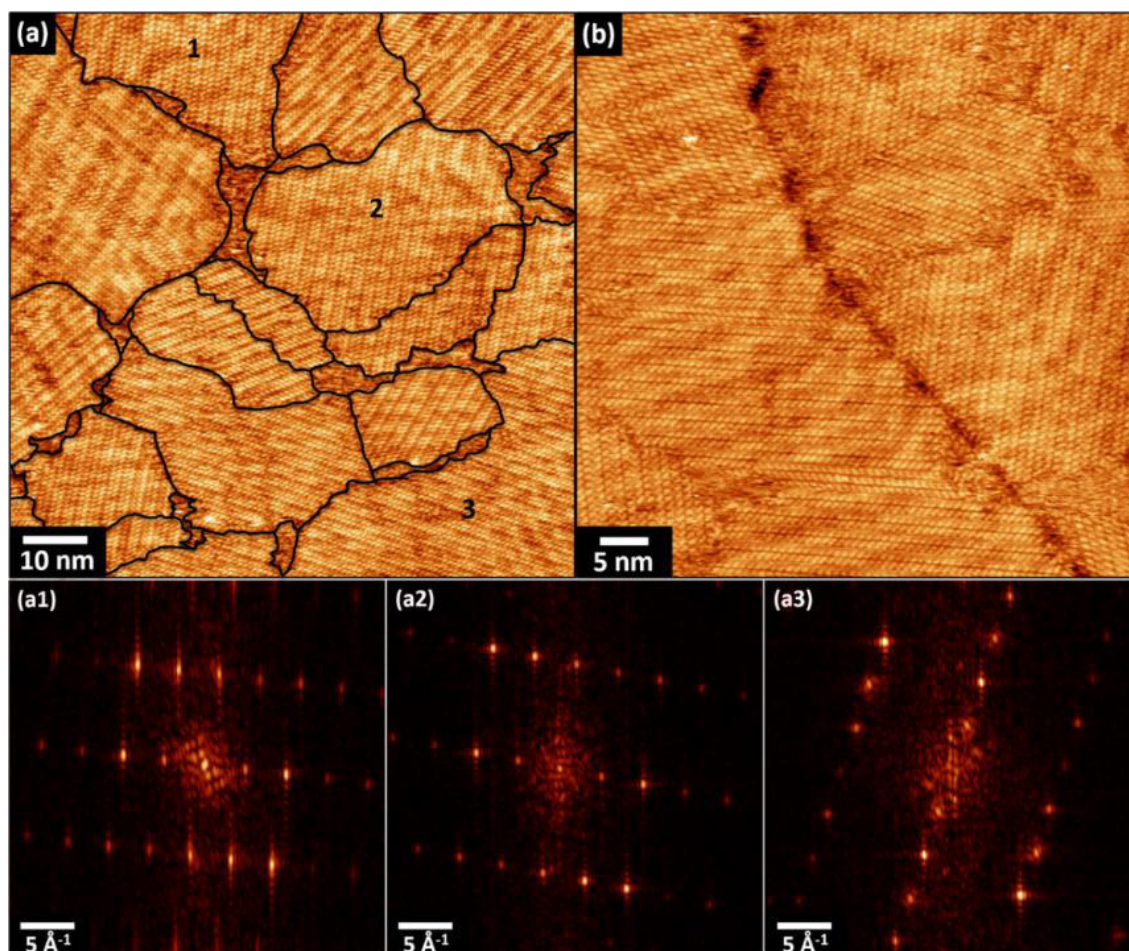


Figure 6. (a) $100 \times 100 \text{ nm}^2$ room temperature STM image of Nile red monolayer on Au(111). Several rotational domains were found on the gold surface (see black borders). (b) $70 \times 70 \text{ nm}^2$ room temperature STM image where the gold herringbone reconstruction (HB) is detected. The gold HB does not influence the orientation of the overlying molecular islands. (a1)-(a3) Fourier analysis of the molecular islands labeled in (a) as "1"- "2"- "3" show that their different orientation on the Au(111) surface. Tunneling parameters: (a) $U_t = 0.7 \text{ V}$, $I_t = 0.1 \text{ nA}$; (b) $U_t = 0.4 \text{ V}$, $I_t = 0.15 \text{ nA}$.

STM imaging at smaller scale gives further information about the molecular assembly. Nile red molecules self-assemble in a dense molecular packing where the identified unit cell is described by considering **a** and **b** as parameters. The molecular cell consists of two molecules per unit cell and the Nile Red density is of $0.93 \text{ molecules/nm}^2$. Inside the molecular cell, the nearest neighbours of each molecule can be identified by the **a** and **c** parameters. The analysis performed by means of STM points out that the aromatic core of Nile Red molecules is flat lying on the gold surface, while the $\text{CH}_3\text{-CH}_2$ groups are free to rotate in all directions.

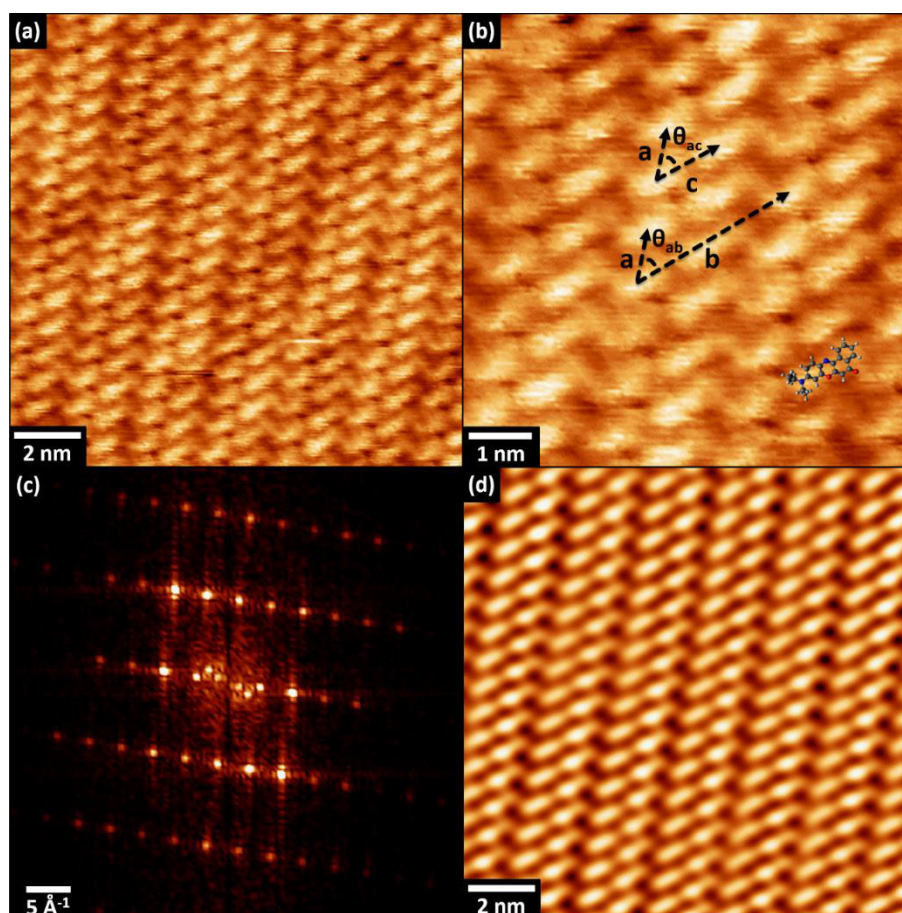


Figure 7. (a) $15 \times 15 \text{ nm}^2$ and (b) $8 \times 8 \text{ nm}^2$ room temperature STM images of Nile red monolayer on Au(111). a , b , θ_{ab} are the parameters of the molecular unit cell, while a , c and θ_{ac} identify the first neighbors of each molecule inside the molecular cell (see the dashed arrows in (b)). (c) FFT analysis of the image deposited in (a); the well-defined spots in the reciprocal space allow to reconstruct the molecular lattice in the real space (see image (d)). Tunneling parameters: (a)-(b) $U_t = 0.1 \text{ V}$, $I_t = 0.1 \text{ nA}$.

In order to determine the parameters of the identified molecular cell, the Fourier analysis of the acquired STM images have to be considered. These parameters can be directly calculated both from the reciprocal space and from the subsequent reconstruction of the molecular lattice, the latter still performed starting from the FFT analysis. The Fourier investigation and the resulting molecular pattern of the previous STM image (i.e. Fig. 7(a)) are depicted in Figs. 7(c) and (d), respectively.

The measured lattice parameters are summarized in the table below:

a (nm)	b (nm)	c (nm)	θ_{ab}	θ_{ac}
0.92 ± 0.01	3.02 ± 0.01	1.16 ± 0.02	$55.0^\circ \pm 1.0^\circ$	$50.5^\circ \pm 0.5^\circ$

Table 1. Experimental parameters of the molecular cell.

These values are the results of a wide statistical analysis performed on several filtered images gained from the reconstruction of the real molecular lattice (see Fig. 7(d)).

In order to find a molecular model to the Nile red self-assembly, theoretical semi-empirical calculations (PM3, Parametrized model number 3)^[15] were performed. By considering only the steric effects and interactions between the atoms of the molecules, and by neglecting the Nile red dipole moment, calculations were made on a molecular tetramer that was left free to arrange itself during the optimization. The resulting model exhibits four Nile Red molecules that lie flat on the Au(111) surface, with the CH₂-CH₃ terminal groups rotating in the free space. As shown in Fig. 8(a), this model consists of a network that involves four molecules bonded by six H-O bonding. The calculated tetramer seems to adapt with the experimental measurements, as shown in the Fig. 8(b).

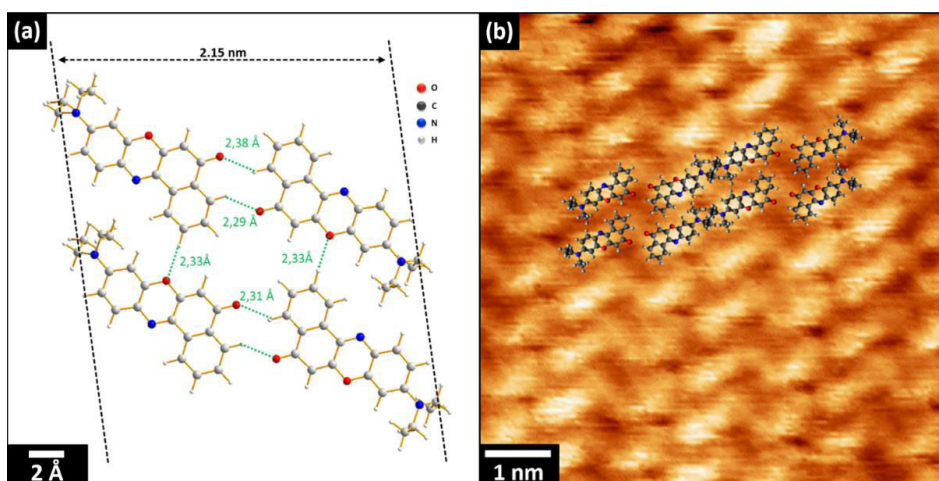


Figure 8. (a) Bonding lengths and distance between the terminal groups calculated by semi-empirical calculation. (b) Best superimposition of the molecular model on the acquired image.

As mentioned above, this semi-empirical calculation in vacuum does not take into account the intrinsic molecular dipole and interactions between Nile red and the substrate. However, the approximations used into the theoretical model are quite consistent with the real case. In fact, firstly, the applied model neglects the molecules-gold interaction; similarly, the STM investigation shows that the molecules substrate interaction is weak, i.e. determined by van der Waals bonding. Secondly, the semi-empirical model also neglects the molecular dipole; once again, the experimental data show that the Nile red dipole seems to be compensated and almost neutralized by the gold surface. In other words, the Nile red polar molecules induce a dipole moment on the gold surface such that, in the normal direction respect to the surface the total dipole moment is zero and it survives the remaining quadrupole

interaction. As a result, the proposed model based on semi-empirical calculations, fits quite well the real case.

Nile Red self-assembly investigation of the “as deposited” samples

As already mentioned in the sub-monolayer case (i.e. 0.5ML), the Nile Red molecules show two distinct molecular packings, when the samples are investigated “as deposited”, i.e. without mild annealing procedure after deposition. Fig. 9(a) exhibits a large scale STM image in which three molecular islands of “four-leaf clover” structure (labeled as “B”) and two islands of the more dense packing (labeled as “A”) are evidenced in the monolayer case. The occurrence of both molecular packings is around 50% for each one. Each molecular island is characterized by different rotational domains for both molecular packings (FFT analysis not shown). The gold HB reconstruction is always shown beneath the molecular adlayer and the Nile Red domains are randomly oriented with respect to the gold surface reconstruction as well as between them.

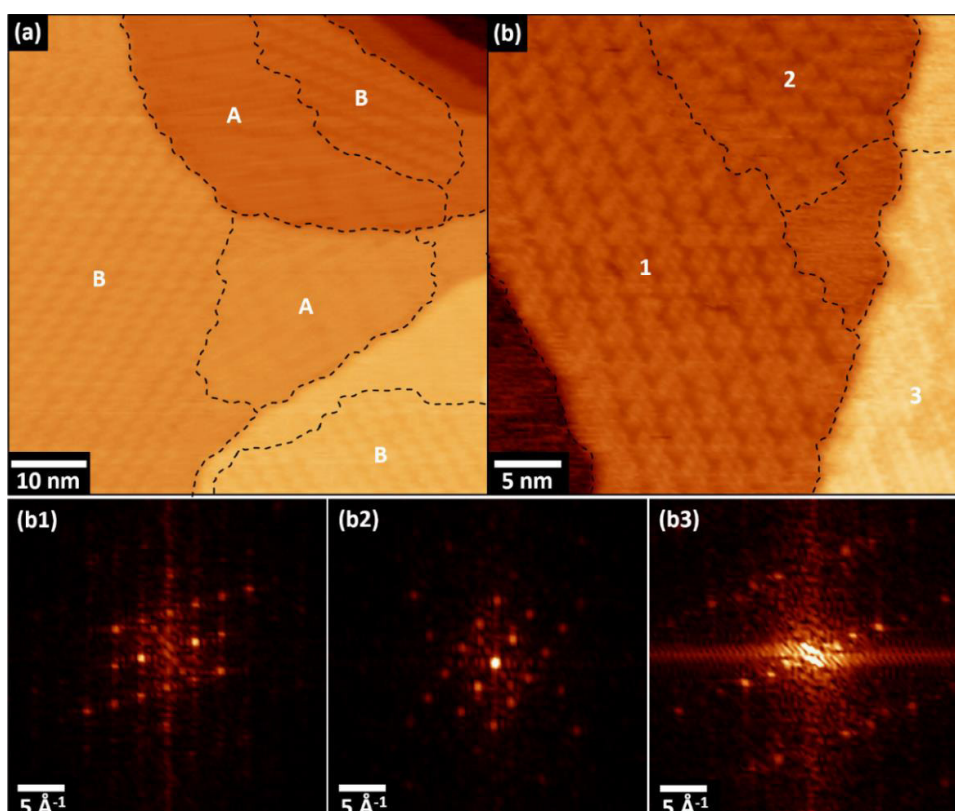


Figure 9. (a) 70x70nm² and (b) 40x40nm² room temperature STM images of Nile Red on Au(111) at monolayer coverage. Tunneling parameters: (a) $U_t=1.4V$, $I_t=0.3nA$; (b) $U_t=1.0V$, $I_t=0.1nA$. Molecular islands of both molecular packings, labeled as “A” and “B”, are evidenced in (a). Three distinct molecular islands are shown in (b). (b1) and (b2) are the corresponding FFTs of the “leaf-clover structure”, i.e. the “B” molecular packing, while (b3) is the Fourier analysis of the “dense chains” structure (“A” packing).

High-resolution STM images allows to study in detail the “four-leaf clover” packing; Figs. 10(a)-(b) show this peculiar molecular assembly. In this case, Nile Red molecules exhibit molecular tetramers that interacting between them in such a way as to form molecular rows of tetramers. The molecular unit cell can be identified by **a** and **b** parameters (see Fig. 10(b)) and shows four molecules for unit cell. The Nile Red density is about 0.58 molecules/nm². Once again, Nile red molecular core appear flat lying on the Au(111) surface, while the CH₃-CH₂ groups are free to rotate in all directions.

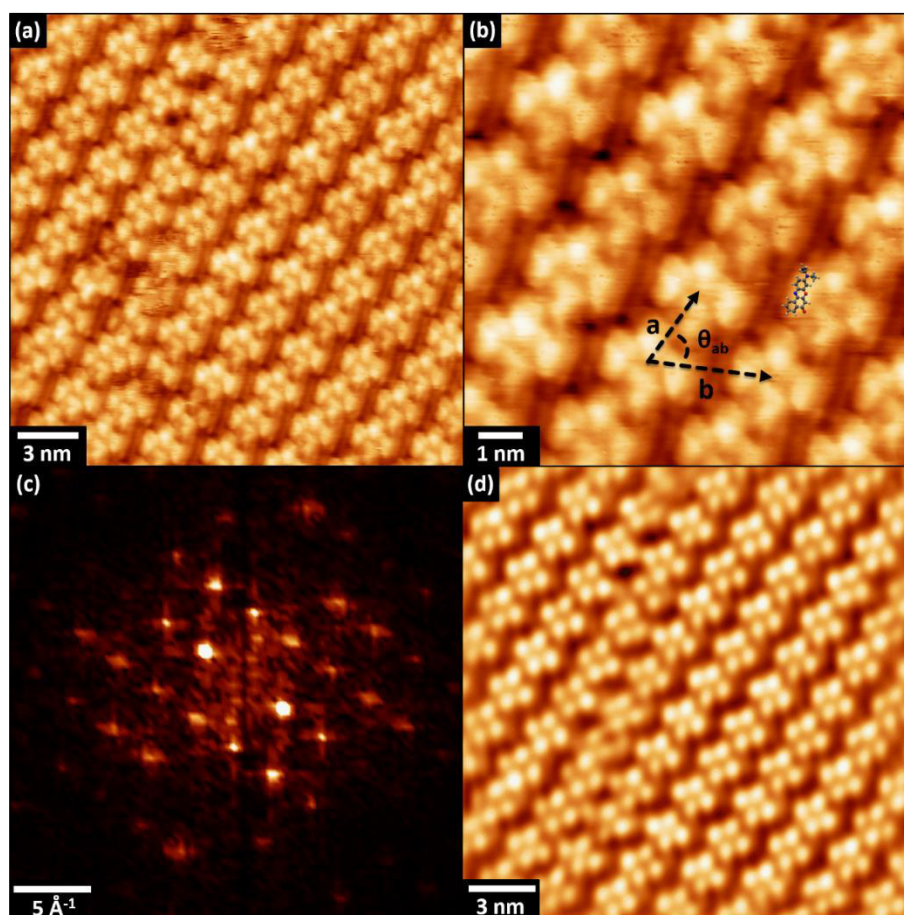


Figure 10. (a) 25x25 nm² and (b) 12x12 nm² room temperature STM images of Nile red “four-leaf clover” self-assembled monolayer on Au(111). Tunneling parameters: (a) $U_t=1.4V$, $I_t=0.3nA$. a , b and θ_{ab} are the parameters of the unit cell. (c) FFT analysis of the image depicted in (a); (d) the well-defined spots in the reciprocal space (see (d)) allow to reconstruct the molecular lattice in the real space.

The measured lattice parameters are summarized in the table below:

a (nm)	b (nm)	θ_{ab}
2.37 ± 0.05	3.31 ± 0.11	$62.2^\circ\pm 1.6^\circ$

Table 2. Unit cell parameters of the “four-leaf clover” molecular packing.

As for the previous case, these values resulting from a wide statistical analysis performed on several filtered images gained from the reconstruction of the real molecular lattice (see Fig. 10(d)).

Currently, semi-empirical theoretical calculation are in progress. Once again, the theoretical model is carried out by neglecting the molecular polarity and by considering only the interaction between the atoms of the Nile red molecules, inside the tetramer structure. Nevertheless, a possible molecular model can be proposed starting from the experimental result, as shown in Fig. 11.

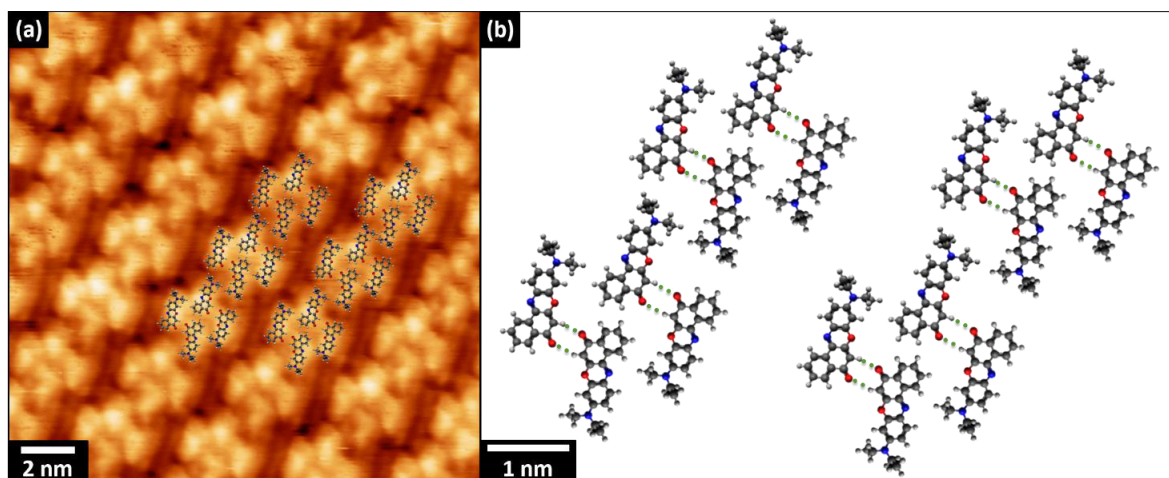


Figure 11. (a) $15 \times 15 \text{ nm}^2$ STM image of “four-leaf clover” molecular packing upon which the proposed molecular model is superimposed. (b) Proposed molecular model structure by considering the interaction between the molecules inside the Nile Red tetramer. Tunneling parameters: (a) $U_t = 1.4 \text{ V}$, $I_t = 0.3 \text{ nA}$.

Unlike the samples thermally treated after deposition, the Nile red self-assembled monolayer on Au(111) investigated by STM “as deposited” show two distinct molecular packings on the substrate, which are present in the same probability on the gold surface. These two self-assembly structures are characterized by a molecular packing that involves hydrogen bonds between the molecules. However, the most obvious evidence is the different molecular density between them, i.e. 0.93 and 0.58 molecules/ nm^2 , respectively. As mentioned above, only the denser packing survives after the thermal annealing, i.e. the “four-leaf clover” structure is reorganized in the “dense chains” packing. As a consequence, a small amounts of thermal energy provided to the system allow to tune the molecular order of Nile Red. This property turns out to be very interesting regarding the possibility to modify the 2D supramolecular order after molecular deposition. In other words, this allows to create

controlled SAMs structure only depending by the thermal treatments. Previous studies performed on other organic molecules^[25-28] also considering the possibility to control the SAMs ordering by investigating the effect of solvent on the two-dimensional (2D) supramolecular self-assemblies at the liquid-solid interface. However, the possibility to tune the molecular ordering by simply heating the sample, without using any solvent, is more beneficial in order to use the polymorphic properties of the supramolecular interface in devices.

STS investigation of the Nile Red self-assembly

In order to gain further information on the Nile Red monolayer self-assembly on Au(111) surface, a scanning tunneling spectroscopy (STS) investigation at room temperature was performed. A typical STS spectrum of the ZnTPP monolayer regime on Au(111) is shown in Fig. 12.

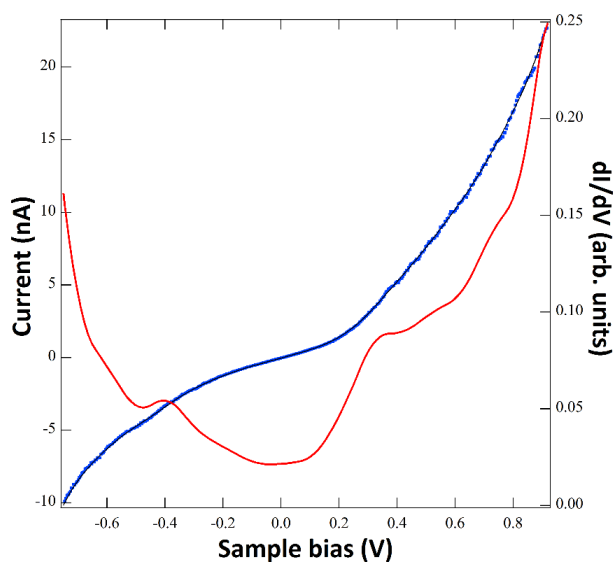


Figure 12. Representative STS spectrum of the Nile red monolayer coverage on Au(111). The spectrum was acquired at room temperature. Blue dotted line represents the I/V acquired data, while the black line is the fitting curve to the experimental data. The red line represents the LDOS, i.e. the dI/dV curve, of molecular assembly.

The main molecular states that are found around -0.4 V can be ascribed to the Nile Red highest occupied molecular orbitals (HOMOs), while the unoccupied states around +0.35 V correspond to the Nile Red lowest unoccupied molecular orbitals (LUMOs). As a result, the HOMO-LUMO gap is of about 0.75eV. Literature data only report ab initio and semi-empirical calculations carried out for the Nile Red molecules that evidence UV/visible electron band

transitions between the HOMO-LUMO bands.^[9,29] In our case, the measured local density of states (LDOS) near the Fermi level corroborates the hypothesis of weak interaction between the molecular superstructure and the Au(111) surface (no detectable Fermi level shift) and moreover also allow to experimentally detect the first HOMO and LUMO states near the Fermi level. Further investigation involving Ultraviolet photoelectron spectroscopy (UPS) and Inverse photoemission spectroscopy (IPS) will permit to obtain additional information on the HOMO and LUMO states of Nile red assembly.

3.3.3 Nile Red mobility

As mentioned above, Nile Red 2D molecular network on Au(111) is characterized by a weak interaction between the molecular coverage and the gold substrate, i.e. van der Waals bond. This behaviour is confirmed by the fact that the gold HB reconstruction is always detected beneath the molecular adlayer. Moreover, the random orientation of molecular islands with respect to the gold surface as well as between them provide further evidence of the weak substrate-adlayer interaction. In addition, the high mobility of Nile red molecules at gold terraces is reflected by the fact that only molecular islands and not isolated molecule are detected on the surface.

A further evidence of Nile Red weak interaction with gold surface is emphasized by the molecular mobility induced by the STM tip on the Nile Red sub-monolayer coverage. Fig. 13 shows three consecutive images acquired by STM on the same region. The first one, i.e. Fig. 13(a), exhibits a small Au(111) surface almost completely covered by the “dense chains” Nile Red molecular packing. Indeed, only a small region of the depicted surface (i.e. the “noisy” area) is uncovered and further characterized by some mobile molecules on the gold substrate. The successive image depicted in Fig. 13(b) shows an area less covered with molecules; the coverage, compared to the previous case, fall down from about 0.90 ML to 0.60 ML. As a consequence, the simple interaction between the STM tip and the sample surface induces molecular mobility. In other words, Nile Red molecules at the borders of molecular islands, i.e. which are not surrounded by other molecules, are induced to molecular mobility by the simple tunnelling current of the STM tip. Fig. 13(c), i.e. the third successive STM image of the same area, show the same gold surface almost totally uncovered. STM tip sent away all the molecules. The tunnelling parameters of the three image are the same. Obviously, in the monolayer case, i.e. where the molecules are locked in the H-bond assembly, the network is

stable enough to allow STM imaging of the same region for long period, without molecular mobility effects.

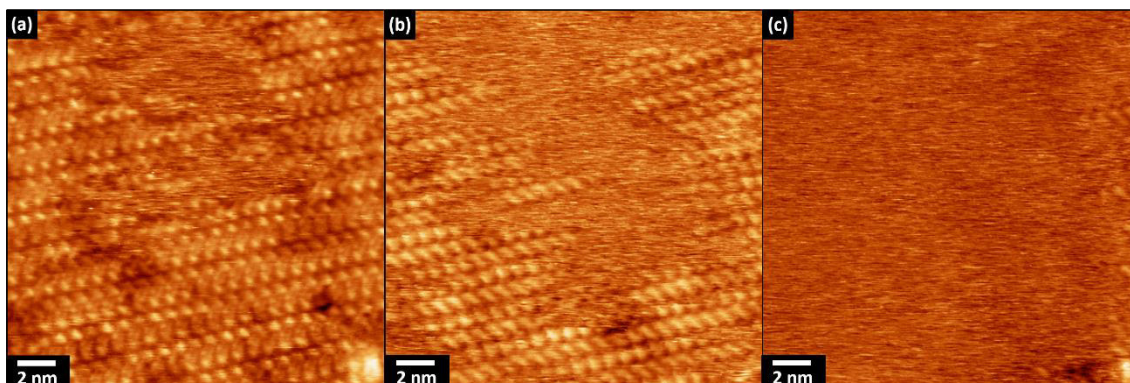


Figure 13. (a)-(c) Three successive $23 \times 23 \text{ nm}^2$ room temperature STM images of Nile red assembly on Au(111). STM tip interaction with the surface covered by Nile Red molecules lead to molecular mobility. Tunneling parameters: (a)-(b)-(c) $U_t=0.4\text{V}$, $I_t=0.15\text{nA}$.

3.4 Conclusions

In this chapter, Nile Red self-assembly on Au(111) surface was investigated by STM imaging and semi-empirical calculations. To the best of our knowledge, is the first time that this molecular self-assembly was experimentally observed by STM. As a consequence, fundamental information were gained on the Nile Red molecular packing, on the interaction between the substrate and molecular adlayer as well as on the intermolecular interaction. Samples resulting from deposition of Nile red molecules in UHV conditions at room temperature without thermal treatments show two distinct two-dimensional molecular packings, a dense one ($0.93 \text{ molecules/nm}^2$), i.e. the “dense chains” structure, and the less dense, i.e. the so-called “four-leaf clover” network ($0.58 \text{ molecules/nm}^2$). Conversely, samples thermally treated after molecular deposition reveal only the denser molecular packing. As a results, the molecular packing reorganizes itself after the mild thermal treatment, that is, in other words, there is the possibility to tune the molecular packing of the self-assembly by simply giving thermal energy to the sample. Other essential information can be obtained on the interaction between the molecular assembly and the substrate. This last interaction is relatively weak, i.e. van der Waals bond, as clearly confirmed by the fact that the gold HB reconstruction is always seen beneath the molecular adlayer. In addition to this, molecular islands are randomly oriented respect to the gold substrate as well as with between them, as a further evidence of the fact that the Au(111) surface does not influence the Nile Red

Chapter 3. Investigation of Nile Red self-assembled monolayer on Au(111)

molecular packing but it acts only as an inert template. The molecular packings shown a pattern that can be explained by only considering the hydrogen bonds between the atomic moieties, completely neglecting the polarity of the molecules. Our hypothesis considers the possibility that the Nile red molecules induce a dipole moment on the gold surface such that the total dipole moment is zero in the direction normal to the surface, while it survives only the remaining quadrupole interaction in the horizontal direction. The preliminary results here obtained pave the way to further Nile Red polar compounds that can be investigated by STM imaging and semi-empirical calculation. In order to gain more quantitative information about the molecules-substrates interaction and the geometry of adsorption of Nile Red on Au(111), further investigation involving Ultraviolet and X-Ray photoelectron spectroscopy (UPS and XPS, respectively), Inverse photoemission spectroscopy (IPS) and Near edge X-ray absorption fine structure (NEXAFS) are in progress.

References

- [1] V.Y. Kutsenko, Y. Y. Lopatina, L. Bossard-Giannesini, O. A. Marchenko, O. Pluchery and S. V. Snegir, *Nanotechnology* 28(23) (2017): 235603.
- [2] C. Vericat, M. E. Vela, G. Benitez, P. Carro and R. C. Salvarezza, *Chemical Society Reviews* 39(5) (2010): 1805-1834.
- [3] J. C. Love, L. A. Estroff, J. K. Kriebel, R. G. Nuzzo and G. M. Whitesides, *Chemical Reviews* 105(4) (2005): 1103-1170.
- [4] C. Vericat, M. E. Vela, G. Corthey, E. Pensa, E. Cortés, M. H. Fonticelli, F. Ibañez, G. E. Benitez, P. Carro and R. C. Salvarezza, *RSC Advances* 4(53) (2014): 27730-27754.
- [5] S. Torbrügge, O. Schaff and J. Rychen, *Journal of Vacuum Science & Technology B, Nanotechnology and Microelectronics: Materials, Processing, Measurement, and Phenomena* 28(3) (2010): C4E12-C4E20.
- [6] I. Horcas, R. Fernández, J. M. Gómez-Rodríguez, J. Colchero, J. Gómez-Herrero and A. M. Baro, *Review of Scientific Instruments* 78(1) (2007): 013705.
- [7] S. D. Fowler and P. Greenspan, *Journal of Histochemistry & Cytochemistry* 33(8) (1985): 833-836.
- [8] P. Greenspan, E.P. Mayer and S.D. Fowler, *The Journal of Cell Biology* 100(3) (1985): 965-973.
- [9] P.O. Tuck, R.C. Mawhinney and M. Rappon, *Physical Chemistry Chemical Physics* 11(22) (2009): 4471-4480.
- [10] A. Kawski, P. Bojarski and B. Kukliński, *Chemical Physics Letters* 463(4) (2008): 410-412.
- [11] <http://www.wikiwand.com/>.
- [12] J. Rumin, H. Bonnefond, B. Saint-Jean, C. Rouxel, A. Sciandra, O. Bernard, J.P. Cadoret and G. Bougaran, *Biotechnology for Biofuels* 8(1) (2015): 42.
- [13] I.R. Sitepu, L. Ignatia, A.K. Franz, D.M. Wong, S.A. Faulina, M.Tsui, A.Kanti and K.Boundy-Mills, *Journal of Microbiological Methods* 91(2) (2012): 321-328.
- [14] M. Ghedini, D. Pucci, A. Crispini, A. Bellusci, M. La Deda, I. Aiello and T. Pugliese, *Inorganic Chemistry Communications* 10(2) (2007): 243-246.
- [15] A. Ionescu, N. Godbert, A. Crispini, R. Termine, A. Golemme, and M. Ghedini, *Journal of Materials Chemistry*, 22(44) (2012), 23617-23626.
- [16] T. F. Mastropietro *et al.*, MAT-INLAB, Dipartimento di Chimica e Tecnologie Chimiche, Università della Calabria, unpublished results.
- [17] G. A. Jeffrey. *An introduction to hydrogen bonding*. Vol. 32. New York: Oxford University press, 1997.
- [18] C. Ruggieri, S. Rangan, R.A. Bartynski and E. Galoppini, *The Journal of Physical Chemistry C* 119 (11) (2015): 6101-6110.
- [19] L. W. Liu, K. Yang, W. D. Xiao, Y. H. Jiang, B. Q. Song, S. X. Du and H.-J. Gao, *Applied Physics Letters* 103(2) (2013): 023110.

Chapter 3. Investigation of Nile Red self-assembled monolayer on Au(111)

- [20] M. Böhringer, K. Morgenstern, W.-D. Schneider, M. Wühn, C. Wöll, and R. Berndt, *Surface Science* 444(1) (2000): 199-210.
- [21] X. Zhang, L. Tang and Q. Guo, *The Journal of Physical Chemistry C* 114(14) (2010): 6433-6439.
- [22] Z. H. Cheng, L. Gao, Z. T. Deng, Q. Liu, N. Jiang, X. Lin, X. B. He, S. X. Du and H.-J. Gao, *The Journal of Physical Chemistry C* 111(6) (2007): 2656-2660.
- [23] L. Scudiero, K.W. Hipps and D.E. Barlow, *The Journal of Physical Chemistry B* 107(13) (2003): 2903-2909.
- [24] T. Yokoyama, S. Yokoyama, T. Kamikado and S. Mashiko, *The Journal of Chemical Physics* 115(8) (2001): 3814-3818.
- [25] L. Cui, X. Miao, L. Xu, Y. Hu and W. Deng, *Physical Chemistry Chemical Physics* 17(5) (2015): 3627-3636.
- [26] X. Zhang, H. Xu, Y. Shen, Y. Wang, Z. Shen, Q. Zeng and C. Wang, *Physical Chemistry Chemical Physics* 15 (30) (2013): 12510-12515.
- [27] G. M. Florio, B. Ilan, T. Müller, T. A. Baker, A. Rothman, T. L. Werblowsky, B. J. Berne and G. W. Flynn, *The Journal of Physical Chemistry C* 113, no. 9 (2009): 3631-3640.
- [28] W. Mamdouh, H. Uji-i,[†] J. S. Ladislaw, A. E. Dulcey, V. Percec, F. C. De Schryver and S. De Feyter, *Journal of the American Chemical Society* 128(1) (2006): 317-325.
- [29] L.C. Dias, R. Custodio, F.B.T. Pessine, *Chemical Physics Letters* 302(5) (1999): 505-510.

Chapter 4

TMA and TPA self-assemblies on graphene

The ability to control the transition from a two-dimensional (2D) monolayer to the three-dimensional (3D) molecular structure in the growth of organic layers on surfaces is essential for the production of functional thin films and devices. This has, however, proved to be extremely challenging, starting from the currently limited ability to attain a molecular scale characterization of this transition. Here, through innovative application of low-dose electron diffraction and aberration-corrected transmission electron microscopy (acTEM), combined with scanning tunneling microscopy (STM), we reveal the structural changes occurring as film thickness is increased from monolayer to tens of nanometers for supramolecular assembly of two prototypical benzenecarboxylic acids – terephthalic acid (TPA) and trimesic acid (TMA) – on graphene. The intermolecular hydrogen bonding in these molecules is similar and both form well-ordered monolayers on graphene, but their structural transitions with film thickness are very different. While the structure of TPA thin films varies continuously towards the 3D lattice, TMA retains its planar monolayer structure up to a critical thickness, after which a transition to a polycrystalline film occurs. These distinctive structural evolutions can be rationalized in terms of the topological differences in the 3D crystallography of the two molecules. The templated 2D structure of TPA can smoothly map to its 3D structure through continuous molecular tilting within the unit cell, whilst the 3D structure of TMA is topologically distinct from its 2D form, so that only an abrupt transition is possible. The concept of topological protection of the 2D structure gives a new tool for the molecular design of nanostructured films.

4.1 Introduction

Supramolecular assembly is a well-established route for the controlled synthesis of nanomaterials, utilizing non-covalent forces to direct the assembly of complex nanostructures from functional molecular precursors that can be precisely tuned through chemical design. Assembly on surfaces can result in well-ordered two-dimensional (2D) molecular crystals, with interactions with the surface stabilizing the molecular overlayer and influencing the nanoscale organization and crystallography.^[1-3] These structures can be further used to direct the assembly of 'host' molecules, acting as templates or traps for the formation of ordered arrays of molecules in subsequent layers.^[4-7] Such templated growth shows promise for creating nanostructured films for applications such as organic electronics and optoelectronics,^[8] or to control surface reactivity.^[2-9-10] The structure of the 2D molecular crystal, influenced by its interaction with the surface, usually differs from the preferred 3D molecular crystallography although, with increasing thickness, a molecular film will eventually adopt the 3D crystalline structure. Understanding how this transition occurs, and at what thickness, is essential since most applications of functional organic layers (e.g. in organic electronics, organic photovoltaics, sensors, etc.) rely on films with thicknesses that fall precisely into this transition regime. On the other hand, studying the 2D–3D evolution is particularly challenging because high-resolution analytical techniques that are traditionally used are optimized either for near monolayers (scanning tunneling microscopy, STM) or for thicker films (X-ray diffraction).

Supramolecular self-assembly at surfaces has been extensively investigated on single crystal metal substrates and highly oriented pyrolytic graphite (HOPG),^[3-11] although more recently the study of molecular assembly on crystalline 2D materials, such as graphene^[12-14] and hexagonal boron nitride (hBN),^[15] has become increasingly important. For example, non-covalent molecular functionalization has been widely explored as a means to controllably alter the electronic properties of graphene,^[16,17] either for electronic doping^[18,19] or in search of a usable electronic band gap.^[20,21] Alternatively, graphene has been proposed as an electrode material in organic electronics,^[22] with the ability to control molecular assembly to increase the crystallinity and define the orientation of the organic thin film, hence improving its electrical properties.^[8, 23-25]

STM has been the method of choice for resolving the 2D structure of the molecular overlayer as it allows direct, nondestructive imaging with sub-molecular resolution.^[2] However, it is limited to monolayer (or close-to-monolayer) films and is unable to resolve the

crystallographic order in multilayer structures. Early studies used transmission electron microscope (TEM) based electron diffraction to probe the structure of self-assembled monolayers and free standing ultrathin molecular films, forming the basis of our understanding of structural transitions from monolayer to multilayer crystalline films.^[26-28] These studies were technically challenging: supramolecular assemblies are rapidly damaged by the electron beam, are extremely thin, and are typically carbon-based making it difficult to acquire TEM data with acceptable signal to noise levels. In addition, studying assembly on surfaces required fabrication of electron transparent single crystal TEM supports^[26] which was both time consuming and complicated. On the other hand, analysis in the TEM through combined diffraction and imaging experiments has in principle the potential to resolve organic structures with sub-molecular resolution.^[29,30] Recent technical advances in TEM, such as aberration correction for sub-angstrom resolution imaging and single electron detection cameras for low noise acquisition, are opening up new possibilities for studying molecular systems at even higher resolution.^[31] For TEM, graphene is a particularly exciting and relevant substrate as it is almost perfectly electron transparent, conductive, crystalline, strong, and stable.^[32] When grown on metal substrates, it is often atomically smooth and hence also well-suited for STM imaging, enabling direct comparison between the two techniques.

In this chapter, we study supramolecular assembly on highly ordered pyrolytic graphite (HOPG) and graphene of benzene-1,4-dicarboxylic acid (terephthalic acid, TPA) and benzene-1,3,5-tricarboxylic acid (trimesic acid, TMA), two molecules with planar phenyl cores that can form intermolecular hydrogen bonds through their carboxylic moieties. Both molecules have been intensively studied as prototypical systems for 2D supramolecular assembly on graphitic substrates.^[13,33-38]

After evaluating the monolayer supramolecular assembly on HOPG, as a preliminary result, we find that both molecules self-assemble on graphene to form well-ordered crystals from a 2D monolayer to thin films of several nanometer thickness. Combining STM, electron diffraction and acTEM imaging, we identify a structural transition that occurs as molecular deposition proceeds, and determine the critical thickness beyond which the film structure is no longer defined by the molecular 2D crystal at the substrate surface. We demonstrate that, despite the chemical similarity between the two molecules, their monolayer-to-thin-film transitions are dramatically different. These results have important implications for how supramolecular self-assembly can be used to design molecular structures grown from surfaces

(from thin films to macroscopic crystals), and demonstrate how recent advances in TEM make it a powerful tool for studying surface-driven supramolecular self-assembly.

4.2 Experimental section

Graphene growth

Graphene was grown on low cost copper foils via low pressure CVD using methane as a carbon source.^[39] First, the copper foils were electropolished in a solution containing orthophosphoric acid and urea (5 V, 1.5 A).^[40] After rinsing off the electrolyte with deionized water and isopropanol, the polished foils were sonicated in acetone, and then rinsed again with isopropanol and dried with nitrogen. Afterwards they were loaded into a quartz tube in a tube furnace, which was pumped to vacuum below 1×10^{-3} mbar. Hydrogen was flowed at 10 standard cubic centimeters per minute (sccm), raising the pressure to 1×10^{-2} mbar. The furnace was heated to 1000 °C, and left to anneal for 20 min. Methane was then added at 3 sccm for 30 min. This yields copper foils that are >99% covered with predominantly single layer graphene of high-quality.^[41] Under these growth conditions, the typical graphene grain size is found to be $\sim 20 \mu\text{m}$.

Graphene TEM grid fabrication

To transfer graphene to TEM grids, the graphene-coated foils were first spin-coated with formvar (3.4 mg mL^{-1}) using spin speed 3000 rpm, ramp 0.1 s, and dwell 45 s. The coated foils were then placed into ammonia persulphate to etch away the copper overnight. Once the copper was removed, the foils were transferred to five successive beakers of deionized water, to remove any remaining etchant. The floating stack was then scooped using SiN TEM supports (from Silson) and left to dry in air. The grids were then placed in chloroform for 10 min to remove the formvar. They were then transferred to acetone, and then to a critical point dryer, to dry without surface tension breaking the films. Finally, the TEM grids were further cleaned by heating on a hotplate at 200 °C for 2 h.

Molecular deposition

TPA or TMA molecules (Sigma Aldrich: TMA 1,3,5 benzenetricarboxylic acid, 95% purity, CAS 554-95-0 and TPA teraphthalic acid, 98% purity, CAS 100-21-0) were deposited by OMBD in a chamber with a base pressure $< 10^{-5}$ mbar, with source deposition temperatures of $\sim 265 \text{ }^\circ\text{C}$

and ~ 230 °C for TMA and TPA, respectively, with the substrates at ambient temperature. The deposition rate was monitored by quartz microbalance, and the film thickness was measured by AFM after deposition (see below and Appendix section A1). Molecules were deposited simultaneously on different substrates: graphene-on-TEM grids, graphene-on-copper, and HOPG.

Scanning tunnelling microscopy (STM)

STM images were acquired under ambient conditions at the liquid–solid interface under a drop of heptanoic acid with a Veeco STM with Nanoscope E controller and an A-type scanner, using mechanically-sheared Pt/Ir (90/10) tip. Typical tunneling parameters were 80 pA and -1 to -1.5 V for molecular imaging and 800 pA and -0.1 V for atomic resolution imaging of the underlying graphene. Negative bias, here applied to the sample, corresponds to filled state imaging. STM images were drift-corrected by using the graphene atomic lattice as a reference. All STM images were processed using the WSxM software.^[42]

Atomic force microscopy (AFM)

An Asylum Research MFP3D-SA was used in AC-mode (or tapping mode) for topographic imaging and combined AC mode and contact mode for thickness measurements, as described in Appendix section A1.

Transmission electron microscopy (TEM)

For electron diffraction, a JEOL 2100 TEM was used, operating at 200 kV: the selected area aperture acquired signal from circular areas 3 μm in diameter. (Note that concomitant with the ~ 20 μm graphene grain size, only one graphene orientation is present in each TEM image or diffraction pattern presented here.) All angles measured from the SAED patterns were averaged across all relevant diffraction peaks and the uncertainties calculated from the standard error of these values. The dose was estimated by measuring the current draining to earth from the phosphor screen when illuminated by the electron beam. This was adjusted to ≈ 5 $\text{e}^- \text{\AA}^{-2} \text{s}^{-1}$ for diffraction. For acTEM, a JEOL ARM 200F was used, operating at 80 kV, with CEOS probe and image aberration correction. Again, the dose was measured through the screen and was adjusted to ≈ 100 $\text{e}^- \text{\AA}^{-2} \text{s}^{-1}$ for high-resolution imaging.

4.3 Results and discussion

4.3.1 Monolayer structure of TMA and TPA on HOPG and graphene

TMA and TPA were deposited onto HOPG and chemical vapor deposition (CVD) grown graphene-on-copper foils by organic molecular beam deposition (OMBD) and imaged in ambient conditions by STM at the liquid–solid interface under a drop of heptanoic acid. The preliminary analysis performed on the HOPG surface was a starting point that paved the way to the investigation of the molecular self-assemblies on the most fascinating graphene surface.

Both molecules are simple aromatic compounds characterized by a planar structure and carboxylic groups, three for TMA and two corresponding moieties for TPA, connected to a central benzene ring (see Fig. 1).

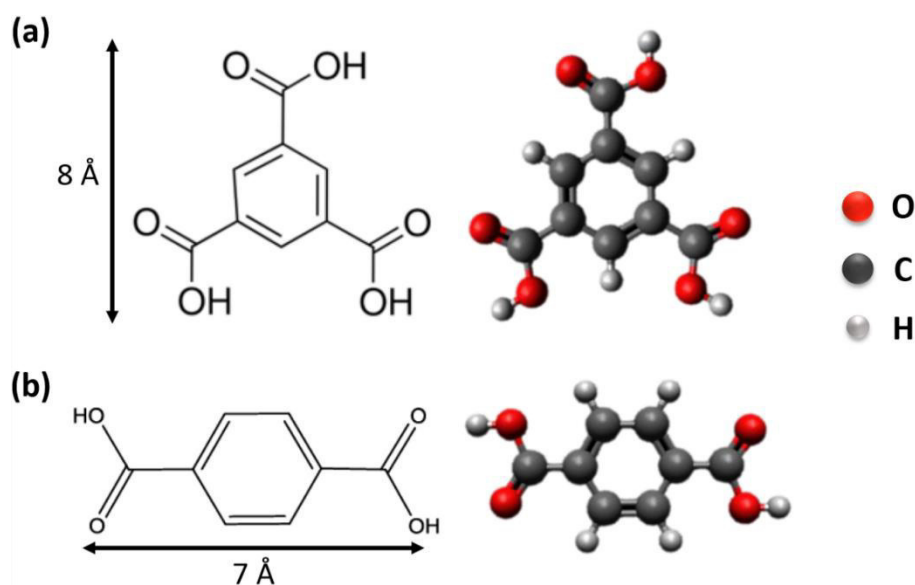


Figure 1. Molecular structure and ball and stick model of (a) TMA and (b) TPA molecules.

The presence of the carboxylic moieties ensure the formation of intramolecular hydrogen bonds that lead to extended supramolecular networks. Unlike the intermolecular bonding, the interaction between the molecules and the typical inert substrates, as noble metal and graphitic surfaces, is the π - π bonding, which involves the core ring electronic orbitals. Although self-assemblies of both molecules are stable on the surfaces, TMA networks are often more stable than the TPA ones. In fact, the higher number of H-bonds formed by TMA in the supramolecular network ensures this behavior.

Fig. 2(a) shows a well ordered self-assembly of TPA molecules that completely cover the HOPG surface.

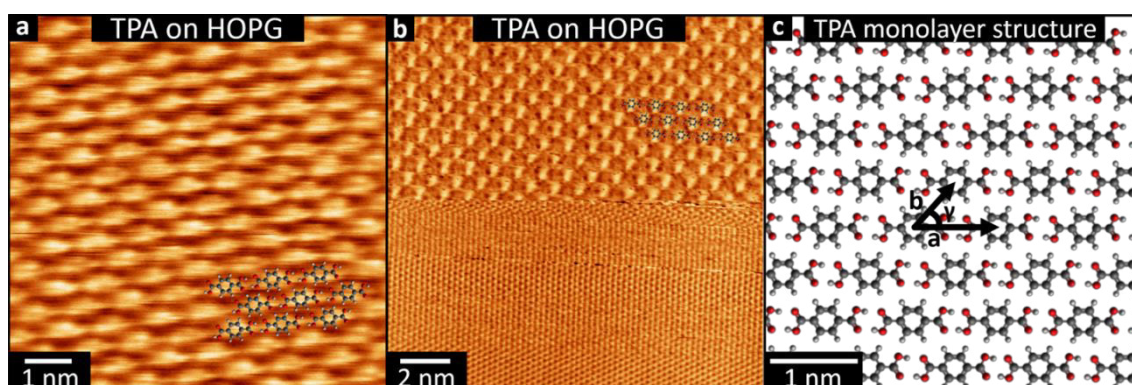


Figure 2. (a) $8 \times 8 \text{ nm}^2$ STM image of TPA on HOPG. Tunneling parameters: $U_t = -1 \text{ V}$, $I_t = 0.08 \text{ nA}$. A molecular model is superimposed on the image, which is not drift-corrected. (b) “half and half” STM image of TPA on HOPG. The proposed brickwork assembly of TPA is overlapped on the molecular side. Tunneling parameter: (top half, molecular resolution) $U_t = -1 \text{ V}$; $I_t = 0.08 \text{ nA}$; (bottom half, atomic resolution) $U_t = -0.08 \text{ V}$; $I_t = 1 \text{ nA}$. (c) Scale drawing of the proposed molecular model, where a , b and γ are the TPA unit cell parameters.

The apparent size and shape of TPA molecules in the STM topography confirm that the molecules adsorb with their molecular plane parallel to the substrate (see the molecular model overlapped in Fig. 2(a)). This adsorption geometry is usual for planar aromatic molecules on inert substrates.^[43] Furthermore, only a single supramolecular packing of TPA molecules was observed on HOPG, in agreement with the previous literature data.^[44]

In order to estimate the unit cell parameters of TPA on HOPG, it is worth noting that STM measurements acquired at room temperature are usually affected by thermal drift. This last effect can hinder the correct determining of the molecular unit cell. However, the acquisition of STM images with both molecular and substrate atomic resolution allows the images to be rescaled based on the known lattice periodicity of HOPG or graphene. Once the correct unit cell of the molecular assembly has been determined, other images showing only molecular resolution can be rescaled accordingly. This procedure was carried out for each measure reported in this work. An example of these so-called “half and half” images, for the case of TPA on HOPG, is shown in Fig. 2(b).

The resulting TPA supramolecular structure is the characteristic brickwork assembly, with lattice parameters $a = 9.79 \text{ \AA} \pm 0.08 \text{ \AA}$, $b = 7.79 \text{ \AA} \pm 0.51 \text{ \AA}$, $\theta = 49^\circ \pm 5^\circ$ (see Fig. 2(c) for the molecular model). This is the energetically favoured 2D structure of TPA on HOPG. The TPA unit cell parameters on HOPG can be compared to values for TPA monolayer on graphite,^[44] as well as

on Au(111)^[45] and Ag(111).^[46] As shown in Fig. 2(a)-(c), TPA molecules form long molecular chains on HOPG characterized by the dimeric hydrogen bonding between carboxylate groups, along the \vec{a} direction. Since the molecule length is of 7 Å, the unit cell vector along the TPA chain suggests a hydrogen bonding distance of about 2.79 Å, which is in agreement with the distance reported for bulk TPA crystals.^[47] TPA chains also interact with each other through secondary hydrogen bonds between the oxygen and the aromatic hydrogen atoms; this ensure a stable molecular packing. In principle, isolated TPA molecules can move on the HOPG surface making the STM probing difficult due to the π - π bonding between the molecules and substrate. Nevertheless, once locked in the H-bond assembly, the network is stable enough to allow STM imaging for long period.

TMA molecules, as well as TPA ones, completely cover the HOPG substrate and form well-ordered islands, but unlike TPA, can form several supramolecular structures on the HOPG surface. Although new supramolecular phases were recently reported,^[48] the most common ones, i.e. the so-called “chicken-wire” and “flower” structures, were measured by STM on HOPG, as shown in Fig. 3 and Fig. 4. Unit cell parameters for the hexagonal chicken-wire assembly and for the more compounded flower structure are $a=1.64\text{Å}\pm 0.05\text{Å}$, $b=1.67\text{Å}\pm 0.08\text{Å}$, $\gamma=59^\circ\pm 2^\circ$, and $a=2.64\text{Å}\pm 0.04\text{Å}$, $b=2.79\text{Å}\pm 0.13\text{Å}$, $\gamma=55^\circ\pm 4^\circ$ respectively. These are consistent with the values reported for the corresponding deposition of TMA on HOPG.^[33-35]

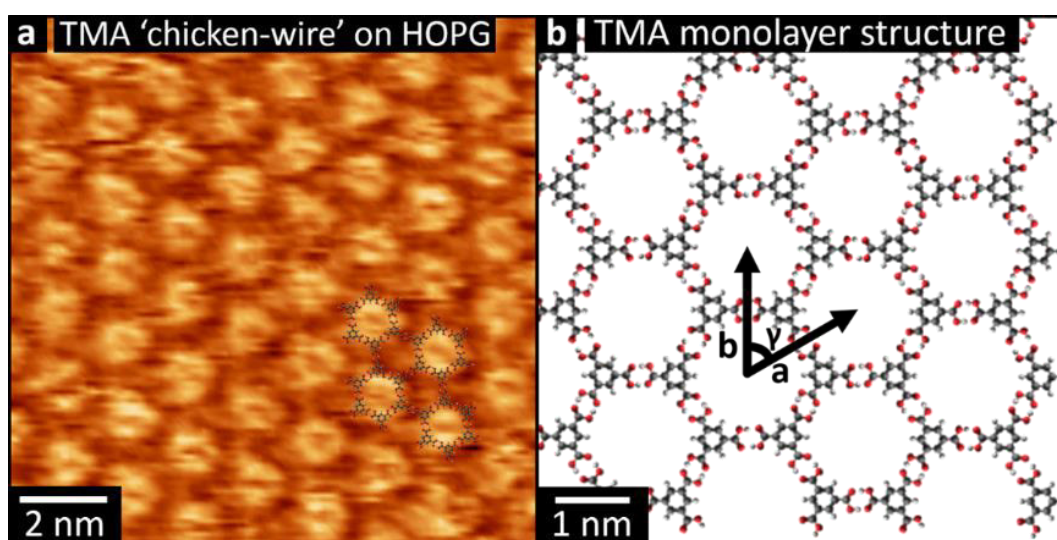


Figure 3. a) $12\times 12\text{ nm}^2$ STM image of TMA chicken-wire self-assembly on HOPG. Tunneling parameters: $U_t = -1.2\text{ V}$, $I_t = 0.05\text{ nA}$. The molecular structures is overlapped on the STM acquisition. b) Structural model of the TMA chicken-wire phase, in which a , b and γ are the unit cell parameters.

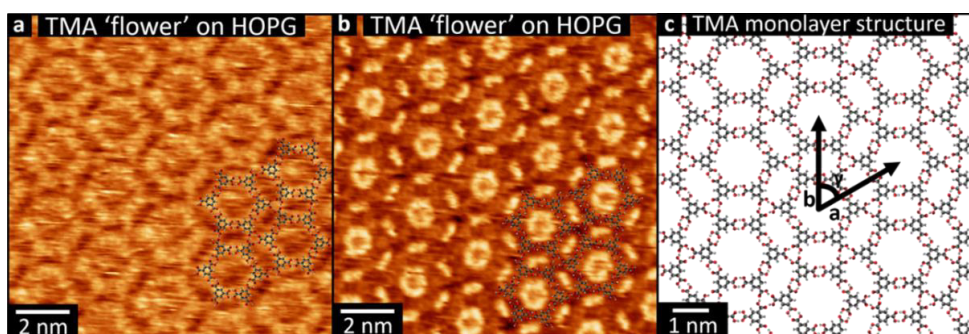


Figure 4. (a)-(b) $12 \times 12 \text{ nm}^2$ STM images of TMA flower phase on HOPG. The different imaging of the same supramolecular structure is only due to the STM tip imaging. Tunneling parameters: (a): $U_t = -1.2 \text{ V}$; $I_t = 0.05 \text{ nA}$, (b): $U_t = -1.6 \text{ V}$; $I_t = 0.05 \text{ nA}$. (c) Structural model of the TMA flower structure, in which a , b and γ are the unit cell parameters.

STM images of TMA on Gr-Cu, as in Fig. 5(a), show a hexagonal lattice, consistent with a monolayer of ‘chicken-wire’ TMA structure (shown in (b)), with lattice parameters $a = b = 1.65 \pm 0.06 \text{ nm}$ and $\gamma = 60 \pm 1^\circ$. These are consistent with the values previously reported for TMA deposited on HOPG^[33-35] and on graphene.^[13,49] Although other types of TMA assemblies have been reported on various graphite and graphene substrates,^[34,35,48,49] including the “flower” structure shown above for the HOPG, we only observed the chicken-wire packing on Gr-Cu, as also described by MacLeod et al.^[13] We note that the absence of other assemblies, such as the flower structure reported for TMA on HOPG, might be due to the deposition conditions used here.

By contrast TPA packs more densely; Fig. 5(d) shows the characteristic brickwork arrangement of TPA molecules, with lattice parameters $a = 0.95 \pm 0.02 \text{ nm}$, $b = 0.75 \pm 0.06 \text{ nm}$, and $\gamma = 53 \pm 3^\circ$, consistent with previous reports for TPA deposited onto graphene on Pt(111),^[37] as well as with measurements performed on HOPG.^[44] For both TPA and TMA, the supramolecular assembly on Gr-Cu is thus similar to that previously found for other graphitic samples.

As noted above, the difference in the 2D supramolecular packing between TMA and TPA is driven by the difference in their chemical structure. The 3-fold symmetric carboxylic acid moieties of TMA lead to hexagonal assembly, whilst dimeric hydrogen bonding between the two linearly-aligned carboxylic acid groups in TPA creates strongly bonded molecular rows with a weak interaction between them (Fig. 5(b) and (e)). The changes in packing are even more profound in their 3D bulk crystalline structures,^[50,51] as shown in Fig. 5(c) and (f). While TMA forms crystals of interweaving planes of TMA molecules that are hydrogen bonded in small units of the chicken-wire structure, for TPA the bulk structure is formed of tilted hydrogen bonded lamellar rows, that resemble quite closely the monolayer structure.

Although the molecular packing is denser in the 3D structure, its projected view (Fig. 5(f)) is very similar to the 2D structure shown in Fig. 5(e).

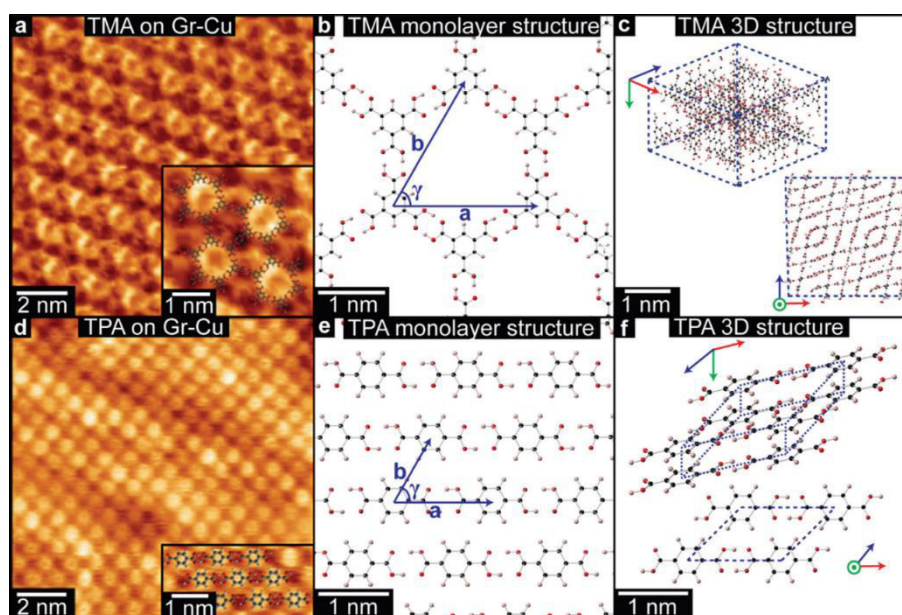


Figure 5. STM images of TMA (a) and TPA (d) on Gr-Cu. (Tunneling parameters: (a) $U_t = -1.3$ V, $I_t = 0.05$ nA, (d) $U_t = -1.5$ V, $I_t = 0.08$ nA.) The insets show enlarged regions with superposed molecular models. Schematics of the 2D chicken-wire structure for TMA (b) and brickwork structure for TPA (e), and of the 3D structures for TMA (c) and TPA (f).

4.3.2 Resolving the structure of TMA thin-films

TEM analysis of TMA deposited on freestanding graphene was used to reveal the structural changes that occur as film thickness increases. Monolayer graphene membranes were fabricated by removing graphene from its copper growth substrate and transferring to TEM support grids, as described in the experimental section. TMA and TPA were deposited by OMBD directly onto these membranes, and the structure of the resultant films was characterized by TEM imaging and diffraction. Simultaneously, the films were deposited on as-grown Gr-Cu for comparative topographic imaging and film thickness measurements by atomic force microscopy (AFM), see Appendix section A1.

Fig. 6(a)–(d) show low-magnification TEM images and corresponding selected area electron diffraction (SAED) patterns of TMA on graphene with increasing deposition time: (a) 15 seconds (measured film thickness of 2.1 ± 0.2 nm, equivalent to ~ 6 monolayers, ML), (b) 1 minute (5.5 ± 0.2 nm, ~ 15 ML), (c) 6 minutes (16 ± 2 nm, ~ 45 ML), and (d) 18 minutes (60 ± 10 nm, ~ 170 ML). For all deposition times less than 18 minutes, the TEM images show uniform contrast and the only obvious features can be attributed to residue from the transfer process

used to make the graphene membranes, suggesting the TMA is deposited as a uniform thin film, as also confirmed by AFM topography images (see Appendix section A1). For the 18 minutes deposition, there are clear variations in TEM contrast, with features of ~ 100 nm, as also seen by AFM (see Appendix section A1), suggesting a granular structure and polycrystalline film.

Despite TEM images showing little contrast, SAED reveals the molecular ordering in TMA layers and their orientation relative to the free-standing graphene substrate. For all films except the 18 minutes deposition, sharp diffraction spots are seen with spacings and (three-fold) symmetry consistent with the 2D chicken-wire TMA structure, as observed by STM, mirrored relative to the graphene lattice (see Appendix section A2). TMA lattice parameters calculated from these diffractions spots are given in Table 1: using the graphene diffraction spots to calibrate the diffraction patterns^[52] allows the TMA lattice parameters to be easily measured from the electron diffractions spots to a significantly higher accuracy and precision than those obtained from STM images.

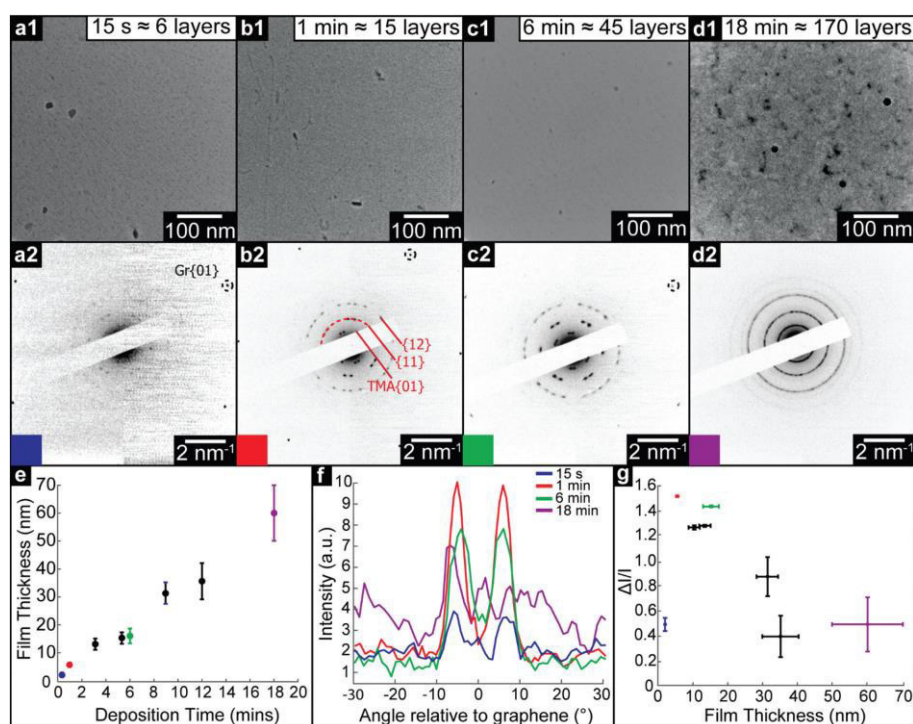


Figure 6. TEM analysis of thin films of TMA deposited onto freestanding graphene. (a1) to (d1), Brightfield TEM images of TMA thin films of increasing deposition time as marked, with corresponding SAED patterns (a2) to (d2) on which graphene and TMA diffraction peaks are labelled. (e) TMA film thickness, as measured by AFM, with deposition time. (f) Azimuthal line profiles of the diffraction intensity through the TMA {11} diffraction peaks, as labelled by the dashed arc on (b2); here 0° is defined by the graphene {01} spots. (g) Modulation of diffraction intensity, $\Delta I/I_0$ along TMA {11} azimuths, as a function of film thickness.

Deposition time	Thickness (nm)	a (nm)	b (nm)	γ (°)	Characteristic dose (electrons per nm ²)
Monolayer (STM)	—	1.65 ± 0.06	1.65 ± 0.06	60 ± 1	—
15 seconds	2.1 ± 0.2	1.64 ± 0.02	1.64 ± 0.02	60.0 ± 0.2	—
1 minute	5.5 ± 0.2	1.64 ± 0.02	1.64 ± 0.02	60.0 ± 0.3	13 ± 3
6 minutes	16 ± 2	1.65 ± 0.02	1.65 ± 0.02	60.0 ± 0.2	100 ± 50

Table 1. Film thicknesses (determined by AFM), lattice parameters and characteristic dose calculated for the monolayer and thin films of TMA. For the 18 min deposition, the angle γ is measured from 2D Fourier transforms of acTEM images (see Appendix section A9).

Two distinct orientations of the chicken wire lattice are observed, equally spaced $6.8^\circ \pm 0.1^\circ$ either side of the graphene orientation, indicating an epitaxial relationship between the TMA and graphene lattices. We also observed two orientations of the TMA chicken-wire superstructure in STM images of monolayer TMA on Gr–Cu (see Appendix section A2). The STM measured angles of $7 \pm 1^\circ$ relative to the graphene lattice are consistent with the electron diffraction results. Macleod et al.^[13] studied supramolecular assembly of monolayer TMA on graphite and graphene by STM, finding similar lattice parameters to those measured here also by STM, and deduced the following epitaxy matrix relating the TMA lattice vectors, \vec{a}_{TMA} , to those of graphene, \vec{a}_{Gr} :

$$\vec{a}_{TMA} = \begin{pmatrix} 6 & 1 \\ -1 & 7 \end{pmatrix} \vec{a}_{Gr}$$

This relationship predicts the TMA lattice parameter to be $\sqrt{43}$ times the graphene lattice constant, i.e. $a = b = \sqrt{43} \times 0.2461 \text{ nm} = 1.614 \text{ nm}$ and the angle between the TMA and the graphene lattice to be $\cos^{-1}\left(\frac{13}{\sqrt{172}}\right) = 7.589^\circ$. Although the STM results are consistent, within uncertainties, with these values, the higher accuracy and precision of the SAED measurements reveals that, for the films analyzed in Fig. 6, the relationship between TMA and graphene lattices is not exactly described by such an epitaxy matrix.

This typifies van der Waals epitaxy.^[53] Due to the weak van der Waals interactions between surface and molecular overlayer, the 2D molecular structure is not constrained to exactly follow the lattice parameters of the surface but is relaxed and unstrained, allowing lattice mismatch and differences in symmetry between surface and overlayer. Despite this, the 2D molecular layer is epitaxial (though incommensurate) to the graphene one, in that the orientation of the TMA lattice is defined relative to the graphene lattice. This conclusion is also in agreement with very recent results obtained by analyzing the Moiré patterns formed by TMA deposited on HOPG.^[54]

For thick films, this epitaxial relationship no longer holds. Electron diffraction from 9 minutes (~95 ML) and 12 minutes (~110 ML) films (see Appendix section A3) show many distinct TMA orientations, while the 18 minutes (~170 ML) TMA deposition shows rings rather than spots, as shown in Fig. 6(d2), though with similar spacings, indicating a polycrystalline film with random in-plane orientation relative to the graphene.

The SAED patterns can be analyzed to give a more quantitative insight into the degree of order in the thin films.^[28] Fig. 6(f) shows azimuthal line profiles through the {11} TMA diffraction peaks; here 0° is defined by the graphene {01} spots. The two peaks corresponding to the two orientations of TMA are readily apparent for all but the 18 min deposition. Defining I_0 as the average intensity and ΔI as the difference between maximum and average intensity, the intensity modulation $\Delta I/I_0$ along the arcs gives a relative measure of the order within the film and is plotted in Fig. 6(g) as a function of film thickness. The apparent order increases up to a maximum at ~20 nm, due to the diffraction peak intensity increasing relative to the local background. Beyond this critical thickness, the intensity modulation (I_0) decays rapidly as more TMA orientations appear, indicating a transition to a rotationally disordered phase with textured but randomly oriented grains.

We note that, as expected, the thin films of TMA rapidly degraded upon exposure to the electron beam. For such materials, structural analysis should be performed with low levels of exposure to the electron beam, below the 'characteristic dose'.^[55] As described in Appendix section A4, the characteristic dose was calculated for each film by measuring the decay in intensity of diffraction spots with exposure time. All diffraction results were acquired under low dose conditions with total doses less than this characteristic dose, and so are representative of the film structure after assembly.

Electron diffraction reveals the spatially averaged crystal structure of TMA on suspended graphene, but leaves important questions open. Are the two orientations within the TMA thin films separated into domains (as suggested by STM in the monolayer), or stacked one on the other? If in domains, what is the domain size? Similarly for the thicker, polycrystalline film, what is the grain size and do they persist through the film thickness? Here we address these questions by directly imaging the TMA layers with acTEM. All images were acquired such that the total exposure was less than the characteristic dose, as measured from the diffraction patterns, to ensure that the observed structure was typical of the as-deposited film (see Appendix section A5 for a description of the low-dose acquisition protocol). An example image

from a 1 minute TMA deposition on graphene is shown in Fig. 7(a); although there are no immediately obvious features, a 2D fast Fourier transform (FFT, inset in top right corner) shows clear spots and closely resembles the SAED patterns in Fig. 6. This FFT of the whole image is consistent with the expected 2D TMA structure with two orientations, labelled by red and blue circles in the FFT (henceforth orientation 1 and 2). Selecting smaller areas of the image, FFTs corresponding to only one orientation are found, as shown in Fig. 7(b1) and (b2) taken from the dashed boxes 1 and 2 in Fig. 7(a). By analyzing the relative intensity of these two orientations in selected area FFTs (see Appendix section A6), a map of the local TMA orientation can be constructed, as shown in Fig. 7(c). Here, the intensity of red gives the intensity of orientation 1 and, correspondingly, the intensity of blue gives that of orientation 2. This color map thus shows that the two orientations are distinct – i.e. they are separated into domains, with stacked layers of the same orientation in each domain – and reveals that the average domain size is ~ 40 nm.

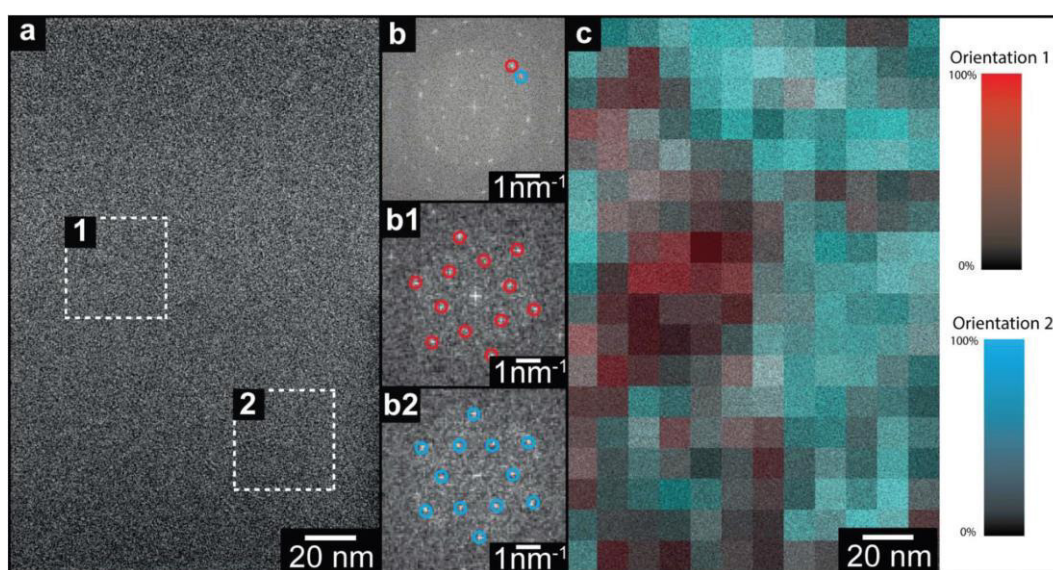


Figure 7. acTEM of TMA (1 minute deposition) on graphene. (a) Brightfield TEM image with corresponding FFTs of selected region 1 (b1) and 2 (b2): spots due to TMA are circled in red/blue showing the two different TMA orientations present. (c) Color map of TMA orientations, formed from processing the image in panel (a); the red intensity corresponds to the intensity of orientation 1 and, correspondingly, the blue intensity is due to orientation 2.

Unlike the diffraction patterns, the Fourier transform operation generates both amplitude and phase information which, when recombined, can be used to reconstruct a real space image. Fig. 8(b) is a reconstructed TEM image of the TMA film (1 minute deposition), taking the amplitude and phase from the peaks in the FFT out to 7 nm^{-1} (for further details see Appendix

section A8). This image is consistent with a multislice image simulation,^[56] Fig. 4(a) assuming a stacked molecular structure, as shown in the molecular models in Fig. (c) and (d), but not with structures that do not assume direct molecular stacking (see Appendix section A7). acTEM imaging thus proves that the TMA molecules are stacked vertically one on another, consistent with density function theory (DFT) calculations of the most energetically favorable stacking geometry,^[57] and hence that initially TMA film growth proceeds via a layer-by-layer, or Frank–van der Merwe, growth mode.^[58] Significantly, this stacking is expected to create well-ordered arrays of high-aspect ratio nanopores, around 1.5 nm in diameter and up to 20 nm deep, open at the top and reaching the pristine graphene surface at the bottom. For films beyond the critical thickness, where SAED shows polycrystalline rings, high-resolution imaging shows a small grain size (<30 nm) with evidence that the grains do not normally persist through the film (see Appendix section A9), again indicative of a polycrystalline film.

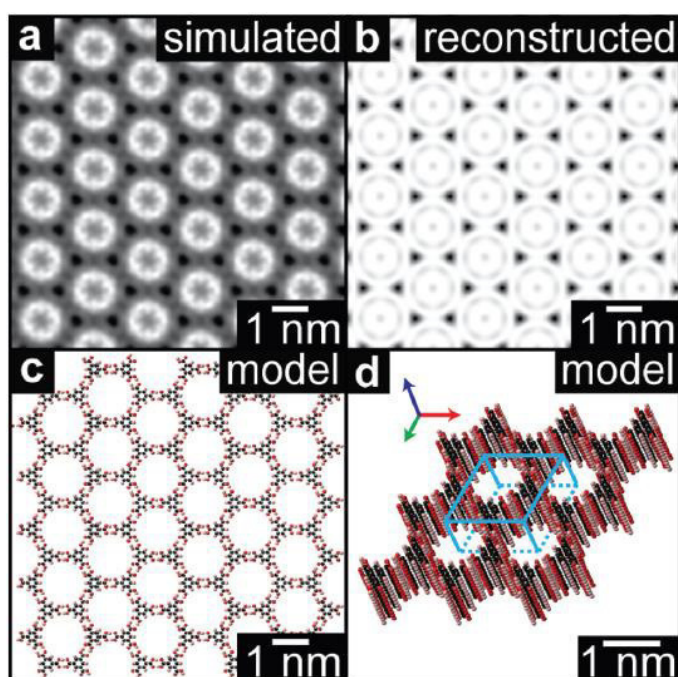


Figure 8. High resolution reconstruction of the TMA film structure. (a) Reconstructed high-resolution image of the TMA structure from the acTEM image data in Fig. 3. (b) Multislice image simulation from the molecular model shown in plan view in (c) and perspective view in (d).

4.3.3 Structural transition in TPA thin-films

We used a similar methodology to study structural transitions in TPA thin films on graphene. Fig. 9(a)–(d) show brightfield TEM images and corresponding SAED patterns of TPA thin films with increasing deposition times as marked. The film thickness was again measured by AFM (see Appendix section A1). The TEM images show a strikingly different trend to that observed for TMA: fiber-like features ~ 100 nm in length are apparent from 1 minute and persist at longer deposition times, suggesting that TPA forms 3D islands from an early stage. These features are also clearly visible in AFM images (see Appendix section A1). Such topographical changes, combined with STM evidence for an initial wetting monolayer, suggest that TPA on graphene is following a layer-plus-island, or Stranski–Krastanov, growth mode.^[58]

The corresponding SAED patterns also show behavior distinct to that observed for TMA. For the 15 s deposition, clear diffraction spots are apparent which are consistent with the brickwork 2D lattice observed for the monolayer by STM, with 6 distinct orientations symmetrically arranged relative to the graphene lattice (see Appendix section A10). As the deposition time increases, although the graphene diffraction spots are still as clear and well-defined as before, SAED from the TPA thin films gives short arcs rather than sharp spots. Azimuthal line profiles through the TPA $\{01\}$ arcs are shown in Fig. 9(f) with the corresponding $\Delta I/I$ shown in Fig. 9(g). The line profiles are roughly symmetric relative to the graphene $\{01\}$, indicating that van der Waals epitaxy still plays an important role in defining the growth orientations. Both the width of the TPA $\{01\}$ diffraction peaks and $\Delta I/I$ increase with deposition time. However, careful analysis of the positions of these diffraction arcs shows an important difference compared to TMA: the electron diffraction spacings, and hence the 2D projection of the lattice parameters, change with deposition time. This is also observed in FFTs of high-resolution images (see Appendix section A11) which show the same lattice parameters as the corresponding diffraction patterns. Interestingly, these FFTs show distinct spots rather than arcs, indicating that the SAED diffraction arcs are due to small changes in orientation between grains rather than molecular tilting within grains.^[59] The sharp spots in the FFTs enable accurate measurements of the angle between lattice vectors, as presented in Table 2. The high-resolution images also show that the crystalline grain size here is ~ 20 nm (see Appendix section A7), consistent with the width of the fibers in the low magnification brightfield images.

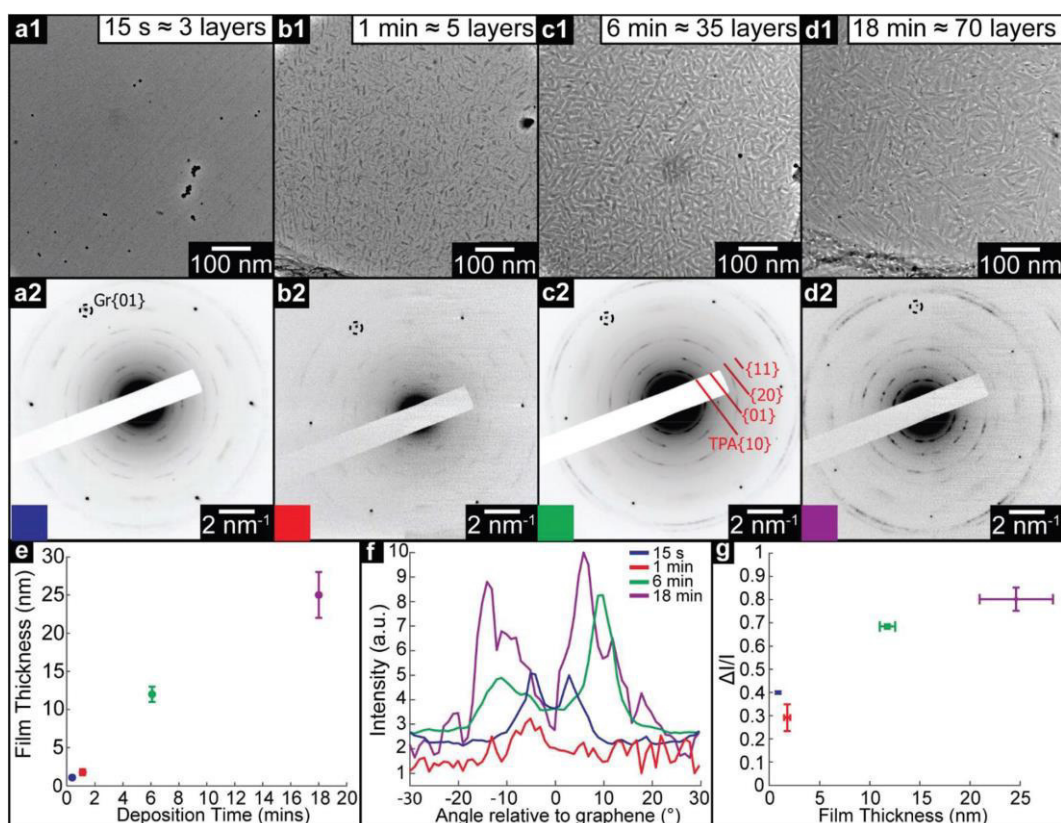


Figure 9. TEM analysis of thin films of TPA on graphene. (a1) to (d1), Brightfield TEM images of TPA thin films of increasing deposition time (15 s, 1 min, 6 min, and 18 min), with corresponding electron diffraction patterns (a2) to (d2) on which graphene and TPA diffraction peaks are labelled. (e) TPA film thickness, as measured by AFM, as a function of deposition time. (f) Azimuthal line profiles of the diffraction intensity through the TPA {01} diffraction peaks; 0° is defined by the graphene {10} spots. (g) Modulation of diffraction intensity, $\Delta I/I_0$ along TPA {11} azimuths, as a function of film thickness.

Deposition time	Thickness (nm)	a (nm)	b (nm)	γ ($^\circ$)	Unit cell area (nm ²)
Monolayer (STM)	—	0.95 ± 0.02	0.75 ± 0.06	53 ± 3	0.57 ± 0.05
15 seconds	1.1 ± 0.4	0.95 ± 0.02	0.74 ± 0.02	50 ± 2	0.54 ± 0.02
1 minute	1.2 ± 0.2	0.90 ± 0.02	0.72 ± 0.02	53 ± 2	0.52 ± 0.02
6 minutes	12 ± 3	0.85 ± 0.02	0.62 ± 0.02	57 ± 2	0.44 ± 0.02
18 minutes	25 ± 1	0.86 ± 0.02	0.60 ± 0.02	56 ± 2	0.43 ± 0.02
Bulk projection	—	0.92 ± 0.01	0.65 ± 0.01	52 ± 1	0.47 ± 0.01

Table 2. Film thickness, lattice parameters and characteristic dose for TPA on graphene. Also shown are the lattice projections looking down the c -axis of the reported TPA bulk structure.^[51] Note that the exact 3D crystallographic orientation of the thicker films here is not known.

The key result from TEM analysis of TPA films on graphene is the change in projected lattice parameters with deposition time, as summarized in Table 2. The reduction in both a and b lattice parameters, and the subsequent contraction of the unit cell area, is consistent with the molecules tilting with respect to the graphene surface and hence packing more densely, as in the bulk structure. The gradual change observed here reflects the smooth transition that can occur from the 2D, flat, structure to the 3D, tilted, structure.

The differences between the TMA and TPA film deposition are intriguing. TMA deposition results in layer-by-layer growth, templating the 2D structure upwards and creating open nanopores up to ~ 20 nm deep and ~ 1.5 nm wide, until, after a critical thickness of >20 nm, the film abruptly becomes polycrystalline with random in-plane orientations. By contrast, TPA rapidly forms fiber-like islands after the first 2D molecular overlayer and its lattice parameters gradually reduce from those of the 2D structure, smoothly becoming more consistent with the bulk structure.

We speculate on the origin of these differences through inspection of their 2D structure relative to their 3D crystallography. Energetically, the 2D structure is stabilized by interactions with the surface whilst the 3D crystallography is determined only by the intermolecular interactions; although the dominant forces driving the transition from 2D to 3D are not obvious and are worthy of future study, the differences in 3D structure between TMA and TPA give insight into their contrasting behaviour. The TPA bulk structure is characterized by parallel hydrogen-bonded lamellar rows and its (001) plane displays a structural similarity with the 2D lattice of TPA-on-graphene (the main difference being a contracted lattice parameter in 3D, through tilting of the molecule towards the [223] direction). As the film thickness increases, surface-interactions become less significant and the intermolecular interactions are expected to increasingly dominate. This explains the observed behavior of TPA; the 2D structure is a distorted (strained) component of the 3D structure and hence a smooth transition can occur. This also explains the formation of crystallites (here fiber-like) to reduce strain.^[60]

However, the 3D crystal structure of TMA is composed by interpenetrating non-planar chicken-wire frameworks and is thus very different and, crucially, topologically distinct from the planar 2D molecular lattice of the monolayer. As a result, the 2D layer cannot be thought of as a strained component of the 3D structure, and no smooth transition is possible. Hence, the TMA templates from the initial 2D layer until an abrupt transition to a polycrystalline phase; the 2D structure is topologically protected against transitions to the 3D structure.

4.4 Conclusions

We demonstrate fundamentally new insight into the growth of supramolecular thin films on surfaces through a detailed study into the structural evolution of layers of prototypical benzenecarboxylic acids. To achieve this, we have used an innovative combination of low-dose acTEM and STM to accurately determine molecular-resolution structural information on films of increasing thickness from monolayer through to tens of nanometers, a precision and range that is difficult to attain by other analytical techniques. Although this approach will not be applicable to all supramolecular assembly problems as it requires atomically thin substrates and comparatively stable molecular assemblies for acTEM, it has the potential to provide sub-nanometre resolution structural information on complex molecular thin films, as demonstrated here for the prototypical systems of TMA and TPA on graphene. For both, the structure and orientation of the first molecular overlayer are dictated by the comparatively strong hydrogen bonding between molecules and the interactions with the graphene surface that determine a weak van der Waals epitaxial relationship. As the film thickness increases beyond a monolayer, however, TMA and TPA display distinctly different behaviors, despite their chemical similarities. TMA templates from the 2D structure, stacking molecular layers directly on top of each other until, above a certain thickness, the film transitions to a polycrystalline phase with random in-plane orientations. By contrast, TPA forms fiber-like islands and the in-plane lattice parameters change continuously with thickness, smoothly becoming more consistent with the bulk structure. We propose that these differences in behavior can be understood through comparison between the 2D and 3D structures of the two molecules: the bulk structure of TMA is topologically distinct from the monolayer structure with no possible smooth transition between the two, whereas, for TPA, tilting of the molecules with respect to the surface gives a continuous transition from 2D to 3D structures. As a result, the 2D TMA structure is topologically protected and templates through the initial film growth. This new concept of topological protection of the 2D monolayer structure is expected to play an important role in the design of functional thin films by controlled supramolecular assembly.

References

- [1] A. G. Slater, P. H. Beton and N. R. Champness, *Chemical Science* 2(8) (2011): 1440-1448.
- [2] J. A. A. W. Elemans, S. Lei and S. De Feyter, *Angewandte Chemie International Edition* 48(40) (2009): 7298-7332.
- [3] J. V. Barth, *Annu. Rev. Phys. Chem.* 58 (2007): 375-407.
- [4] J. A. Theobald, N. S. Oxtoby, M. A. Phillips, N. R. Champness and P. H. Beton, *Nature* 424(6952) (2003): 1029-1031.
- [5] S. Stepanow, M. Lingenfelder, A. Dmitriev, H. Spillmann, E. Delvigne, N. Lin, X. Deng, C. Cai, J. V. Barth and K. Kern, *Nature materials* 3(4) (2004): 229-233.
- [6] H. Liang, Y. He, Y. Ye, X. Xu, F. Cheng, W. Sun, X. Shao, Y. Wang, J. Li and K. Wu, *Coordination Chemistry Reviews* 253(23) (2009): 2959-2979.
- [7] T. Kudernac, S. Lei, J. A. A. W. Elemans and S. De Feyter, *Chemical Society Reviews* 38(2) (2009): 402-421.
- [8] J. Yang, D. Yan and T. S. Jones, *Chemical Reviews* 115(11) (2015): 5570-5603.
- [9] D. Grumelli, B. Wurster, S. Stepanow and K. Kern, *Nature Communications* 4 (2013): 2904.
- [10] C. Copéret, M. Chabanas, R. Petroff Saint-Arroman and J.-M. Basset *Angewandte Chemie International Edition* 42(2) (2003): 156-181.
- [11] R. Otero, J. M. Gallego, A. L. V. De Parga, N. Martín and R. Miranda, *Advanced Materials* 23(44) (2011): 5148-5176.
- [12] A. J. Pollard, E. W. Perkins, N. A. Smith, A. Saywell, G. Goretzki, A. G. Phillips, S. P. Argent, H. Sachdev, F. Müller, S. Hufner, S. Gsell, M. Fischer, M. Schreck, J. Osterwalder, T. Greber, S. Berner, N. R. Champness and P. H. Beton, *Angewandte Chemie International Edition* 49(10) (2010): 1794-1799.
- [13] J. M. MacLeod, J. A. Lipton-Duffin, D. Cui, S. De Feyter and F. Rosei, *Langmuir* 31, no. 25 (2015): 7016-7024.
- [14] J. M. Macleod and F. Rosei, *Small* 10(6) (2014): 1038-1049.
- [15] V. V. Korolkov, S. A. Svatek, A. Summerfield, J. Kerfoot, L. Yang, T. Taniguchi, K. Watanabe, N. R. Champness, N. A. Besley and P. H. Beton, *ACS Nano* 9(10) (2015): 10347-10355.
- [16] Z. X. Zhang, H. L. Huang, X. M. Yang and L. Zang, *The Journal of Physical Chemistry Letters* 2(22) (2011): 2897-2905.
- [17] V. Georgakilas, M. Otyepka, A. B. Bourlinos, V. Chandra, N. Kim, K. C. Kemp, P. Hobza, R. Zboril and K. S. Kim, *Chem. Rev* 112(11) (2012): 6156-6214.
- [18] W. Chen, S. Chen, D. C. Qi, X. Y. Gao and A. T. S. Wee, *Journal of the American Chemical Society* 129(34) (2007): 10418-10422.
- [19] C. Coletti, C. Riedl, D. S. Lee, B. Krauss, L. Patthey, K. von Klitzing, J. H. Smet and U. Starke, *Physical Review B* 81(23) (2010): 235401.
- [20] X. Dong, Y. Shi, Y. Zhao, D. Chen, J. Ye, Y. Yao, F. Gao, Z. Ni, T. Yu, Z. Shen, Y. Huang, P. Chen and L. J. Li, *Physical Review Letters* 102(13) (2009): 135501.

- [21] S. M. Kozlov, F. Viñes and A. Görling, *Advanced Materials* 23(22-23) (2011): 2638-2643.
- [22] G. Jo, M. Choe, S. Lee, W. Park, Y. H. Kahng and T. Lee, *Nanotechnology* 23(11) (2012): 112001.
- [23] A. J. Marsden, L. A. Rochford, D. Wood, A. J. Ramadan, Z. P. L. Laker, T. S. Jones and N. R. Wilson, *Advanced Functional Materials* 26(8) (2016): 1188-1196.
- [24] W. H. Lee, J. Park, S. H. Sim, S. Lim, K. S. Kim, B. H. Hong and K. Cho, *Journal of the American Chemical Society* 133(12) (2011): 4447-4454.
- [25] H. Huang, Y. Huang, S. Wang, M. Zhu, H. Xie, L. Zhang, X. Zheng, Q. Xie, D. Niu and Y. Gao, *Crystals* 6(9) (2016): 113.
- [26] L. Strong and G. M. Whitesides, *Langmuir* 4(3) (1988): 546-558.
- [27] A. Bonnerot, P. A. Chollet, H. Frisby and M. Hoclet, *Chemical Physics* 97(2-3) (1985): 365-377.
- [28] M. Cheng, J. T. Ho, S. W. Hui and R. Pindak, *Physical Review Letters* 59(10) (1987): 1112.
- [29] C. R. Pope and V. M. Unger, *Current Opinion in Structural Biology* 22(4) (2012): 514-519.
- [30] I. Ubarretxena-Belandia and D. L. Stokes, *Current Opinion in Structural Biology* 22(4) (2012): 520-528.
- [31] E. Nogales, *Nature Methods* 13(1) (2016): 24-27.
- [32] R. S. Pantelic, J. C. Meyer, U. Kaiser and H. Stahlberg, *Solid State Communications* 152(15) (2012): 1375-1382.
- [33] M. Lackinger, S. Griessl, W. M. Heckl, M. Hietschold and G. W. Flynn, *Langmuir* 21(11) (2005): 4984-4988.
- [34] S. Griessl, M. Lackinger, M. Edelwirth, M. Hietschold and W. M. Heckl, *Single Molecules* 3(1) (2002): 25-31.
- [35] V. V. Korolkov, S. Allen, C. J. Roberts and S. J. B. Tendler, *Journal of Physical Chemistry C* 116(21) (2012): 11519-11525.
- [36] F. Shayeganfar and A. Rochefort, *Langmuir* 30(32) (2014): 9707-9716.
- [37] R. Addou and M. Batzill, *Langmuir* 29(21) (2013): 6354-6360.
- [38] W. Zhang, A. Nefedov, M. Naboka, L. Cao and C. Wöll, *Physical Chemistry Chemical Physics* 14(29) (2012): 10125-10131.
- [39] X. Li, W. Cai, J. An, S. Kim, J. Nah, D. Yang, R. Piner, A. Velamakanni, I. Jung, E. Tutuc, S. K. Banerjee, L. Colombo and R. S. Ruoff, *Science* 324(5932) (2009): 1312-1314.
- [40] B. Zhang, W. H. Lee, R. Piner, I. Kholmanov, Y. Wu, H. Li, H. Ji and R. S. Ruoff, *ACS nano* 6(3) (2012): 2471-2476.
- [41] N. R. Wilson, A. J. Marsden, M. Saghir, C. J. Bromley, R. Schaub, G. Costantini, T. W. White, C. Partridge, A. Barinov, P. Dudin, A. M. Sanchez, J. J. Mudd, M. Walker and G. R. Bell, *Nano Research* 6(2) (2013): 99.
- [42] I. Horcas, R. Fernández, J. M. Gómez-Rodríguez, J. Colchero, J. Gómez-Herrero and A. M. Baro, *Review of Scientific Instruments* 78(1) (2007): 013705.

- [43] M. Lackinger, T. Müller, T.G. Gopakumar, F. Müller, M. Hietschold, M. and G.W. Flynn, J. The Journal of Physical Chemistry B 108(7) (2004): 2279-2284.
- [44] W. Song, N. Martsinovich, W.M. Heckl and M. Lackinger, Journal of the American Chemical Society 135(39) (2013): 14854-14862.
- [45] S. Clair, S. Pons, A.P. Seitsonen, H. Brune, K. Kern and J.V. Barth, The Journal of Physical Chemistry B 108 (38) (2004): 14585-14590.
- [46] T. Suzuki, T. Lutz, D. Payer, N. Lin, S.L. Tait, G. Costantini and K. Kern, Physical Chemistry Chemical Physics 11 (30) (2009): 6498-6504.
- [47] M. Śledź, J. Janczak and R. Kubiak, Journal of Molecular Structure, 595(1) (2001): 77-82.
- [48] Q. Zhou, Y. Li, Q. Li, Y. Wang, Y. Yang, Y. Fang and C. Wang, Nanoscale 6(14) (2014): 8387-8391.
- [49] K. Banerjee, A. Kumar, F. F. Canova, S. Kezilebieke, A. S. Foster and P. Liljeroth, The Journal of Physical Chemistry C 120(16) (2016): 8772-8780.
- [50] D. J. Duchamp and R. E. Marsh, Acta Crystallographica Section B: Structural Crystallography and Crystal Chemistry 25(1) (1969): 5-19.
- [51] M. Bailey and C. J. Brown, Acta Crystallographica 22(3) (1967): 387-391.
- [52] N. R. Wilson, P. Pandey, R. Beanland, R. J. Young, I. Kinloch, L. Gong, Z. Liu, K. Suenaga, J. P. Rourke, S. J. York and J. Sloan, ACS Nano 3(9) (2009): 2547-2556.
- [53] M. I. B. Utama, Q. Zhang, J. Zhang, Y. Yuan, F. J. Belarre, J. Arbiol and Q. Xiong, Nanoscale 5(9) (2013): 3570-3588.
- [54] S. Spitzer, O. Helmle, O. Ochs, J. Horsley, N. Martsinovich, W. M. Heckl and M. Lackinger, Faraday Discuss., DOI:10.1039/C7FD00113D.
- [55] R. F. Egerton, Ultramicroscopy 127 (2013): 100-108.
- [56] K. Ishizuka and N. Uyeda, Acta Crystallographica Section A: Crystal Physics, Diffraction, Theoretical and General Crystallography 33(5) (1977): 740-749.
- [57] F. Shayeganfar, Journal of Physics: Condensed Matter 26(43) (2014): 435305.
- [58] C. Ratsch and J. A. Venables, Journal of Vacuum Science & Technology A: Vacuum, Surfaces, and Films 21(5) (2003): S96-S109.
- [59] S. Hui, Microscopy Research and Technique 11(4) (1989): 286-297.
- [60] D. Käfer, L. Ruppel and G. Witte, Physical Review B 75(8) (2007): 085309.

4.5 Appendix section

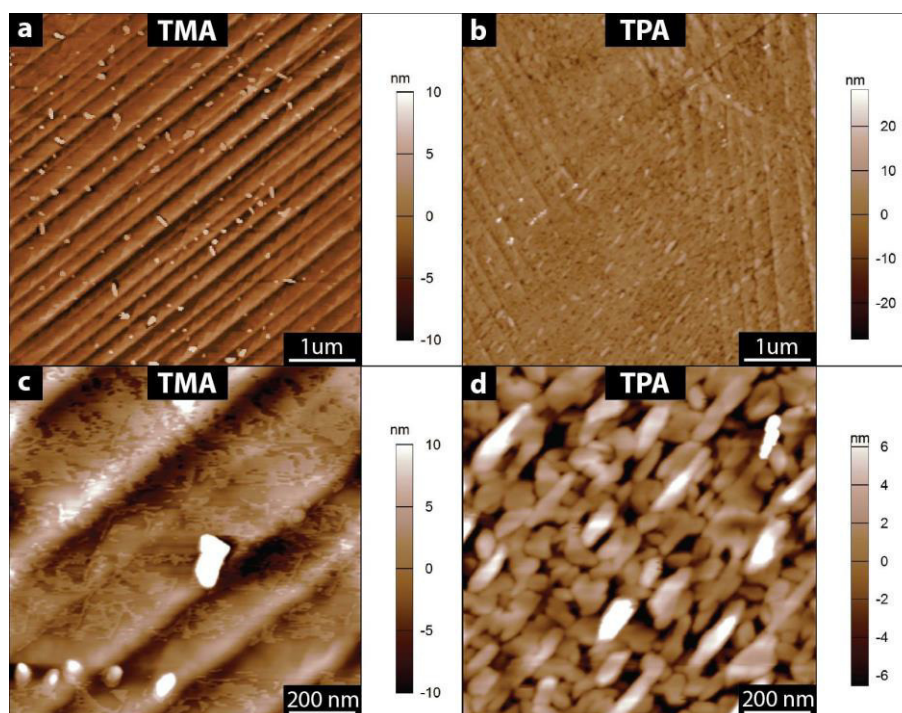
A1: Atomic force microscopy (AFM) of TMA and TPA thin films on graphene

Figure A1a. Tapping mode AFM images of TMA, (a) and (c), and TPA films, (b) and (d), on graphene on copper for 6 minute depositions.

The topography of TMA and TPA films was studied using AFM. Figure A1a shows tapping mode images of 6 minute deposition films for TMA (a,c) and TPA (c,d). The TMA and TPA films themselves appear in stark contrast to each other; TMA shows a flat, continuous thin film whereas TPA appears to grow in small lozenge-shaped crystallites. This is in agreement with the structures studied using TEM.

The thicknesses of TMA and TPA films were also measured using AFM. Figure A1b shows measurements of film thickness for the TMA and TPA depositions onto graphene on copper. Panel (a) is a tapping mode AFM topography image of an 18 minute-deposition film of TPA on graphene on copper after a trench has been scratched through the film. The trench is scratched by repeatedly scanning a small region in contact mode. Panel (b) is an averaged line profile from the white dashed rectangle in (a), from which the film thickness was measured.

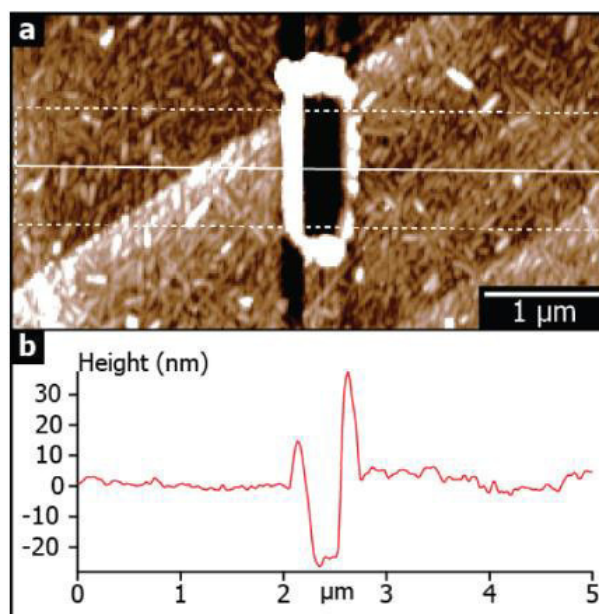


Figure A1b. AFM film thickness measurement. Panel (a) shows an AFM image of an 18-minute deposition of TPA on graphene on copper, after a trench has been scratched using contact mode. Panel (b) is an average line profile, from the dashed rectangle in (a), from which the film thickness is measured.

A2: Two orientations of TMA on graphene observed by SAED and STM

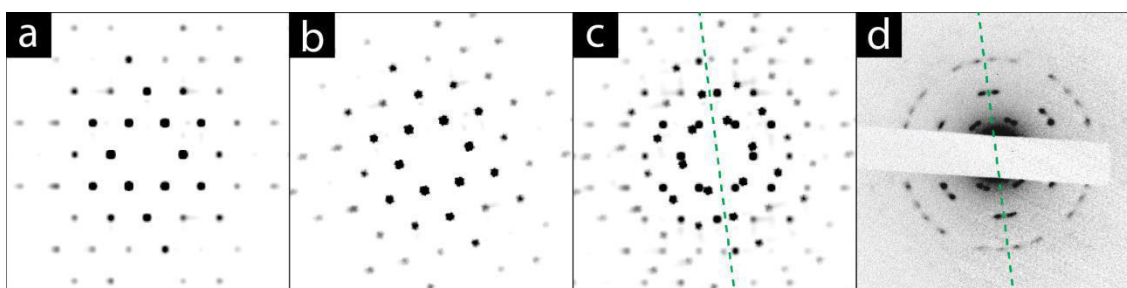


Figure A2a. SAED simulations of TMA on graphene. (a) Simulated SAED of a TMA monolayer. (b) Simulated SAED of a TMA monolayer rotated 13.6° relative to (a). (c) Addition of SAED simulations presented in (a) and (b) showing close similarity to experimental SAED image presented in (d). The green dashed line in (c) and (d) shows the orientation of graphene reflections which the two TMA grains are oriented with respect to. Simulations were performed using *cITEM*, an open-source multislice simulation package (M. A. Dyson, *cITEM: OpenCL TEM/STEM simulation code*, URL (<http://github.com/ADyson/cITEM>), 2014).

Analysis of SAED simulation patterns from TMA reveals how two distinct orientations of the chicken-wire superstructure arise in the experimental SAED patterns through addition of individual SAED patterns from separate TMA grains. Combining individual SAED simulation patterns of TMA monolayers rotated 13.6° relative with respect to each other reveals a SAED pattern similar to the experimental images.

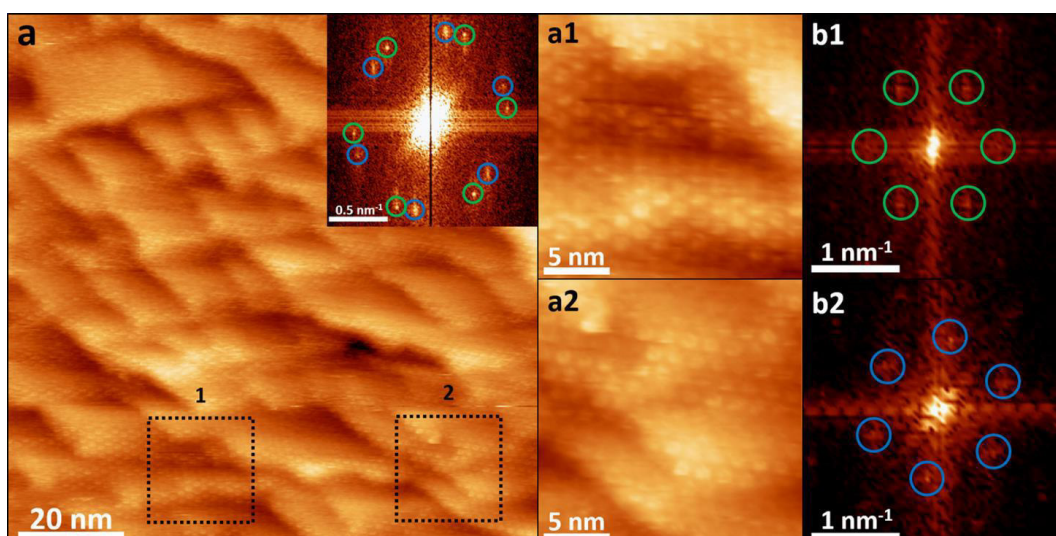


Figure A2b. STM of TMA on graphene. (a) Large scale STM image ($100 \times 100 \text{ nm}^2$) of a TMA monolayer at the interface between heptanoic acid and graphene on copper. Tunneling parameters: $U_t = -1.3 \text{ V}$, $I_t = 0.05 \text{ nA}$. Inset: FFT of the whole image indicating the presence of two distinct orientations of the TMA chicken-wire lattice. (a1) and (a2) are magnified views of the regions in (a) labelled as 1 and 2, respectively. (b1) and (b2) are the corresponding FFTs. (a1) and (a2) images have been drift-corrected by using atomic resolution images of the graphene substrate.

Analysis of STM images from TMA on Gr-Cu shows two distinct orientations of the chicken-wire superstructure with respect to the underlying graphene lattice. Figure A2b (a) shows a large-scale STM image with TMA molecules completely covering the graphene surface and the inset displays its fast Fourier transform (FFT). Two different rotational domains (relative angle of $14^\circ \pm 2^\circ$) can be identified in the FFT for the TMA chicken-wire structure, and are indicated by green and blue circles, respectively. Figures A2b (a1) and (a2) show magnified images of the two distinct sub-regions marked by dotted squares in Figure A2b (a). The corresponding FFTs are shown in Figures A2b (b1) and (b2), respectively, and display only one orientation each. STM images were drift-corrected by using the graphene atomic lattice as a reference. In particular, the acquisition of STM images with both molecular and substrate atomic resolution allows the images to be rescaled based on the known lattice periodicity of graphene. Once the correct unit cell of the molecular assembly has been determined, other images showing only molecular resolution can be rescaled accordingly.

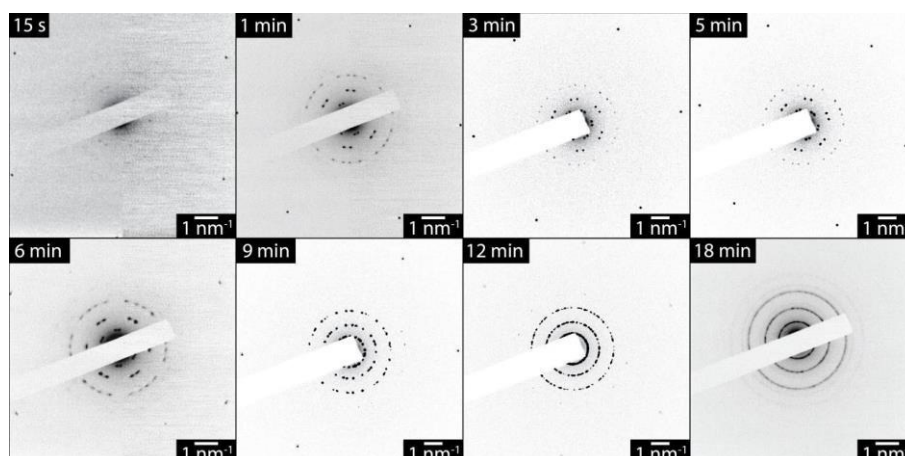
A3: Film thickness dependence of diffraction from TMA on graphene

Figure A3. Electron diffraction patterns from TMA thin films of increasing thickness on graphene. Two distinct orientations are visible until 6 min; longer depositions show increasing amounts of orientational disorder.

A4: Measuring the characteristic dose of TMA on graphene

The use of electron microscopy to study organic thin films is restricted by the lifetime of the organic molecules, and their supramolecular structure, under the electron beam. To quantify this lifetime, diffraction patterns from organic thin films can be analyzed to find the characteristic dose DC – defined as the dose after which the diffraction spot intensity has been reduced by a factor $1/e$, and after which the structure is believed to have been significantly damaged.^[A1]

$$D_c = Dt_c$$

where D is the electron dosing rate of the electron beam at the sample plane and t_c is the time after which the diffraction spot intensity has been reduced by a factor $1/e$ (characteristic time). Figure A4 (a) to (d) show four images from a sequence of diffraction patterns that were recorded continuously over 38 seconds, with a diffraction pattern acquired every 0.3 seconds, from a 1 minute-deposition of TMA on graphene. Throughout the exposure, the dosing rate was kept constant at $(1.3 \pm 0.3) \text{ e-}\text{\AA}^{-2}\text{s}^{-1}$. The spots attributed to TMA are clear, as are those from the graphene substrate. From the series it is apparent that the TMA diffraction spots reduce in intensity with increasing exposure time, and are not visible after 33 seconds, whilst the graphene spots remain constant.

The intensity in a diffraction peak can be quantified by summing the intensity in a small area around its maximum, and then subtracting this value by the average background intensity

summed over an equivalent area. This is repeated for each image in the sequence. Three diffraction peaks for the TMA are chosen, one from each order of the diffraction pattern, and one diffraction peak for the graphene. The resulting intensities are plotted against exposure time in Figure A4 (e).

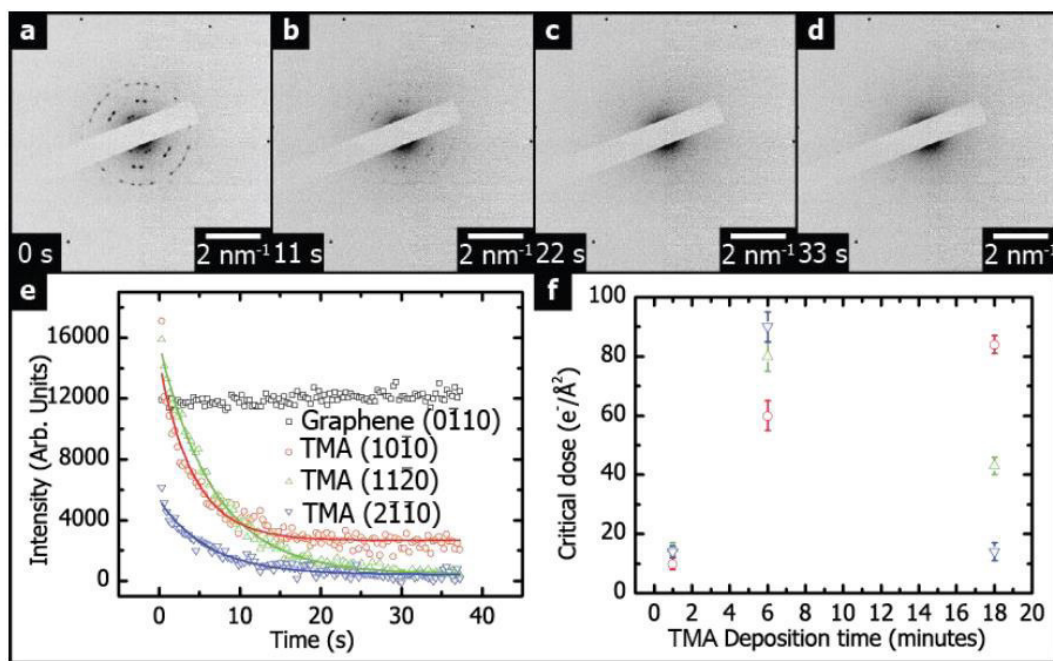


Figure A4. Measuring the critical electron dose for TMA thin films. (a)-(d) show diffraction patterns from a series taken from the same area with increasing exposure time. The time of each image is indicated in the bottom left corner. Plotting the intensity of the diffraction spots, (e), shows exponential decays, caused by the damage from the electron beam. The characteristic dose of the decay is plotted for the 1, 6 and 18 minute-depositions in (f).

For the graphene diffraction spot, the intensity remains constant throughout the exposure, suggesting only negligible damage to the graphene lattice. On the other hand, for all the TMA diffraction peaks there is an exponential decrease in intensity. This demonstrates a disruption to the crystal structure of the TMA layer. After a long exposure, there are no diffraction spots, consistent with a disordered material. The weak bonding, poor conductance, and large population of light atoms present in organic molecular systems such as TMA result in rapid damage when subject to the TEM beam. High energy electrons act to break bonds between atoms as well as intermolecular bonds, leaving collections of atoms and free radicals which can desorb from the crystal or attack neighboring molecules, resulting in further damage. These areas rapidly become amorphous, losing all crystallinity, and no longer contribute to the diffraction reflections for the remaining crystal. The damaged areas continue to grow, with

undamaged crystalline areas decaying in proportion, until the molecular crystal is fully amorphous.^[1-3]

A5: Low dose acTEM image acquisition protocol

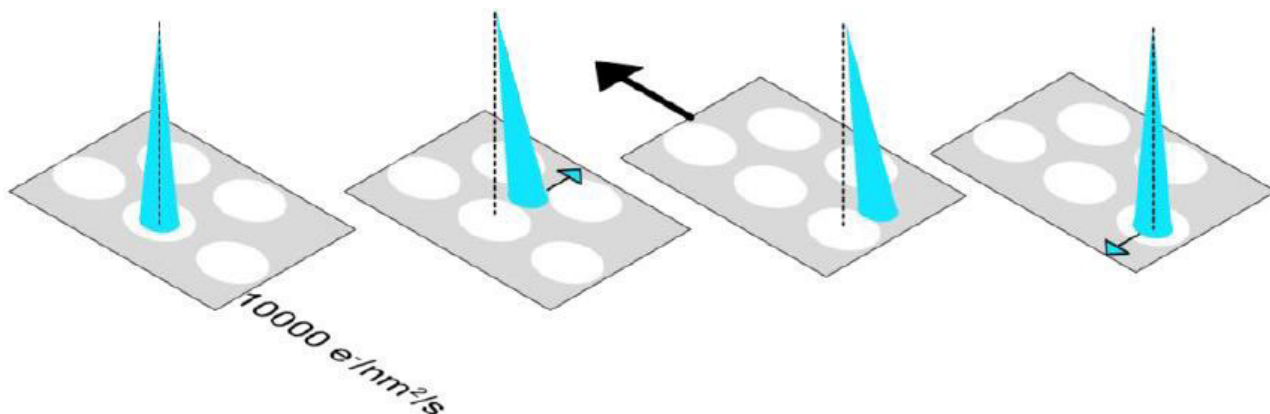


Figure A5. Schematic of the low dose acquisition procedure.

The low dose image acquisition protocol implemented for this work takes advantage of the regularly spaced holes in the TEM supports, and of the fact that the molecular film covers the holes uniformly. First, the microscope conditions (focus and astigmatism) are set using part of the film that has already been damaged by the electron beam. The beam is then shifted away from the sample and the stage moved by a known distance to another hole. After that, and allowing time for the stage drift to settle, the beam is shifted back and images are captured instantly.

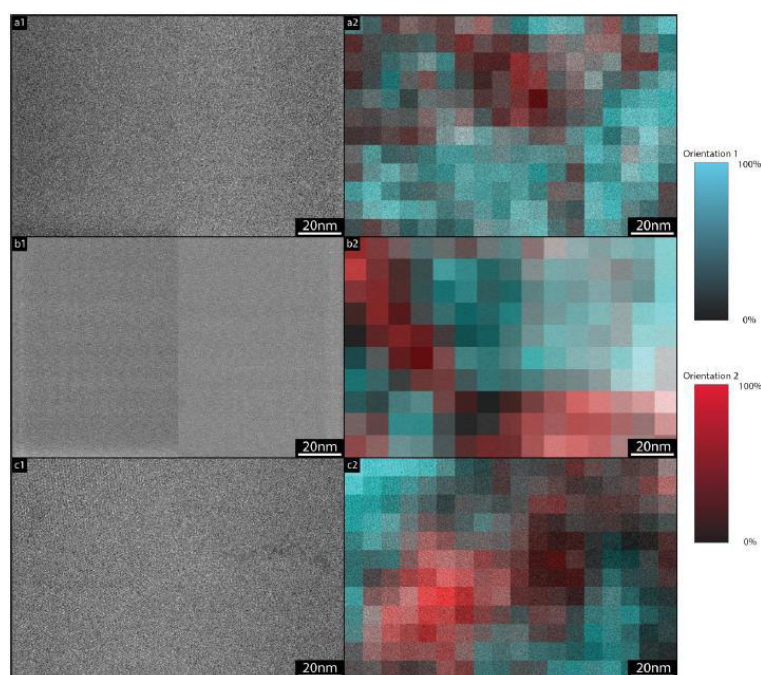
A6: Mapping the orientation of domains in the TMA thin film

Figure A6. acTEM grain orientation maps for different thickness TMA. Red/Cyan ‘pixels’ are overlaid on the original acTEM image to indicate regions with one preferential grain orientation. (a1, a2) 1 minute deposition without/with grain overlay. (b1, b2) 6 minutes deposition without/with grain overlay. (c1, c2) 18 minutes deposition without/with grain overlay.

For 15s TMA deposition, only a single orientation was visible in acTEM imaging mode, indicating that the domain sizes can exceed $150 \times 150 \text{ nm}^2$ (the area visible to the CCD at the magnification used). For 1, 6 and 18 minute depositions two grains of different orientation relative to the underlying graphene were visible. The typical domain size for each film thickness is summarized below:

Deposition Time	Domain Sizes (Height \times Width) / nm^2
15 s	$>150 \times 150$ (greater than acTEM image frame)
1 minute	$(50 \pm 10) \times (50 \pm 10)$
6 minutes	$(60 \pm 10) \times (60 \pm 10)$
18 minutes	$(50 \pm 10) \times (50 \pm 10)$

Table A1. acTEM grain orientation map sizes for different thickness TMA. Width and height of grains were measured directly from overlaid grain maps.

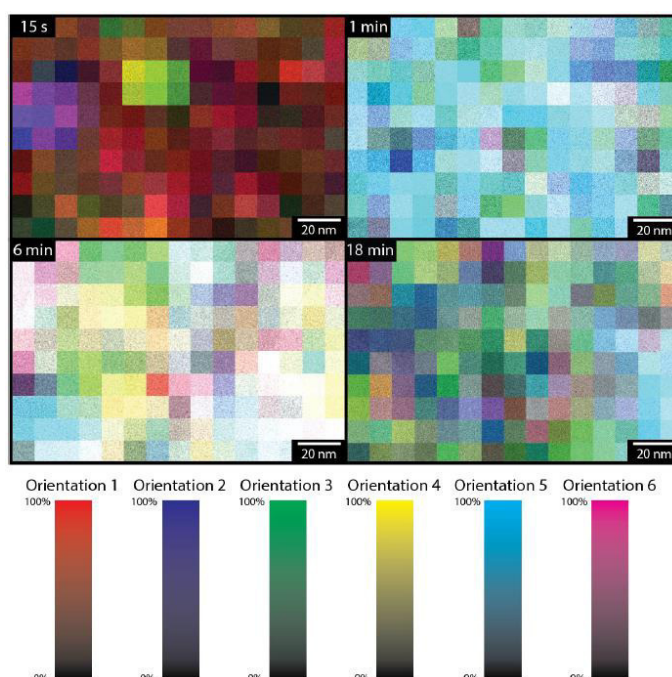
A7: Mapping the orientation of grains in the TPA thin films

Figure A7. acTEM grain orientation maps for different thickness TPA. Different coloured ‘pixels’ are overlaid on the original acTEM image to indicate regions with one preferential grain orientation. Regions of white present in the 6 minute film indicate approximately equal contributions from all orientations.

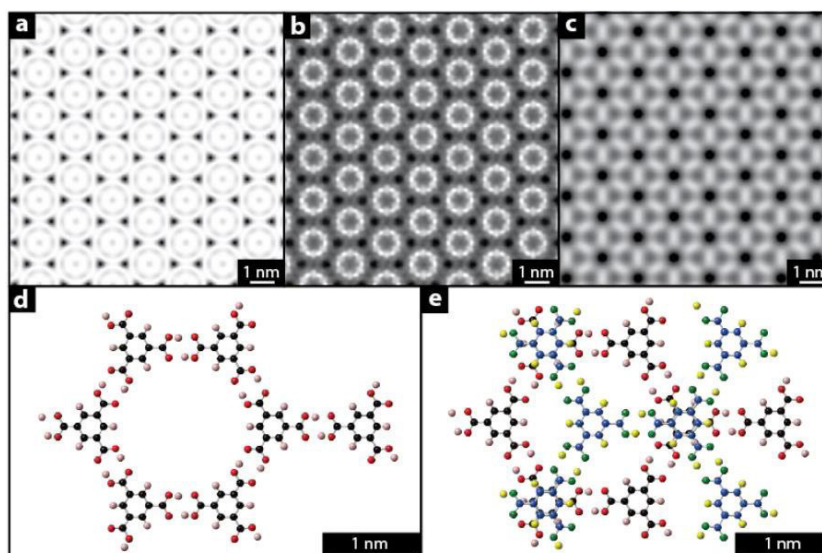
S8: Multislice acTEM image simulations of TMA thin films

Figure A8a. TMA acTEM reconstructed image (a) and multislice image simulations for direct stacking (b) and offset stacking models (c) for 1 minute deposition thickness. Molecular models for direct stacking (d) and offset stacking (e) used for the multislice simulations. Multislice simulations were performed using spherical aberration $-1\mu\text{m}$ and defocus $\approx 40\text{nm}$ (as measured for imaging). Simulations were performed using cITEM, an open-source multislice simulation package (M. A. Dyson, cITEM: OpenCL TEM/STEM simulation code, URL <http://github.com/ADyson/cITEM>), 2014).

The simulated image assuming direct stacking (AA stacking) is clearly more consistent with the reconstructed one, than the simulated image based on an offset model (AB stacking). acTEM imaging thus proves that the TMA is stacking in a direct (AA) fashion, creating nanopores.

TEM image reconstruction background

For an electron wavefunction propagating through a unit cell with N atoms located at positions \underline{a}_j , where $j = 1, \dots, N$, the electrostatic potential $\varphi(\underline{r})$ felt by the electron at a point \underline{r} may be determined through a summation of all potentials at point \underline{r} :

$$\varphi(\underline{r}) = \sum_{j=1}^N \varphi_j(\underline{r} - \underline{a}_j)$$

Here, φ_j are the individual potentials of each atom. The potential (\underline{r}) is a continuous real space function. The Fourier components (\underline{u}) of potential (\underline{r}) are related by:

$$\Phi(\underline{u}) = \mathcal{F}\{\varphi(\underline{r})\} = \frac{1}{V} \int_V \varphi(\underline{r}) e^{-i2\pi(\underline{u}\cdot\underline{r})} d\underline{r}^3$$

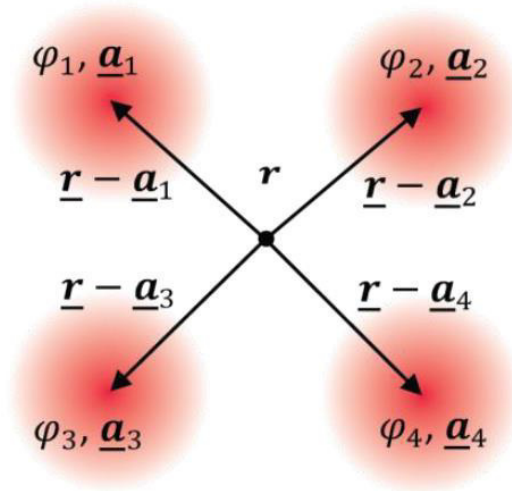


Figure A6b. Reconstruction theory model. Atoms with electrostatic potentials $\varphi_{1,2,3,4}$ are located at coordinates $\underline{a}_{1,2,3,4}$

These (\underline{u}) are related to the structure factor $F(\underline{u})$ by a scaling factor:

$$\Phi(\underline{u}) = \frac{h^2}{2\pi m_e V} F(\underline{u}),$$

where the structure factor (\underline{u}) is defined as a discrete sum of structure factor amplitudes $|F_j(\underline{u})|$ and phases $ei2(\underline{u}\cdot\underline{a}_j)$ for each atom in the unit cell:

$$F(\underline{u}) = \sum_{j=1}^N |F_j(\underline{u})| e^{i2\pi(\underline{u}\cdot\underline{a}_j)}.$$

Individual structure factor amplitudes and phases are measured in a Fourier transform (power spectrum) of an image of a unit cell or multiple unit cells (these appear as the lattice spots in the power spectrum). The original unit cell potential (\mathbf{r}) is therefore related to the structure factor (\mathbf{u}) for the unit cell through a scaled inverse Fourier transform:

$$\varphi(\mathbf{r}) = \mathcal{F}^{-1}\{F(\mathbf{u})\} = \frac{h^2}{2\pi m_e V} \sum_{i=1}^{\infty} F(\mathbf{u}_i) e^{i2\pi(\mathbf{u}_i \cdot \mathbf{r})}.$$

Truncating this series to some finite order of \mathbf{u} gives an approximation to the unit cell potential (\mathbf{r}):

$$\varphi(\mathbf{r}) \approx \sum_{i=1}^M F(\mathbf{u}_i) e^{i2\pi(\mathbf{u}_i \cdot \mathbf{r})}.$$

This truncation results in a loss of resolution, resulting from the limited resolving power of the microscope and finite number of structure factors present in the image Fourier transform.

Notes on application to real acTEM images: For a acTEM image, image interpretation is difficult due to the effect of lens aberrations on the final image. In addition, multiple scattering occurring due to the large interaction between the incident electrons and sample atoms results in the final image not being a faithful representation of the sample electrostatic potential. Instead, the final image represents the exit-wave of the incident electron beam, convoluted with the various lens aberrations present.^[4] These lens aberrations arise due to imperfections in the imaging optics, and may be represented in the form of a contrast transfer function with which the exit wave is convoluted:

$$I = E \otimes CTF,$$

where I is the final image, E is the exit wave and CTF is the contrast transfer function. For particularly thin samples (few atom thick), the exit-wave may be approximated to the projected potential.

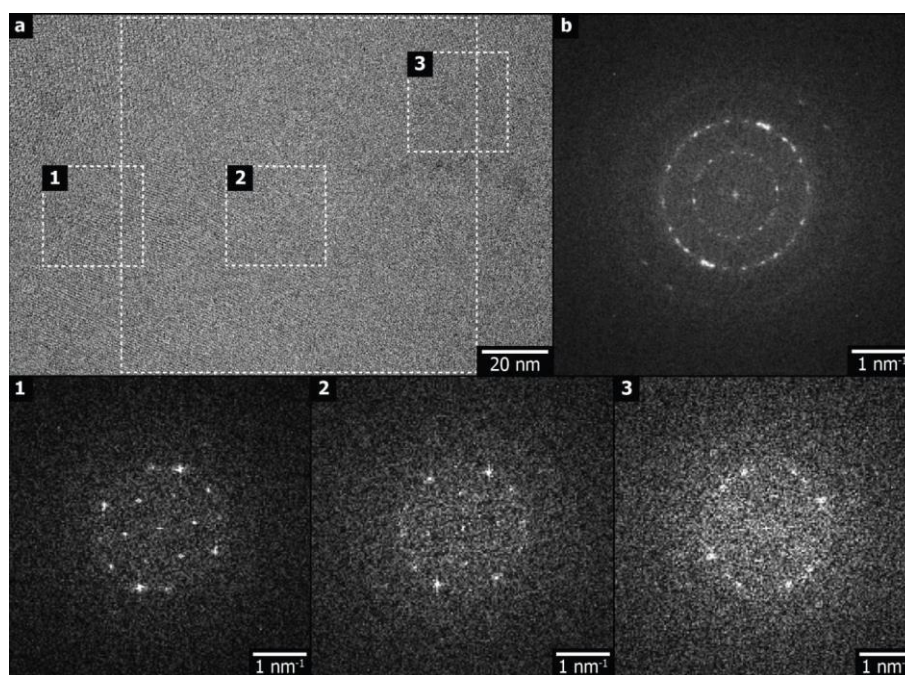
A9: acTEM imaging of polycrystalline nature of thicker TMA films

Figure A9. acTEM of the 18 minute-deposition of TMA. The image (a) and the FFT (b) from the large white box demonstrate the polycrystalline nature of the TMA at this thickness. 1, 2, and 3 are FFTs from the boxes as labelled in (a).

Figure A9(a) shows an acTEM image of an 18 minute-deposition of TMA on graphene. Periodic features are apparent, as also observed for thinner films, resulting in clear spots in the FFT (b) of the large white box in (a). The FFT shows spots that have the same spacings as seen for lower coverage, suggesting the presence of TMA in a chicken-wire structure. However, there are now several hexagonal arrays present, indicating multiple in-plane orientations, in agreement with diffraction patterns from the same films.

Selected area FFTs can help revealing the structure at smaller lengthscales. In the FFT of region 1, a single set of hexagonal spots is clear, but with another orientation weakly present. This suggests that the templated structure is still dominant in some small regions. However, in most places more than one orientation is visible, as demonstrated by FFTs in regions 2 and 3. The two preferred orientations ($6.8 \pm 0.1^\circ$ either side of the graphene orientation) are not dominantly visible in the diffraction patterns of the 18 minute-deposition film. As shown in Figure A3, this suggests that somewhere between the 6 and 9 minute-deposition point, new and random in-plane orientations appear in small domains, rather than just a continuation of the templating of the original orientations. These new orientations also appear to template upwards, as shown by the presence of discrete spots in the FFTs of the 18 minute-deposition:

a nontemplated polycrystalline film would present itself as rings or arcs in the acTEM image FFTs.

A10: Demonstration of the 6 orientations of TPA apparent by SAED

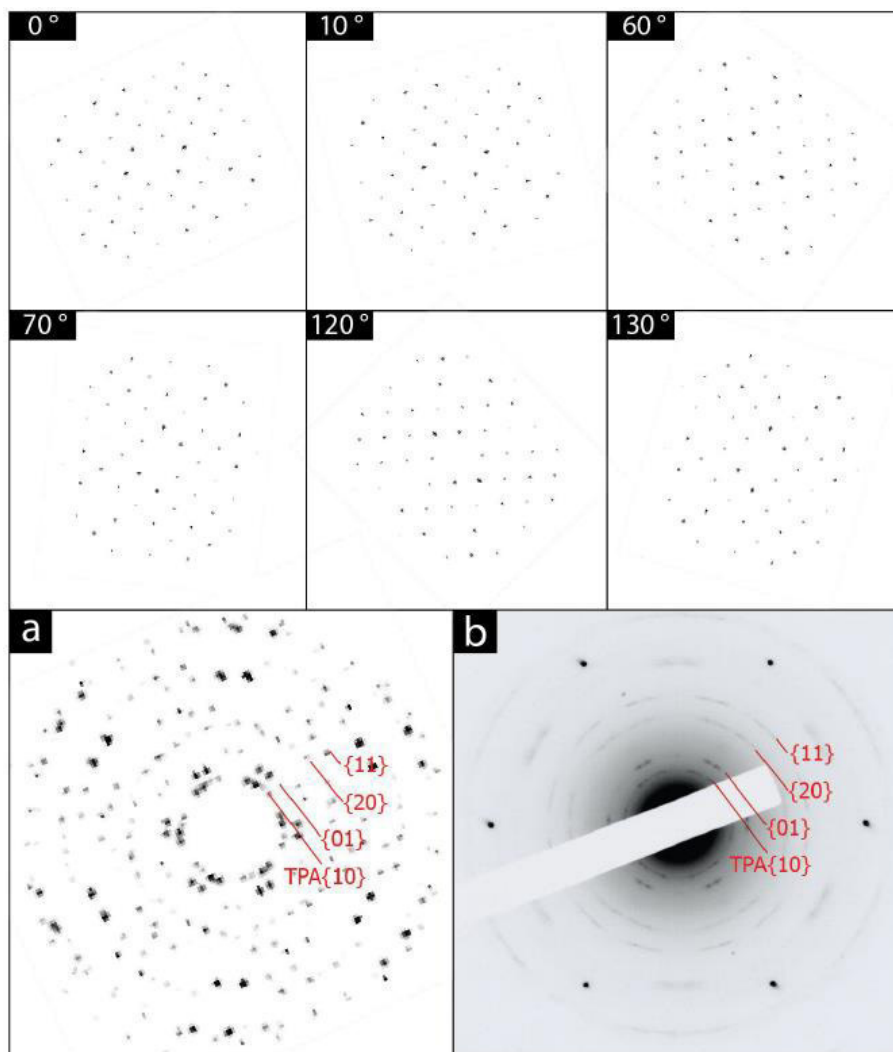


Figure A10. Comparison between simulated diffraction patterns and experimental measurements for 15s TPA deposition. Simulated electron diffraction patterns, assuming the 2D brickwork structure, are shown at six different orientations as labelled. The sum of these simulations is presented in (a) and shows good correspondence with the experimental pattern shown in (b). This indicates the presence of six TPA grains within the selected area used for diffraction. Simulations were performed using cITEM, an open-source multislice simulation package (M. A. Dyson, cITEM: OpenCL TEM/STEM simulation code, URL <http://github.com/ADyson/cITEM>), 2014).

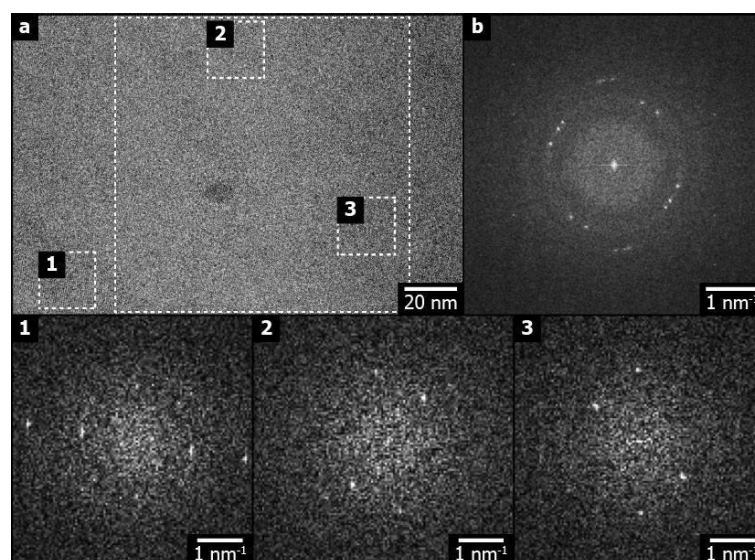
A11: acTEM imaging of TPA thin films

Figure A11a. acTEM of the 1 minute-deposition of TPA. Brightfield image, (a), and corresponding FFTs from the large dashed box, (b), and the smaller dashed boxes 1, 2 and 3 as labelled.

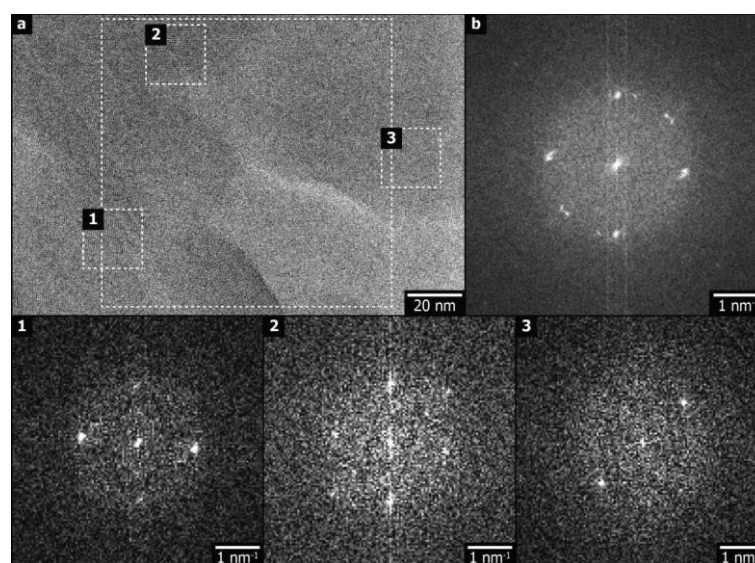


Figure A11b. acTEM of the 18 minute-deposition of TPA. Brightfield image, (a), and corresponding FFTs from the large dashed box, (b), and the smaller dashed boxes 1, 2 and 3 as labelled.

Figures A11a and A11b show acTEM images of 1 minute and 18 minute-depositions of TPA on graphene respectively. The spacings of peaks in the FFT are consistent with the corresponding diffraction patterns shown in Figure 5 of the main article. FFTs of smaller subregions show the ordering across the film, demonstrating that the 18 minute deposition is polycrystalline as opposed to forming large single-crystal domains. The angle γ reported in Table 2 is measured from FFTs such as these.

References

- [A1] R. F. Egerton, *Microscopy research and technique* 75(11) (2012): 1550-1556.
- [A2] R. F. Egerton, P. Li and M. Malac, *Micron* 35(6) (2004): 399-409.
- [A3] R. F. Egerton, *Ultramicroscopy* 127 (2013): 100-108.
- [A4] X. Zou, S. Hovmoller and P. Oleynikov, *Electron Crystallography: Electron Microscopy and Electron Diffraction*, Oxford University Press, 2011.

Chapter 5

TCNQ physisorption on the Bi_2Se_3 Topological Insulator

Topological insulators are promising candidates for spintronic applications due to their topologically protected, spin-momentum locked and gapless surface states. The breaking of the time-reversal symmetry after the introduction of magnetic impurities, such as metal atoms embedded in two-dimensional molecular networks, could lead to several phenomena interesting for device fabrication. The first step towards the fabrication of metal-organic coordination networks on the surface of a topological insulator is to investigate the adsorption of the pure molecular layer, which is the aim of this study. In this chapter, the effect of the deposition of the electron acceptor 7,7,8,8-tetracyanoquinodimethane (TCNQ) molecules on the surface of a prototypical topological insulator, bismuth selenide (Bi_2Se_3), is investigated. Scanning tunnelling microscope images at low-temperature reveal the formation of a highly ordered two-dimensional molecular network. The essentially unperturbed electronic structure of the topological insulator observed by photoemission spectroscopy measurements demonstrates a negligible charge transfer between the molecular layer and the substrate. Density functional theory calculations confirm the picture of a weakly interacting adsorbed molecular layer. These results reveal significant potential of TCNQ for the realization of ferromagnetic metal-organic coordination networks on the topological insulator surface.

5.1 Introduction

Topological insulators (TIs) are a class of materials potentially interesting for applications in the field of optoelectronics and spintronics,^[1,2] due to their uncommon electronic structure. TIs are characterised by an insulating bulk state and by a surface state (TSS) which presents a Dirac-cone-like dispersion located at the centre of the Brillouin zone.^[3-5] The spin and momentum degrees of freedom of the TSS are locked^[3] and the electrons are topologically protected from elastic backscattering on defects by time-reversal symmetry.^[6] This property leads to a variety of fascinating processes,^[7-12] such as nearly dissipationless currents.^[7,8,12] The stability of these effects against local magnetic perturbations, which break time-reversal symmetry, is a prerequisite for the realization of spintronic devices based on TI material.^[6,13] On the other hand, the breaking of the time-reversal symmetry and the opening of an energy gap at the Dirac point of the TSS leads to a different class of phenomena,^[14] such as the anomalous quantum Hall effect,^[15,16] with a potential interest for the possible fabrication of low-power consumption electronics.^[17]

The effects of impurity doping on the electronic and magnetic properties of TIs have been under debate in the last years and seem to strongly depend on the presence of intrinsic defects of the pristine crystals,^[18] on the chemical nature of the magnetic impurities,^[19, 20] on the type of doping (surface or bulk),^[11, 14, 19-24] on the possible clustering of impurities,^[19, 25-28] and, in the specific case of surface doping, on the adsorption sites^[19, 20] and on the orientation of the magnetic easy axis with respect to the surface plane.^[14, 19, 20]

An interesting proposal to avoid clustering and obtain ordered and equivalent adsorption sites for surface magnetic impurities, is the use of highly-ordered two-dimensional (2D) metal-organic coordination networks (MOCNs), formed by co-depositing strong electron acceptor molecules (such as tetracyanoethylene (TCNE, C₆H₄) or tetracyanoquinodimethane (TCNQ, C₁₂H₄N₄)) together with the magnetic impurities (e.g. Fe, Co, Ni) on the surface of TIs.^[25] Interestingly, these MOCNs can even show ferromagnetic order in some cases, as reported on metal surfaces.^[29-35] In particular, X-ray magnetic circular dichroism (XMCD) measurements^[36] showed that Ni adatoms assume a spin-quenched configuration when deposited on their own on Ag(100) and Au(111) surfaces, whereas exhibit an out of plane ferromagnetic ordering when coordinated to TCNQ ligands into a MOCN. Similar networks may be also realised on TI surfaces and could be used to induce a magnetic perturbation of the TSS. Recent

calculations^[25] indicate that such MOCNs could display an out-of-plane magnetic anisotropy on Bi₂Se₃, break the time-reversal symmetry and induce the opening of an energy gap at the Dirac point of the TSS. The first step towards the fabrication of this type of networks is to investigate the adsorption of a pure layer of electron acceptor molecules and to verify that, on their own, they do not induce a significant modification or disruption of the TSS Dirac cone, as observed for other molecular species on Tis^[37-42] or for similar molecular species on graphene.^[43]

To this aim, we investigated the deposition of the strong acceptor TCNQ molecules on a pristine Bi₂Se₃ surface by means of scanning tunnelling microscopy (STM), angle-resolved photoemission spectroscopy (ARPES), X-ray photoemission spectroscopy (XPS) measurements and Density Functional Theory (DFT) calculations. Low-temperature STM measurements reveal the formation of a highly ordered H-bonded organic network of TCNQ molecules on the Bi₂Se₃ surface, while photoemission spectroscopy investigations evidence a nearly unperturbed electronic states of the topological insulator. These findings are supported by DFT simulations and strongly suggest a rather weak TCNQ-Bi₂Se₃ interaction.

5.2 Experimental section

The Bi₂Se₃ samples used are (0001) oriented single crystals grown by the modified Bridgman method. These samples have been previously characterized by X-ray diffraction, low-energy electron diffraction and Auger electron spectroscopy.^[44-46] Samples were cleaved in-situ in ultra-high vacuum (UHV) conditions at a base pressure of low 10⁻⁹ mbar. TCNQ molecules (purchased from Sigma Aldrich, no further treatment) were evaporated onto the Bi₂Se₃ sample held at room temperature (RT). STM measurements were performed at 77K and 100K in two different UHV chambers (base pressures of low 10⁻¹⁰ mbar), with typical tunnelling current of few tens of pA up to hundred pA. XPS and ARPES investigations were carried out at RT at the APE and VUV end-stations (base pressures of low 10⁻¹⁰ mbar) at the ELETTRA synchrotron by depositing increasing amounts of TCNQ molecules on a freshly cleaved Bi₂Se₃ surface.

Theoretical methods

First principles density functional theory calculations (DFT)^[44,47] have been performed using the Vienna Ab initio Simulation Package (VASP) that is a plane wave based code.^[47-49] We have used the GGA-PBE approximation to treat exchange and correlation,^[50] as well as van der

Waals corrections within the vdW-DFT^[51,52] approach to give an adequate description of an individual TCNQ molecule on the Bi₂Se₃ surface. For a description of the TCNQ-Bi₂Se₃ interaction we used a quintuple layer thick slab, whose crystal structure was obtained from the experimental data.^[45] Concerning the lateral extension of the surface supercell, it is enough to use a rectangular $2\sqrt{3} \times 2$ supercell that contains eight atoms in each layer. The sufficiency of the lateral separation between the molecules located in the neighbouring cells (4.04 Å in this case) was confirmed on the basis of a test calculation that revealed essentially no changes in the unsupported molecule density of states with the increase of separation. The k-point sampling of the two-dimensional Brillouin zone was chosen to be $5 \times 9 \times 1$ and the energy cut-off for the plane wave expansion was set to 400 eV.

5.3 Results and discussion

Pristine Bi₂Se₃ surfaces were prepared by cleavage before every molecular deposition experiment resulting in atomically flat (0001) oriented substrates (Fig. 1). These are characterised by terraces typically larger than 100 nm (Fig. 1(a)). The deposition of TCNQ molecules resulted in the formation of extended and ordered 2D islands, as demonstrated by the STM image in Fig. 2(b). Molecules interact through H-bonds and arrange in a typical brickwork manner (Fig. 2(c)), as also reported for the deposition of TCNQ on Au(111).^[53] Within the H-bonded islands, each TCNQ binds to other four molecules, with the four hydrogens of the central ring of one molecule interacting with the electronegative nitrogen atoms of the neighbouring molecules. This results in a rhombic unit cell for the supramolecular structure (see Fig. 3(b)), with dimension: $a_1=(7.7 \pm 0.1)$ Å, $a_2=(8.6 \pm 0.1)$ Å, $\alpha=(94 \pm 2)^\circ$, compatible with what found for TCNQ on Au(111).^[54] These values of the lattice parameters are smaller than those obtained in DFT calculations for the TCNQ free-standing monolayer (see Fig. A2.1 in the Appendix section), demonstrating the relevance of the adsorption potential exerted on the molecules by the Bi₂Se₃ substrate. Atomic resolution images reveal that the molecules are aligned along the crystallographic directions of the substrate.

The bias voltage dependence STM imaging of TCNQ molecules on Bi₂Se₃ is reported in Figs. 3(a) and (b). At negative voltage (occupied sample states imaging), TCNQ molecules appear as elliptic protrusions. Instead, at positive voltage (empty sample states), the images of the molecules show a close similarity to the shape of the DFT-calculated isosurface for the lowest

unoccupied molecular orbital (LUMO) of the free-standing TCNQ monolayer. In fact, the characteristic nodal central plane separates two symmetric U-like protrusions and circular protrusions appear in the middle of the dicyanomethylene groups.

The resemblance of the empty sample states STM images of TCNQ with the DFT-calculated LUMO strongly suggests negligible charge transfer, similarly to what reported for TCNQ on Au(111)^[53,54] and on graphene on Ir(111).^[55] This assumption is further supported by the observed H-bond brickwork assembly of TCNQ that has been reported only for TCNQ interacting weakly with the underneath substrate and in the absence of charge transfer.^[53,55] The brickwork structure does indeed correspond to the lowest energy configuration that is obtained for the assembly of an isolated planar sheet of TCNQ molecules in the gas phase (for further information see Fig. A2.1 in the Appendix section).

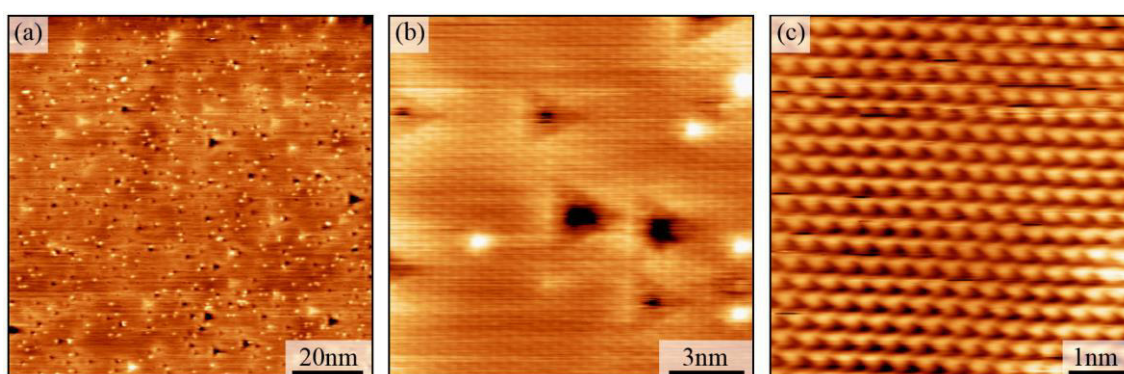


Figure 1. (a) STM images showing a pristine cleaved Bi_2Se_3 surface and (b, c) corresponding zoom-in images at increasing magnification.

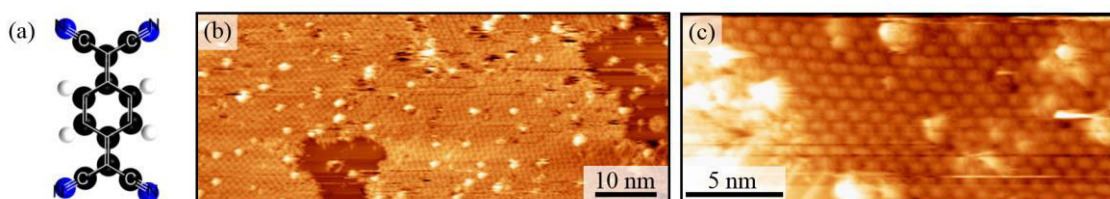


Figure 2. (a) Chemical structure of a TCNQ molecule. Black atoms correspond to carbon, dark blue to nitrogen and white to hydrogen. (b, c) STM images showing the supramolecular assembly resulting from the deposition of TCNQ on the Bi_2Se_3 surface.

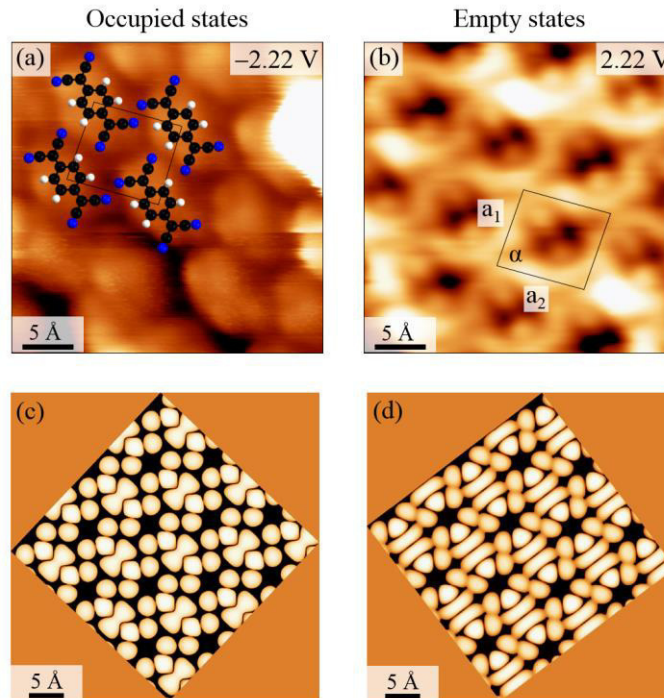


Figure 3. (a) and (b) high magnification STM images acquired on a TCNQ island at negative (occupied sample states) and positive (empty sample states) bias voltages, respectively. Structural models are superposed in (a) as a guide for the eye. (c) and (d) DFT calculated isosurfaces of the HOMO and LUMO for a free standing TCNQ monolayer, respectively.

The electronic band structure of Bi_2Se_3 measured by ARPES before and after the deposition of (2.5 ± 0.5) ML of TCNQ is reported in Fig. 4(a) and (b), respectively. The topological surface state of the pristine sample displays sharp and well-defined Dirac cone close to the Fermi level, with a Dirac point energy of 0.32 eV below E_F , in agreement with previous studies (Fig. 4(a)).^[44,56] No extra electronic states due to “aging effects” can be observed,^[57,58] implying a negligible amount of contaminants of the Bi_2Se_3 sample.

The adsorption of TCNQ leads to a considerable broadening of the Dirac surface state (Fig. 4(b)), potentially due to a partial disorder of the molecular overlayer. However, the adsorbed TCNQ does not strongly affect the Bi_2Se_3 electronic structure otherwise. In particular, ARPES data do not show the appearance of any additional electronic states in the valence or conduction bands or significant (>100 meV) upward shifts of the Dirac cone, in contrast to what observed for the adsorption of contaminants and atomic dopants on the same surface.^[57-60] We consider these findings a further evidence of the relatively weak TCNQ- Bi_2Se_3 interaction (as also suggested by the XPS measurements reported in the Appendix section).

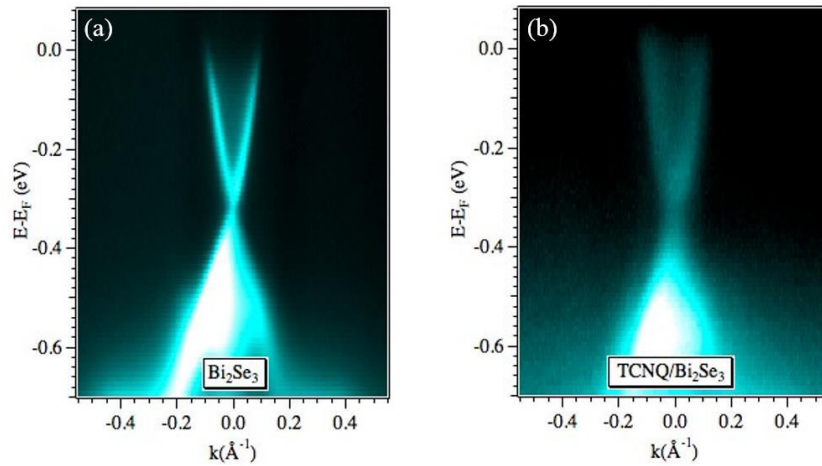


Figure 4. ARPES spectra (a) before and (b) and after deposition of 2.5 ML of TCNQ on the Bi₂Se₃ surface. Spectra have been collected with 50 eV photon energy.

All the experimental evidence clearly points to a neutral state for TCNQ adsorbed on Bi₂Se₃: STM measurements performed in the sub-monolayer regime evidence an unoccupied LUMO peak and a H-bond assembly, energetically favourable for neutral species,^[53] whereas ARPES and XPS data in the multi-layer coverage range display an almost unperturbed Bi₂Se₃ electronic structure. Hence, despite the common charging behaviour observed for TCNQ on a number of more reactive surfaces,^[61,62-66] on Bi₂Se₃ TCNQ adsorbs as a *neutral* species forming characteristic hydrogen bonded networks, similarly to what observed on other inert surfaces.^[53,61]

To get a better insight into the adsorption and electronic properties of the TCNQ/Bi₂Se₃ system we have performed *ab initio* calculations. Since the H-bonded molecular TCNQ layer studied here is not commensurate with the substrate, the calculations have been performed for a single TCNQ molecule adsorbed on the Bi₂Se₃ surface. Fig. 5(a) shows the dependence of the total energy on the adsorption distance calculated for two different lateral locations of the TCNQ monomer with respect to the substrate (shown in Figs. 5(c)-(d)). It can be seen that both registries yield an equilibrium distance of 3.4 Å that corresponds to the physisorption of TCNQ on Bi₂Se₃(0001). The densities of states projected onto different atomic orbitals of TCNQ and Bi₂Se₃ are shown in Fig. 5(b) for the two registries at the equilibrium adsorption distance. It is clear from Fig. 5(b) that the interaction between an individual TCNQ molecule and the Bi₂Se₃ surface is independent of the registry and is very weak, because there is neither charge transfer nor any significant hybridization between the HOMO/LUMO of TCNQ and the Bi₂Se₃ substrate. Since the TCNQ monomer is expected to be equally or possibly even more reactive

than the H-bonded TCNQ network, these results point towards a weak interaction of the H-bonded network with $\text{Bi}_2\text{Se}_3(0001)$, in agreement with the STM and photoemission results.

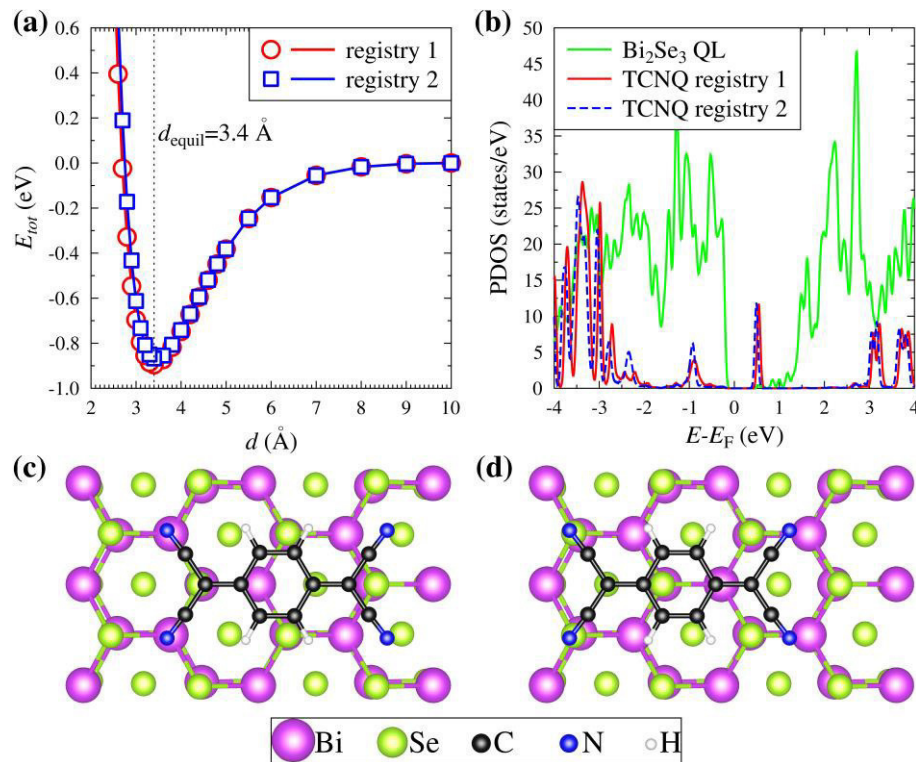


Figure 5. (a) Total energy as a function of the TCNQ monomer vertical distance to $\text{Bi}_2\text{Se}_3(0001)$ for the two different registries shown in panels (c) and (d). (b) Projected densities of states onto TCNQ and Bi_2Se_3 orbitals at the equilibrium adsorption distance (3.4 Å). The Bi_2Se_3 DOS corresponds to the one calculated for the adsorption configuration shown in (c). That for the adsorption configuration in (d) is not presented since the differences between the two are marginal.

5.4 Conclusions

By performing detailed STM investigations we provide evidence that a TCNQ molecules arrange themselves in an ordered H-bonded organic network on the Bi_2Se_3 surface. The presented results strongly suggest a physisorbed TCNQ on Bi_2Se_3 surface, with negligible charge transfer, in agreement with DFT calculations. Additionally, ARPES and XPS measurements performed on multilayer TCNQ/ Bi_2Se_3 confirm a *nearly* unperturbed topological surface state and no significant modifications of the topological electronic structure. This type of organic network represents the first step towards the realization of an ordered array of local magnetic moments on a TI surface and, possibly, drive the system to novel and relevant phenomena as predicted by theory.^[25]

References

- [1] M. Z. Hasan and C. L. Kane, *Reviews of Modern Physics*, 2010, 82, 3045-3067.
- [2] H. Peng, W. Dang, J. Cao, Y. Chen, D. Wu, W. Zheng, H. Li, Z.-X. Shen and Z. Liu, *Nature Chem.*, 2012, 4, 281-286.
- [3] H. Zhang, C.-X. Liu, X.-L. Qi, X. Dai, Z. Fang and S.-C. Zhang, *Nat. Phys.*, 2009, 5, 438-442.
- [4] Y. Xia, D. Qian, D. Hsieh, L. Wray, A. Pal, H. Lin, A. Bansil, D. Grauer, Y. S. Hor, R. J. Cava and M. Z. Hasan, *Nat. Phys.*, 2009, 5, 398-402.
- [5] X.-L. Qi and S.-C. Zhang, *Reviews of Modern Physics*, 2011, 83, 1057-1110.
- [6] P. Roushan, J. Seo, C. V. Parker, Y. S. Hor, D. Hsieh, D. Qian, A. Richardella, M. Z. Hasan, R. J. Cava and A. Yazdani, *Nature*, 2009, 460, 1106-1109.
- [7] L. Fu and C. L. Kane, *Phys. Rev. Lett.*, 2008, 100, 4.
- [8] L. Fu and C. L. Kane, *Phys. Rev. Lett.*, 2009, 102, 216403.
- [9] X.-L. Qi, R. Li, J. Zang and S.-C. Zhang, *Science*, 2009, 323, 1184-1187.
- [10] P. Sessi, F. Reis, T. Bathon, K. A. Kokh, O. E. Tereshchenko and M. Bode, *Nat. Commun.*, 2014, 5, 8.
- [11] J. Zhang, C.-Z. Chang, P. Tang, Z. Zhang, X. Feng, K. Li, L.-l. Wang, X. Chen, C. Liu, W. Duan, K. He, Q.-K. Xue, X. Ma and Y. Wang, *Science*, 2013, 339, 1582-1586.
- [12] D. Hsieh, Y. Xia, L. Wray, D. Qian, A. Pal, J. H. Dil, J. Osterwalder, F. Meier, G. Bihlmayer, C. L. Kane, Y. S. Hor, R. J. Cava and M. Z. Hasan, *Science*, 2009, 323, 919-922.
- [13] S. A. Wolf, D. D. Awschalom, R. A. Buhrman, J. M. Daughton, S. von Molnar, M. L. Roukes, A. Y. Chtchelkanova and D. M. Treger, *Science*, 2001, 294, 1488-1495.
- [14] Y. L. Chen, J.-H. Chu, J. G. Analytis, Z. K. Liu, K. Igarashi, H.-H. Kuo, X. L. Qi, S. K. Mo, R. G. Moore, D. H. Lu, M. Hashimoto, T. Sasagawa, S. C. Zhang, I. R. Fisher, Z. Hussain and Z. X. Shen, *Science*, 2010, 329, 659-662.
- [15] C.-Z. Chang, J. Zhang, X. Feng, J. Shen, Z. Zhang, M. Guo, K. Li, Y. Ou, P. Wei, L.-L. Wang, Z.-Q. Ji, Y. Feng, S. Ji, X. Chen, J. Jia, X. Dai, Z. Fang, S.-C. Zhang, K. He, Y. Wang, L. Lu, X.-C. Ma and Q.-K. Xue, *Science*, 2013, 340, 167-170.
- [16] R. Yu, W. Zhang, H.-J. Zhang, S.-C. Zhang, X. Dai and Z. Fang, *Science*, 2010, 329, 61-64.
- [17] J. Zhang, *Transport Studies of the Electrical, Magnetic and Thermoelectric properties of Topological Insulator Thin Films*, Springer Berlin Heidelberg, 2016.
- [18] T. S. Chen, Q. Chen, K. Schouteden, W. K. Huang, X. F. Wang, Z. Li, F. Miao, X. R. Wang, Z. G. Li, B. Zhao, S. C. Li, F. Q. Song, J. L. Wang, B. G. Wang, C. Van Haesendonck and G. H. Wang, *Nat. Commun.*, 2014, 5, 8.
- [19] J. Honolka, A. A. Khajetoorians, V. Sessi, T. O. Wehling, S. Stepanow, J. L. Mi, B. B. Iversen, T. Schlenk, J. Wiebe, N. B. Brookes, A. I. Lichtenstein, P. Hofmann, K. Kern and R. Wiesendanger, *Phys. Rev. Lett.*, 2012, 108, 256811.
- [20] E. Y. Wang, P. Z. Tang, G. L. Wan, A. V. Fedorov, I. Miotkowski, Y. P. Chen, W. H. Duan and S. Y. Zhou, *Nano Lett.*, 2015, 15, 2031-2036.

- [21] C.-Z. Chang, P. Tang, Y.-L. Wang, X. Feng, K. Li, Z. Zhang, Y. Wang, L.-L. Wang, X. Chen, C. Liu, W. Duan, K. He, X.-C. Ma and Q.-K. Xue, *Phys. Rev. Lett.*, 2014, 112, 056801.
- [22] W. Q. Liu, D. West, L. He, Y. B. Xu, J. Liu, K. J. Wang, Y. Wang, G. van der Laan, R. Zhang, S. B. Zhang and K. L. Wang, *ACS Nano*, 2015, 9, 10237-10243.
- [23] J. Henk, A. Ernst, S. Eremeev, E. Chulkov, I. Maznichenko and I. Mertig, *Phys. Rev. Lett.*, 2012, 108, 206801.
- [24] J. Henk, M. Flieger, I. Maznichenko, I. Mertig, A. Ernst, S. Eremeev and E. Chulkov, *Phys. Rev. Lett.*, 2012, 109, 076801.
- [25] M. M. Otrokov, E. V. Chulkov and A. Arnau, *Phys. Rev. B*, 2015, 92, 165309.
- [26] M. Ye, S. V. Eremeev, K. Kuroda, E. E. Krasovskii, E. V. Chulkov, Y. Takeda, Y. Saitoh, K. Okamoto, S. Y. Zhu, K. Miyamoto, M. Arita, M. Nakatake, T. Okuda, Y. Ueda, K. Shimada, H. Namatame, M. Taniguchi and A. Kimura, *Phys. Rev. B*, 2012, 85, 205317.
- [27] T. Schlenk, M. Bianchi, M. Koleini, A. Eich, O. Pietzsch, T. O. Wehling, T. Frauenheim, A. Balatsky, J. L. Mi, B. B. Iversen, J. Wiebe, A. A. Khajetoorians, P. Hofmann and R. Wiesendanger, *Phys. Rev. Lett.*, 2013, 110, 126804.
- [28] L. A. Wray, S.-Y. Xu, Y. Xia, D. Hsieh, A. V. Fedorov, Y. S. Hor, R. J. Cava, A. Bansil, H. Lin and M. Z. Hasan, *Nat. Phys.*, 2011, 7, 32-37.
- [29] M. N. Faraggi, V. N. Golovach, S. Stepanow, T. C. Tseng, N. Abdurakhmanova, C. S. Kley, A. Langner, V. Sessi, K. Kern and A. Arnau, *J. Phys. Chem. C*, 2015, 119, 547-555.
- [30] M. N. Faraggi, N. Jiang, N. Gonzalez-Lakunza, A. Langner, S. Stepanow, K. Kern and A. Arnau, *J. Phys. Chem. C*, 2012, 116, 24558-24565.
- [31] T. R. Umbach, I. Fernández-Torrente, M. Ruby, F. Schulz, C. Lotze, R. Rurali, M. Persson, J. I. Pascual and K. J. Franke, *New J. Phys.*, 2013, 15, 083048.
- [32] D. Wegner, R. Yamachika, Y. Wang, V. W. Brar, B. M. Bartlett, J. R. Long and M. F. Crommie, *Nano Lett.*, 2008, 8, 131-135.
- [33] S. Bedwani, D. Wegner, M. F. Crommie and A. Rochefort, *Phys. Rev. Lett.*, 2008, 101, 216105-216105-216105-216104.
- [34] N. Abdurakhmanova, A. Floris, T. C. Tseng, A. Comisso, S. Stepanow, A. De Vita and K. Kern, *Nat. Commun.*, 2012, 3, 940.
- [35] J. Rodríguez-Fernández, K. Lauwaet, M. Á. Herranz, N. Martín, J. M. Gallego, R. Miranda and R. Otero, *J. Chem. Phys.*, 2015, 142, 101930.
- [36] N. Abdurakhmanova, T. C. Tseng, A. Langner, C. S. Kley, V. Sessi, S. Stepanow and K. Kern, *Phys. Rev. Lett.*, 2013, 110, 027202-027202.
- [37] T. Bathon, P. Sessi, K. A. Kokh, O. E. Tereshchenko and M. Bode, *Nano Lett.*, 2015, 15, 2442-2447.
- [38] P. Sessi, T. Bathon, K. A. Kokh, O. E. Tereshchenko and M. Bode, *Nano Lett.*, 2014, 14, 5092-5096.

- [39] J. Wang, A. S. Hewitt, R. Kumar, J. Boltersdorf, T. Guan, F. Hunte, P. A. Maggard, J. E. Brom, J. M. Redwing and D. B. Dougherty, *J. Phys. Chem. C*, 2014, 118, 14860-14865.
- [40] Y. Tanabe, K. K. Huynh, R. Nouchi, S. Heguri, G. Mu, J. T. Xu, H. Shimotani and K. Tanigaki, *J. Phys. Chem. C*, 2014, 118, 3533-3538.
- [41] D. Kim, S. Cho, N. P. Butch, P. Syers, K. Kirshenbaum, S. Adam, J. Paglione and M. S. Fuhrer, *Nat. Phys.*, 2012, 8, 459-463.
- [42] M. Caputo, M. Panighel, S. Lisi, L. Khalil, G. D. Santo, E. Papalazarou, A. Hruban, M. Konczykowski, L. Krusin-Elbaum, Z. S. Aliev, M. B. Babanly, M. M. Otrokov, A. Politano, E. V. Chulkov, A. Arnau, V. Marinova, P. K. Das, J. Fujii, I. Vobornik, L. Perfetti, A. Mugarza, A. Goldoni and M. Marsi, *Nano Lett.*, 2016, 16, 3409-3414.
- [43] L. M. Kong, A. Enders, T. S. Rahman and P. A. Dowben, *J. Phys.: Condens. Matter.*, 2014, 26, 27.
- [44] S. Roy, H. L. Meyerheim, A. Ernst, K. Mohseni, C. Tusche, M. G. Vergniory, T. V. Menshchikova, M. M. Otrokov, A. G. Ryabishchenkova, Z. S. Aliev, M. B. Babanly, K. A. Kokh, O. E. Tereshchenko, E. V. Chulkov, J. Schneider and J. Kirschner, *Phys. Rev. Lett.*, 2014, 113, 116802.
- [45] S. Roy, H. L. Meyerheim, K. Mohseni, A. Ernst, M. M. Otrokov, M. G. Vergniory, G. Mussler, J. Kampmeier, D. Grützmacher, C. Tusche, J. Schneider, E. V. Chulkov and J. Kirschner, *Physical Review B*, 2014, 90, 155456.
- [46] R. Shokri, H. L. Meyerheim, S. Roy, K. Mohseni, A. Ernst, M. Otrokov, E. Chulkov and J. Kirschner, *Phys. Rev. B*, 2015, 91, 205430.
- [47] G. Kresse and J. Furthmüller, *Phys. Rev. B*, 1996, 54, 11169-11186.
- [48] P. E. Blöchl, *Phys. Rev. B*, 1994, 50, 17953-17979.
- [49] G. Kresse and D. Joubert, *Phys. Rev. B*, 1999, 59, 1758-1775.
- [50] J. P. Perdew, K. Burke and M. Ernzerhof, *Phys. Rev. Lett.*, 1996, 77, 3865-3868.
- [51] K. Jiří, R. B. David and M. Angelos, *J. Phys.: Condens. Matter*, 2010, 22, 022201.
- [52] J. Klimeš, D. R. Bowler and A. Michaelides, *Phys. Rev. B*, 2011, 83, 195131.
- [53] I. F. Torrente, K. J. Franke and J. I. Pascual, *Int. J. Mass Spectrom.*, 2008, 277, 269-273.
- [54] A. Della Pia, M. Riello, D. Stassen, T. S. Jones, D. Bonifazi, A. De Vita and G. Costantini, *Nanoscale*, 2016, 8, 19004-19013.
- [55] D. Maccariello, M. Garnica, M. A. Niño, C. Navío, P. Perna, S. Barja, A. L. Vázquez de Parga and R. Miranda, *Chem. Mater.*, 2014, 26, 2883-2890.
- [56] M. Bianchi, D. Guan, S. Bao, J. Mi, B. B. Iversen, P. D. C. King and P. Hofmann, *Nat Commun*, 2010, 1, 128.
- [57] M. Bianchi, R. C. Hatch, D. D. Guan, T. Planke, J. L. Mi, B. B. Iversen and P. Hofmann, *Semicond. Sci. Technol.*, 2012, 27, 14.
- [58] K. Park, C. De Beule and B. Partoens, *New J. Phys.*, 2013, 15, 16.

- [59] M. Bianchi, R. C. Hatch, J. L. Mi, B. B. Iversen and P. Hofmann, *Phys. Rev. Lett.*, 2011, 107, 4.
- [60] Z. H. Zhu, G. Levy, B. Ludbrook, C. N. Veenstra, J. A. Rosen, R. Comin, D. Wong, P. Dosanjh, A. Ubaldini, P. Syers, N. P. Butch, J. Paglione, I. S. Elfimov and A. Damascelli, *Phys. Rev. Lett.*, 2011, 107, 5.
- [61] C. Wackerlin, C. Iacovita, D. Chylarecka, P. Fesser, T. A. Jung and N. Ballav, *Chem. Commun.*, 2011, 47, 9146-9148.
- [62] T.-C. Tseng, N. Abdurakhmanova, S. Stepanow and K. Kern, *J. Phys. Chem. C*, 2011, 115, 10211-10217.
- [63] W. Erley and H. Ibach, *Surf. Sci.*, 1986, 178, 565-577.
- [64] R. Otero, J. M. Gallego, A. L. V. de Parga, N. Martin and R. Miranda, *Adv. Mater.*, 2011, 23, 5148-5176.
- [65] T.-C. Tseng, C. Urban, Y. Wang, R. Otero, S. L. Tait, M. Alcamí, D. Ecija, M. Trelka, J. Maria Gallego, N. Lin, M. Konuma, U. Starke, A. Nefedov, A. Langner, C. Woell, M. Angeles Herranz, F. Martin, N. Martin, K. Kern and R. Miranda, *Nature Chem.*, 2010, 2, 374-379.
- [66] J. Giergiel, S. Wells, T. A. Land and J. C. Hemminger, *Surf. Sci.*, 1991, 255, 31-40.

5.5 Appendix section

A1. XPS measurements

The X-ray photoemission spectra (XPS) performed on 2.5ML of TCNQ on Bi_2Se_3 are presented in Fig. A1.1. The lineshape of the C1s and N1s peaks is similar to that reported for TCNQ on weakly interacting substrates^[A1-A3] thus suggesting the absence of any chemical interaction between TCNQ molecules and the substrate.

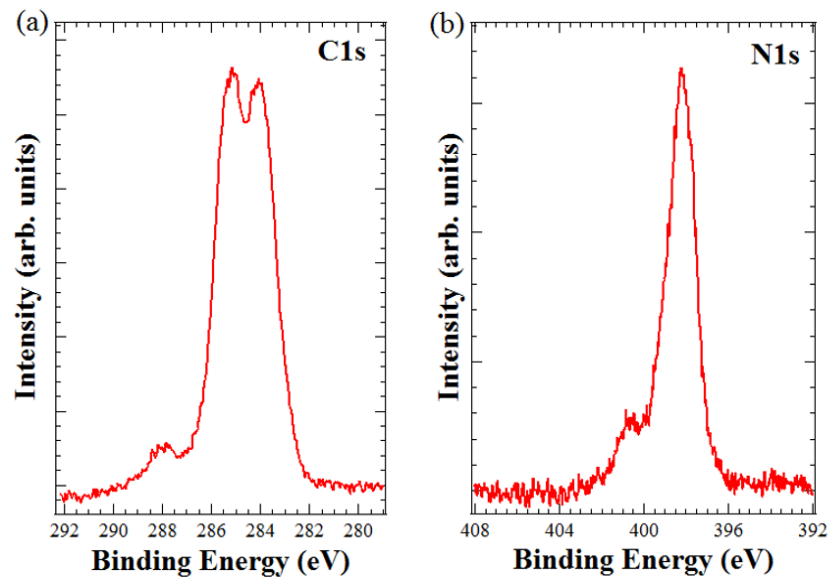


Figure A1.1. XPS spectra of (a) C1s and (b) N1s core levels for 2.5 ML TCNQ deposition on Bi_2Se_3 , collected with 600 eV photon energy.

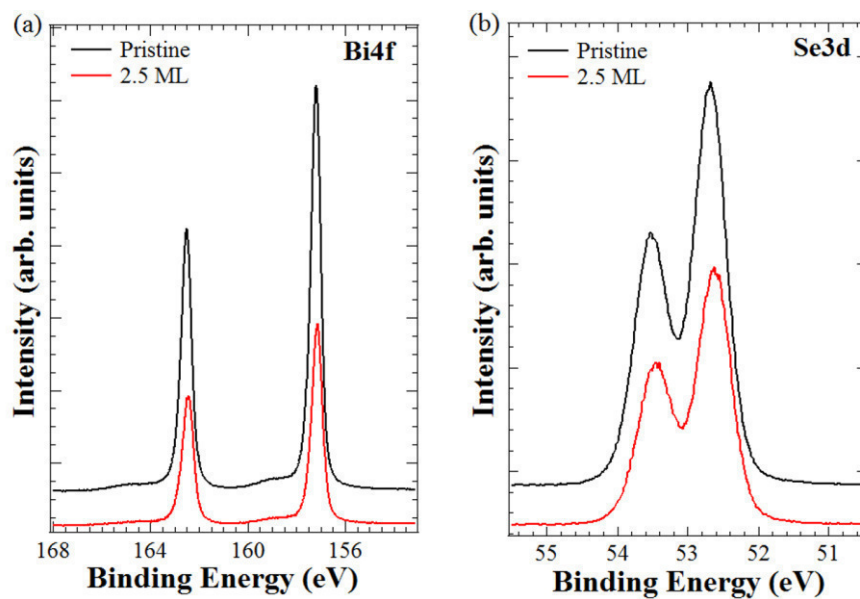


Figure A1.2. XPS spectra of (a) Bi4f and (b) Se3d core level spectra for pristine (black curve) and 2.5ML (red) of TCNQ on Bi_2Se_3 , collected with 600 eV photon energy at normal emission.

In Fig. A1.2 we report the XPS spectra of Bi *4f* and Se *3d* states before and after deposition of 2.5 ML of TCNQ. The pristine sample exhibits both Bi *4f* and Se *3d* states split by spin-orbit interaction into the doublets *4f*_{5/2}, *4f*_{7/2} and *3d*_{3/2}, *3d*_{5/2} at 162.50 eV, 157.19 eV and 53.50 eV, 52.68 eV binding energy, respectively, in agreement with earlier studies.^[A4,A5] The adsorbed TCNQ does not significantly modify neither the line-shape nor the binding energy (within 50 meV) of the Bi *4f* and Se *3d* states.

The molecular coverage of TCNQ was carefully evaluated by considering the attenuation of the measured photoelectron intensity of the Bi *4f* and Se *3d* states prior and after molecular deposition.^[A6] The formula used to estimate the coverage is:

$$\frac{A_{peak}^{ads}}{A_{peak}^{clean}} = (1 - S + S * e^{-(d_{TCNQ-Se1}/\cos\theta)/\lambda_{Ekads}}) * e^{-(N*d_{TCNQ-Se1}/\cos\theta)/\lambda_{Ekads}} \quad (1)$$

where A_{peak} is the experimental XPS area of the peak of interest (Bi *4f* or Se *3d* states) measured prior (A_{peak}^{clean}) or after (A_{peak}^{ads}) molecular deposition; N is the number of layer completely covered by molecules; S is the partial coverage of the upper layer, $d_{TCNQ-Se1}$ is the adsorption distance between TCNQ and the surface Se layer, λ_{Ekads} is the inelastic mean free path of photoelectron with kinetic energy E_k inside the adsorbate, θ is the emission angle. Equation (1) is valid under the assumption of a layer-by-layer growth and the accuracy of the value is limited by the uncertainties in the electron mean free paths in organic layers,^[A7] and by the value used for the adsorption distance.

We considered an electron mean free path of 14.57 Å at 440eV E_k and 17.04 Å at 550eV E_k ,^[A8] $d_{TCNQ-Se1}$ equal to 3.4 Å (as computed by DTF calculations, see main paper), and θ equals to 0° (normal emission).

Molecular coverage and its error (2.5 ± 0.5) ML for the spectra reported above have been set equal to the mean value and half of the difference between the values estimated by using equation (1) for the Bi *4f* and Se *3d* states.

A2. DFT measurements - Free-standing TCNQ monolayer

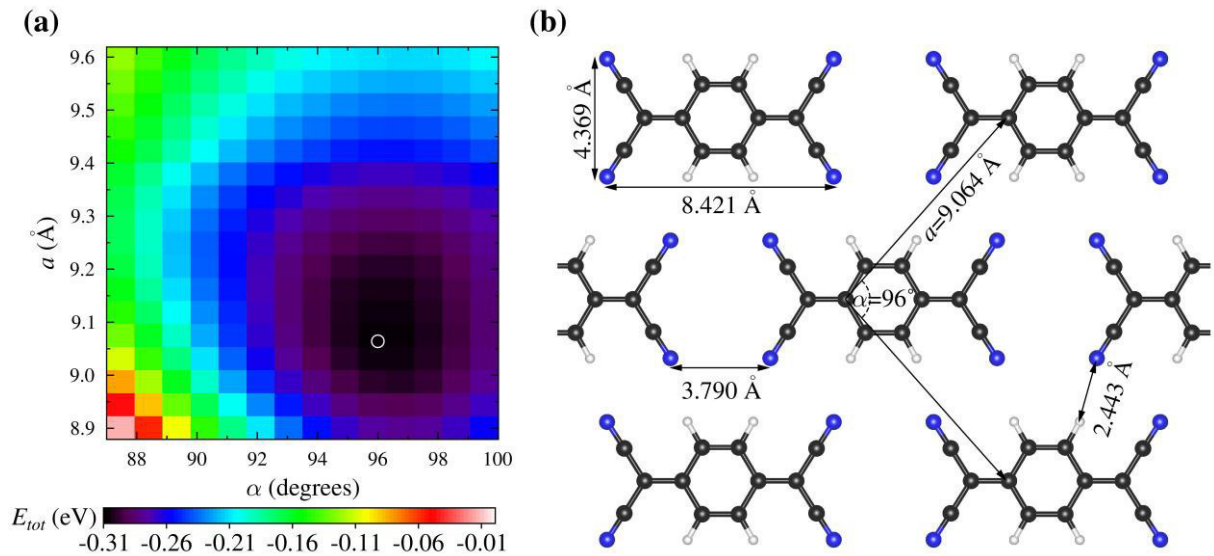


Figure A2.1. (a) DFT calculated energy landscape $E(a, \alpha)$ of the planar TCNQ free-standing monolayer showing a minimum at $a = 9.064 \text{ \AA}$ and $\alpha = 96^\circ$. (b) Top view of the optimized planar TCNQ hydrogen bonded network.

References

- [A1] C. Wackerlin, C. Iacovita, D. Chylarecka, P. Fesser, T. A. Jung and N. Ballav, Chem. Commun., 2011, 47, 9146-9148.
- [A2] S. K. Wells, J. Giergiel, T. A. Land, J. M. Lindquist and J. C. Hemminger, Surf. Sci., 1991, 257, 129-145.
- [A3] D. Maccariello, M. Garnica, M. A. Niño, C. Navío, P. Perna, S. Barja, A. L. Vázquez de Parga and R. Miranda, Chem. Mater., 2014, 26, 2883-2890.
- [A4] M. Bianchi, R. C. Hatch, Z. Li, P. Hofmann, F. Song, J. Mi, B. B. Iversen, Z. M. Abd El-Fattah, P. Löptien, L. Zhou, A. A. Khajetoorians, J. Wiebe, R. Wiesendanger and J. W. Wells, ACS Nano, 2012, 6, 7009-7015.
- [A5] V. V. Atuchin, V. A. Golyashov, K. A. Kokh, I. V. Korolkov, A. S. Kozhukhov, V. N. Kruchinin, S. V. Makarenko, L. D. Pokrovsky, I. P. Prosvirin, K. N. Romanyuk and O. E. Tereshchenko, Cryst. Growth Des., 2011, 11, 5507-5514.
- [A6] S. Hüfner, Photoelectron Spectroscopy: Principles and Applications, Springer, 2003.
- [A7] W. D. Grobman and E. E. Koch, in Photoemission in Solids II, eds. L. Ley and M. Cardona, Springer Berlin Heidelberg, 1979, vol. 27, ch. 5, pp. 261-298.
- [A8] C. J. Powell and A. Jablonski, NIST Electron Inelastic-Mean-Free-Path Database - Version 1.2, National Institute of Standards and Technology, Gaithersburg, MD, 2010.

Part II: CVD graphene on Cu foil

Chapter 6

Coupled and freestanding behaviour of monolayer graphene deposited by low pressure CVD (LP-CVD) on Cu foil

The growth of graphene on copper foil has been performed, following the consolidated low-pressure chemical vapour (LP-CVD) procedure. The as-deposited monolayer graphene clearly exhibits two different states of coupling to the metal substrate, as demonstrated by visual microscopic investigation, Scanning Electron Microscopy (SEM), micro-Raman spectroscopy and Scanning Tunneling Microscopy (STM). The single graphene sheet shows indeed both large areas where it is coupled to the metal surface and others where it exhibits freestanding-like features. This phenomenology appears to be related to some oxidation of the metal substrate to Cu_2O . In addition, we demonstrate the possibility to induce a variation of the coupling state by visible-light irradiation above a proper power threshold. The resulting change of the coupling with the metal substrate is associated to a localized work function variation. Applications in high-performance electronic devices can be suitably tailored by optical methods and, in principle, by any local probe producing “hot spots” such as STM tips and electron beams.

6.1 Introduction

The experimental discovery of graphene^[1-3] opened the doors to the world of nanomaterials. Thanks to its extraordinary properties, graphene and its derivatives will play a critical role in nanotechnology in the future across various technological domains.^[4] A large number of techniques for the production of graphene were developed over the years, including epitaxial growth,^[5] mechanical^[6] and chemical exfoliation,^[7] as well as chemical vapor deposition (CVD).^[8-10] Graphene grown on metal surfaces can interact strongly or weakly with the underlying substrate; in particular, a strong coupling is reported for Ru(0001),^[11,12] Rh(111)^[13,14] and Ni,^[15,16] while a weak interaction involves Pt(111),^[17,18] Ir(111)^[5,19] and Cu^[20,21] surfaces.

The ability to synthesize high quality graphene on non-interacting substrates would allow preserving the graphene's intrinsic properties, which is a fundamental prerequisite for graphene electronic devices (i.e. graphene directly deposited on a dielectric surface). Unfortunately, this route has not been developed yet. Direct growth of freestanding graphene on a surface would eliminate the transfer step on a nearly non-interacting substrate.^[22] This last consolidate transfer procedure usually involves the PMMA/PVA methods to transfer graphene on the inert Si/SiO₂ surface.^[23-26] A good alternative proposed to this purpose is to grow graphene directly on the metal oxides surfaces.^[27] As reported by Gottardi et al.^[28] high-quality monolayer graphene can be grown on a pre-oxidized Cu(111) surface, which is effectively decoupled from the underlying substrate (i.e. freestanding like). Another change to realize freestanding graphene is to grow it on metal surfaces and after to intercalate an oxygen layer in the graphene/metal interface. In fact, as reported by Voloshina et al.,^[29] the strong-coupled graphene/Ru(0001) interface was successfully decoupled by the intercalation of an oxygen layer.

Taking into account all these factors, in this chapter, monolayer graphene films were obtained on copper (Cu) foil by the consolidate Chemical Vapor Deposition at low-pressure conditions (LP-CVD). The coexistence of two kinds of monolayer graphene, in terms of coupling with the underlying metal surface, is evidenced by optical and electronic microscopy as well as micro-Raman mapping and STM investigation. These two distinct regions clearly show a monolayer graphene coupled and freestanding-like with respect to the copper surface, respectively. This phenomenon appears to be related to partial oxidation of the metal substrate (i.e. presence of Cu₂O).

The possibility to induce on a microscopic scale a transition from the coupled to freestanding-like graphene via visible-light irradiation above a proper power threshold is evidenced. The resulting change of the coupling with the metal substrate is also associated to a localized work function variation. Applications in high-performance electronic devices can be suitably tailored by optical methods and, in principle, by any local probe producing “hot spots” such as STM tips and electron beams. In fact, such evidences open the doors to creation several graphene-based electronic devices, like gas sensors,^[30,31] solar cells,^[32,33] and field emitters.^[34,35]

6.2 Experimental section

Graphene samples were grown on a thin copper foil (25 μm thickness, 99.999% purity, ESPI Metals). The growth took place in a quartz-tube vacuum furnace where the base pressure was about 10^{-5} mbar.^[36] The Cu surface was prepared by etching with H_2SO_4 0.25M for 5 minutes and subsequently rinsed in milli-Q water. The samples were rinsed in ethanol and dried with argon, before being placed in the furnace. To avoid the formation of native oxide on the Cu surface, the samples were annealed at a temperature ranging between 907 and 977°C in hydrogen flow (0.5 mbar). Subsequently, the samples were exposed to a mixture of hydrogen (0.5 mbar, MesserGas, purity 99.999%) and methane (0.5 mbar, MesserGas, purity 99.995%) for a time ranging between 2 and 4 minutes.^[21] Then the samples were cooled down in argon atmosphere (99.999% purity, MesserGas, pressure 0.1 mbar) with an initial rate of 10°C/min (in the range 927-477°C) and, later, with a rate of 5°C/minute (in the range 477-77°C).^[37]

A systematic characterization of different samples was carried out to investigate their structural, morphological and electronic properties, by Scanning Electron Microscopy (SEM) and Raman spectroscopy. Scanning electron images were recorded using a Quanta FEG 400 (FEI) scanning electron microscope (SEM). All SEM images were collected by using an electron beam of 15 keV on areas ranging from 25 μm^2 up to 250 μm^2 and magnification in the order of 10000X. Micro-Raman spectra were collected by Horiba-Jobin Yvon apparatus, model LabRam HR, consisting of a single spectrograph equipped with: an objective 80X, a holographic grating (600 lines/mm) and a He-Ne laser. The maximum laser power flux impinging the samples is about of 109 W/m^2 ; it can be reduced by using neutral filters of optical density (OD) ranging from 0.3 up to 4.

6.3 Results and discussion

6.3.1 Monolayer graphene coupling on Cu foil

Optical images of graphene grown on copper foil by LP-CVD are shown in Fig. 1. Here, the typical grain structure of Cu substrate, which appears as a mosaic, is due to the annealing procedure during the CVD growth, while the diagonal stripes are representative of the synthesis process of the metal foil. A different optical contrast is also pointed out by the visual analysis, which show a surface with large brighter and darker areas, regardless of the size and structure of the single copper grains.

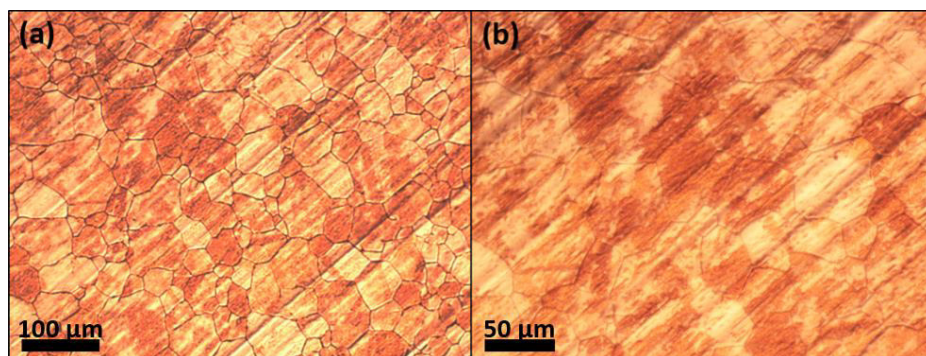


Figure 1. (a)-(b), Optical images of graphene grown on Cu foil. The typical mosaic structure of the copper substrate is evident.

Fig. 2(a) shows a large-scale SEM image of graphene on Cu substrate where the Cu grains are clearly visible on the surface. The different shades of gray that appear in this last SEM acquisition can be related to the different optical contrast shown both in Fig. 1 and in Fig. 2(b), where the last picture was collected by optical microscope of the Raman apparatus.

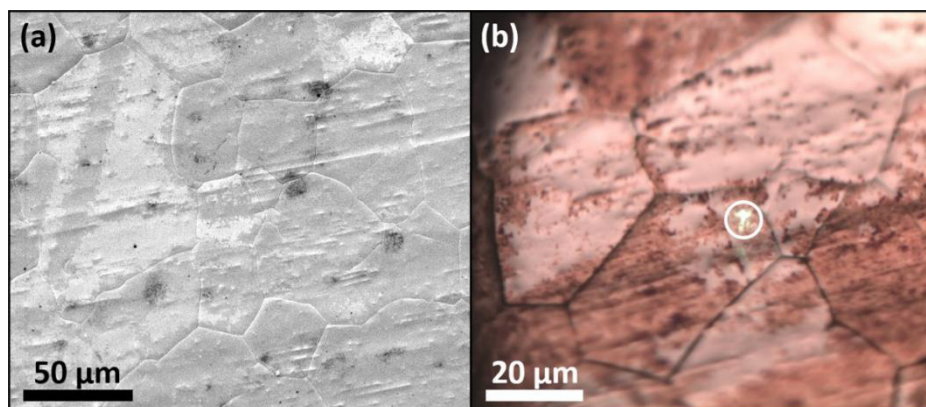


Figure 2. (a) SEM image of graphene on Cu surface acquired on an area of about $210 \times 180 \mu\text{m}^2$. (b) Optical image collected by the microscope of the Raman apparatus, with the objective 80X. The area here represented is approximately $90 \times 70 \mu\text{m}^2$. The spot circled in white near the center is the focus of the attenuated laser beam (OD4).

Generally, in systems where graphene covers partially or entirely the whole surface, different shades of grey in SEM acquisitions can be observed. One possible explanation involves the different graphene film thickness:^[38-40] lighter areas correspond to graphene thin films (e.g. monolayer graphene) while darker regions represent more substantial depositions. Zhou et al.^[39] clearly pointed out that secondary electron (SE) contrast of SEM acquisitions is strictly related to work function changes, depending on the number of graphene layers. In particular, they show that graphene work function rises as the thickness increases. However, other explanations are possible. Graphene work function also depends both on the chemical composition and morphology^[18,41,42] of the substrate. Moreover, the specific crystalline surface^[41] and graphene/surface reciprocal orientation^[43] can also influence the graphene work function.

The lower work function, associated to the shinier areas, can also be explained in terms of variation of the graphene-to-metal surface distance. DFT calculation performed by Giovannetti et al.^[44] show that the work function of the graphene layer on copper substrate shows an estimated shift of 0.55 eV by passing from the equilibrium separation (ca. 3.3 Å) to a larger distance (greater than 4.2 Å), when it assumes the freestanding-like value. This is due to the graphene/metal electron transfer resulting from the chemical interaction. In our case, as confirmed below by Raman analysis, the different shade of grey in SEM analysis, i.e. the local work function variation of graphene, is related to the different coupling between the single-layer graphene and the Cu surface.

Color differences appear also in the optical images as shown in Fig. 2(b). In particular, the regions that preserving color and reflectivity of the clean Cu surface are labeled as “bright”, while the areas appear brown colored, showing decreased reflectivity and are labeled “dark” ones. The size of both regions is comparable. Micro-Raman spectroscopy is among the most effective techniques to characterize these areas with different optical contrast^[45,46] and, in fact, they reveal significant differences in their Raman spectra, as reported in details below.

Summarizing, “bright” regions in optical images correspond to monolayer graphene in close contact with copper substrate, while the “dark” ones are the regions of graphene decoupled from the metal surface (Fig. 2(b)). A consistent description for the SEM evidences and micro-Raman data from areas of different color, on similar scale, can be given by supposing that the contrast is reversed: i.e. the regions of low SE emission in electronic microscopy appear “bright” at the optical microscope. Taking into account the spatial resolution of micro-Raman

analysis ($\sim 1 \mu\text{m}$) we could assert to get adequate physical information about the apparent contrast. Two representative spectra from these different regions are shown in Fig. 3. Raman spectra of the “bright” regions exhibit, in general, a very weak signal, but the intensity ratio between the G band and the overtone 2D is consistent with graphene monolayer formation.^[9,45,46] This layer appears also highly ordered, being the D band absent or very weak. It is interesting to note that the G band falls at about 1600 cm^{-1} , a frequency value higher than usual.^[47,48] When the G band exhibits this high frequency value, the 2D overtone is centered at about 2660 cm^{-1} . These evidences indicate an appreciable coupling between graphene and metal substrate. In the “dark” regions, on the contrary, all the Raman bands are stronger, while the intensity ratio 2D/G remarkably increases, being the shape of 2D band still well represented by a single mode curve.

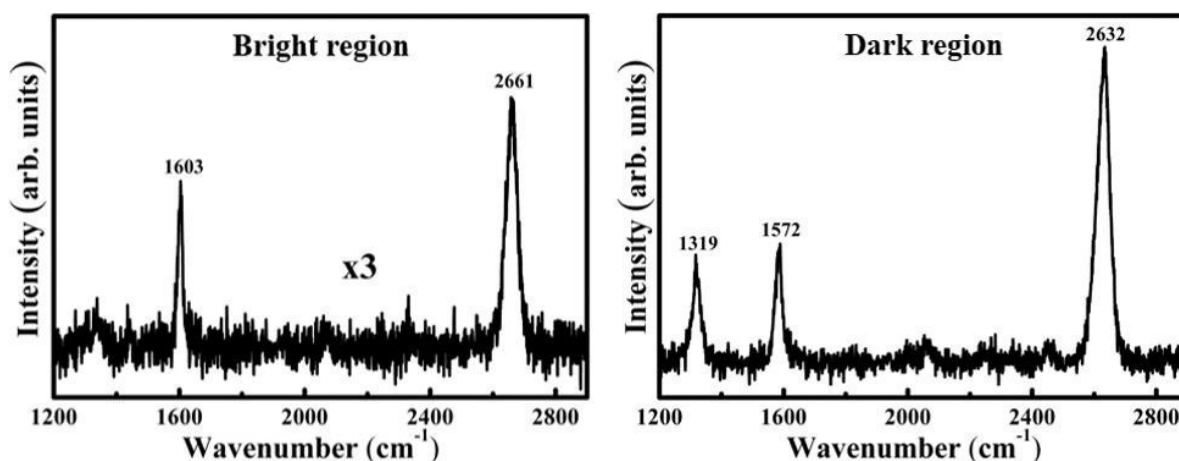


Figure 3. Representative Raman spectra from optically appearing different areas of CVD graphene on Cu foil, collected by the apparatus described in the text, with 633nm excitation. The left spectrum is collected on a “bright” region, and is amplified by a factor 3 for comparison purposes with the near one, coming from a “dark” region.

These findings are neither compatible with the formation of multilayer graphene having typical Bernal stacking^[45,46] or with turbostratic multilayer.^[49] Moreover, the G and the 2D bands shift to lower frequency at about 1572 cm^{-1} and 2630 cm^{-1} , respectively, which are typical of “freestanding-like graphene”;^[45,46,50] finally, the rising of D band reveals some amount of disorder.^[51] To complete the analysis, measurements in the low frequency region of the Raman spectra reveals no significant peaks for the “bright” regions, while typical Raman bands of Cu_2O ^[52-56] at 145 cm^{-1} and 215 cm^{-1} are found in all the “dark” areas (Fig. 4). This result, confirming the previous one of Cermak,^[53] suggests that the decoupled configuration

of monolayer graphene is associated to the oxidation of the copper substrate, which inhibits the graphene-metal electron exchange, inducing changes in the graphene work function.

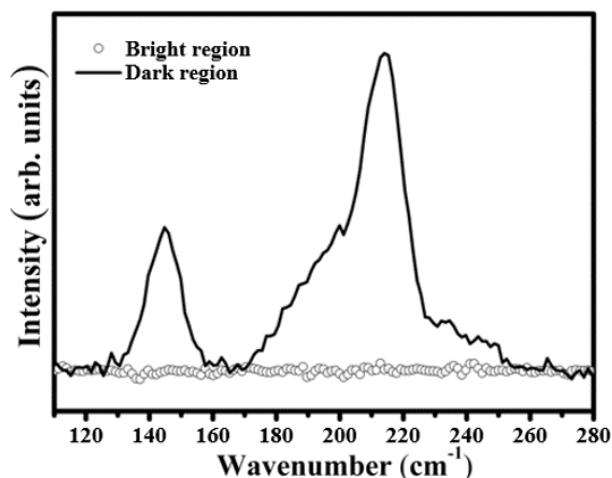


Figure 4. Representative Raman spectra at the low frequency region from “bright” and “dark” regions of CVD graphene on copper foil. The spectrum collected on the “dark” region (solid line) shows two structures at about 145 cm⁻¹ and 215 cm⁻¹, typical of Cu₂O. Conversely, Raman acquisition performed on the “bright” region (empty circles) does not show these Cu₂O bands.

Further investigations of the sample were performed by means of AFM (Atomic Force Microscopy) and STM (Scanning Tunneling Microscope). Wide AFM scans simply point out the three-dimensional topography of the graphene/Cu surfaces (see Fig. 5), where a microterraced structure of the Cu substrate is evident. Copper terraces are devoid of impurities and contaminations and can achieve micrometric dimensions. However, the graphene islands are not readily evident in the AFM topography images, because the surface roughness far exceeds the thickness of a graphene sheet.^[57]

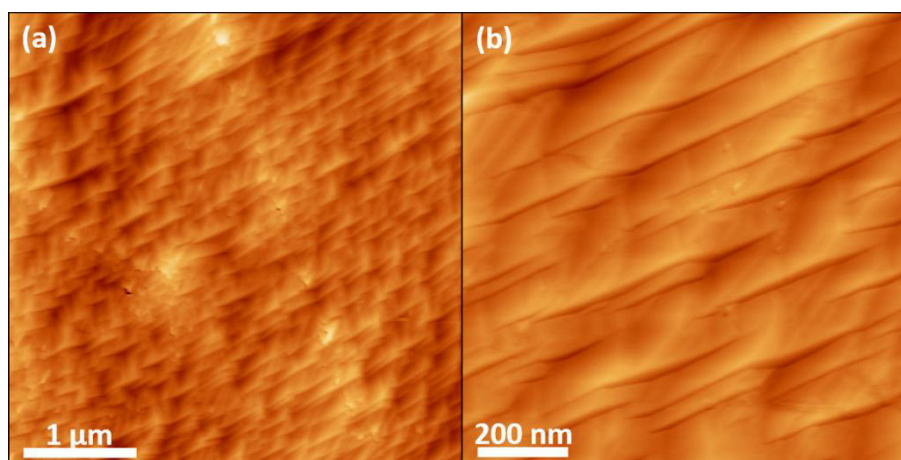


Figure 5. (a) 4x4 μm² and (b) 1x1 μm² AFM topography images of graphene on Cu foil.

A deeper investigation on nanometer scale carried out by STM corroborates the Raman and SEM results previously reported. In fact, the wide microscopic statistical analysis performed allows identifying two distinct kind of graphene on the copper surface, in terms of coupling with the substrate. The first one is the graphene layer coupled with Cu surface (see Fig. 6(a) below). In this case, the presence of the Moiré superstructure, which arises from the mismatching between the graphene and the Cu surfaces, ensure the coupling between the two lattices. These areas of graphene can be connected to the optical “bright” region well-characterized by Raman spectroscopy.

Moiré pattern is commonly observed when graphene is grown on metal surfaces, regardless of whether the metal-surface interaction is stronger^[12,14] or weaker.^[18,58] In both cases, the difference between the lattice constants and the relative rotation of the graphene layer respect to the metal surfaces are responsible for its appearance. In the case of graphene grown on Cu(111), the lattice mismatch between the overlayer and the copper surface is 3.906%, and the Moiré pattern appears, as well as in the of graphene grown on 4d and 5d metals, in which the mismatch is higher than this value. Indeed, the resulting structure of graphene grown on Ni(111) and Co(0001) is commensurate, because the lattice difference is lower than the 2%.^[59]

The second kind of graphene is completely decoupled from the Cu surface, as a “free-standing like” graphene (see Fig. 9 below). This is confirmed by the absence of Moiré superstructure. These graphene areas are related to the decoupled region (“dark region”) characterized by Raman spectroscopy. A recent work of Gottardi et al.^[28] reports the case of graphene growth on bare Cu(111) and Cu(111) oxidized surfaces. The STM images collected on these two samples are quite similar to our acquisitions: the coupled graphene shows the Moiré pattern, while graphene growth on the oxidized Cu surface is free from this superstructure. In that case, in fact, the interaction between the substrate and the over-layer is mediated by the Cu₂O formation. Similarly, Voloshina et al.^[29] shows that intercalation of oxygen in graphene grown on Ru(0001) can allows to obtain a decoupled graphene layer on the surface.

As reported above, the STM measures are in agreement with the SEM and Raman investigation. However, a more complete description of STM analysis performed on this sample is given below, which permits to achieve additional information about this system.

A representative STM image of the coupled graphene on the Cu surface is shown in Fig. 6(a). This last picture exhibits the atomic resolution of graphene on which the Moiré superlattice is

superimposed. As mentioned above, this typical superstructure arises from the interference pattern caused by the misalignment between the graphene and copper periodic lattices, and clearly indicate that the graphene is coupled to the substrate.

The Fast Fourier Transform (FFT) analysis performed on the last morphological STM acquisition, allows to gain significant information about graphene deposited on the Cu surface. In Fig. 6(b), the outer and inner spots arranged at the vertices of two hexagons represent the graphene and Moiré lattices in the reciprocal space, respectively. The hexagonal symmetry of the Moiré structure clearly shows that the Cu surface geometry is hexagonal, compatible with the Cu(111) facets. The well-defined spots of the FFT image also indicate a well-ordered surface. The graphene and Moiré lattice periodicities calculated from the FFT analysis are equal to $2.46\text{\AA} \pm 0.01\text{\AA}$ and $1.20\text{nm} \pm 0.02\text{nm}$, respectively. In order to better visualize the honeycomb and Moiré lattices, Figs. 6(c)-(d) show their reconstructions gained by Fourier filtering.

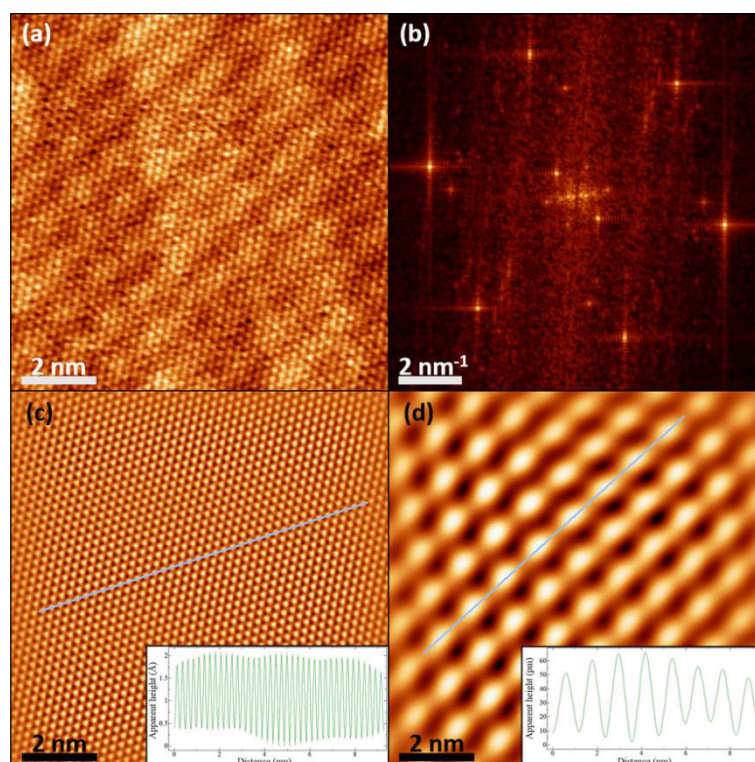


Figure 6. (a) $10 \times 10 \text{nm}^2$ STM topography image of graphene surface in which Moiré pattern is superimposed to the atomic resolution. Tunneling parameters: $U_t = -0.05 \text{mV}$, $I_t = 1 \text{nA}$. (b) Fourier analysis of the STM acquisition. (c)-(d) Reconstruction of graphene lattice and Moiré pattern, respectively. Insets: line profile along graphene and Moiré reconstructed networks, respectively.

To the best of our knowledge, the $1.20 \times 1.20 \text{nm}^2$ Moiré cell is the smallest experimental graphene superlattice reported on Cu (111) so far. This new Moiré phase is also the only

observed on the sample. This suggests that graphene could have preferred orientations with the underlying Cu(111).

Fourier analysis performed on the acquired image allows also reconstructing the STM real space image from the FFT filtering. The well-defined picture (see Fig. 7(a)) exhibits the filtered graphene image on which the Moiré phase is superimposed.

The corresponding angle between the graphene and Cu(111) surface can be calculated starting from the Moiré periodicity. Following the mathematical calculation performed on graphene grown on hexagonal boron nitride (h-BN),^[60] the Moiré pattern in real space has a wavelength

$$L = \frac{(1 - \mu) \cdot a_{Cu}}{\sqrt{2 \cdot (1 - \mu)(1 - \cos\varphi) - \mu^2}} = \frac{a_{gr}}{\sqrt{2 \cdot (1 - \mu)(1 - \cos\varphi) - \mu^2}} \quad (1)$$

where a_{gr} is the graphene lattice periodicity, while μ and φ are the lattice mismatch and the misorientation angle between graphene and the Cu(111) surface, respectively. Clearly, from this last equation is easy to determine the relation for the φ angle

$$\varphi = \cos^{-1} \left[\frac{1}{2 \cdot (\mu - 1)} \left(\frac{a_{gr}^2}{L^2} - \mu^2 + 2\mu - 2 \right) \right] \quad (2)$$

In our case, the superlattice periodicity of 1.20 nm give us a misoriented angle of $\varphi = 11.8^\circ \pm 0.4^\circ$, and the simulated Moiré pattern is reported in Fig. 7(b).

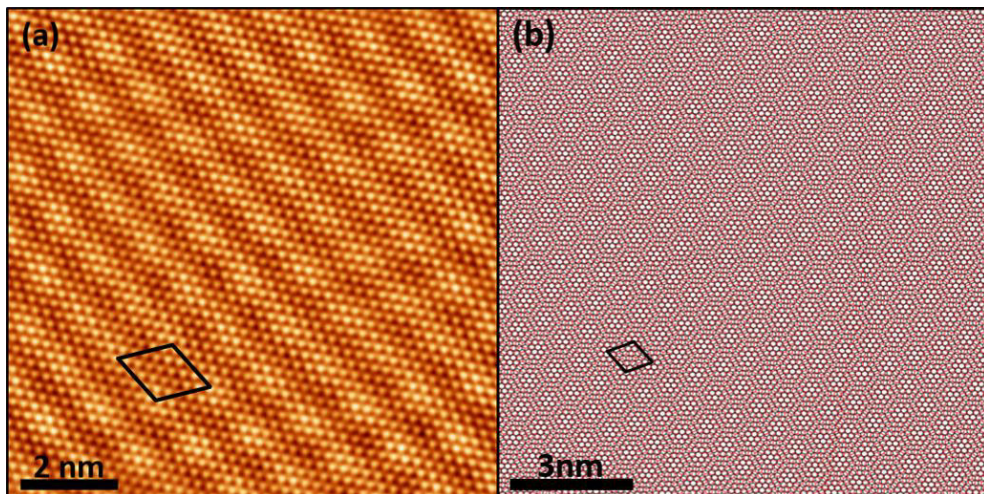


Figure 7. (a) Reconstructed STM image of coupled graphene on Cu(111) from Fourier analysis. The Moiré unit cell is superimposed on the picture. (b) Simulated Moiré pattern of graphene on Cu(111).

Previously, several Moiré periodicities of graphene grown on Cu(111) were reported in literature. The most common results are summarized in Table 1, which includes both experimental, STM and LEED, than theoretical (CMD) data.

(a)	Method	θ	L (nm)	(b)	Method	θ	L (nm)		
STM		0°	6.6 ^{61,62}	CMD		0°	6.1 ⁶⁴		
		1.2°	5.6 ⁶²			1°	6 ⁶⁶		
		3°	4 ⁶²			2.2°	4.3 ⁶⁴		
		7°	2 ^{61,62,63}			6.7°	2.5 ⁶⁴		
		10.4°	1.5 ⁶⁴			8°	1.7 ⁶⁶		
		11.8°	1.2			8.7°	1.75 ⁶⁴		
LEED		0.8°	6.1 ⁶⁵			10°	1.4 ⁶⁶		
		4.2°	3.1 ⁶⁵			10.4°	1.4 ⁶⁴		
								16.1°	0.88 ⁶⁴

Table 1. (a) Experimental and (b) theoretical Moiré superstructure periodicities reported in literature.

As shown in Table 1, the periodicity L of Moiré pattern decreases with increasing misorientation angle φ . In particular, the largest superstructure lattice occurs when the rotation angle between is 0°, that is when the lattice orientation of graphene is aligned with the Cu(111) lattice. As said before, the experimental smallest lattice periodicity is here reported for the first time.

As reported by the theoretical work of Smirman et al.^[67] (see Fig. 8(a)), the Moiré pattern periodicity also depends on the ratio between the adhesion and elastic energies per unit area (W/K). In other words, as also reported by Zeller et al.^[65] (see Fig. 8(b)), the strain of graphene deposited on Cu surface can influence the “theoretical” Moiré periodicity at a certain angle. In particular, the superlattice wavelength increases with larger W/F (see Fig. 8(a)). The increase in L with respect to W/K occurs since when the adhesion force is stronger, the commensurate regions between the two lattices are larger. As a result, the Moiré periodicity is larger. Equation (1) reported above can be considerate as a simple mathematical relation at the limit of $W/F=0$, i.e. without strain effects. However, as shown by simulations in Fig. 8, the dependence is noteworthy only for small angle.

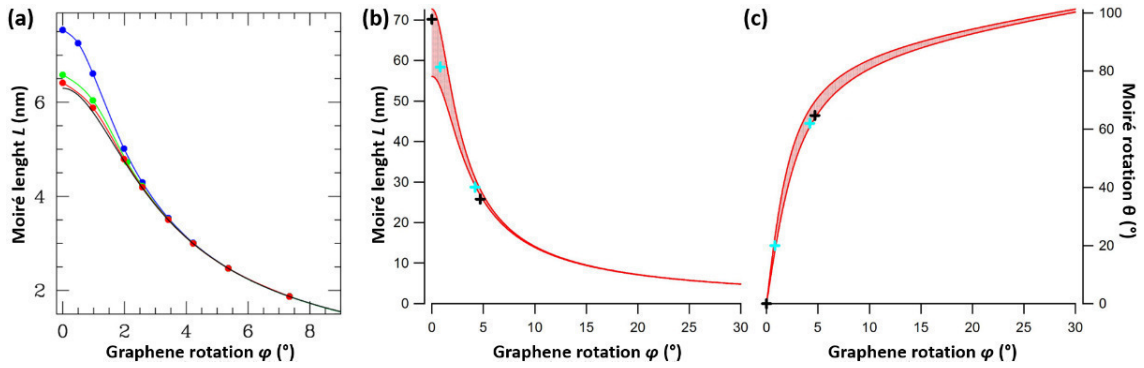


Figure 8. (a) Simulated periodicity of Moiré patterns as a function of ϑ for graphene/Cu(111)] where the blue, green, and red solid points correspond to $W/K = 0.72 \times 10^{-3}$, 0.43×10^{-3} , and 0.29×10^{-3} , respectively. The solid black line corresponds to the $W/K = 0$ limit. Image adapted from [67]. (b)-(c) Predicted Moiré length L and rotation Moiré angle φ for graphene on Cu(111). The displayed curves relate to a $\pm 0.5\%$ strained graphene layer. Image adapted from [65].

Furthermore, Fourier analysis allows also calculating the lattice mismatch between graphene and Moiré superstructure. In fact, the misalignment between the two hexagons in Fig. 6(b) represents the orientation angle between graphene and Moiré lattices. The analysis performed on Fig. 6(b), shows an angle between the two hexagons equal to $\theta_{\text{exp}} = 23.3^\circ \pm 0.8^\circ$. However, this angle can also be determined theoretically, using the following mathematical relation

$$\theta_{th} = \tan^{-1} \left(\frac{\sin \varphi}{\cos \varphi + \mu - 1} \right) \quad (3)$$

This last equation return the value of $\theta_{th} = 85.0^\circ \pm 4.0^\circ$. Although this predicted angle θ_{th} appears in disagreement with the analogous measurement derived from the FFT analysis, i.e. θ_{exp} , actually the two measures are consistent, because the angle reported by the Equation (3) is shifted by 60° for symmetry considerations. In fact, owing to six-fold symmetry in the lattice of both graphene and Cu(111), Moiré pattern from graphene/Cu(111) stacking produces a periodicity of 60° in their twisted angle.^[60] As a result, the misorientation angles between graphene lattice and Moiré superstructure measured by both methods are $\theta_{\text{exp}} = 23.3^\circ \pm 0.8^\circ$ and $\theta_{th} = 25.0^\circ \pm 4.0^\circ$, respectively.

As mentioned above, the Moiré pattern ensure a coupling between the graphene and copper surface, which is the Cu(111) facets. However, other regions of the sample investigated by STM show atomic resolution of graphene resolved without Moiré pattern, as clearly visible from the lattice image and the corresponding Fourier Transform in Fig. 9. In the last case, the

absence of the Moiré superstructure clearly indicate a decoupled graphene with respect to the surface.

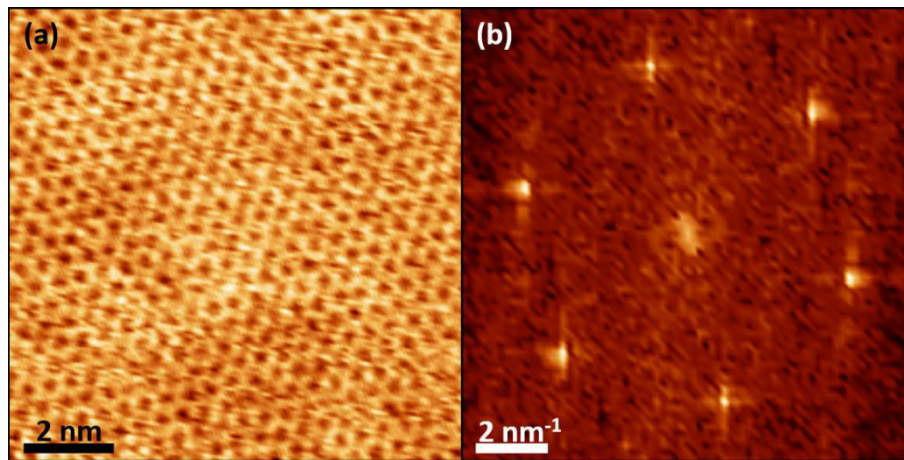


Figure 9. (a) $5 \times 5 \text{ nm}^2$ STM image of graphene surface on Cu foil. No Moiré pattern is observed. (b) Fourier transform of the previous scan shows only the graphene spots.

6.3.2 Laser-induced transition from coupled- to freestanding- graphene

Further investigation on this particular system, in which graphene is differently coupled with the Cu surface, were performed by Raman spectroscopy. In particular the transition from coupled- to freestanding graphene (i.e. from bright to dark regions), can be induced by a proper amount of laser irradiation. To provide more detailed evidences about that, a controlled experiment has been carried out, as described below.

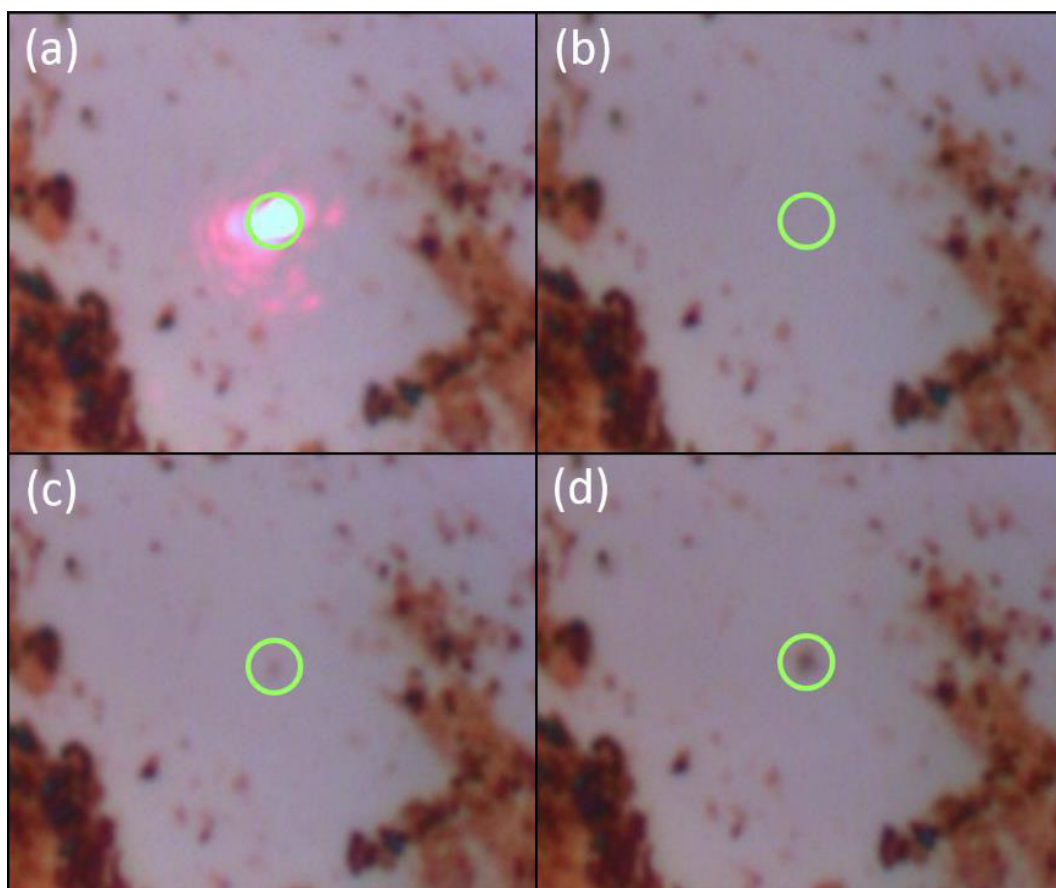


Figure 10. (a) Strongly attenuated laser beam pointing out the irradiated spot. (b) Same image of graphene surface without laser beam: observe the bright coloration. (c) First small change in coloration (see green circle) after increased laser irradiation (50% full power). (d) Final greater change after full power irradiation (see green circle).

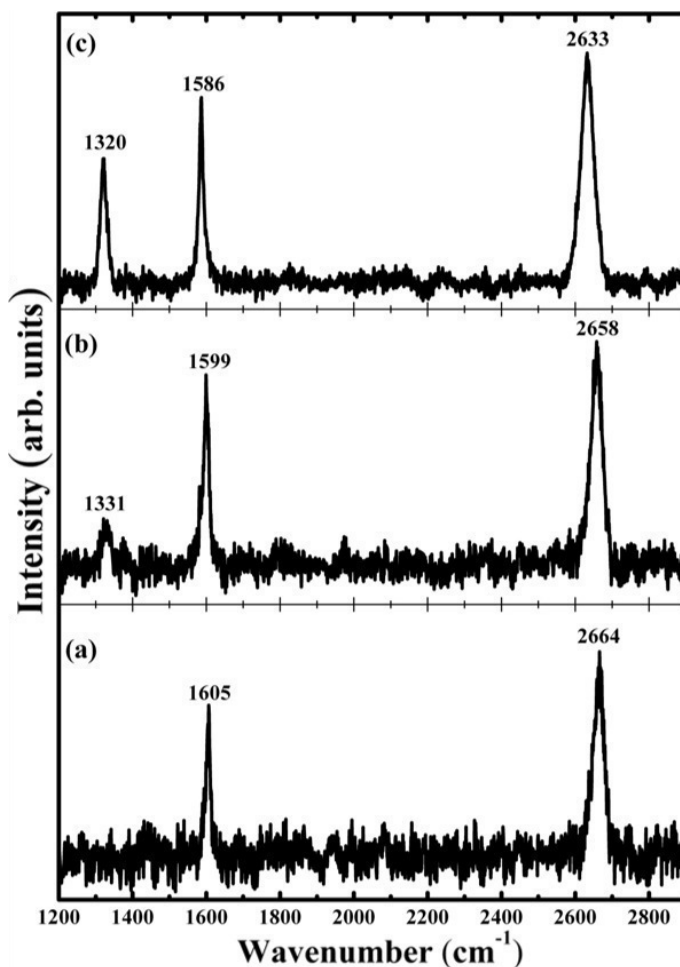


Figure 11. Spectral evolution of the laser irradiated spot (the intensity scale has been properly adjusted for easy comparison of the three spectra): (a) First spectrum, collected with low intensity (25% full power). (b) Second spectrum, collected with higher laser power (50% full power). (c) Spectrum collected with low intensity, but after irradiation at full power.

A Raman spectrum has been collected by using the laser source at 25% of the full power, on a “bright” region, (see Figs. 10(a)-(b)). This spectrum, shown in Fig. 11(a), indicates a well ordered graphene sheet (non-detectable D band) closely coupled with the copper substrate (very weak Raman signal in general), while the G band is peaked at 1605 cm^{-1} and the 2D overtone at 2664 cm^{-1} , typical of the bright regions (see Fig. 2). Another spectrum, collected from the same spot by using an increased laser power (50% of the full power for 600s), is reported in Fig. 11(b), and exhibits some minor but interesting changes. The D band is peaked at 1331 cm^{-1} , the G band slightly downshifts from 1605 cm^{-1} to 1599 cm^{-1} and the 2D overtone from 2664 cm^{-1} to 2658 cm^{-1} , while the intensity ratio 2D/G does not change appreciably. These variations could be explained even as a simple thermal effect of the increased laser power. It is interesting to note a very little change of the color for the irradiated spot, after exposure to this higher laser power (Fig. 10(c)).

Finally, the same region previously investigated was exposed to the full power of the laser source for 600 s. This treatment induced a stronger and irreversible change of the optical color (see Fig. 10(d)), clearly related to a different interaction with the substrate. A new spectrum is collected from that spot, after the strong irradiation, in the same “non-perturbative” conditions of the first spectrum (25% full laser power): it reveals appreciable spectral changes (see Fig. 11(c)). The D band increases in intensity, and downshifts to 1320 cm^{-1} , while the G and 2D bands downshifts to 1586 cm^{-1} and to 2633 cm^{-1} , respectively. As a result, the Raman features of this irradiated region assumed the typical values of the dark regions. Moreover, the Raman signal is generally higher, as revealed by the increased signal to noise ratio. In fact, the intensity ratio 2D/G shows an appreciable increase, confirming once again that such Raman spectrum is due to a graphene monolayer region and not to a turbostratic multilayer accumulation,^[49] which is, in any case, very difficult to invoke as explanation of those changes, because only a local thermal treatment in air has been performed on the sample. Furthermore, the shape of the 2D band still corresponds to single-layer graphene rather than bilayer and few-layers ones.^[68-70] Clearly all these changes cannot be due to a thermal effect during the measurement, because we are using the same low power of the spectrum shown in Fig. 11(a). Another possible explanation for the spectral modifications could be, in principle, a thermal oxidation for the pure graphene monolayer under the previous strong laser irradiation. However, a previous study,^[71] carried out to obtain purposely the oxidation by thermal treatment of exfoliated 1-L graphene on Si/SiO₂, shows a quite different evolution of the Raman spectral parameters. In fact, the frequencies of G band as well as those of the 2D overtone were remarkably up-shifted upon graphene thermal oxidation, while in our case we observe the opposite trend. Another experiment^[72] investigated the evolution of monolayer graphene, deposited on insulating substrate Si/SiO₂, under laser irradiation, for impinging powers comparable to those employed in Raman measurements. Once again, the resulting changes of the Raman bands do not correspond to our results. In that case, the G band frequency appears insensitive to the laser irradiation, while in our study we observe a remarkable softening.

In summary, we suggest that our observed Raman spectral changes are mainly due to the decoupling of the monolayer graphene from the metal substrate, because of the growth of a metal oxide layer in between, favored probably by the thermal effect of laser irradiation. As a result, we can state that a proper laser irradiation can modify the strength of the metal-

graphene electronic interaction, which characterize the two main configurations occurring spontaneously in our CVD samples after the cooling. This switch between different configurations is also associated to different optical properties in reflection, generating the apparent color change before and after laser irradiation (Fig. 10(d)). In fact, the deposition of a graphene monolayer in the metal-coupled configuration do not change appreciably the Cu reflectivity, at least in the visible range, so that these bright regions appear to the visual microscopic analysis as almost identical to the naked copper surface. In the dark regions, on the contrary, the graphene layer is less coupled to the metal substrate, because of the oxide layer grown in between, and the resulting reflectivity is lower.

The weak Raman signals in the bright regions are ascribed to the anti-resonance effect of the strong coupling substrate-graphene, observed on several metals and leading to the total cancellation in some case, like Ni.^[73] In this configuration, the graphene layer undergoes also to a compressive stress and the Raman bands frequencies result higher than in “dark” regions, which can be considered more similar to the freestanding case.^[74] In this latter case, the Raman intensity is higher and the frequencies are closer to the values found for mechanically exfoliated samples. In fact, it is well known that graphene layers grown by CVD on strongly interacting metals, like Ni, cannot be observed by Raman spectroscopy when deposited on the metal, but can give a good Raman signal after removal from metal substrate and deposition on Si-SiO₂.^[75] In the case of metals not so strongly interacting, Raman spectra of graphene were observable both on the metal and after detachment,^[76] and the spectral differences between these two configurations are comparable to those observed in the present work between dark and bright regions.

The investigation of the effect of laser heating, confirms such hypothesis: the local heating induce an expansion of graphene and its detachment from the substrate, associated with some fracture of the hexagonal carbon network, allow to the oxygen of the environment to penetrate and react with the copper. The observed increase of D band intensity is a specific evidence for carbon bond breaking. The Raman spectral patterns after this irreversible event become more similar to those of freestanding graphene. Similar effects due to residual post deposition stress, occurs in the deposited samples after CVD process, generating the many dark regions observed in this work, without strong laser irradiation. Based on our hypothesis we can expect also to find sometimes-such “detached spots”, giving good Raman signal, in CVD deposited graphene on other metals, even in the case of strong coupling metals.

6.4 Conclusions

In this chapter, the growth of graphene on copper foil has been performed following the consolidate low-pressure chemical vapour (LP-CVD) technique. The as-deposited monolayer graphene clearly exhibits two different states of coupling to the metal substrate. Furthermore, an evolution from the metal-coupled graphene configuration to the one detached from the metal can be induced by a proper amount of laser irradiation, overcoming some power threshold. Certainly, further investigation can be necessary to better investigate this phenomenon, which appears quite promising for the development of many graphene-based electronic devices. The most obvious advantage concerns the possibility to create well-defined freestanding-like graphene island on metallic substrates. Furthermore, we point out that the exposure to a suitable laser flux could allow to “write” paths of freestanding-like graphene on a coupled graphene layer modulating in this way both its optical response and the local work function. This could pave the way to a tailored manipulation of the electro-optical response over large areas such those needed for the control of the electron emission from graphene in thermionic energy converter (TIC),^[34] electro-catalytic devices,^[77] graphene-based plasmonic systems,^[78] and many others fields.

References

- [1] K.S. Novoselov, A.K. Geim, S.V. Morozov, D. Jiang, Y. Zhang, S.V. Dubonos, I.V. Grigorieva, and A.A. Firsov, *Science* 306, 666 (2004).
- [2] K.S. Novoselov, D. Jiang, F. Schedin, T.J. Booth, V.V. Khotkevich, S.V. Morozov and A.K. Geim, *Proceedings of the National Academy of Sciences of the United States of America* 102, 10451 (2005).
- [3] A. K. Geim, and K. S. Novoselov, *Nat. Mater.* 6, 183 (2007).
- [4] S. Kumar and K. Chatterjee, *ACS Appl. Mater. Interfaces* 2016, 8, 26431–26457.
- [5] J. Coraux, T.N. Plasa, C. Busse, and T. Michely, *New Journal of Physics* 10, 043033 (2008).
- [6] M. Yi and Z. Shen, *J. Mater. Chem. A*, 2015, 3, 11700.
- [7] K. Parvez, Z. S. Wu, R. Li, X.J. Liu, R. Graf, X. Feng and K. Müllen, *Journal of the American Chemical Society*, 136(16), 6083-6091.
- [8] A. Reina, H. Son, L. Jiao, B. Fan, M.S. Dresselhaus, Z. Liu, and J. Kong, *The Journal of Physical Chemistry C* 112, 17741 (2008).
- [9] X. Li, W. Cai, J. An, S. Kim, J. Nah, D. Yang, R. Piner, A. Velamakanni, I. Jung, E. Tutuc, S.K. Banerjee, L. Colombo, R.S. Ruoff, *Science* 2009, 324, 1312–1314.
- [10] P. Avouris, and C. Dimitrakopoulos, *Materials today* 15, 86 (2012).
- [11] P. W. Sutter, J.-I. Flege and E. A. Sutter, *Nature Materials* 7, 406 - 411 (2008).
- [12] S. Marchini, S. Günther, and J. Wintterlin, *Phys. Rev. B* (2007) 76, 075429.
- [13] P. Stojanov, E. Voloshina, Y. Dedkov, S. Schmitt, T. Haenke and A. Thissen, *Procedia Engineering* 93 (2014): 8-16.
- [14] E. N. Voloshina, Yu. S. Dedkov, S. Torbrügge, A. Thissen, and M. Fonin *Appl. Phys. Lett.* 100, 241606 (2012).
- [15] A. Dahal and M. Batzill, *Nanoscale*, 2014,6, 2548-2562.
- [16] J. Lahiri, T.S. Miller, A.J. Ross, L. Adamska, I.I. Oleynik and M. Batzill, *New Journal of Physics*, 13(2), 025001.
- [17] M. Gao, Y. Pan, L. Huang, H. Hu, L. Z. Zhang, H. M. Guo, S. X. Du, and H.-J. Gao, *Appl. Phys. Lett.* 98, 033101 (2011).
- [18] P. Sutter, J.T. Sadowski, E. Sutter, *Physical Review B*, 80(24), 245411 (2009).
- [19] J. Coraux, A. T. N'Diaye, M. Engler, C. Busse, D. Wall, N. Buckanie, F.-J. M. Zu Heringdorf, R. van Gastel, B. Poelsema and T. Michely, *New Journal of Physics* 11(2) (2009): 023006.
- [20] L. Gao, J. R. Guest and N. P. Guisinger, *Nano Lett.*, 2010, 10 (9), pp 3512–3516.
- [21] C. Mattevi, H. Kim and M. Chhowalla, *J. Mater. Chem.*, 2011, 21, 3324–3334.
- [22] A. K. Geim, *Science* 2009, 324, 1530.
- [23] G.B. Barin, Y. Song, I. de Fátima Gimenez, A.G. Souza Filho, L.S. Barreto and J. Kong, *Carbon* 84 (2015) 82 – 90.

- [24] X. Li, Y. Zhu, W. Cai, M. Borysiak, B. Han, D. Chen, R. D. Piner, L. Colombo and R. S. Ruoff, *Nano Lett.*, Vol. 9, No. 12, 2009.
- [25] B. Marta, C. Leordean, T. Istvan, I. Botiz and S. Astilean, *Appl. Surf. Science* 363 (2016) 613–618
- [26] H. Van Ngoc, Y. Qian, S.K Han and D.J. Kang, *Scientific reports* 6 (2016): 33096.
- [27] M. Zabeti, W.M.A. Wan Daud, M. K. Aroua, *Fuel Process. Technol.* 2009, 90, 770–777.
- [28] S. Gottardi, K. Müller, L. Bignardi, J.C. Moreno-López, T.A. Pham, O. Ivashenko, M. Yablonskikh, A. Barinov, J. Björk, P. Rudolf, M. Stöhr, *Nano Letters* 15.2 (2015): 917-922.
- [29] E. Voloshina, N. Berdunov, Y. Dedkov, *Scientific Reports* 6 (2016): 20285.
- [30] T. Wang, D. Huang, Z. Yang, S. Xu, G. He, X. Li, N. Hu, G. Yin, D. He, and L. Zhang, *Nano-Micro Letters* 8, 95 (2016).
- [31] S.S Varghese, S. Lonkar, K.K. Singh, S. Swaminathan, and A. Abdala, *Sensors and Actuators B: Chemical* 218, 160 (2015).
- [32] J. D. Roy-Mayhew, and I. A. Aksay, *Chemical reviews* 114, 6323 (2014).
- [33] X.Wang, L. Zhi, and K. Müllen, *Nano letters* 8, 323 (2008).
- [34] S. J. Liang and L. K. Ang, *Phys. Rev. Applied* 3, 014002 (2015).
- [35] S. Kumar, G.S. Duesberg, R. Pratap, and S. Raghavan, *Applied Physics Letters* 105, 103107 (2014).
- [36] L. Bignardi, *Electronic and structural properties of graphene/metal interfaces*. Groningen: s.n., 2013. 137 p.
- [37] L. Bignardi, W. F. van Dorp, S. Gottardi, O. Ivashenko, P. Dudin, A. Barinov, J. T. M. De Hosson, M. Stohr, and P. Rudolf, *Nanoscale* 5, 9057 (2013).
- [38] F. Yang, Y. Liu, W. Wu, W. Chen, L. Gao, and J. Sun, *Nanotechnology* 23, 475705 (2012).
- [39] Y. Zhou, D. S. Fox, P. Maguire, R. O’Connell, R. Masters, C. Rodenburg, H. Wu, M. Dapor, Y. Chen, and H. Zhang, *Scientific reports* 6, 21045 (2016).
- [40] H. D. Le, T. T. T. Ngo, D. Q. Le, X. N. Nguyen, and N. M. Phan, *Advances in Natural Sciences: Nanoscience and Nanotechnology* 4, 035012 (2013).
- [41] N. Srivastava, Q. Gao, M. Widom, R. M. Feenstra, S. Nie, K. McCarty, and I. Vlassiouk, *Physical Review B* 87, 245414 (2013).
- [42] E. Loginova, S. Nie, K. Thürmer, N. C. Bartelt, and K. F. McCarty, *Physical Review B* 80, 85430 (2009).
- [43] Y. Murata, E. Starodub, B. B. Kappes, C. V. Ciobanu, N. C. Bartelt, K. F. McCarty, and S. Kodambaka, *Applied Physics Letters* 97, 143114 (2010).
- [44] G. Giovannetti, P. A. Khomyakov, G. Brocks, V. M. Karpan, J. van den Brink, and P. J. Kelly, *Physical Review Letters* 101, 026803 (2008).
- [45] A. C. Ferrari, J. C. Meyer, V. Scardaci, C. Casiraghi, M. Lazzeri, F. Mauri, S. Piscanec, D. Jiang, K. S. Novoselov, S. Roth, and A. K. Geim, *Physical Review Letters* 97, 187401 (2006).

- [46] L. M. Malard, M. A. Pimenta, G. Dresselhaus, and M. S. Dresselhaus, *Physics Reports* 473, 51 (2009).
- [47] A. Guermoune, T. Chari, F. Popescu, S. S. Sabri, J. Guillemette, H. S. Skulason, T. Szkopek, and M. Sijaj, *Carbon* 49, 4204 (2011).
- [48] O. Frank, J. Vejpravova, V. Holy, L. Kavan, and M. Kalbac, *Carbon* 68, 440 (2014).
- [49] D. R. Lenski, and M. S. Fuhrer, *Journal of Applied Physics* 110, 013720 (2011).
- [50] M. Castriota, E. Cazzanelli, D. Pacilè, L. Papagno, C. O. Girit, J. C. Meyer, A. Zettl, M. Giarola and G. Mariotto, *Diamond and Related Materials* 19, 608 (2010).
- [51] A. C. Ferrari, *Solid State Communications* 143, 47-57 (2007).
- [52] X. Yin, Y. Li, F. Ke1, C. Lin, H. Zhao, L. Gan, Z. Luo, R. Zhao, T. F. Heinz, and Z. Hu, *Nano Research* 7, 1613 (2014).
- [53] J. Cermák, T. Yamada, K. Ganzerová, and B. Rezek, *Adv. Mater. Interfaces* 3, 1600166 (2016).
- [54] J. Cermák, T. Yamada, M. Ledinsky, M. Hasegawa, and B. Rezek, *J. Mater. Chem. C* 2, 8939 (2014).
- [55] T. Sander, C. T. Reindl, M. Giar, B. Eifert, M. Heinemann, C. Heiliger, and P. J. Klar, *Phys. Rev. B* 90, 045203 (2014).
- [56] P. F. Williams, and S. P. S. Porto, *Phys. Rev. B* 8, 1782 (1973).
- [57] N.R. Wilson, A.J. Marsden, M. Saghir, C.J. Bromley, R. Schaub, G. Costantini, T.W. White, C. Partridge, A. Barinov, P. Dudin, A.M. Sanchez, *Nano Research* 6 (2), 99-112 (2013).
- [58] I. Pletikosić, M. Kralj, P. Pervan, R. Brako, J. Coraux, A.T. N'diaye, C. Busse and T. Michely, *Physical Review Letters* 102(5), 2009: 056808.
- [59] Y. Dedkov and E. Voloshina 2015 *J. Phys.: Condens. Matter* 27 303002.
- [60] S. Tang, H. Wang, Y. Zhang, A. Li, H. Xie, X. Liu, L. Liu, T. Li, F. Huang, X. Xie and M. Jiang, *Sci Rep.* 2013; 3: 2666.
- [61] L. Gao, J. R. Guest and N. P. Guisinger, *Nano Lett.* 2010, 10, 3512–3516.
- [62] E. Soy, Z. Liang and M. Trenary, *J. Phys. Chem. C* 2015, 119, 24796–24803.
- [63] E. Soy, N. P. Guisinger and M. Trenary, *J. Phys. Chem. B*, Article ASAP, DOI: 10.1021/acs.jpcc.7b05064.
- [64] P. Sule a, M. Szendro, C. Hwang and L. Tapaszto, *Carbon* 77 (2014) 1082 – 1089.
- [65] P. Zeller, X. Ma and S. Günther, *New J. Phys.* 19 (2017) 013015.
- [66] A. V. Sidorenkov, S. V. Kolesnikova, and A. M. Saletsky, *Eur. Phys. J. B* (2016) 89: 220.
- [67] M. Smirman, D. Taha, A. K. Singh, Z.-F. Huang and K. R. Elder, *Physical Review b* 95, 085407 (2017).
- [68] V. N. Popov, In *Journal of Physics: Conference Series* 682, 012013 (2016).
- [69] J. S. Park, A. Reina, R. Saito, J. Kong, G. Dresselhaus, and M. S. Dresselhaus, 2009. *Carbon* 47, 1303 (2009).
- [70] A. C. Ferrari, and D. M. Basko, *Nature nanotechnology* 8, 235 (2013).

- [71] S. P. Surwade, Z. Li, and H. Liu, *Journal of Physical Chemistry C* 116, 20600 (2012).
- [72] G. Amato, G. Milano, U. Vignolo, and E. Vittone, *Nano Research* 8, 3972 (2015).
- [73] A. Allard, and L. Wirtz, *Nano Letters* 10, 4335 (2010).
- [74] O. Frank, G. Tsoukleri, J. Parthenios, K. Papagelis, I. Riaz, R. Jalil, K. S. Novoselov, and C. Galiotis, *ACS Nano* 4, 3131 (2010).
- [75] T. H. Bointon, M. D. Barnes, S. Russo, and M. F. Craciun, *Advanced Materials* 27, 4200 (2015).
- [76] 53W. Cai, R. D. Piner, Y. Zhu, X. Li, Z. Tan, H. C. Floresca, C. Yang, L. Lu, M. J. Kim, and R. S. Ruoff, *Nano Research* 2, 851 (2009).
- [77] Y. Yan, Q. Liu, X. Dong, N. Hao, S. Chen, T. You, H. Mao and K. Wang, *Microchimica Acta* 183, 1591 (2016).
- [78] L. De Sio, U. Cataldi, T. Bürgi, N. Tabiryan, and T. J. Bunning, *AIP Advances* 6, 075114 (2016).

Chapter 7

Characterization of graphene grown on copper foil by Chemical Vapor Deposition (CVD) at ambient pressure conditions

In order to get high quality graphene films, with large domains and free from impurities, minimizing also the manufacturing costs, we investigate the graphene grown on copper (Cu) foil by Chemical Vapor Deposition (CVD) at ambient pressure conditions, by using methane (CH_4) as carbon source, diluted in a suitable mixture of argon (Ar) and hydrogen (H_2). Graphene samples were synthesized varying the duration of the exposure to hydrocarbon precursor in the range from 1 minute to 1 hour. The quality of the graphene films together with their structural, morphological and electronic properties were evaluated by Micro-Raman Spectroscopy and several other techniques, including, Scanning Tunneling Microscopy (STM), Atomic Force Microscopy (AFM) and Scanning Electronic Microscopy (SEM). In particular, samples obtained with shorter growth time (less than 10 min) exhibit a non-uniform coverage of the Cu surface while those synthesized with exposure time between 10 and 30 minutes show a prevalence of well-ordered monolayer graphene domains. For longer deposition, the area covered by disordered graphene domains increases with respect to the ordered ones, as revealed by Raman analysis, showing a non-self-limiting growth behavior of CVD graphene/Cu at atmospheric conditions. In addition, we observed two kinds of monolayer graphene, in terms of coupling with the Cu surface, for the samples synthesized between 10 and 20 minutes. To the best of our knowledge, “coupled” and “decoupled” graphene regions have never been reported at the same time on copper surface. This difference, which is appreciable also by the optical microscopy inspection, could be related to the local copper oxidation and to oxygen intercalation after graphene growth. Furthermore, a Raman statistical analysis has been performed on the G and 2D bands measured in both the kinds of regions, gaining evidence of a bimodal behavior for the graphene spots, corresponding to “coupled” and “decoupled” configurations.

7.1 Introduction

Since its first isolation by mechanical exfoliation of graphite by Novoselov et al.^[1], graphene has been attracting enormous attention in the scientific community. In fact, thanks to its extraordinary and unique physical properties, such as outstanding thermal conductivity^[2], high carrier mobility^[3], optical^[4] and mechanical features^[5], graphene can be used in a wide range of applications as sensors^[6,7], solar cells^[8,9], energy storage^[10,11] and electronic devices.^[12] Obviously, graphene films required for commercial devices have to be both of high quality (i.e. free from impurities and with extended domains), and produced optimizing the manufacturing costs. Nowadays, among all the commonly synthesis techniques used, chemical vapor deposition (CVD) could be one of the most promising methods which allows a proper balance between these two objectives. Furthermore, CVD on transition metal surfaces is a well-suited method to large-scale production of graphene^[13,14]. Among all the metallic surfaces, Cu is one of the most popular catalytic substrate, due to its low carbon solubility at typical growth temperatures^[15] that, at least under low pressure and ultra-high vacuum (UHV) conditions, ensures a self-limited growth of graphene on its surface.^[16,17] On the contrary, graphene grown at atmospheric pressure is not self-limiting leading to non-homogeneous samples in which bi- and few layer islands are present.^[18] Regardless to the growth conditions, the polycrystalline structure, the surface roughness, the presence of grain boundaries and imperfections can affect the extension of the domains and the overall quality of the deposited layer on the copper substrate.^[19-22] In addition, the proper balance between the synthesis parameters, including the annealing temperature of the substrate and the sample exposure to the carbon source gas, play a leading role in the resulting quality of the graphene grown.^[23-26]

Bearing in mind these aspects, in this work, graphene films on commercial copper foil were synthesized by atmospheric-pressure chemical vapor deposition (APCVD), using CH₄ gas as carbon source diluted in a suitable mixture of argon Ar and H₂. The structural, morphological and electronic properties of graphene were studied as a function of the exposure time of the metal surface at the carbon source. As a result, a range of exposure times optimizing the quality of graphene films was determined. In addition, we investigate about the two different kinds of the observed graphene, in terms of coupling with the copper surface, for the samples synthesized between 10 and 20 minutes. These differences can be immediately discriminated by the optical microscopy analysis and further deep investigated by the micro-Raman

spectroscopy. Finally, the statistical analysis of the Raman spectra involving the G and 2D bands Raman positions, collected on both “coupled” and “decoupled” graphene, demonstrate the occurrence of the two different physical configurations.

7.2 Experimental

Film deposition

Graphene monolayer was grown on commercial Cu foil with a thickness of 25 μm and purity of 99.98% (from Matek) by catalytic CVD at atmospheric pressure condition and by using CH_4 as carbon source. The Cu surface was prepared by etching in a HNO_3 (65wt%, Sigma-Aldrich) solution for few seconds and subsequently rinsed in distilled water. Afterwards, the substrate was rinsed again in acetone and then quickly dried, before being introduced in a carbolite furnace. The Cu foil was placed in the center of a quartz tube in an Ar- H_2 mixture at room temperature for 5 minutes. Then the quartz tube was loaded in a tubular horizontal CVD reactor pre-heated at a temperature of 766°C and so, the sample was annealed at the same temperature for 20 minutes under the flow of an Ar- H_2 gas mixture of 400 sccm and 6.7 sccm, respectively. After that, the temperature was increased at the rate of 10°C/min, from 766°C up to 1000°C. At a temperature of 1000°C, after 10 minutes of annealing, the graphene growth mechanism started on Cu-foil following the addition of CH_4 (20 sccm) to the H_2 -Ar mixture. During the entire synthesis procedure the gas were supplied at constant flow rates as indicated above. Different growth durations have been tested, ranging from 1 minute to 1 hour of exposition to the CH_4 flux (for further details, see Fig. 1). After any growth time, the quartz tube was extracted by the furnace and lead to room temperature (i.e. slow cooling) by flowing Ar- H_2 gases in the quartz tube. According to the growth time, samples were labeled as reported in table 1.

Label	G1	G2	G3	G4	G5	G6	G7	G8
Growth time (min)	1	2.5	5	10	15	20	30	60

Table 1. Labeling of the probed samples.

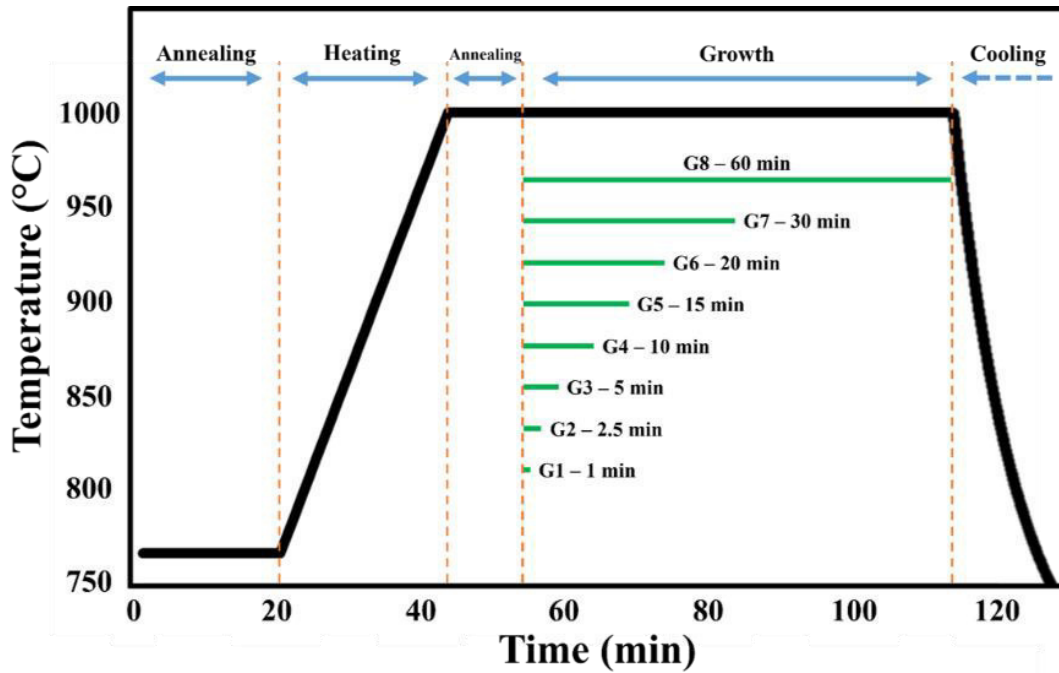


Figure 1. Temperature-time diagram summarizing the different steps of the graphene growth conditions. The argon and hydrogen flows are fixed for all the steps at 400 sccm and 6.7 sccm, respectively, while the CH_4 carbon source during the growth step is 20 sccm.

Characterization

Micro-Raman spectra were collected using a Horiba-Jobin Yvon microprobe apparatus (spectral resolution $\sim 2 \text{ cm}^{-1}$), equipped with a CCD (256x1024 pixels) detector cooled at $-134 \text{ }^\circ\text{C}$, and a Nd–Yb laser (532 nm emission) with incident power of 50 mW. A 100x Mplan Olympus objective was used (Numerical Aperture 0.90), focusing a laser spot of 2–3 μm apparent diameter. Tapping mode AFM and low current STM images of the samples were acquired under ambient condition with a Veeco Multimode AFM/STM (Bruker) with Nanoscope IIIa controller and an A-type scanner. TAP150A cantilevers (Bruker) and mechanically-cut Pt/Ir tips were used for the AFM and STM experiments, respectively. Scanning electron images were recorded using a Quanta FEG 400 (FEI) scanning electron microscope (SEM). The SEM images were acquired by using an electron beam ranging from 5 to 15 keV.

7.3 Results and discussion

In order to get a deep understanding of our system, we performed analysis using the different techniques to investigate the structural, morphological and electronic features, which are related to the different synthesis parameters of the graphene growth.

Representative SEM and AFM images of the graphene grown on Cu foil are shown in Fig. 2.

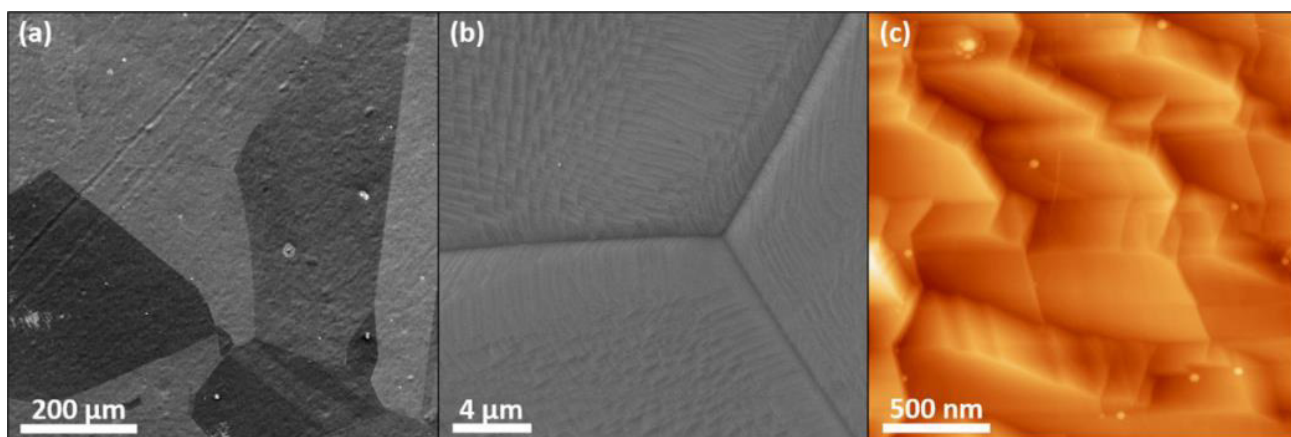


Figure 2. Typical (a) large scale and (b) small scale SEM images of graphene grown on Cu foil. (c) AFM image of graphene on Cu surface.

The heterogeneous SEM contrast at large scale, as shown in Fig. 2(a), is related to the polycrystalline nature of Cu foil due to electron channeling^[27], while at small scale the details about the Cu terraces are pointed out (see Fig. 2(b)). The microstructure of the copper surface is clearly visible in the AFM analysis, where Cu terraces, almost without impurities, are evidenced (see Fig. 2(c)). The graphene islands are not readily evident in the AFM topography images, because the surface roughness far exceeds the thickness of a graphene sheet.^[28]

The typical XRD patterns of the graphene samples, reported in Fig.A1 (see Appendix section A1), show the Cu(111) crystal face for all samples at $2\theta=43.34^\circ$. Sometimes, also the Cu(200) crystalline component, is even noticeable at $2\theta=50.44^\circ$; this is probably due to the variable heating procedure related to the graphene growth phase and confirm the polycrystalline feature of the copper foil after the annealing procedure. Furthermore, XRD extended spectra do not show any significant evidence of signals related to graphite^[29], graphene-oxide^[30] and Cu oxide^[31] structures.

Raman analysis was performed on all samples to point out the difference between the graphene grown at several deposition durations. The shapes, the intensities and positions of the typical Raman peaks of graphene, the D, G and 2D bands, gives a considerable amount of

information on the graphene domains, including the numbers of layers and the overall quality of the film.^[30,31]

The G band is due to regular first order Raman scattering from doubly degenerate phonon mode (E_{2g}) at the Brillouin zone centre, while the defect-activated D band corresponds to the breathing modes of six atoms rings and is generated from TO phonons around the Brillouin zone corner K.^[32, 34-36] The 2D band, theoretically allowed independently from the crystal disorder, is an overtone of the D band. The D peak intensity is associated to the amount of defects^[37], while the intensity ratio between the 2D and G peaks changes as a function of the number of layers of the graphene film.^[38] In particular, $I_{2D}/I_G > 2$ is typical of monolayer graphene while $1 < I_{2D}/I_G < 2$ indicates a bilayer deposition; if $I_{2D}/I_G < 1$ graphene film is made up of three or more graphene layers. Furthermore, the full width at half-maximum (FWHM) and the fitting curve of the 2D peak have to be considered to be linked at the film thickness. In fact, in the monolayer case, the 2D band is quite narrow and unimodal, and it can be fitted with a single Lorentzian component, while in the bilayer graphene a wider 2D band is found that have to be fitted by four components.^[33,37] The total absence of the D band in a Raman spectrum suggests not only a high quality graphene surface without defects, but also the mono-crystallinity of the domains, as grain boundaries between misoriented domains within a polycrystalline domain produce a detectable D peak.^[39]

In our study, the Raman features due to the stretching mode of atmospheric molecular oxygen (O_2) and nitrogen (N_2), located at 1555 cm^{-1} and 2330 cm^{-1} respectively, are detected in all spectra. As a consequence, these bands provide surely a good internal standard frequency for the collected spectra, allowing a precise measurement of the position of the other bands. In addition, they constitute a reasonable standard for the intensity of the graphene peaks, too, because in the same focusing conditions their intensity appears to be quite similar in all the spectra, independently on the probed graphene samples.

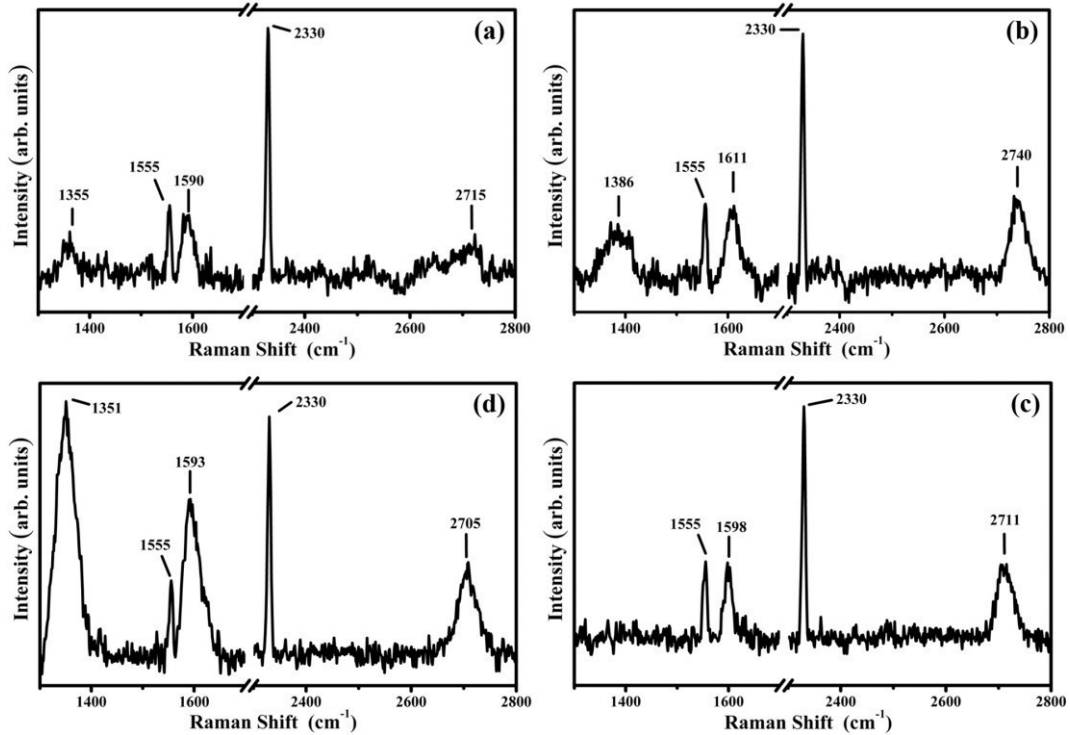


Figure 3. Representative Raman spectra of graphene films grown as a function of deposition times: (a) 2.5 min; (b) 5 min; (c) 30 min; (d) 60 min. Spectra were collected in the same experimental conditions.

Raman spectra acquired on the G1 (1 min) and G2 (2.5 min) samples show similar features and a representative spectrum is reported in Fig.3(a). Here, the main Raman features of graphene are detected, though they appear broad and relatively not intense. In particular, the D, G and 2D bands, are detectable at about 1355 cm^{-1} , 1590 cm^{-1} and 2715 cm^{-1} , respectively. As a result of the Raman analysis, the overall quality of the graphene film at 1min and 2.5 min deposition times is quite low. In this case, the signal is compatible with the presence of small graphene domains on the polycrystalline copper surface. In fact, the weak signal to noise ratio suggests that the surface is not completely covered by a uniform graphene film, while the presence of the D band point out that the small graphene domains are disordered and/or form a connected structure with an extended edge. The weak Raman signal can also be related to the coupling between graphene and Cu surface. In fact, a strong substrate-graphene coupling leads to the anti-resonance effect, which results in a weak Raman signal. A borderline case is represented by graphene growth on Nickel where no Raman signal is detected.^[40]

The evident blue shift of both G ($\sim 10\text{ cm}^{-1}$) and 2D ($\sim 15\text{ cm}^{-1}$) bands can be related in principle to several factors, including hole doping^[37,41,42] and compressive strain.^[43]

The Raman spectrum shown in Fig. 3(b) is representative of a wide set of measurements, showing a variability on the 2D band in the range $2735\text{--}2747\text{ cm}^{-1}$, while the G band is found

between 1610 and 1616 cm^{-1} . For increasing growth time, the overall quality of graphene improves. Fig. 3(b) shows the characteristic Raman spectrum of the sample synthesized at 5 min (i.e. G3 sample). The D band is still detected, but the 2D band increases its height and becomes narrower. The relatively low signal to noise ratio could be still related to a high graphene/Cu interaction. In this case, our interpretation of the results is that graphene domains became larger albeit some disorder is still present as pointed out by the presence of D band. Also in these cases, a blue shift of the G and 2D bands is present. In between the two cited mechanisms as cause of this shift, the presence of a compressive strain is compatible with a strong graphene/Cu interaction.

A better quality of graphene films is gained for the samples synthesized at increasing growth time, in particular for those ranging from 10 to 30 minutes (G4-G5-G6-G7 samples). Fig.3(c) shows a representative spectrum collected for G7 sample (i.e. 30 min. of exposure). The absence of the D band point out the lack of disorder of the graphene domains, which can be also assumed as monocrystalline^[40], at least on the typical micrometric scale of the laser spot used in the Raman analysis. Furthermore, the narrow lineshapes as well as the intensity ratio between the 2D and G bands indicate a well-coupled graphene monolayer, in which the compressive strain is still present as evidenced by the blue-shift of both bands.

Finally, graphene quality get worse by a further increase of the growth time. In particular, the sample synthesized at 60 min shows that the graphene growth process is not self-limiting for a long exposure to carbon precursor at ambient pressure condition and the resulting graphene film appears much more disordered. As shown in Fig.3(d), the intense D band ($I_D/I_G > 1$) and the low ratio between the 2D and G Raman modes (< 1) confirm that, after a critical time, the graphene keep on growing and the presence of a few layer graphene can be assumed.

In summary, a monolayer graphene film with optimal characteristics in terms of crystalline order is obtained for a growth time between 10 and 30 minutes; for lower growth time, the graphene domains are small and disordered, while for a longer time the graphene growth continues beyond the monolayer.

The monocrystalline graphene/Cu samples, synthetized between 10 and 20 min (i.e. G4-G5-G6 samples), actually exhibit two families of Raman spectra. The first kind of graphene spectra is depicted in Fig.3c, in which the G and 2D bands are weak and blue-shifted; as already noted this is linked to a strongly coupled system. The graphene areas showing this kind of spectrum are those appearing as bright extended regions as depicted in Fig.4(a). On the other hand, a

second kind of Raman spectra is typical of the isolated darker regions in Fig.4(a). A typical example of these spectra is shown in Fig.4(b).

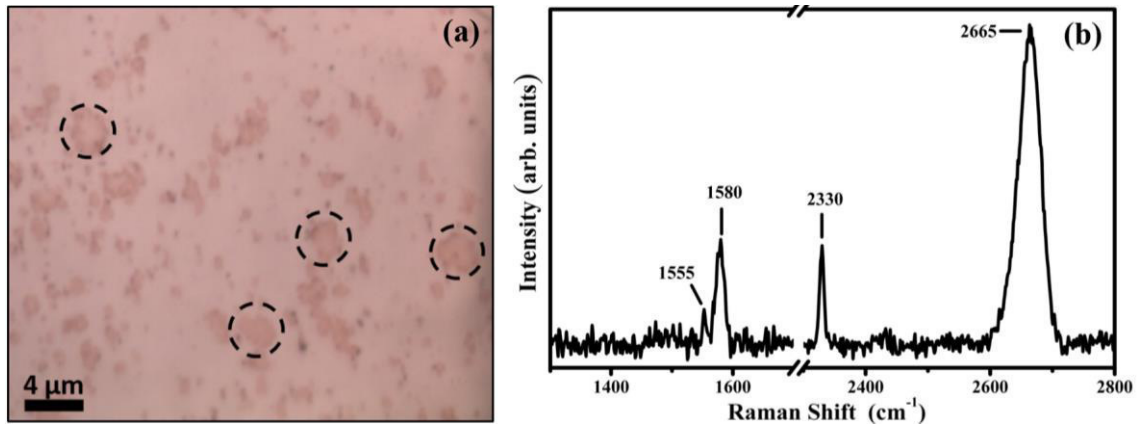


Figure 4. (a) Representative optical image of the G4-G5-G6 graphene samples (100X magnification). (b) Typical Raman spectrum from “decoupled” graphene (see dashed circle); in this case, the spectrum belongs to G5 sample.

It exhibits all the characteristic of an ordered monolayer graphene film. Firstly, the intensity ratio between the 2D and G band is well above 2, while the D band due to the disorder or defects presence is non-detectable. Furthermore, the 2D Raman feature is unimodal, as reported in Fig.A2 (see Appendix section A2). In addition, the peak positions of the G (~ 1580 cm^{-1}) and 2D (~ 2670 cm^{-1}) bands show values quite similar to those of exfoliated graphene on Si/SiO₂.^[21,22] This last evidence suggests that the graphene of these dark regions is weakly coupled to the substrate, with the same characteristic of the free-standing one. Moreover, the signal to noise ratio is higher with respect to the graphene grown on the brighter regions, where the coupling to the metal substrate appear stronger. In fact, the intensity comparison between the G and 2D bands with the stretching modes of air molecules N₂ and O₂ (see and compare Fig. 3(b)-(c) and Fig.4(b)) shows it clearly.

The G and 2D bands of “coupled” and “decoupled” regions show remarkable differences also after a quantitative analysis about the peak position of the two graphene bands of the G4, G5 and G6 samples. The histograms for both G and 2D bands positions are shown in Fig.5 where it is evident that the distributions of the Raman frequencies are bimodal. This result confirms the occurrence of two physically different kind of graphene regions, even taking into account the influence of some factor, like varying mechanical stress, responsible for data dispersion.

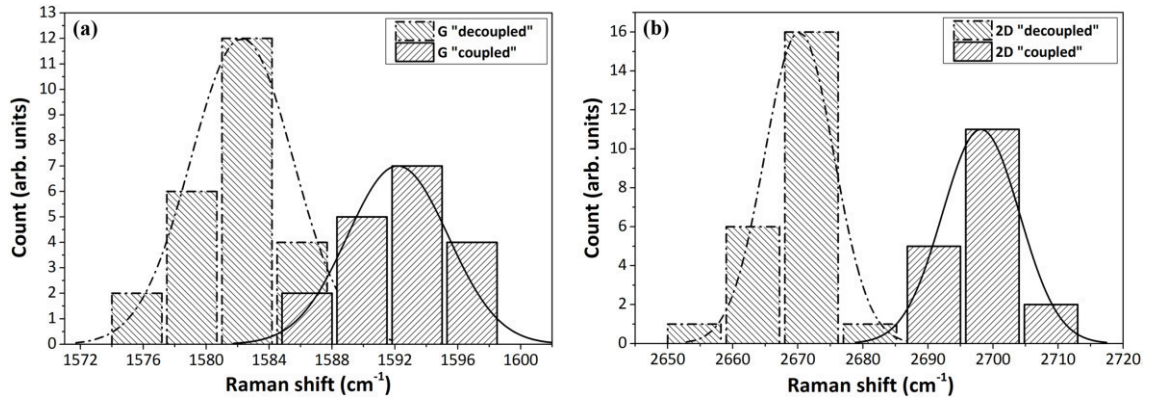


Figure 5. Histograms of the peak positions for (a) G band and (b) 2D band, collected both in the “decoupled” (i.e. the optical brown spots) and in “coupled” (i.e. the bright zones) graphene, for the G4-G5-G6 samples. All curves superimposed on the histograms are normal (Gaussian) distributions. Separation between the “decoupled” and “coupled” graphene is about 12 cm^{-1} and 28 cm^{-1} for G and 2D bands, respectively.

A further data analysis performed on the same set of samples confirms such hypothesis. By plotting the G vs 2D peaks frequencies, two well distinct set of data are obtained, each one with a fairly good linear correlation (see Fig.6). In this way, we can discriminate the spectrum on the basis of the G-2D correlation, which reveals a clear discontinuity between the spectral characteristic of the optical dark spots (i.e. spectra of “decoupled” graphene) and those of the bright zones (i.e. metal-“coupled” graphene).

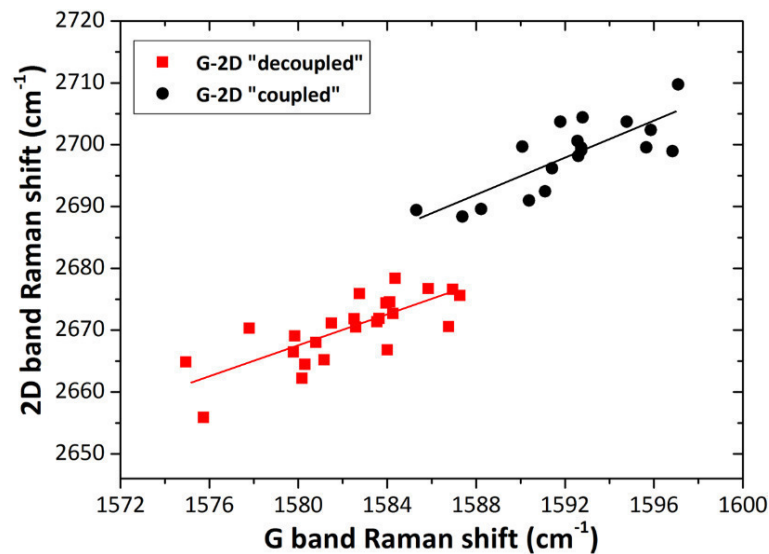


Figure 6. Linear correlation between the G and 2D modes of graphene domains acquired on the “decoupled” (red squares) and “coupled” (black circles) regions (i.e. the optical brown and bright regions, respectively). The equations of the two linear fits are: $y_{2D}=1.24x_G+706.16$ (red line) and $y_{2D}=1.47x_G+358.50$ (black line).

To the best of our knowledge, islands of “decoupled” regions on a “coupled” monolayer graphene have never been observed before on a copper surface at the same time. These two different graphene films can be evidenced firstly by optical microscopy investigation, and confirmed by the Raman analysis.

A further in-depth investigation on the nanometer scale carried out by STM corroborates the previously reported Raman results. Indeed, a wide microscopic analysis performed over the monocrystalline graphene/Cu samples (G4-G5-G6 samples), allows identifying the two different kind of graphene. In the “coupled” graphene areas (see Fig.7(a)-(b)), a Moiré superstructure superimposed on the atomically-resolved graphene is observed, due to the mismatching between the graphene and the copper surface. As a consequence, it provides a good evidence of the coupling between the two lattices. On the contrary, the absence of Moiré superstructure (see Fig.7(c)-(d)) in the “decoupled” graphene regions is compatible with a “free-standing-like” graphene.

Therefore, STM investigation confirms the presence of both “coupled” and “decoupled” graphene on the copper foil substrate. Usually, graphene grown by CVD on metal surfaces can be decoupled in presence of both oxidized surfaces and oxygen intercalation, as reported by Gottardi et al.^[44] and Voloshina et al.^[45], respectively. In addition, the oxidation of polycrystalline copper due to the oxygen encapsulated by the graphene layer during the graphene growth could play a leading role in the graphene decoupling. In fact, as reported by a recent work of Alvarez-Fraga et al.^[46], the initial amount of oxygen present below the Cu surface at the grain boundaries can survive to the annealing procedure. Later, it could slowly migrate toward the surface, generating a partial re-oxidation of the copper surface below the graphene layer.

In our study, though the presence of Cu oxides grains can be excluded considering the XRD data (see Fig.A1, Appendix section A1), a lasting local oxidation of copper surface and the oxygen migration after the graphene growth from the grain boundaries could play a leading role in the formation of islands of “decoupled” graphene.

Finally, a third mechanism could be the atmospheric O₂ intercalation below the graphene layer after the sample preparation.

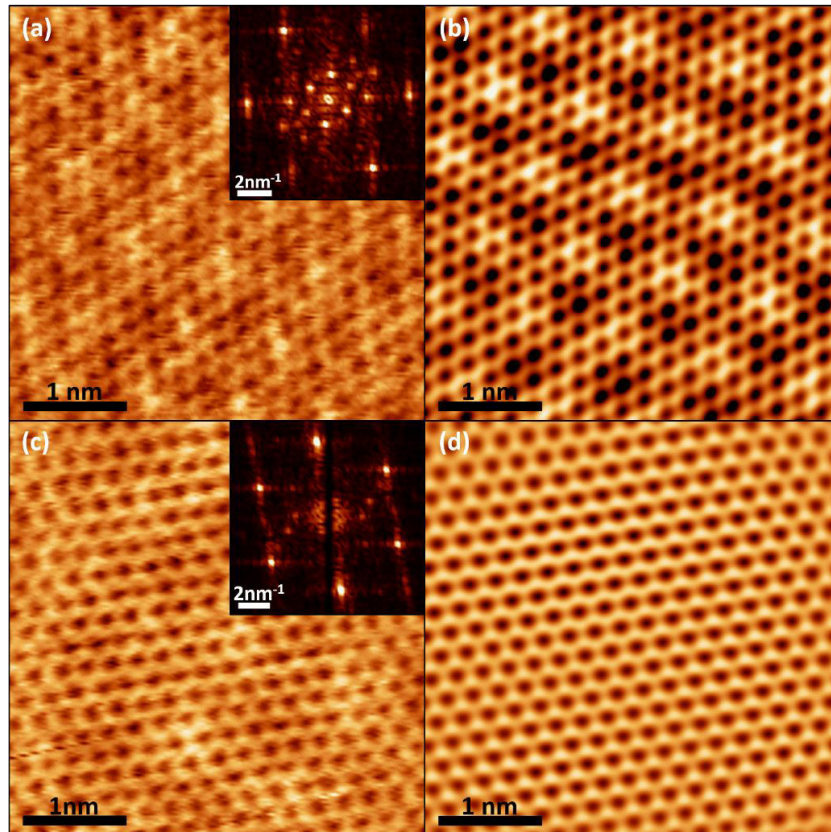


Figure 7. (a) $4 \times 4 \text{ nm}^2$ STM acquisition (drift corrected image) shows Moiré pattern superimposed on the atomic resolution of graphene. Tunneling parameters: $U_t = -0.03 \text{ V}$; $I_t = 0.80 \text{ nA}$. Inset: FFT analysis of the STM image. (b) graphene lattice reconstructed from the FFT analysis exhibits clearly the Moiré superstructure. (c) $4 \times 4 \text{ nm}^2$ STM drift-corrected image shows atomic resolution of graphene. Tunneling parameters: $U_t = -0.03 \text{ V}$; $I_t = 0.85 \text{ nA}$. Inset: FFT analysis of the STM image. (d) reconstruction of graphene lattice from FFT analysis.

7.4 Conclusions

In this chapter, we investigated the graphene grown on copper foil by chemical vapor deposition (CVD) at atmospheric pressure. By changing only the exposure times to the carbon precursor, we identified the optimal conditions to obtain well-ordered monolayer graphene films, corresponding to deposition times ranging from 10 to 30 minutes. We find two separated areas on the monolayer graphene differentiated by the optical, Raman and STM response. The results of those techniques lead us to assign the observed contrast, in terms of graphene/Cu coupling. To the best of our knowledge, for the first time “decoupled” graphene islands on a “coupled” monolayer were found, coexisting on the Cu surface. The “decoupled” islands could be linked to the presence of Cu oxide surface areas remaining after the annealing procedure or due to oxygen migration/intercalation between the graphene layer and the metal substrate. In addition, the Raman statistical analysis performed on the “coupled” and

“decoupled” graphene islands allows to unequivocally discriminate the two regions on the basis of the linear correlation between the G and 2D peak positions. Finally, a wide STM statistical analysis corroborates the previous finding.

References

- [1] K. S. Novoselov, A. K. Geim, S. V. Morozov, D. Jiang, Y. Zhang, S. V. Dubonos, I. V. Grigorieva, A. A. Firsov, *Science* 306.5696 (2004): 666-669.
- [2] E. Pop, V. Varshney, A. K. Roy, *MRS bulletin* 37.12 (2012): 1273-1281.
- [3] K.I. Bolotin, K.J. Sikes, Z.Jiang, M.Klima, G.Fudenberg, J.Hone, P.Kim, H.L.Stormer, *Solid State Communications*, 146 (2008) 351-355.
- [4] R. R. Nair, P. Blake, A. N. Grigorenko, K. S. Novoselov, T. J. Booth, T. Stauber, N. M. R. Peres, A. K. Geim, *Science* 320.5881 (2008): 1308-1308.
- [5] C. Lee, X. Wei, J.W. Kysar, J. Hone, *Science* 321.5887 (2008): 385-388.
- [6] Q. He, S. Wu, Z. Yin, H. Zhang, *Chem. Sci.*, 2012, 3, 1764-1772.
- [7] W. Yuan, G. Shi, *J. Mater. Chem. A*, 2013, 1, 10078-10091.
- [8] L. Kavan, J.H. Yum, M. Graetzel, *Physica Status Solidi (b)* 250.12 (2013): 2643-2648.
- [9] X. Li, H. Zhu, K. Wang, A. Cao, J. Wei, C. Li, Y. Jia, Z. Li, X. Li, D. Wu, *Advanced Materials*, 22 (2010) 2743-2748.
- [10] N. Mahmood, C. Zhang, H. Yin, Y. Hou *J. Mater. Chem. A*, 2014, 2, 15-32.
- [11] Z.-S. Wu, K. Parvez, X. Feng, K. Müllenb, *Nature communications* 4 (2013).
- [12] K. S. Novoselov, V. I. Fal'ko, L. Colombo, P. R. Gellert, M. G. Schwab, K. Kim, *Nature* 490.7419 (2012): 192-200.
- [13] S. Bae, H. Kim, Y. Lee, X. Xu, J.-S. Park, Y. Zheng, J. Balakrishnan, T. Lei, H. R. Kim, Y. Il Song, Y.-J. Kim, K.S. Kim, B. Özyilmaz, J.-H. Ahn, B. H. Hong, S. Iijima, *Nature nanotechnology* 5.8 (2010): 574-578.
- [14] C. Mattevi, H. Kim, M. Chhowalla, *J. Mater. Chem.*, 2011, 21, 3324-3334.
- [15] X. Li, W. Cai, J. An, S. Kim, J. Nah, D. Yang, R. Piner, A. Velamakanni, I. Jung, E. Tutuc, S.K. Banerjee, L. Colombo, R.S. Ruoff, *Science* 2009, 324, 1312-1314.
- [16] P. Zhao, A. Kumamoto, S. Kim, X. Chen, B. Hou, S. Chiashi, E. Einarsson, Y. Ikuhara, S. Maruyama, *The Journal of Physical Chemistry C* 117.20 (2013): 10755-10763;
- [17] N.S. Mueller, A.J. Morfa, D. Abou-Ras, V. Oddone, T. Ciuk, M. Giersig, *Carbon* 78 (2014): 347-355
- [18] M. P. Lavin-Lopez, J. L. Valverde, M. C. Cuevas, A. Garrido, L. Sanchez-Silva, P. Martinez, A. Romero-Izquierdo, *Phys. Chem. Chem. Phys.*, 2014, 16, 2962-2970.
- [19] J. D. Wood, S. W. Schmucker, A. S. Lyons, E. Pop, J. W. Lyding, *Nano letters* 11.11 (2011): 4547-4554.
- [20] A. T. Murdock, A. Koos, T. B. Britton, L. Houben, T. Batten, T. Zhang, A. J. Wilkinson, R. E. Dunin-Borkowski, C. E. Lekka, N. Grobert, *Acs Nano* 7.2 (2013): 1351-1359.
- [21] G. H. Han, F. Güneş, J. J. Bae, E. S. Kim, S. J. Chae, H.-J. Shin, J.-Y. Choi, D. Pribat, Y. H. Lee, *Nano letters* 11.10 (2011): 4144-4148.

- [22] Z. Luo, Y. Lu, D. W. Singer, M. E. Berck, L. A. Somers, B. R. Goldsmith, A. T. C. Johnson, *Chemistry of Materials* 23.6 (2011): 1441-1447.
- [23] L. Liu, H. Zhou, R. Cheng, Y. Chen, Y.-C. Lin, Y. Qu, J. Bai, I. A. Ivanov, G. Liu, Y. Huang, X. Duan, *J. Mater. Chem.*, 2012, 22, 1498-1503.
- [24] W. Wu, Q. Yu, P. Peng, Z. Liu, J. Bao, S.S. Pei, *Nanotechnology-Bristol* 23.3 (2012): 035603.
- [25] Y. Yao, Z. Li, Z. Lin, K.S. Moon, J. Agar, C. Wong, *The Journal of Physical Chemistry C* 115.13 (2011): 5232-5238.
- [26] M. Regmi, M.F. Chisholm, G. Eres, *Carbon* 50.1 (2012): 134-141.
- [27] N. Reckinger, X. Tang, F. Joucken, L. Lajaunie, R. Arenal, E. Dubois, B. Hackens, L. Henrard, J.F. Colomer, *Nanoscale* 8.44 (2016): 18751-18759.
- [28] N.R. Wilson, A.J. Marsden, M. Saghir, C.J. Bromley, R. Schaub, G. Costantini, T.W. White, C. Partridge, A. Barinov, P. Dudin, A.M. Sanchez, *Nano Research* 6 (2), 99-112 (2013).
- [29] K. Zhang, Y. Zhang, S. Wang, *Scientific reports* 3 (2013): 3448.
- [30] D.C. Marcano, D.V. Kosynkin, J.M. Berlin, A. Sinitskii, Z. Sun, A. Slesarev, L.B. Alemany, W. Lu, J.M. Tour, *ACS nano* 4.8 (2010): 4806-4814.
- [31] B. Zhao, P. Liu, H. Zhuang, Z. Jiao, T. Fang, W. Xu, B. Lu, Y. Jiang, *J. Mater. Chem. A*, 2013, 1, 367-373.
- [32] A.C. Ferrari, D.M. Basko, *Nature nanotechnology* 8.4 (2013): 235-246.
- [33] A. C. Ferrari, J. C. Meyer, V. Scardaci, C. Casiraghi, M. Lazzeri, F. Mauri, S. Piscanec, D. Jiang, K. S. Novoselov, S. Roth, A. K. Geim, *Phys. Rev. letters* 97.18 (2006): 187401.
- [34] F. Tuinstra, J. Lo Koenig, *The Journal of Chemical Physics* 53.3 (1970): 1126-1130.
- [35] A.C. Ferrari, J. Robertson, *Phys. Rev. B* 61, 14095–14107 (2000).
- [36] C. Thomsen, S. Reich, *Phys. Rev. Lett.* 85, 5214–5217 (2000).
- [37] A.C. Ferrari, *A. C. Solid State Commun.* 2007, 143, 47-57.
- [38] A. Reina, X. Jia, J. Ho, D. Nezich, H. Son, V. Bulovic, M. S. Dresselhaus, J. Kong, *Nano letters* 9.8 (2009): 3087-308.
- [39] Q. Yu, L.A. Jauregui, W. Wu, R. Colby, J. Tian, Z. Su, H. Cao, Z. Liu, D. Pandey, D. Wei, T.F. Chung, *Nat. Mater.* 2011, 10, 443-449.
- [40] A. Allard, L. Wirtz, *Nano Letters* 10, 4335 (2010).
- [41] W.X. Wang, S.H. Liang, T. Yu, D.H. Li, Y.B. Li, X.F. Han, *Journal of Applied Physics* 109, 07C501 (2011).
- [42] A. Das, S. Pisana, B. Chakraborty, S. Piscanec, S.K. Saha, U.V. Waghmare, K.S. Novoselov, H.R. Krishnamurthy, A.K. Geim, A.C. Ferrari, A.K. Sood, *Nature Nanotechnology* 3, 210 - 215 (2008).
- [43] O. Frank, G. Tsoukleri, J. Parthenios, K. Papagelis, I. Riaz, R. Jalil, K.S. Novoselov, C. Galiotis, *ACS Nano*, 4(6), 3131-3138.

[44] S. Gottardi, K. Müller, L. Bignardi, J.C. Moreno-López, T.A. Pham, O. Ivashenko, M. Yablonskikh, A. Barinov, J. Björk, P. Rudolf, M. Stöhr, *Nano Letters* 15.2 (2015): 917-922.

[45] E. Voloshina, N. Berdunov, Y. Dedkov, *Scientific Reports* 6 (2016): 20285.

[46] L. Álvarez-Fraga, J. Rubio-Zuazo, F. Jiménez-Villacorta, E. Climent-Pascual, R. Ramírez-Jiménez, C. Prieto, A. de Andrés, *Chemistry of Materials* 29.7 (2017): 3257-3264.

7.5 Appendix section

A1. XRD analysis

The XRD data were collected on a Philips PW 1830 diffractometer using a Cu-K α filtered radiation. All measurement, acquired in reflection mode, were performed at room temperature and the patterns were recorded in 2-theta (2θ) range from 5° to 70°, in steps of 0.02° and counting time 3s per step.

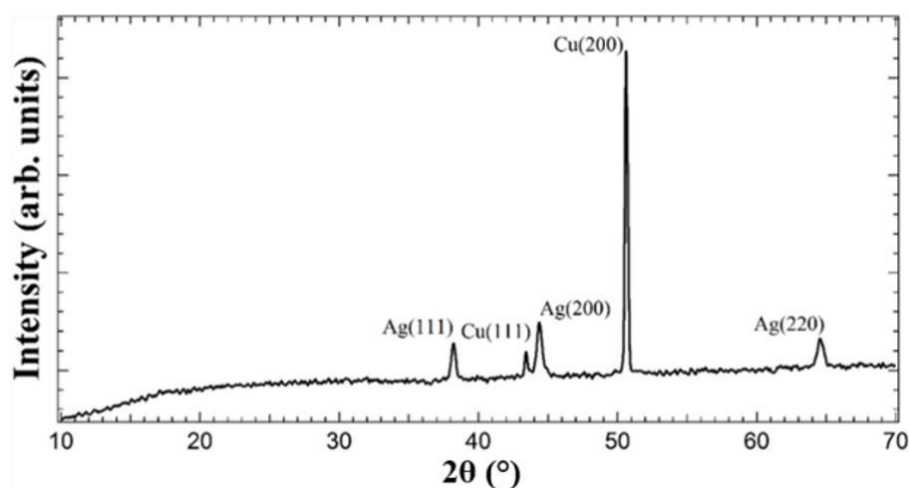


Figure A1. Representative wide XRD spectrum of graphene/Cu sample. All peaks were indexed using the JCPDS database.^[A1]

The typical XRD pattern of a graphene/Cu sample is reported in Fig. A1. The diffraction peaks analysis reveals the presence of the Cu(111) crystal face for all samples at $2\theta=43.34^\circ$ while the Cu(200) peak is present at $2\theta=50.44^\circ$. The other three diffraction structures at $2\theta=38.02^\circ$, $2\theta=44.2^\circ$ and $2\theta=64.4^\circ$ can be indexed to Ag(111), Ag(200) and Ag(220), respectively. These peaks are due to the silver conductive paste present in the electrical contact glue between the specimen and the sample holder used for the STM analysis.

XRD extended spectrum in Fig.A1 does not show any evidence of signals related to graphite^[A2], graphene-oxide^[A3] and Cu oxide^[A4] structures.

A2. Raman analysis

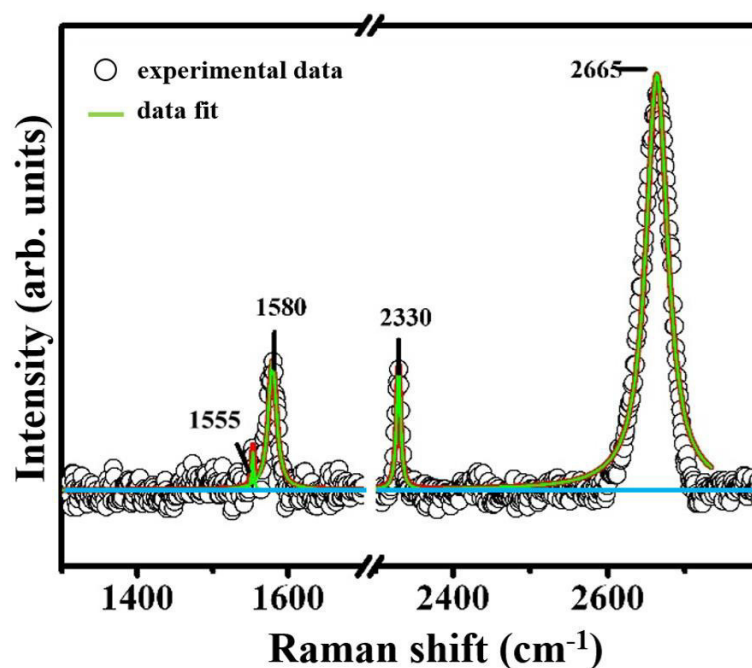


Figure A2. Fitting procedure of the Raman spectrum shown in Fig. 4(b) in the main paper, where a typical Raman spectrum belongs to an optical brown region (“decoupled” graphene) is shown. The 2D band is fitted by a single Lorentzian peak (FWHM is about 34 cm^{-1}).

References

- [A1] W. Wong-Ng, H.F. McMurdie, B. Paretzkin, C.R. Hubbard, A.L. Dragoo, J.M. Stewart, Powder Diffraction 2 (1987): 200
- [A2] K. Zhang, Y. Zhang, S. Wang, Scientific reports 3 (2013): 3448.
- [A3] D.C. Marcano, D.V. Kosynkin, J.M. Berlin, A. Sinitskii, Z. Sun, A. Slesarev, L.B. Alemany, W. Lu, J.M. Tour, ACS nano 4.8 (2010): 4806-4814.
- [A4] B. Zhao, P. Liu, H. Zhuang, Z. Jiao, T. Fang, W. Xu, B. Lu, Y. Jiang, J. Mater. Chem. A, 2013, 1, 367-373.

Part III: Metal clusters on metallic surface

Chapter 8

Nucleation and growth of Iron clusters on MgO/Ag(100)

This chapter reports the growth of iron clusters on MgO/Ag(100). Although the nucleation and growth of Fe clusters strongly depends on the surface defects of the MgO substrate, relevant information was obtained on the cluster size dependence on substrate temperature during deposition and on the nominal iron coverage. Our findings provide a first step in the investigation of this model system for catalysis studies. The first part of the chapter provides a theoretical background on the nucleation and diffusion process, while in the second section the experimental results are presented.

8.1 Introduction

In recent years, thin film growth on crystalline substrates has attracted considerable attention both in fundamental and applied research, due to the possibility to synthesize structures with novel physical and chemical properties. The nucleation of stable clusters is the preliminary step to the formation of thin atomic or molecular films. Epitaxial thin films are commonly grown from the vapor phase onto single crystal substrates under ultra-high vacuum (UHV) conditions by Molecular Beam Epitaxy (MBE).^[1] The prerequisite to the epitaxial growth is that this process occurs far from the thermodynamic equilibrium. This last condition is indeed needed to have a net film growth rate, because in a hypothetical equilibrium phenomenon, the condensation and desorption events appear with equal rates, i.e. clusters form and decay at the same rate. Far away from the equilibrium, the film growth proceeds and it is influenced by kinetics. The resulting film morphology is determined by both the degree to which growth proceeds away from the equilibrium and by all the processes typical of the system, including terrace diffusion of single adatoms, cluster formation and diffusion, as well as aggregation and interlayer diffusion.^[2] Nowadays, the knowledge gained from several studies about clusters growth and diffusion allows to obtain, at least for specific systems, clusters with a well-defined size and shape at single crystal surfaces.

8.2 Nucleation and growth

Upon deposition, the adatom is brought into the thermal equilibrium with the substrate and starts immediately to diffuse along the surface, provided that it overcomes the energy migration barrier E separating the adjacent atomic sites. The adatoms diffuse randomly on the surface through a hopping motion between neighboring adsorption sites with a jump frequency ν , which can be described by the Boltzmann term:

$$\nu = \nu_0 \exp\left(\frac{-E}{k_B T}\right) \quad (6.1)$$

where ν_0 is the attempt frequency, which is in the range of the Debye frequencies ($10^{12} - 10^{13}$ Hz), E is the diffusion energy barrier, k_B the Boltzmann constant and T the substrate temperature.

Among all the diffusion processes (see Fig. 1), including interlayer jump and diffusion along an edge, the terrace migration of single adatoms is the most fundamental, and leads to nucleation of islands on substrate terraces.^[2] Cluster densities can be determined by the tracer (or intrinsic) diffusion coefficient D , given by the Einstein relation:^[3]

$$D = D_0 \exp\left(\frac{-E}{k_B T}\right) \alpha^2, \quad D_0 = \frac{1}{4} v_0 \quad (6.2)$$

where α is the lattice constant of the crystal surface. The factor $\frac{1}{4}$ is valid only for 2D diffusion. Equation (6.2) is well-defined only assuming that the density of the diffusing particles is rather small ($<10^{-3}$ adatoms per adsorption site).

After single or multiple collisions between the nuclei, and neglecting the presence of structural and chemical defects, the diffusion process ends. In this case, i.e. homogeneous nucleation, the resulting clusters can remain stable or decay again. This depends essentially on the lateral bond (E_b) and the number of neighbours. A cluster can be considered as stable if it is large enough to grow more rapidly than it decays on the time-scale of deposition. The critical cluster size i is defined by the number of atoms in the smallest stable nucleus minus one. In other words, the attachments of one more atom turns a critical cluster into a stable one.

The 2D cluster shape is determined by the mobility of aggregating adatoms along the cluster edge (see barrier E_e in Fig. 1). For instance, low mobility leads to ramified clusters with fractal dimensions.

Moreover, the interlayer diffusion determines whether the resulting growing films are 2D or 3D. In the first case, the clusters remain 2D until they coalesce as the adatoms deposited onto the cluster top descend very fast to the substrate level before than other adatoms are deposited onto cluster top. If they cannot descend sufficiently fast, the clusters growth will be 3D.

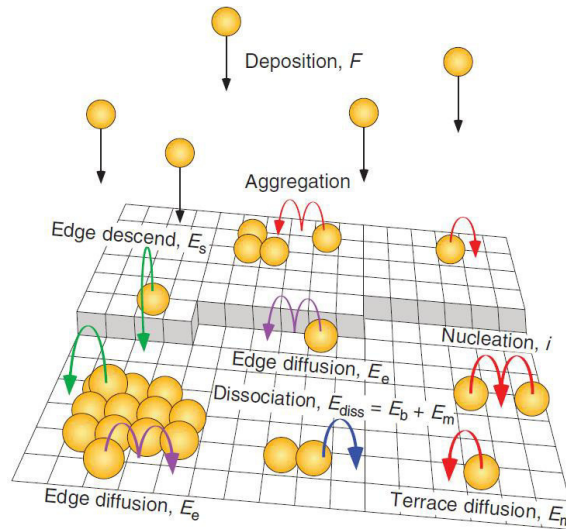


Figure 1. Schematic representation of the elementary diffusion processes of Molecular Beam Epitaxial (MBE) growth. Figure adapted from [4].

8.2.1 Clusters irreversible growth

The simplest case to consider in the irreversible growth regime is represented by the scenario in which the mobile critical cluster is a monomer ($i=1$) while the dimer is stable and immobile. In the early stage of deposition, the nuclei arrive with a rate F and diffuse with a diffusion coefficient D on the surface, until they meet another diffusing adatom to create a dimer. The diffusion process thus progressively leads to an increase of the number of dimers, until their density n_2 becomes comparable to that of monomers n_1 . At this point, a diffusing monomer on the surface has the same probability to meet a stable dimer or another mobile monomer. As a consequence, the growth of stable clusters starts to compete with the creation of new ones. In this case, the intensity of stable clusters increase until it saturates at a coverage of $\Theta=0.15\text{ML}$. At this point, all adatoms that land on the surface diffuse and reach existing islands, because at this saturation regime the mean-free path of diffusing adatoms is equal to the mean islands separation. For increasing coverage ($>0.2\text{ML}$) the 2D islands start to coalesce, becoming more extended, until at 0.55ML the monolayer film percolates.

The rate equations (6.3) and (6.4) given by the mean-field nucleation theory, in the mean-field approximation,^[5,6,7] describe the time evolution for mobile monomers and stable dimers:

$$\frac{dn_1}{dt} = F - 2\sigma_1 D n_1^2 - \sigma_x D n_1 n_x - F(Ft - n_1) - 2F n_1 \quad (6.3)$$

$$\frac{dn_x}{dt} = \sigma_1 D n_1^2 + F n_1 \quad (6.4)$$

where F and D are the deposition flux and the diffusion coefficient, respectively, n_x is the stable island density, σ_1 the capture efficiency of a monomer to merge with another monomer and σ_x the capture efficiency of a monomer to incorporate to a stable island. In equation (6.3) the flux F represents the increase of monomer density due to deposition, the second term describes the monomer decrease due to the formation of stable dimers, the third one describes the decrease occurring when a monomer is captured by a stable island while the last two terms indicate the monomer decrease caused by direct impingement onto stable islands. Equation (6.4) includes the growth rate of stable islands formed both by the binding of two monomers to form a dimer (first term) and the direct deposition onto an adatom (second term). In this last equation, coalescence phenomenon is neglected.

The rate equation (6.4) can be generalized for any cluster size. As reported by mean-field nucleation theory, the saturation island density n_x depends on diffusion D and deposition rate F and to the cluster binding energy, as reported by the following relation

$$n_x = \eta(\theta, i) \left(\frac{D}{F}\right)^{-\chi} \exp\left(\frac{E_i}{(i+2)k_B T}\right), \quad \chi = \frac{i}{i+2} \quad (6.5)$$

which is the general equation describing the steady state regime of stable islands with density n_x .

At low temperature, where $i = 1$ and $E_1 = 0$, (6.5) reduces to

$$n_x = \eta(\theta, i) \left(\frac{D}{F}\right)^{-\frac{1}{3}} \quad (6.6)$$

with $\eta(\theta, i) = 0.25$ in the coverage range of saturation.^[7,8]

In the range of $10^5 \leq D/F \leq 10^9$, the experimental measurements are in agreement with the theoretical model. However, for $D/F < 10^5$, monomers diffuse too slowly to reach other adatoms and create clusters during the deposition. As a consequence, they can be now considered as stable nuclei ($i = 0$) in the time of deposition. Monomers continue to diffuse after deposition until they nucleate and the density n_x becomes independent of deposition temperature.^[9,10] A representative example is shown by the Arrhenius plot for the 2D Ag island density on Pt(111) (see Fig. 2)

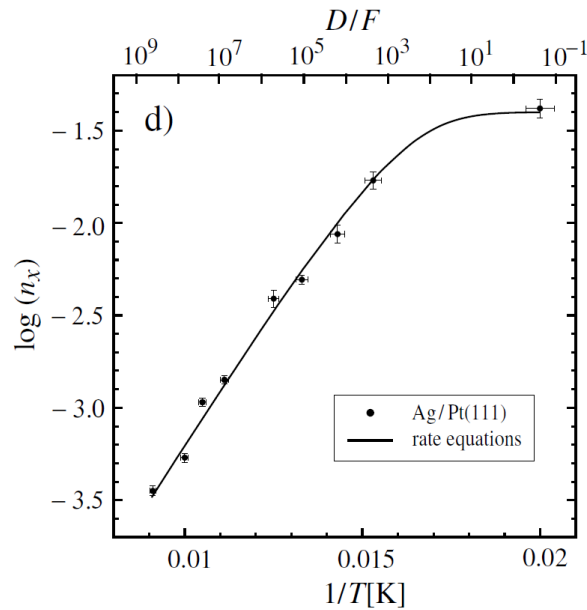


Figure 2. Arrhenius plot of the saturation island density for deposition of $\Theta = 0.12$ ML Ag onto a Pt(111) surface, in which dimers are the stable nuclei ($F = 1.1 \times 10^{-3}$ ML/s). The solid line represents the results obtained by the rate equation from mean-field nucleation theory.^[8]

8.2.2 Ostwald and Smoluchowski Ripening

Ostwald ripening phenomenon^[11,12] reports as the rapid dissociation of smaller islands occur in favour of larger ones. The preparation of small clusters on a surface at low temperatures, and the subsequent annealing allow to monitor by STM the cluster density and thus the average size as a function of annealing temperature. An example of Ostwald ripening is shown in Figure 3 for the case of Ag/Pt(111).^[13]

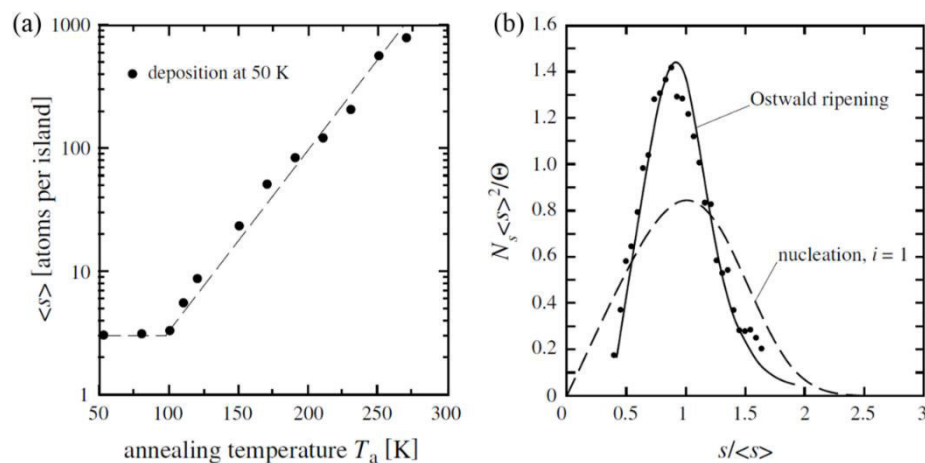


Figure 3. STM investigation of 2D Ostwald ripening for Ag/Pt(111).^[12] (a) The plateau until $T_a = 100$ K is followed by an exponential increase at higher annealing temperature due to the Ostwald ripening. (b) Scaled island size distributions for Ostwald ripening^[14] are significantly more narrow as compared to nucleation (dashed line theoretical $i = 1$ scaling curve^[15])

In Fig. 3(a), the mean island size $\langle N_i \rangle$ stays constant until it exhibits an exponential increase due to Ostwald ripening for annealing temperatures $T_a > 100$ K. Moreover, the resulting size distributions obtained for Ostwald phenomenon are narrower as compared to nucleation (see Fig. 3(b)). Therefore, island coarsening by Ostwald ripening allows preparing compact surface supported 2D clusters with narrow size distributions and average sizes $\langle N_i \rangle$ adjustable from 3 to 10^3 atoms.^[14]

A second mechanism of coarsening is the Smoluchowski ripening, concerning the diffusion and subsequent coalescence of entire islands. This last phenomenon can dominate the Ostwald ripening especially for systems with high cohesive energy and also low diffusion barriers.^[4] An example when the Smoluchowski ripening was observed is shown in Figure 4, in the case of Co metal adatoms on Pt(111).^[16]

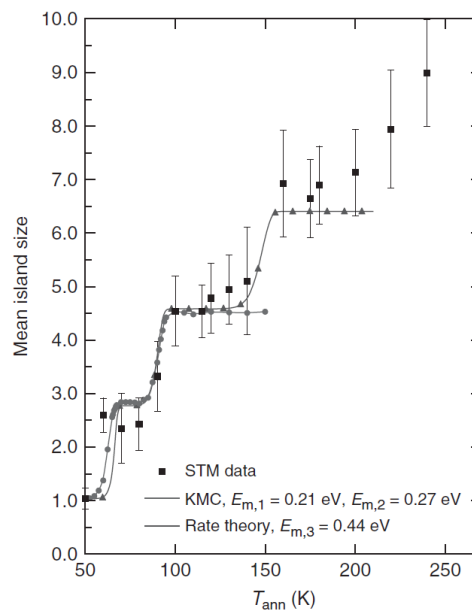


Figure 4. Mean island size in atoms as a function of annealing temperature derived from STM for Co/Pt(111) ($\Theta = 0.01$ ML, $T_a = 1$ h). The solid curves point out the KMC simulations with monomer and dimer diffusion (curve with circle) and the integration of mean-field rate equations considering in addition trimer diffusion (curve with triangles) ($v_0 = 1.5 \times 10^{15}$ Hz for all processes).^[16]

Here, every cluster size has its characteristic onset temperature of diffusion, giving rise to a stepwise increase in the mean island size as a function of annealing temperature.^[4] The height of each plateau can be understood in terms of diffusing nuclei, which at the beginning are only monomers, and then dimers that giving rise to a mixture of tetramers, pentamers and remaining trimers. Afterwards, at higher temperature, the trimers start to move and join the other islands. Upon reaching a certain cluster size, the Ostwald and Smoluchowski ripening

compete with each other. The critical size for this depends on the cohesive energy of the cluster element and on the corrugation of the interaction potential with the surface.

Clearly, both Ostwald than Smoluchowski ripening work on a substrate devoid of chemical and structural defects , i.e. in case of homogeneous nucleation. The presence of defects significantly influences the diffusion process, since these can act as nucleation sites for the adsorbates or can have a repulsive interaction with them. Particularly interesting cases of heterogeneous nucleation are represented by metal clusters diffusion on surfaces that show regularly spaced attractive defects, as Moiré pattern of CVD graphene on metals.^[17,18] Another interesting case of attractive point defect is the nucleation of metal clusters on MgO single crystal.^[19,20] Quantitative information concerning average cluster densities as a function of deposition temperature are given by a VT-AFM investigation^[21] of Pd on MgO(100). Although the cluster nucleation takes place at terraces rather than at the steps, the Arrhenius plot shown in Fig. 5 points out an heterogeneous nucleation in which defects, located at terraces, play a fundamental role.

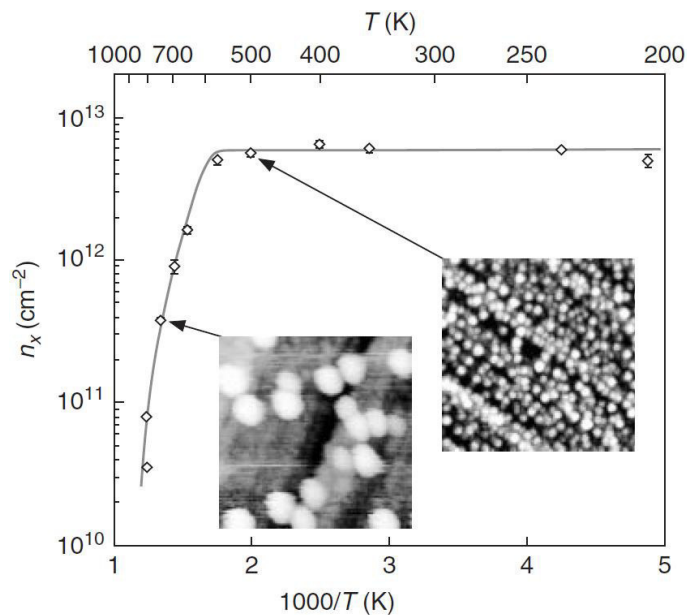


Figure 5. Arrhenius plot of saturation island densities for Pd deposits on Ar-cleaved MgO(100) obtained with noncontact AFM (size of images $100 \times 100 \text{ nm}^2$). The solid line represents a mean-field rate equation model. Figure adapted from [21].

Mean-field nucleation theory including trapping defects, i.e. the solid line in Figure 5, allows to derive the relevant parameters for this system. The minimum trapping energy $E_t=1.2\text{eV}$ can be derived by the length of the plateau, while the knee at 600 K, which is best fitted

considering a transition from $i = 1$ to $i = 3$, indicate that only 4 atoms represent a stable cluster at a trap.

8.3 Nucleation and growth of Fe clusters on MgO/Ag(100)

Supported metal clusters can play a leading role in nanoscience and nanotechnology.^[22-26] Clusters reveal indeed unique physical and chemical properties as their dimensions are reduced to nanoscale.^[27] One of the most immediate application is related to catalysis.^[28] By simply changing the cluster size, in a nanocatalysis experiment, it is possible to tune their reactivity and selectivity^[29] because intrinsic cluster properties relevant for catalytic behavior are strongly related to the cluster size. The presence of a catalytically active or inert surface, as the metal–oxide interfaces, suggests the tunability of catalytic activity via engineering of metal–oxide interfaces.^[30] As a consequence, small metal clusters on a metal/oxide interface represent an interesting system to investigate the catalytic activity as a function of the support, of the clusters size and shape, etc.

Here, the growth of iron (Fe) clusters on MgO/Ag(100) surface has been considered. As reported by Šljivančanin et al.,^[31] the presence of Fe clusters of well-defined size supported by the inert MgO surface can be employed as a model system for the N_2 - NH_3 conversion, i.e. the nitrogen fixation. In particular, as shown by their density functional theory (DFT) calculations, the catalytic properties of the Fe_7 clusters can be tuned by their passivation with N or S species, in order to improve the adsorption of nitrogen in its molecular form which results in a better ammonia synthesis.^[32] Such a realization would pave the way toward a new route for industrial nitrogen fixation with obvious economic and ecologic advantages.^[31]

8.3.1 Experimental setup

Experimental measurements were carried out in a home-built low-temperature scanning tunneling microscope (LT-STM)^[33] at 50K and in UHV condition ($pressure=1 \times 10^{-10}$ mbar). The Ag(100) surface was prepared in UHV by repeated Ar^+ ion sputtering and annealing ($T \sim 550^\circ C$) cycles. MgO was grown by evaporation of Mg from a Knudsen cell in an oxygen environment ($p_{O_2}=5 \times 10^{-7}$ mbar), while the Ag(100) substrate was kept at $T=470^\circ C$. After that, the sample was cooled down gently to room temperature with a rate of $\sim 4^\circ C/min$. The slow cooling procedure plays a non-negligible role in the quality of the resulting MgO layer^[34] in terms of formation of extended mono- and bi- layer islands. Iron (Fe) adatoms were deposited at

different nominal coverages, 0.0040 ML, 0.0085 ML and 0.0170 ML, at 50 K and 300 K (i.e. room temperature) on the MgO/Ag(100) surface. Furthermore, annealing of the samples initially deposited at R.T. were carried out at $T=580$ K. After acquisition all STM images were processed by WSxM software.^[35]

8.3.2 Results and discussion

The STM images show that the MgO grown on Ag(100) is characterized by the coexistence of two thicknesses, i.e. 1ML and 2ML. This is evident in Fig. 6(a), in which MgO darker islands are included in a more extended lighter region. The common evaluation of STM morphological images would suggest that these darker and lighter areas represent the lowest and the highest levels of MgO, i.e. the first and second layer, respectively. However, the apparent height of MgO is strongly bias-dependent^[36] and is inverted in this case, as confirmed by the field emission resonance measurements in Fig. 6(c). Here, the energy separations between the two evident peaks in the dI/dV spectra are representative for the MgO mono- and bi- layer, respectively, and are comparable with the literature data.^[37,38] Although a recent work^[39] proposed a different calibration of MgO thickness, which differs by one layer from the one used in the current literature and also in the present study, our method to study the diffusion process can be considered independent of the thickness of the single MgO terrace. Atomically resolved images acquired on the MgO monolayer in Fig. 6(b) show a square unit cell, with lattice vectors of 2.90 \AA . The agreement with the square Ag(100) unit cell ($2.89 \text{ \AA} \times 2.89 \text{ \AA}$) and the absence of Moiré superstructure suggests that the MgO(100) film forms a pseudomorphic (1x1) structure on Ag(100). Moreover, since Mg or O atoms can both be imaged by STM, an open debate in theory is currently opened in order to clarify the atomic protrusions observed by STM.^[38,40-42]

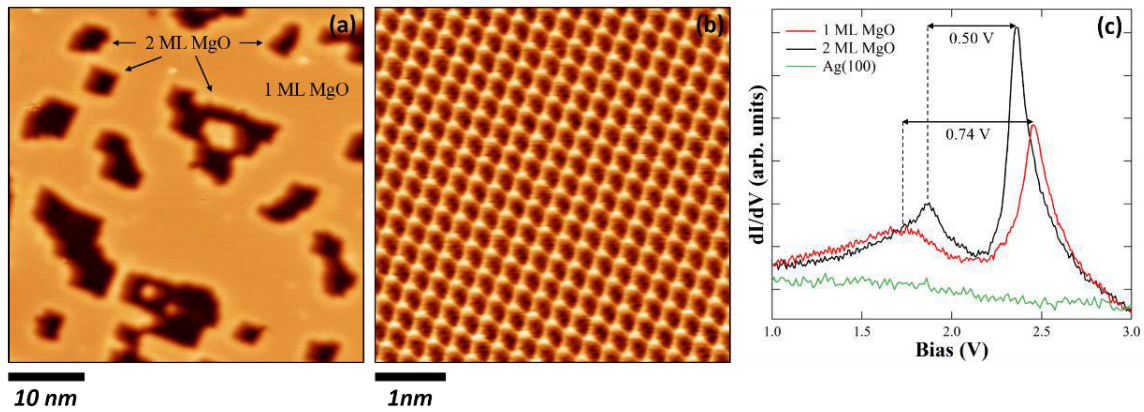


Figure 6. (a) STM image of pristine MgO grown on Ag(100) (Tunneling parameters: $U_t = -0.1V$, $I_t = 20pA$). (b) Atomic resolution of 1ML-MgO (Tunneling parameters: $U_t = -20mV$, $I_t = 6nA$). Field emission resonance spectra recorded above 1- and 2-ML MgO as well as clean Ag(100) (peak-to-peak modulation amplitude $U_{mod} = 10mV$).

Fe atoms were deposited at different coverages and substrate temperatures onto the MgO surface in order to study the diffusion processes involving the Fe atoms and clusters. At low temperatures, the migration of the Fe adatoms on MgO is very slow compared to the deposition time resulting in a high density of stable, small iron nuclei on the MgO surface. As a consequence, depositions of Fe atoms at 50 K result in iron monomers on MgO, as shown in Fig. 7 for two different coverages.

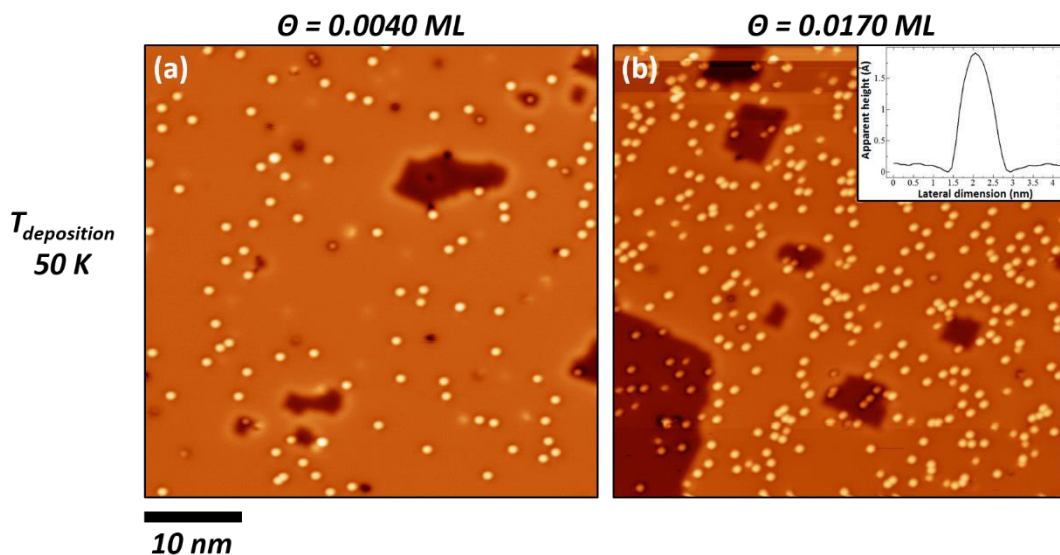


Figure 7. (a)-(b): STM images of Fe monomers on the MgO surface deposited at 50K (STM imaging at 50 K). Nominal Fe coverage: (a) 0.40%ML and (b) 1.70%ML. Tunneling parameters (both images): $U_t = -0.1V$, $I_t = 20pA$.

By increasing the substrate temperature during deposition, large iron clusters grow on MgO. Clearly, it is worth noting that the diffusion process strictly depends on the defects present at surface. In our case indeed, the presence of second layer islands of MgO on the monolayer lead to a defective surface, in which the edges at the MgO mono- and bi-layer represent particular adsorption sites. As a result, these edges act as nucleation centers in which the Fe clusters can be pinned. The essential role played by the MgO edges in the iron clusters diffusion can be qualitatively observed comparing the diffusion in flat areas and in more defective regions. As clearly shown in Fig. 8, the regions with a small number of defects exhibit a lower cluster density with respect to the other areas characterized by the presence of many MgO bi-layer islands.

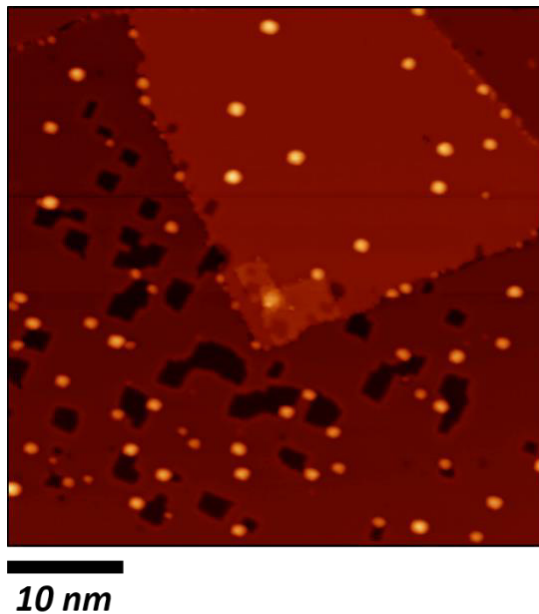


Figure 8. STM image showing the influence of the presence of defects on the cluster density. $\Theta=0.017$ ML, $T_{deposition}=300K$ and $T_{annealing}=580K$. Tunneling parameters ($U_t=-0.5V$, $I_t=20pA$).

Although the adatom diffusion is strongly influenced by the non-homogeneous MgO surface, the investigation of Fe clusters evolution allows to obtain essential information about their peculiar features, i.e. size and apparent height, as a function of coverage and deposition/annealing temperature of the surface. As mentioned above, the preliminary knowledge gained from this study is aimed to obtaining metallic clusters with well-defined sizes and shapes that could be employed in heterogeneous catalysis experiments.

Fe atoms deposited at 300 K (i.e. room temperature) lead to iron cluster formation, as shown in Figs. 9(a)-(b)-(c). Furthermore, larger clusters are obtained by growing Fe clusters at room

temperature with subsequent annealing at 580 K, as shown in Figs. 9(d)-(e)-(f). As a result, the clusters ripening clearly show that the small clusters disappear to the benefit of the formation of larger ones. However, the acquired data do not allow to determine if the mechanism is Ostwald or Smoluchowski ripening.

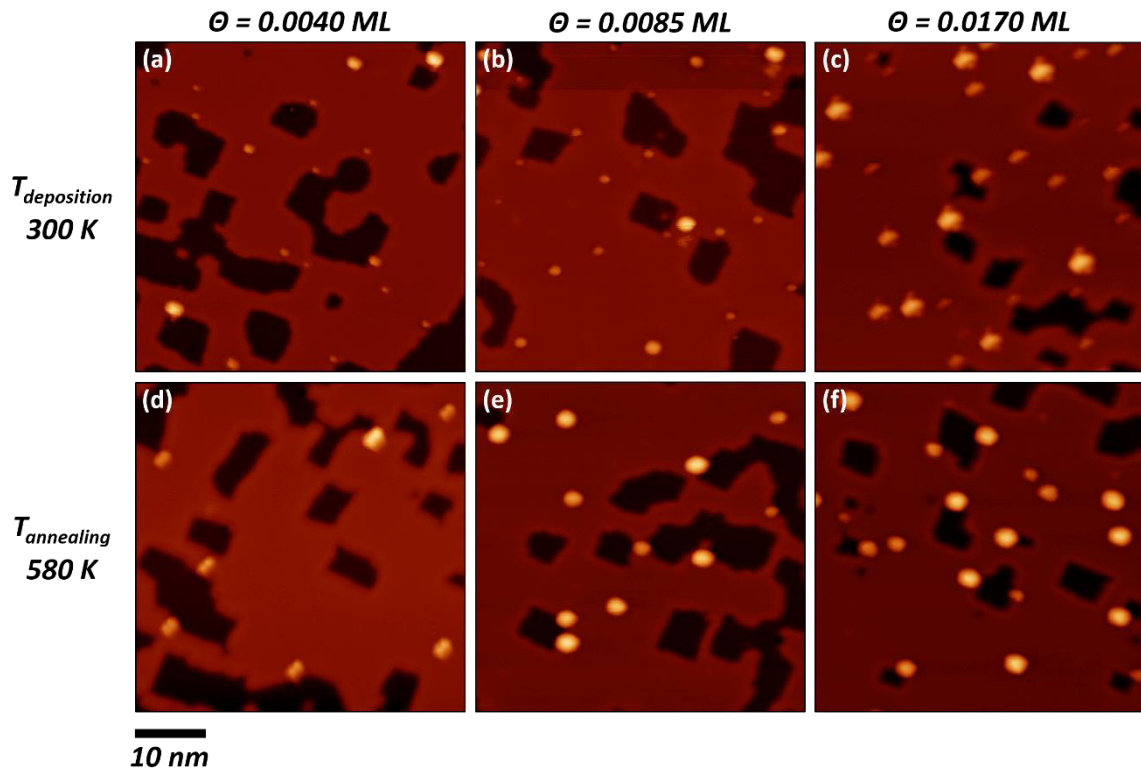


Figure 9. (a)-(c): STM images of Fe clusters grown at 300 K on MgO/Ag(100) at various coverages. (d)-(e) Evolution of the Fe clusters after annealing at $T=580$ K. Tunneling parameters: (a)-(b)-(e)-(f): $U_t=-0.5$ V, $I_t=20$ pA ; (c)-(d) $U_t=-0.1$ V, $I_t=20$ pA.

Although the presence of small defects on the flat MgO surface cannot be ruled out, it can be noted that, in all cases, part of the Fe cluster lie on the edges and part on the defect-free MgO surface. By assuming that the sticking coefficient at room temperature is comparable with that at 50 K, the average size of iron clusters can be calculated for each case. The density of Fe clusters and their average size with respect to the coverage, at 300 K and 580 K, are reported in Fig. 10.

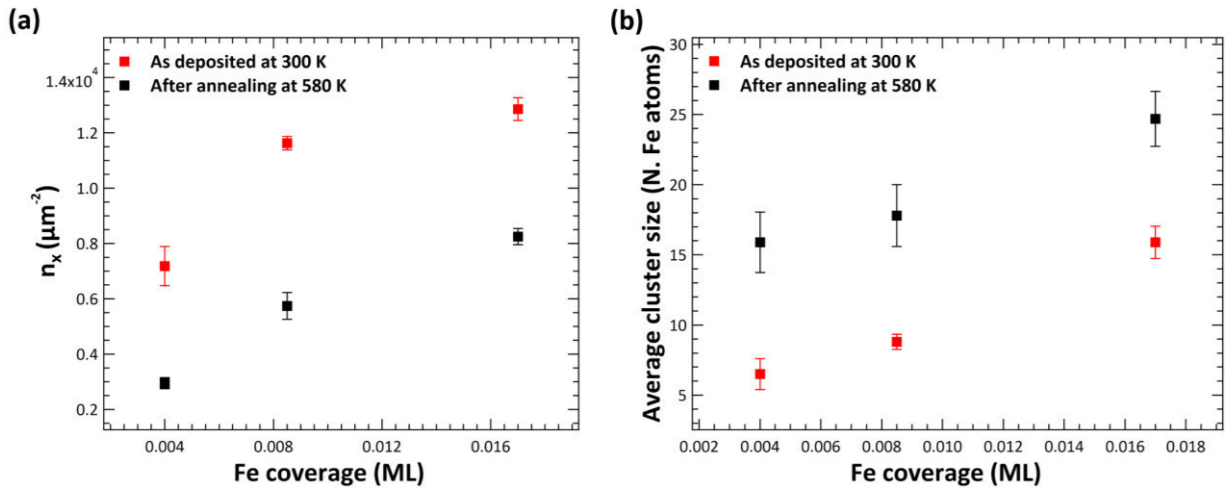


Figure 10. (a) Fe cluster density and (b) average Fe cluster size as a function of coverage.

Here, as expected, the average cluster size is coverage-dependent, i.e. it increases for increasing coverage. Moreover, for each coverage, the clusters became larger after the annealing procedure. As a consequence, the clusters size depends on the growth parameters, while the involved diffusion processes are the same, i.e. monomer/small clusters diffusion, instable nuclei and possibly diffusion of larger clusters.

As shown in Fig. 9, Fe cluster size depends on the substrate temperature and on the coverages. Although the MgO surface defects influence the clusters formation, the investigation of the apparent heights allows gaining information about the cluster size distribution after the growth at 300 K and the successive annealing at 580 K. After cluster growth at room temperature, the majority of the clusters have the lowest apparent height while their number decreases for high values (see Fig. 11 (a)-(b)-(c)). Although the distributions corresponding to the three coverages are not identical, the general trend seems to be the same, well fitted by a lognormal distribution.

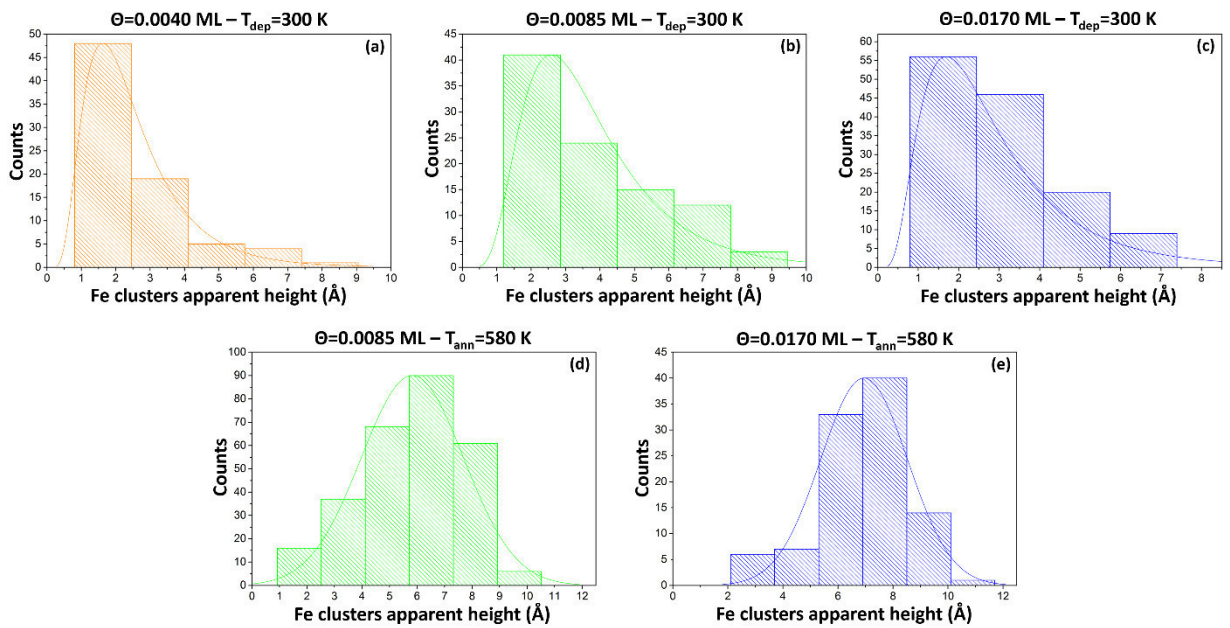


Figure 11. Apparent height distributions of Fe clusters deposited at various coverages at room temperature (a)-(b)-(c) and after annealing at 580 K (d)-(e).

On the contrary, after annealing at 580 K, the apparent height distributions deeply change. As shown in Fig. 11 (d)-(e), they appear at first glance as asymmetrical distributions. By comparing these results to the lognormal distribution reported at 300 K, it is worth noting that the lower clusters height disappear, while the distributions at 580 K show a maximum. As a first approximation, these distributions can be considered as Gaussian one (see the fit curves in Fig. 11(d)-(e)). Once again, most likely it is the presence of the surface defects that deeply influence the clusters dimensions after the annealing.

It is worth noting that the apparent height of the clusters depends on the tunneling parameters used during the acquisition (see Fig. 12), as well as on the STM tip conditions. For these reasons, the absolute value of the obtained apparent heights cannot be taken into account, while the general trend gained within a particular case is representative, assuming that tip is not modified.

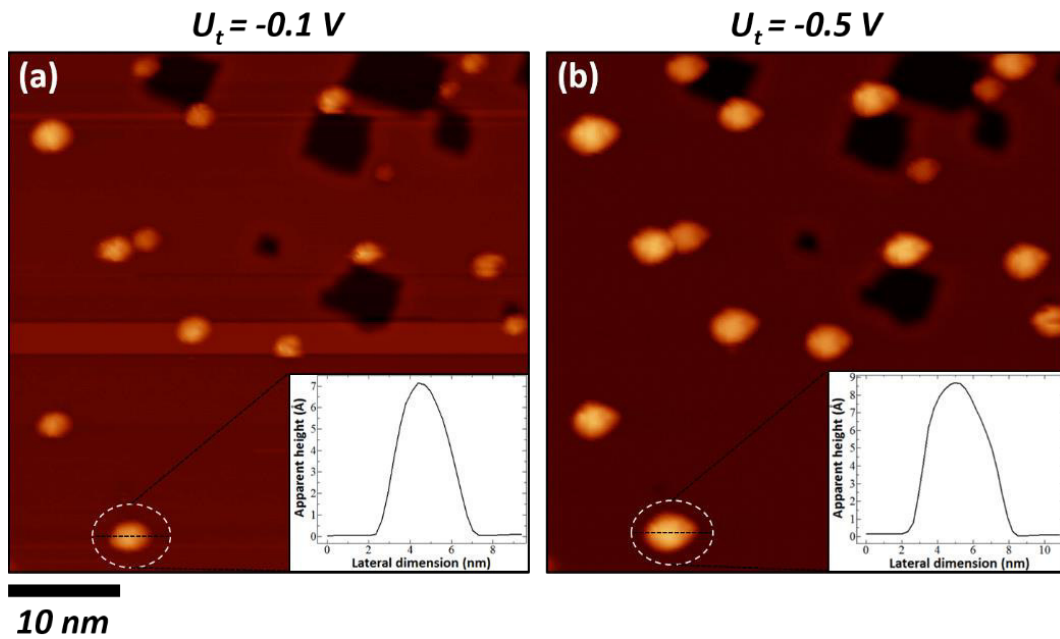


Figure 12. STM images of Fe clusters on MgO/Ag(100). (Fe coverage: 1.7% ML – $T=580$ K). (Tunneling parameters: (a) $U=-0.1$ V, $I=20$ pA; (b) $U=-0.5$ V, $I=20$ pA). The cluster apparent height depends on the bias voltage.

Although the apparent heights of the Fe clusters depend on the tunneling parameters, their average values after the annealing at 580 K suggest that the Fe clusters on the MgO surface are 3D rather than 2D.

8.3.3 Conclusions and outlooks

In this chapter, the nucleation and growth of Fe clusters on MgO/Ag(100) was investigated both as a function of coverage than substrate temperature during deposition. Although the adatom and cluster diffusion is influenced by the non-homogeneous MgO surface, which consists of MgO mono- and bi- layer coverage, the presence of these defects allow obtaining clusters with a determined average size, which can be accurately tuned by properly changing the coverage and/or the substrate temperature. The preliminary results obtained here open the way to catalysis studies on Fe clusters with well-defined size on MgO surface. However, only further studies as a function of the deposition temperature could allow to better understand the behavior of the system and to deduce the essential parameters, including the diffusion barrier for the adatoms and the ripening mechanism.

References

- [1] King, David Anthony, and D. P. Woodruff. Growth and properties of ultrathin epitaxial layers. Vol. 8. Elsevier, 1997.
- [2] Brune, Harald. "Growth of metal clusters at surfaces." *Metal Clusters at Surfaces* (2000): 67-105.
- [3] J.W. Evans, P.A. Thiel and M.C. Bartelt, *Surface Science Reports* 61(1) (2006): 1-128.
- [4] Brune, H. (2013) *Epitaxial Growth of Thin Films*, in *Surface and Interface Science*, Volume 4: Solid-Solid Interfaces and Thin Films (ed K. Wandelt), Wiley.
- [5] G. Zinsmeister, *Thin Solid Films* 2 (5), 497 (1968).
- [6] G. Zinsmeister, *Thin Solid Films* 7(1), 51 (1971).
- [7] J.A. Venables, *Philos. Mag.* 27(3), 697 (1973).
- [8] H. Brune, G.S. Bales, J. Jacobsen, C. Boragno and K. Kern, *Physical Review B* 60, 5991 (1999).
- [9] H. Brune, H. Roder, C. Boragno and K. Kern, *Physical Review Letters* 73, 1955 (1994).
- [10] B. Müller, L. Nedelmann, B. Fischer, H. Brune and K. Kern, *Physical Review B* 54, 17858 (1996).
- [11] W. Ostwald, *Zeitschrift für Physikalische Chemie* 34(1) (1900): 495-503.
- [12] L. M. Lifshitz and V. V. Slyozov, *Journal of Physics and Chemistry of Solids* 19(1-2) (1961): 35-50.
- [13] H. Brune, *Surface Science Reports* 31(4-6) (1998): 125-229.
- [14] H. Roder, E. Hahn, H. Brune, J.P. Bucher and K. Kern, *Nature* 366, 141 (1993).
- [15] J. G. Amar and F. Family, *Physical Review Letters* 74, 2066 (1995).
- [16] Buluscek, Philipp. "Submonolayer growth of cobalt on metallic and insulating surfaces studied by scanning tunneling microscopy and kinetic Monte-Carlo simulations." (2008).
- [17] F.D. Natterer, S. Rusponi, M. Papagno, C. Carbone and H. Brune, *Journal of Physics: Condensed Matter* 24.31 (2012): 314203.
- [18] A. T. N'Diaye, S. Bleikamp, P. J. Feibelman and T. Michely, *Physical Review Letters* 97, 215501 (2006).
- [19] S. Abbet, E. Riedo, H. Brune, U. Heiz, A.M. Ferrari, L. Giordano and G. Pacchioni, *Journal of the American Chemical Society* 123.25 (2001): 6172-6178.
- [20] A. Bogicevic, and D. R. Jennison, *Surface Science* 515.2 (2002): L481-L486.
- [21] G. Haas, A. Menck, H. Brune, J.V. Barth, J.A. Venables and K. Kern, *Physical Review B*, 61, 11105 (2000).
- [22] C.R. Henry, (1998) *Surface Science Reports* 31:231.
- [23] G. Schmid, M. Baumle, M. Geerkens, I. Heim, C. Osemann and T. Sawitowski *Chemical Society Reviews* 28:179 (1999).
- [24] H.J. Freund (2002) *Surface Science* 500(1) (2002): 271-299.
- [25] C.T. Campbell, *Surface Science Reports* 27(1-3) (1997): 1-111.

- [26] G. Pacchioni, "Theory of Metal Clusters on the MgO Surface: The Role of Point Defects." In *Nanocatalysis*, pp. 193-243. Springer Berlin Heidelberg, 2007.
- [27] T. Bernhardt, U. Heiz and U. Landman. "Chemical and catalytic properties of size-selected free and supported clusters." In *Nanocatalysis*, pp. 1-191. Springer Berlin Heidelberg, 2007.
- [28] R.M. Lambert and G. Pacchioni, eds. *Chemisorption and Reactivity on Supported Clusters and Thin Films: Towards an Understanding of Microscopic Processes in Catalysis*. Vol. 331. Springer Science & Business Media, 2013.
- [29] A. Kaldor, D.M. Cox and M.R. Zakin, *Advances* (2009): 211.
- [30] J.Y.Park "Current trends of surface science and catalysis", Springer New York, 2014.
- [31] Ž. Šljivančanin, H. Brune and A. Pasquarello, *Physical Review B*, 80(7), 075407, 2009.
- [32] Ž. Šljivančanin and A. Pasquarello, *Physical Review B*, 71(8), 081403, 2005.
- [33] R. Gaisch, J.K. Gimzewski, B. Reihl, R.R Schlittler, M. Tschudy and W.D. Schneider, *Ultramicroscopy* 42 (1992): 1621-1626.
- [34] J. Pal, M. Smerieri, E. Celasco, L. Savio, L. Vattuone and M. Rocca, *Physical Review Letters* 112(12) (2014): 126102.
- [35] I. Horcas, R. Fernández, J. M. Gómez-Rodríguez, J. Colchero, J. Gómez-Herrero and A. M. Baro, *Review of Scientific Instruments* 78(1) (2007): 013705.
- [36] S. Baumann, I.G. Rau, S. Loth, C.P. Lutz and A.J. Heinrich, *ACS Nano* 8(2) (2014): 1739-1744.
- [37] S. Schintke, S. Messerli, M. Pivetta, F. Patthey, L. Libioulle, M. Stengel, A. De Vita and W.D. Schneider, *Physical Review Letters* 87(27) (2001): 276801.
- [38] E. Fernandes, F. Donati, F. Patthey, S. Stavrić, Ž. Šljivančanin and H. Brune, *Physical Review B* 96, 045419 (2017).
- [39] W. Paul, K. Yang, S. Baumann, N. Romming, T. Choi, C. P. Lutz, and A. J. Heinrich, *Nature Physics* 13, no. 4 (2017): 403-407.
- [40] N. Lopez and S. Valeri, *Physical Review B* 70, 125428 (2004).
- [41] A. Malashevich, E. I. Altman, and S. Ismail-Beigi, *Physical Review B* 90, 165426 (2014).
- [42] H. Y. T. Chen and G. Pacchioni, *Physical Chemistry Chemical Physics* 16(39) (2014): 21838-21845.

9. Conclusions and outlooks

This thesis reports an extensive study of two-dimensional supramolecular networks deposited on gold crystalline surfaces and two-dimensional materials. The work aims to evidence the formation of the molecular assemblies and their related interaction with the underlying substrates. In particular, we focused the attention on different model systems that could be used as a starting point in order to develop advanced functional materials.

For deposition of ZnTPP molecules on Au(111), we found that the interaction between the molecular layer and the gold surface is noteworthy, and not so weak as one could expect from this metal-organic interface. This behavior is clearly observed by means of STM imaging and XPS investigation performed as a function of the molecular coverage from the sub- to the few layers regime. In fact, the disappearance of the gold herringbone (HB) reconstruction after the deposition of ZnTPP and the loss of their typical four-fold structure shown by STM, combined with the nonequivalence of nitrogen (N) atoms of the molecular macrocycle and the zinc (Zn) atom evidenced by XPS analysis, prove that the first molecular layer interacts considerably, i.e. through a chemical bond, with the gold surface. Conversely, the intermolecular interaction assumed is dominated by the weak van der Waals bonds. Furthermore, the molecular second layer grows epitaxially on the first one, and the relative interaction between these two layers is weak as confirmed by the molecular mobility of the partial second layer.

On the contrary, the studies performed on Nile red molecules deposited on Au(111) show a whole different picture. First, we found that the molecular packing is strictly dependent from thermal treatments. In fact, after deposition at room temperature, two distinct molecular domains were evidenced, one more dense than the other one. After a mild annealing treatment at 120°C only the more dense domain, i.e. the so-called “dense chains” packing, was found. This behavior turns out to be very interesting regarding the possibility to modify the 2D supramolecular order after molecular deposition. In other words, the polymorphic properties of this supramolecular interface can be leveraged in order to gain advanced functional devices. Moreover, the intermolecular interaction is determined by hydrogen bond, in both molecular packings. This important outcome clearly points out that the polarity of the Nile Red molecules does not play any role in the resulting molecular packing of the molecules. In other words, the Nile Red molecules induce a dipole moment on the gold surface such that the total dipole moment is zero in the normal direction respect to the surface. Finally, the

molecular mobility evidenced by means of STM analysis clearly proves that the interaction between the molecular assembly and the gold surface is considerably weak.

TMA and TPA molecular self-assemblies were also investigated on graphene substrates. These two supramolecular structures of carboxylic acids weakly interacting with the underlying surface, i.e. $\pi - \pi$ bonding, while their intermolecular interaction show network of hydrogen bonds. Although TMA and TPA self-assemblies exhibit these similarities at monolayer regime, their structural transitions with film thickness are very different. In fact, while the structure of TPA thin films varies continuously towards the 3D lattice, TMA retains its planar monolayer structure up to a critical thickness, after which a transition to a polycrystalline film occurs. These distinctive structural evolutions can be rationalized in terms of the topological differences in the 3D crystallography of the two molecules. The templated 2D structure of TPA can smoothly map to its 3D structure through continuous molecular tilting within the unit cell, whilst the 3D structure of TMA is topologically distinct from its 2D form, so that only an abrupt transition is possible.

Finally, for deposition of TCNQ molecules on the Bi_2Se_3 surface, a highly ordered two-dimensional molecular network was found at monolayer regime by STM analysis, where the intermolecular interaction is dominated by hydrogen bonds. Despite TCNQ is an electron acceptor molecule, a negligible charge transfer between the molecular layer and the substrate were experimentally found by ARPES and XPS analysis and further confirmed by DFT calculations. In other words, the molecular-substrate interaction is weak and the molecules are physisorbed on the Bi_2Se_3 .

In addition to the main topic of the work, i.e. the study of two-dimensional supramolecular networks on several substrates, the thesis also reports other research activities connected to the two-dimensional systems. In particular, the growth and characterization of graphene films on copper foil, by means of Chemical Vapor Deposition (CVD) are performed. The different coupling of graphene layer on the Cu foil and the possibility to induce a variation of the graphene coupling with respect to the Cu substrate by visible-light irradiation above a proper power threshold are evidenced. Finally, the investigation performed on the nucleation and growth of iron clusters on $\text{MgO}/\text{Ag}(100)$ allows to gain relevant information on the cluster size dependence from the substrate temperature during deposition and from the nominal iron coverage, and on the surface defects of MgO .

This work aims to become the starting point of further investigations in order to exploit the most appealing features of the described systems.

For instance, the properties and the self-assembly of organic networks, as ZnTPP or Nile Red molecules, could be investigated on a coupled/decoupled graphene surfaces. The possibility to open a controlled band gap by simply changing the molecular self-assembly^[1,2] and/or the samples preparation conditions will allow to create advanced functional interfaces that could be employed in the next years in a wide range of applications, including dye-sensitized solar cells (DSSCs), optical and biological sensors.

Moreover, a new tool for the molecular design of nanostructured films is given that the concept of topological protection of the 2D structure, as shown in case of TMA and TPA self-assemblies on graphene, when the transition between the monolayer to the multilayer coverage of the self-assembly is considered.

Furthermore, the results reported in the case of TCNQ / Bi₂Se₃ interface reveal the significant potential of TCNQ for the realization of ferromagnetic metal-organic coordination networks on the topological insulator surface. Indeed, this type of organic network represents only the first step towards the realization of an ordered array of local magnetic moments on a topological insulator (TI) surface and, possibly, drive the system to novel and relevant phenomena as predicted by TI theory.^[3]

In addition, the possibility to synthesize high-quality monolayer graphene on copper foil, which can be locally decoupled by the exposure to a suitable laser flux could allow to “write” paths of freestanding-like graphene, modulating in this way both its optical response and the local work function. This could pave the way to a tailored manipulation of the electro-optical response over large areas such those needed for the control of the electron emission from graphene in thermionic energy converter (TEC),^[4] electro-catalytic devices,^[5] graphene-based plasmonic systems,^[6] and many other fields.

Finally, as regards the study carried out on the iron clusters formation on the MgO surface, only further investigation on this system, and on related ones, will lead to a deeper understanding of the clusters properties in order to apply these interfaces to catalysis experiments.

References

- [1] H. Yang, A. J. Mayne, G. Comtet, G. Dujardin, Y. Kuk, Ph. Sonnet, L. Stauffer, S. Nagarajan and A. Gourdon, *Physical Chemistry Chemical Physics* 15(14) (2013): 4939-4946.
- [2] H.J. Karmel, T.Y. Chien, V. Demers-Carpentier, J. J. Garramone and Mark C. Hersam, *The Journal of Physical Chemistry Letters* 5(2) (2013): 270-274.
- [3] M. M. Otrokov, E. V. Chulkov and A. Arnau, *Physical Review B* 92(16) (2015): 165309.
- [4] S. J. Liang and L. K. Ang, *Phys. Rev. Applied* 3, 014002 (2015).
- [5] Y. Yan, Q. Liu, X. Dong, N. Hao, S. Chen, T. You, H. Mao and K. Wang, *Microchimica Acta* 183, 1591 (2016).
- [6] L. De Sio, U. Cataldi, T. Bürgi, N. Tabiryan, and T. J. Bunning, *AIP Advances* 6, 075114 (2016).

Acknowledgment

First of all, I would like to thank my group leader, prof. Raffaele G. Agostino, for giving me the opportunity to be part of his research team. Some years ago, he introduced me to the scientific research and I'm sure that I will never thank him enough for this.

I would also like to thank my PhD supervisor, Dr. Tommaso Caruso, for his guidance during the research activity and for pushing me to grow up in the academic life.

Many thanks also go to all guys of Agostino's scientific staff, in particular Victor, Francesco, Raffaele and Marco. I would like also to thank Giuseppe and Sara, my wonderful office mates, for their constant support. A big thank goes also to Rossella. I'm so proud to have such a colleague and friend so special. I would like also to give a big thank to Dr. Alfonso Policicchio, a dear colleague and a true friend, for his scientific support as well as constant and collaborative presence in all operating choices.

A special thank also goes to Dr. Marco Papagno and Dr. Daniela Pacilé, for their precious advice and scientific support, as well as for all research activity in which they have involved me. I'll never forget the three beamtime at the Elettra Synchrotron!

A big thank also goes to the Harald Brune research group (EPFL, Switzerland), where I spent five fantastic months during the last year of my PhD course. In particular, I would like to thank Dr. Marina Pivetta for her constant guidance, for her patience and for the support she gave me.

Special thanks also go to Prof. Giovanni Costantini (University of Warwick – UK) for the scientific collaboration, and to Dr. Ada Della Pia for her precious contribution to my scientific background on the wonderful world of scanning tunnelling microscopy.

I would also like to thank you all my PhD colleagues, in particular Ilenia, which showed me a lot of patience in the last year of the course. A big thank goes also to Giovanni Desiderio and Andrea Perrone for their continuous technical and scientific support.

I would like also to thank all the research groups with whom we have collaborated (and we will continue to cooperate in the coming years). A big thank goes also to all people that contributed to my academic growth.

Clearly, I would like also to thank my family, especially my brother that is all my life, and all the relatives that have supported me over the years.

Last but not least, I would like to thank all people who fill my life every day.

Curriculum Vitae

Personal information

Name: Oreste De Luca
E-mail: oreste.deluca@unical.it - oreste.deluca89@gmail.com
Nationality: Italian
Date of birth: 15/10/1989

Education and training

01/11/2014 – to date PhD course in Physical, Chemical and Material Sciences and Technologies (STFCM) - Università della Calabria, Italy

2012 – 2014 Master's degree in Physics, Università della Calabria, Italy
Master obtained on 02/10/2014
Final degree mark: 110/110 cum laude

2008 - 2011 Bachelor's degree in Physics, Università della Calabria, Italy
Bachelor obtained on 13/12/2011
Final degree mark: 110/110 cum laude

2003 - 2008 High school diploma, Scientific High School "G.B.Scorza", Cosenza, Italy

Research activities in national and international laboratories

01/05/2017 – 30/09/2017 Visiting PhD student at École polytechnique fédérale de Lausanne (EPFL), Switzerland.
Group leader: Prof. Harald Brune.

07/12/2016 – 13/12/2016 Beamtime at Elettra Synchrotron – Basovizza (TS), Italy

13/12/2015 – 19/12/2015 Beamtime at Elettra Synchrotron – Basovizza (TS), Italy

06/09/2015 – 14/09/2015 Beamtime at Elettra Synchrotron – Basovizza (TS), Italy

31/03/2014 – 30/06/2014 Visiting Master student at University of Warwick – Coventry, UK
Group leader: Prof. Giovanni Costantini.

Teaching experiences

10/2017 – to date Teaching assistant at the Undergraduate Program in Biological Sciences and Technologies - Department of Biology, Ecology and Earth Sciences - Università della Calabria (Italy)
Teaching subject: Physics

12/2016 – 09/2017 Tutor at the Undergraduate Program in Biological Sciences and Technologies - Department of Biology, Ecology and Earth Sciences - Università della Calabria (Italy)
Teaching subject: Physics

- 10/2016 – 09/2017 Teaching assistant at the Undergraduate Program in Biological Sciences and Technologies - Department of Biology, Ecology and Earth Sciences - Università della Calabria (Italy)
Teaching subject: Physics
- 06/2016 – 09/2016 Tutor at the Undergraduate Program in Mathematics and Computer Sciences
Department of Mathematics and Computer Sciences - Università della Calabria (Italy)
Teaching subject: Physics
- 05/2015 – 06/2015 Tutor at the Undergraduate Program in Engineering Management -
Department of Mechanical, Energy and Management Engineering - Università della Calabria (Italy)
Teaching subject: Physics

Publications

1. “STM and XPS investigation of Zinc(II) tetraphenylporphyrin (ZnTPP) adsorption on Au(111) surface”. O. De Luca, T. Caruso, I. Grimaldi, D. Pacilé, A. Policicchio, V. Formoso, M. Papagno and R.G. Agostino. – In preparation
2. “Nile red self-assembly on Au(111) surface”. T. Caruso, O. De Luca, M. Turano, A. Ionescu, N., Godbert, A. Policicchio and R.G. Agostino. – In preparation
3. “Different spectroscopic behavior of coupled and freestanding graphene monolayer deposited by CVD on Cu foil”. E. Cazzanelli, M. Castriota, A. Fasanella, R. Grillo, O. De Luca, A. Policicchio, G. Desiderio, R.G. Agostino, M. Giarola, and G. Mariotto. – In preparation
4. “Characterization of graphene grown on copper foil by Chemical Vapor Deposition (CVD) at ambient pressure conditions”. E. Cazzanelli, O. De Luca, D. Vuono, A. Policicchio, M. Castriota, G. Desiderio, M. P. De Santo, A. Aloise, A. Fasanella, T. Rugiero, R. G. Agostino. – Submitted. Manuscript ID JRS-17-0312. Accepted with minor revision.
5. “TCNQ physisorption on the Bi₂Se₃ topological insulator.” A. Della Pia, S. Lisi, O. De Luca, D. Warr, M. M. Otrokov, Z. S. Aliev, E. V. Chulkov, R. G. Agostino, A. Arnau, M. Papagno and G. Costantini. – Submitted
6. “Monolayer-to-thin-film transition in supramolecular assemblies: the role of topological protection”. A. J. Marsden, Z. P. L. Laker, O. De Luca, A. Della Pia, L. M. A. Perdigao, G. Costantini, N. R. Wilson. *Nanoscale*, 2017, 9, 11959–11968.
7. “FePc Adsorption on the Moiré Superstructure of Graphene Intercalated With a Co Layer”. G. Avvisati, S. Lisi, P. Gargiani, A. Della Pia, O. De Luca, D. Pacilé, C. Cardoso, D. Varsano, D. Prezzi, A. Ferretti, and M. G. Betti. *J. Phys. Chem. C*, 2017, 121 (3), 1639–1647.
8. “Chemical bond and charge transfer dynamics of a dye-hierarchical TiO₂ hybrid interface”. C. Castellarin-Cudia, T. Caruso, E. Maccallini, A. Li Bassi, P. Carrozzo, O. De Luca, A. Goldoni, V. Lyamayev, K. C. Prince, F. Bondino, E. Magnano, R. G. Agostino, C. S. Casari. *J. Phys. Chem. C*, 2015, 119 (16), 8671–8680.